Development of a coupled simulation tool for urban building energy demand, district energy systems and microclimate modeling

Georgios-Evrystheas Kyriakodis

Université de La Rochelle - UFR Science et Technologie
Laboratoire des Sciences de l'Ingenieur pour l'Environment

THÈSE

Présentée par

KYRIAKODIS Georgios - Evrystheas

Pour l'obtention du
Doctorat de L'Université de La Rochelle
Spécialité Génie Civil

Development of a coupled simulation tool for urban building energy demand, district energy systems and microclimate modeling

Directeur de thèse: **BOZONNET Emmanuel**
Co-directeur de thèse: **RIEDERER Peter**

Thèse soutenue le 26 août 2020

Composition du jury:

AUGENBROE Godfried Emeritus Professor, School of Architecture Georgia Tech Energy Faculty, USA	Rapporteur
SANTAMOURIS Mattheos Anita Lawrence Professor of High Performance Architecture, University of New South Wales, Australia	Rapporteur
INARD Christian Professor, Université de La Rochelle	Examinateur
MENEZO Christophe Professor, Université Savoie Mont Blanc	Examinateur
MUSY Marjorie PhD, Chercheur, CEREMA Ouest	Examinatrice
WOLOSZIN Monika Professor, Laboratoire LOCIE Université Savoie Mont Blanc	Examinatrice
BOZONNET Emmanuel MCF HDR, Université de La Rochelle	Examinateur
RIEDERER Peter PhD , Centre Scientifique et Technique du Bâtiment, CSTB	Examinateur
PEIRANO Eric Deputy General Director in charge of R&D of Efficacity Institute	Invité
MURESAN Cristian PhD, Head of Future Building ENGIE Lab CRIGEN	Invité

In Memory of my grandfather *Georgios Kostoglou*

Acknowledgements

First and foremost I would like to express my sincere gratitude to my supervisors *Asst. Pr. Bozonnet Emmanuel*, and *Dr. Riederer Peter* for giving me the opportunity to extend my scientific background and knowledge by this wonderful project on the topic: *Development of a coupled simulation tool for urban building energy demand, district energy systems and microclimate modeling*. Without their motivation, patient guidance, tremendous encouragement and, thorough support this thesis would not have been possible.

A special thank you to my esteemed professor - *Santamouris Mattheos* for his invaluable tutelage during all the years of my studies.

My gratitude extends to the *Laboratoire des Science de l'Ingenieur pour l'Environment* for the funding opportunity to undertake my studies at the Department of Civil Engineering, University of La Rochelle under the framework of the PEDOBUR project, as well as to the directors of the hosting institutes *Pr. Inard Christian* and *M. Guiot Thierry*, from the University of La Rochelle and the CSTB of Sophia - Antipolis respectively.

I would like to thank the members that completed the scientific committee, *Pr. Augenbore Godfried*, *Pr. Menezo Christophe*, *Pr. Woloszin Monika*, *Dr. Musy Marjorie* and the invited members of the committee *Dr. Peirano Eric* and *Dr. Muresan Cristian* for their precious comments on my thesis work.

Some special words of gratitude go to my close friends *Dr. Kabore Madi* and *Dr. Falaize Antoine* for introducing me to the french society, softening my sentiments, and for their kind support. I also appreciate all the support I received from the Ph.D. students in LaSiE and CSTB. It is their kind help that has made my study and life in France favorable.

Last but not least, my deepest gratitude goes to my parents, *Mike Kyriakodis* and *Nina Kostoglou*, my sisters *Eleni* and *Athina Kyriakodi* for their unconditional love and support; to my grandmother *Eleni Labropoulou-Kostoglou* for acting as pedagogue and supporter to all of my life; to my partner, *Dr. Kyrou Christina*, who inspired me with her skills and her unconditional love.

G-E Kyriakodis

Abstract

This PhD work investigates the complex links between urban physical processes, through the development of coupled simulation platforms to account simultaneously for building energy demand, individual or district energy systems, and urban microclimate. The spatial and temporal scales correspond to urban neighborhoods under explicit geometries, and annual simulations respectively. Several coupling strategies have been evaluated, regarding thermal efficiency indicators, and the determination of the diversity of coupled phenomena. The synchronous coupling schemes can effectively assess the dynamical interactions between buildings and the local microclimate. Nevertheless, the coupling variable is sensitive to the thermal properties of the building. The simplification of the urban canopy layer to a single-node description reveals significant variability in building energy demand. Besides, the developed model has been employed to assess the thermal performance of an urban neighborhood in La Rochelle. The transition from local energy systems to the district energy network eliminates anthropogenic heat from buildings, and improves the outdoor thermal comfort conditions, acting as a local heat island mitigation strategy. However, it is associated with an energy penalty due to the ground losses of the piping circuit. This energy penalty is amplified when a passive mitigation strategy (cool materials) is implemented concurrently.

Keywords: Urban Building Energy Modeling (UBEM), microclimate modeling, site-specific effects, synchronous coupling, chaining coupling, district energy network (DEN)

Résumé

Ce travail de thèse aborde les liens complexes entre les processus physiques urbains, par le développement de modèles couplés pour tenir compte simultanément de la demande énergétique des bâtiments, les systèmes énergétiques individuels ou de quartier, et du microclimat urbain. L'échelle spatiale correspond aux quartiers urbains explicités géométriquement, et l'échelle temporelle est annuelle. Différentes stratégies de couplage ont été évaluées, pour leur capacité de représentation des effets thermiques, et des phénomènes couplés. Les schémas de couplages synchrones sont efficaces pour les interactions dynamiques entre bâtiments et microclimat. Néanmoins, ce couplage est sensible aux propriétés thermiques du bâtiment. La simplification de la canopée urbaine á un noeud de calcul entraîne une variation significative de la demande énergétique. Par ailleurs, le modèle développé a été utilisé pour évaluer les performances thermiques d'un quartier de La Rochelle. Le remplacement des climatiseurs individuels par un réseau urbain de froid élimine la contribution anthropique des bâtiments, et améliore le confort thermique extérieur, agissant comme une stratégie d'atténuation locale d'îlot de chaleur. Cependant, il entraîne une pénalité énergétique due aux pertes par le sol du réseau urbain. Cette pénalité énergétique est amplifiée lorsqu'une stratégie d'atténuation passive (matériaux froids) est mise en oeuvres simultanément.

Mots clés: modélisation énergétique des bâtiments urbains, modélisation du microclimat, effets spécifiques au site, couplage synchrone, couplage chaînage, réseau énergétique du quartier

Contents

Theoretical Background

Chapter 1

Existing Challenges in Urban built Environment

Contents

1.1 Urban growth and climate change

Urbanization is defined as the spatial distribution shifting of a population from rural to urban areas [1]. This population displacement causes severe alterations of the urban environment's land cover and use by increasing buildings and infrastructures. The even growing urbanization process has manifold social impacts, continuously affecting the needs, cultural habits and lifestyle of the urban population. Unequivocally, the emergency for the access of population in more and more services (i.e. transportation, telecommunication etc) is intimately related to increasing energy consumption.

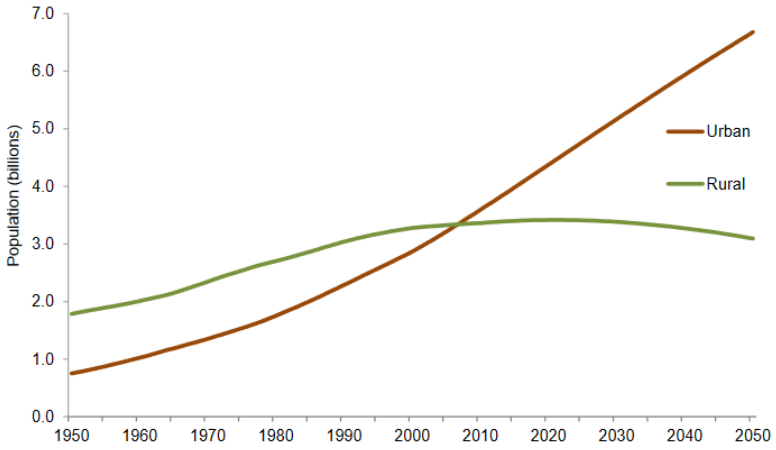

Figure 1.1: Actual and projected population growth, source: [1].

More in detail, 1950 can be determined as the starting point of urban growth. At this period 70% of the global population was located in rural areas. In the last decade, urban inhabitants exceeded for the first time the rural ones, as shown in Figure 1.1. Population projection to 2050, highlights the increasing trend with an estimated rate of almost 70% for the city's inhabitants compared to rural, reversing the regime of residence in almost a hundred years.

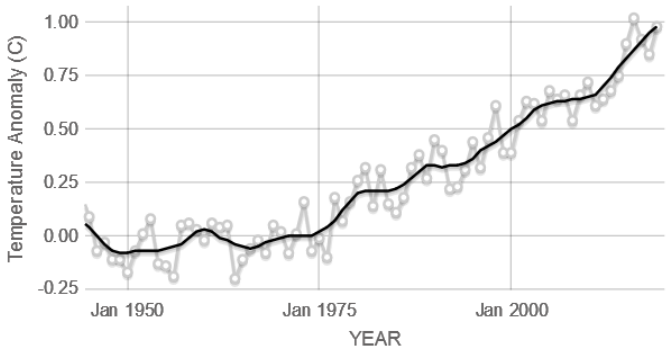

Figure 1.2: Global surface temperature anomaly relative to base period 1951-1980 average temperatures, source: NASA's Goddard Institute for Space Studies.

At the same time, the Intergovernmental Panel on Climate Change (IPCC) in the Fifth Assessment Report claimed that human activity constitutes the dominant cause of the observed warming. According to the last published report, entitled "Global Warming of 1.5^{o}C", the

human-induced warming reached approximately 1^{o}C. The latter is evident in the global temperature tracking service, Figure 1.2. The global surface temperature observed anomaly (as shown in Fig. 1.2), is attributed to the continuous increase of the urban population (Fig. 1.1), showing a corresponding rising trend of 1^{o}C. This climate behavior is strongly related to GHG emissions, especially with the levels of carbon dioxide in the atmosphere, which are mainly affected by the burning of fossil fuels.

1.2 Energy regime & challenges

The building sector constitutes the dominant energy consumer of France and Europe approximating 42% (Figure: 1.3) and 39% [2] of the total energy use respectively. In parallel, the total building use of electricity reaches 37%. Since France is a heating dominated country, the total energy consumption for heating is almost 36% [3].

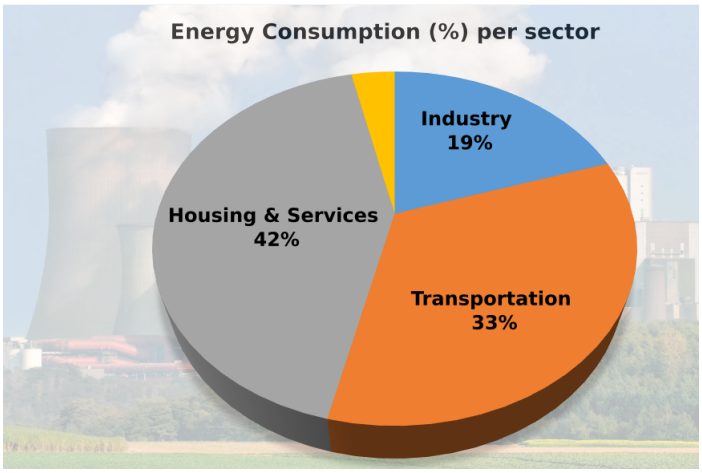

Figure 1.3: Energy consumption per sector in France.

In parallel, the final energy consumption in the residential sector for cooling in Europe represents a very small fraction of end-use, reaching 1.3%. It is highlighted that 100% of the amount for space cooling, is associated with electricity. Nevertheless, the cooling degree days increased significantly from 76.02 ^{o}C.days in 2009 to 104.78 ^{o}C.days in 2017. For France, the respective shift during the same period is 23.92 ^{o}C.days. At the same time, heating degree days illustrate a slight decrease from 2389.49 ^{o}C.days to 2337.95 ^{o}C.days [4].

Although the cooling energy consumption is still low compared to the heating one, the global temperature increase and the increasing trend of building construction in developing countries tend to deregulate the thermostat of the cities. According to [5], cooling is the fastest-growing end-use in buildings. Globally, the energy demand for cooling has been tripled between 1990 and 2018, leading to a 2000 TWh amount of consumed electricity. From this amount, almost 50% is due to space cooling in buildings, as demonstrated by the daily peaks in Beijing during the summer heatwave of 2017.

To this end, the cheaper and easier to install solution for cooling provision is is the usage of AC units (ACU). It is remarkable that a rise of 15% in the global AC sales has been reported between 2017 and 2018. This increase, has been attributed to the extreme heat events occurred

in 2018 [5]. The growing cooling demand impacts distribution capacity, placing under stress energy providers [6]. We will present further in this thesis several studies related to cooling consumption (especially the usage of ACU) and its interconnection with the local warming.

1.2.1 Built environment adaptation strategies

The European Union has committed to 80-95% GHG reduction by 2050 as part of its roadmap for moving to a competitive low-carbon economy in 2050 [7]. Moreover, the Energy Performance of Buildings Directive [8] requires all new buildings to be nearly zero-energy by the end of 2020. New buildings with implemented energy management systems and sustainable energy technologies can meet these targets. However, at least 75% of the building stock (70-80% of this is residential) is already in existence and it will be present in the next decades. Studies on European buildings have shown that more than 40% of residential buildings have been constructed before the 1960s when energy building regulations were limited or non-existent [9]. This has a serious impact upon their energy performance and carbon footprint. It has been found that older buildings consume on average 5 times more than new ones [10].

In this context, the existing knowledge and experience embedded with the development of new efficient materials and energy solutions as well as the integration of renewable energy sources lead to radical policies and a more sustainable way of construction. Considering buildings as a unified system with their ambient environment, the perspective of single building elements is shifted towards the urban neighbourhoods and districts. In this proof of concept, several national (e.g., ÉcoCité[1]) or higher scale projects consider buildings as part of a system in which the proposed solutions require multidisciplinary approaches. As an example, the perception of "resilient cities", defined as a city in transition that mobilises collective intelligence, adapts its operations, and cooperates with its surrounding territories tend to gain the acceptance of policymakers and stakeholders. The City Resilience Strategy is one of the core tools that propels 100 Resilient Cities [11] - member cities through the process of building and urban resilience. Furthermore, large scale rehabilitation projects of open-spaces have been realized [12] or they are on-going in order to adapt urban neighbourhoods in the existing challenges, in the forthcoming decades. One can mention the research article [13], where the authors analyse and present the mitigation potential of more than two hundred real scale urban rehabilitation projects. To conclude, since the built environment dominates the energy regime, it is straightforward to represent an efficient and feasible option for mitigation and adaptation plans.

1.2.2 Transition to energy districts

The policy framework combined with various initiatives towards zero energy and zero carbon future world, have identified the pivotal role of buildings in this transition. The conception of zero energy buildings is practically feasible and economically viable at individual building level especially for new constructions [14], nevertheless, the transition for the entirety of building stock is not feasible. A possible solution to overcome this problem, is by employing a "zero energy district" which will treat the urban neighborhood as a unity. The latter, has the principal ambition to provide environmental and social benefits, considering an "energy trading" concept within and among the district's subunits [15]. An energy community-district can facilitate the

[1] updated on 2018, aiming to respond to the challenges of sustainable development and cohesion of districts

local generation and operation of renewable energy and manage the energy distribution by developing local scale connections such as micro-grids. The local grids can play a crucial role in energy transmission and distribution, especially considering that by 2050 almost half of EU households are expected to be producing renewable energy [16]. Thus, neighboring buildings can directly contribute to each other's carbon reduction target by sharing the energy surplus through the potential micro-grid installation. Moreover, the construction (or rehabilitation) of high energy performance buildings combined with their optimal positioning inside a district, can allow them to act as active barriers on climate forces (e.g., providing solar shadings to others) which indirectly affect the thermal performance of the neighboring ones, without requiring an additional intervention on them.

1.2.3 From individual to district energy systems

The utilization of individual or centralized (at building scale) energy systems constitutes the most common solution for providing heating or cooling. The boundary expansion of building research field combined with the decentralized energy generation is gaining prominence in research and policy-making circles, allowing urban planners to invest in the development of district energy system solutions. The most common type of district energy system is the district heating and/or cooling network, usually consisted of a group of buildings with a shared facility generating the required power, in which the distribution of the fluid (water) circulates through tubes' connection [17]. According to [18] and [19], the beneficial role of a district energy system can be expressed by:

- improved efficiency compared with traditional heating and cooling systems,
- increase of available area and flexibility in building design
- enhancement of acoustic comfort,
- enhancement of energy management,
- penetration of local energy resources,
- minimization of operational cost for building owners and tenants,
- minimization of waste heat

Nevertheless, the initial investment combined with the operational cost of the piping network encompasses significant drawbacks [20].

In the last years, given the growing cooling demand, the performance of district cooling networks compared to conventional cooling systems has attracted attention. A recent study in Hong Kong [21], revealed that a district cooling system consumes approximately 15% less primary energy compared to conventional air conditioning units while at the same time the operational cost is reduced by 10% for a subtropical case study in Hong Kong, under various control strategies. We mention that the energy loss due to the piping system is not taken into account in this study. Moreover, according to International District Energy Association (IDEA) a cooling network improves the air quality of the local district as a combustion-free system and contributes to the improvement of the global environment. However, in the existing literature,

quantitative information regarding cooling networks and local overheating mitigation are scarce. In Europe, as shown in Figure: 1.4, there are few installations of district cooling systems, especially in the southern Europe, where the UHI effect is more intense.

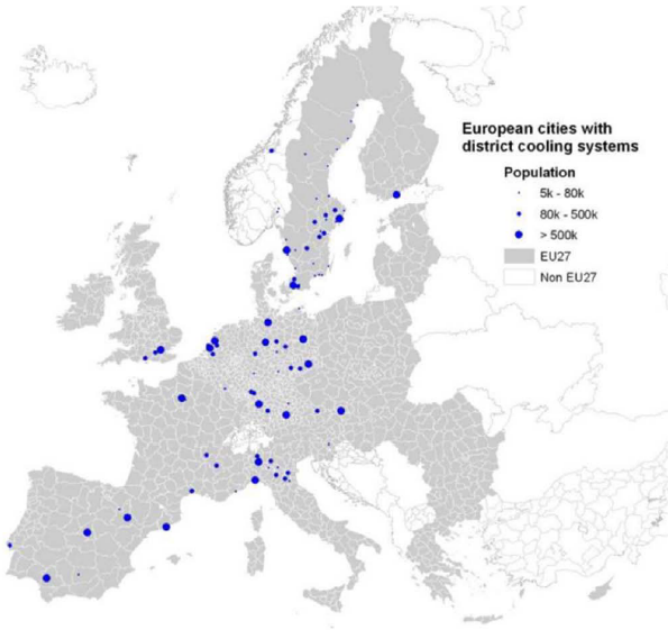

Figure 1.4: Distribution of district cooling systems in Europe, source: [20].

1.3 Local climate challenges

1.3.1 UHI effect: Causes and implications

The urban heat island phenomenon refers to the increase of the ambient temperature of cities compared to their surrounding suburban and rural environment (Figure: 1.5). Increased urban temperature is the result of the positive thermal balance of cities caused by the additional heat released and stored in the urban structure, and the lack of low temperature environmental sinks [22]. The urban heat island is the most studied phenomenon of climate change, and there are more than 400 cities around the world where experimental documentation is available [23]. The amplitude of the phenomenon varies as a function of the local characteristics and of the strength of the heat sources and may exceed 6-7 K [24]. EPA [25], summarizes the main factors that contribute to the development of the phenomenon as:

1. **The thermal and optical properties of urban materials** characterized by increased heat capacity and absorptivity, lead to higher heat storage and thus to higher surface temperatures. As a consequence, the air temperature adjacent to them is heated but also the amount of radiative exchanges with surrounding surfaces is higher.

2. **The urban geometry** obstructs wind flow circulation and increases the thermal mass of the city. Heat-trapping by multiple reflections and emissions contribute to heat island intensity.

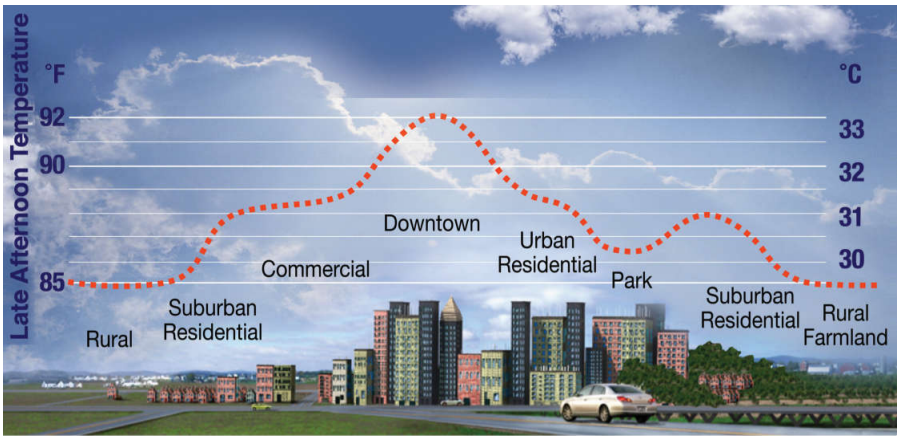

Figure 1.5: Temperature distribution over a city, (adapted from: ebook of Abstracts from the 5th International Conference on Countermeasures to Urban Heat Islands, Hyderabad, 2019).

3. **Waste anthropogenic heat** rejected from energy systems, transportation and industrial processes contribute to the phenomenon.

4. **The reduction of urban greenery** decreases natural shading and the potential of air temperature decrease through the evapotranspiration mechanism.

5. **Air pollution** increases the longwave radiation emitted from the atmosphere to the earth's surface.

6. **Weather conditions** influence the magnitude of the phenomenon especially under low wind speed and clear sky conditions.

7. **The geographic location** of the city, as the presence of water bodies (rivers, sea) or physical obstacles (mountains) develops microscale mechanisms of wind circulation (e.g., sea breeze).

Given the definition and the main contributors of the UHI effect, it is straightforward to provide a classification between the different types of this phenomenon. Each of the types follows a different methodological path to be analysed or studied. According to [26], [27], and [28], four types can be detected:

- The subsurface UHI or UHI_{Sub}, refers to the temperature difference of soil (aquifer can be included) between urban and rural space.
- The surface UHI or SUHI, refers to the temperature difference in the interfaces between build environment or ground (rural) with the adjacent air.
- The canopy layer UHI or CUHI, is the difference between the air temperature of a city with the rural areas inside the canopy layer (surface to roof-top).
- The boundary layer UHI or UHI_{UBL} is the air temperature difference from the canopy layer up to the ABL (approximately at 1.5km), compared to similar elevations of the rural region.

At UHI_{Sub} type, the soil and the subterranean built fabric are affected. The temperature increase at this level might question the quality of the supplied water but also enhances the geothermal capacity for space heating [29] when geothermal energy of shallow aquifers technology is considered. It can be modelled with heat diffusion methods considering the subsurface energy balance or monitored with underground sensors and logging equipment conducted in wells.

The SUHI is mainly a local scale phenomenon, which can be monitored either in-situ with sensors attached to the surface (IR-thermometers can effectively capture the phenomenon) or with satellite images. It can be modelled using the surface energy balance approach.

The CUHI is also a local scale phenomenon. It can be monitored from air temperature sensors located in fixed spots, usually protected by meteorological shelters. There are also many examples where the monitoring campaign is carried out through mobile stations with attached sensors. The modeling technique is more complicated than the SUHI as coupled phenomena occur at this scale. A coupled surface and volume energy balance could be an efficient modeling approach.

The UHI_{UBL} is a mesoscale phenomenon. It is usually captured by meteorologists using either meteorological towers or balloons enhanced with sensors. Lidar techniques are also commonly used. It can be modelled with the energy balance method of the boundary layer (the urban canopy level represents the boundary). Usually coupled models are used to account for the interactions between free atmosphere - ABL and the roughness sublayer.

To this end, the implications caused by several types of UHIs must be assessed, as they influence both the outdoor environment and the energy consumption of the buildings.

1.3.2 Impact on energy Loads

The impact of UHIs on energy loads could be either beneficial or detrimental, depending on location and climate. As an example, a heating-dominated country can be positively affected by the presence of the phenomenon, as the heating needs can be reduced. On the contrary in warm or hot climates[2], the cooling energy needs are exacerbated [31] and the possible energy decrease during the winter period could not be compensated. Increased air temperatures are causing a respective boost in energy consumption for cooling. To maintain the indoor thermal comfort at adequate levels, a wide usage of cooling systems is generally employed. Eventually, this reciprocal procedure increases further the outdoor air temperature and thus the cooling loads. In the city of New Orleans (USA), it is estimated that a peak urban electric demand increases 1.5% to 2% for 0.6^{o}C increase in summertime temperature [32]. Similar outcomes have been documented for the city of Los Angeles (USA) [31]. It is estimated an energy penalty of around 150.000$ per hour due to the added electricity demand of 1.5 GW caused by the UHI effect for a period of 50 years. At the same time, a comparative assessment conducted from several studies, showed that the potential rise of the electricity demand varies between 0.5% and 8.5% per degree of temperature increase [33], as shown in Figure:1.6. In London, it is estimated that the ratio of cooling demand between a rural and a central cellular office is 86% during a hot typical week [34].

Moreover, steadily increasing temperatures have a significant impact on peak loads. For a study in Athens it is estimated that UHI causes an increase of peak demand by 30% [35]. The

[2]For France the central south and south-eastern regions are characterized by Mediterranean climates [30]

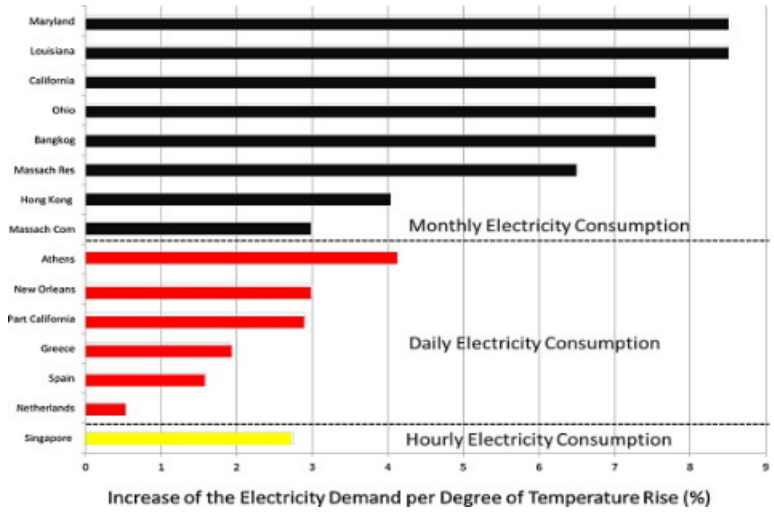

Figure 1.6: Increase of the electricity demand (%) per degree of ambient temperature rise for various countries, source: [33].

increase on peak demand is either increasing the price of kWh or it can role to power outages [25]. Consequently, the price augmentation could lead to further economic unbalances and rise further challenges as the energy poverty [36].

Energy poverty, defined as the difficulty or inability of a household to afford covering adequately its energy needs, due to high cost of energy, low household income and building's energy inefficiency, or a combination of them, has become a serious problem in Europe affecting mainly the vulnerable population. It has been estimated that rates of fuel poverty range from 10% to 15% of the European population [37].

1.3.3 Impact on human health

Human health can be affected by the rise of air temperature. Heatwave episodes combined

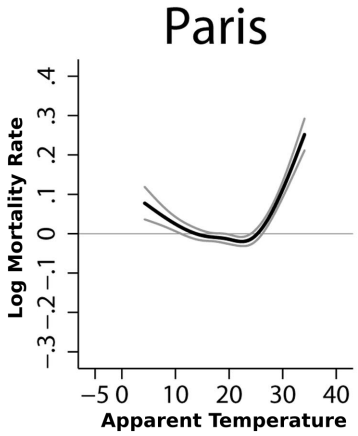

Figure 1.7: Exponential increase of mortality rate when air temperature exceeds 24.1^{o}C for the city of Paris, source: [38].

with high pollution levels could cause thermal stress, respiratory difficulties (or asthma), heat

cramps and exhaustion, non-fatal heat stroke, and heat-related mortality, especially to the vulnerable population. The aforementioned are caused due to the inability of the human body to release the excess heat through evaporation in the presence of high ambient temperatures and humidity levels. Some efforts to correlate the heat mortality with increased air temperatures exhibit an increase in mortality rate by 21.6% for people aged 65+ [39], while [38] illustrated that above a threshold temperature the mortality rate is increasing exponentially (Figure: 1.7). The European heatwave of 2003 caused almost 15.000 additional deaths, according to [40]. A study conducted for the most lethal day of the heatwave event in France found that the share of deaths increased by 9.5%, 16.5%, 26.8% and 46% for people aged higher than 65, 75, 85 and 95 [41] respectively, showing the sensitivity of vulnerable population.

1.3.4 Impact on ambient environment & air quality

The impact of UHIs in ambient air temperatures is evident and incontrovertible. The deterioration of the ambient environment is estimated through various terms, such as ecological footprint, pollutant concentration, ozone levels. It can be assessed with various methods, either by simulations and monitored data or by a combination of both.

In this context, a case study in Rome for UHI-affected lighting systems shows that a 1^oC ambient temperature increase would be responsible for an equivalent carbon footprint of 240 tCO_{2eq}/yr [42]. In Athens, a rough estimation of the ecological footprint of the city revealed that the last can potentially increase up to 2 times the city's area due to UHI, considering air-conditioning buildings [43].

Moreover, air quality is also affected by the presence of temperature anomalies. Pollutant concentration is strongly correlated with elevated air temperatures. The increased electricity consumption for cooling rises emissions from power plants due to the combustion of fossil fuels. Thus, the rising concentration of harmful emitted pollutants to human health, such as carbon monoxide (CO), sulphur dioxide (SO_2), particulate matter (PM) and nitrogen oxides (NO_x) contribute to air quality problems such as acid rain. Emissions of carbon dioxide (CO_2) contribute directly to global climate change.

Furthermore, the development and formation of the tropospheric ozone (O_3), which is also a harmful pollutant, are significantly affected by ambient air temperatures [44]. Ozone is produced when NO_x and volatile organic compounds (VOCs) react in the presence of sunlight. Elevated air temperatures accelerate the formation procedure. According to [45], the total amount of ozone captured in the roughness layer is larger in the presence of UHI. Besides, ozone concentration variations under conditions of polluted urban atmospheres lead to episodes of photochemical smog formation [46]. Decreased air temperatures can reduce peak concentrations by up to 7% and exceedance exposure by up to 16% [47].

1.4 Objectives & thesis structure

In this introductory chapter, we set the general existing challenges in the urban build environment in terms of energy and microclimate performance. The urban building energy demand as well as the several types of UHI effect are estimated through different approaches under various spatial and temporal scales. Distinct models have emerged intending to study and assess the building energy demand and the microclimate conditions. Nevertheless, there is still a lack

of a coupled approach that can simulate simultaneously the three pillars: urban energy demand, district energy systems, and site-specific effects concurrently. In parallel, given the transition from the individual (system or building) to the neighborhood scale and towards the development of zero energy districts, the policymaking process and the stakeholders require tools capable to evaluate and assess the concurrent effects of the aforementioned pillars as well as to pave the way for future policy implications and research initiatives.

This study aims to develop an integrated model to account for urban energy demand, individual and district energy systems, and site-specific effects, serving the neighborhood scale under explicit urban geometries and extended temporal conditions. The micro urban energy modeling approach, based on heat and mass transfer modeling, can estimate the surface and canopy heat island along with a detailed calculation of the waste anthropogenic heat rejected from energy systems and building exhausts that contribute to the local overheating. Consequently, this intermediate approach between typical building energy simulation and meso-scale ratio-coverage-governed models can investigate more accurately the building energy demand and the feedback generated by the aforementioned. The model can be used as a standalone model for studying the reciprocal physical interactions at this scale. Besides, it can be employed as an intermediate object, where the building heat discharges and the multinodal microclimatic conditions of the canopy layer can feed a mesoscale meteorological model. A further refinement of the thesis objectives is given in section: 2.7 after a detailed description of the existing models and approaches following the establishment of a coherent tool selection process.

The structure of the manuscript consists of two parts, the state of the art and the applications. The first part consists of two chapters, the ongoing introductory chapter and a second one where a comprehensive review of the methods, the approaches, and the developed tools operating at the neighborhood scale are presented. The second part of the manuscript presents the developed simulation models, pointing emphasis on the specific submodules that were used to conduct this research. Further on, we present the development of different coupling strategies between the models, from asynchronous to synchronous coupling schemes under different exchanged variables. A parametric study is conducted to verify the sensitivity of the coupled model under various boundary conditions and different building insulation capacities. In the last chapter, we implement the coupled model to a real case study with the objective to evaluate the neighborhood energy demand and the outdoor thermal comfort conditions. Moreover, we study the potential capability of a district energy network (DEN) to counterbalance the local overheating. In addition, we inspect if the energy penalty of the district network, due to the thermal losses of the piping circuit, can be balanced by the reduction of heat discharges of the individual systems and, by extension, the additional building energy consumption.

Chapter 2

On the need of an Urban building energy and microclimate model

Contents

2.1 Introduction

In the previous chapter, we presented the existing challenges of the urban build environment, pointing emphasis on the pivotal role of buildings and their implications in the local climate change. Taking the dependency and the interconnection of urban microclimate and building energy demand as a starting point, this chapter is devoted to the modeling challenges and the eminent approaches employed to describe the reciprocal phenomena that occur in these complex systems.

More in detail, the transition from building to district-scale requires the extension of the simulation boundaries, as well as a reduction in the high-fidelity complex phenomena using minimal computational resources. Based on the latter, we initially present the scale of interest adapted in this study and a short review of the reduced-order building energy modeling techniques. To adjust our study to the boundaries expansion, we progressively expand the research overview from building to urban scale, by simultaneously highlighting the dominant physical phenomena and the commonly used methods to study them. Further on, we describe the state of the art in the existing numerical packages, focusing on both urban building energy demand and local microclimate research fields. In this context, the eminent coupling techniques of the distinct models as well as the current limitations in the modeling research field, are in the foreground of the discussion. Our major aspiration is not only to eliminate these limitations but also to provide novel scientific and technological insights in the fundamental field of urban building energy modeling.

2.2 Scale of Interest

The urban environment constitutes a large physical system in which several interactions are taking place. Natural or artificial (man-made), these interactions occur at different scales, spatial or temporal, leading to discrete methodologies regarding the studying approaches and the implementation techniques employed to describe their particular characteristics. Due to the high cost and the limited resources of experimental and numerical requirements, a holistic research study is difficult to be conducted. Thus, before explicitly present the various methodologies obtained to capture the physical phenomena, one must first define the scale of interest.

The Earth's atmosphere is divided into several vertical levels, where the lowest part is in contact with Earth's surface defined as the Atmospheric Boundary Layer (ABL). The part of the ABL influenced by the presence of a city is called Urban Boundary Layer (UBL); its scaling varies during a day mainly due to surface heating and urban roughness. The lowest part of it, the Surface Layer (SL), consist of the Inertial Sublayer (ISL) - occupying the upper part, and the Roughness Sublayer (RSL) in which the airflow is determined from the individual elements. The part of the RSL where the human activities are taking place is called *Urban Canopy Layer* (UCL) extending from earth's surface up to the height of the main elements (buildings inside a city). This atmospheric part is governed by significant horizontal variations (heterogeneities) and comprises the "meeting point" of the outdoor and indoor environment.

To this end, the indoor environment is another unique system where humans and appliances, through operating schedules, act as heat sources enveloped by facets. The local microclimate is existent at this scale, penetrating either naturally through openings and cracks or mechanically through ventilation systems, forming the interior climate and the indoor thermal comfort lev-

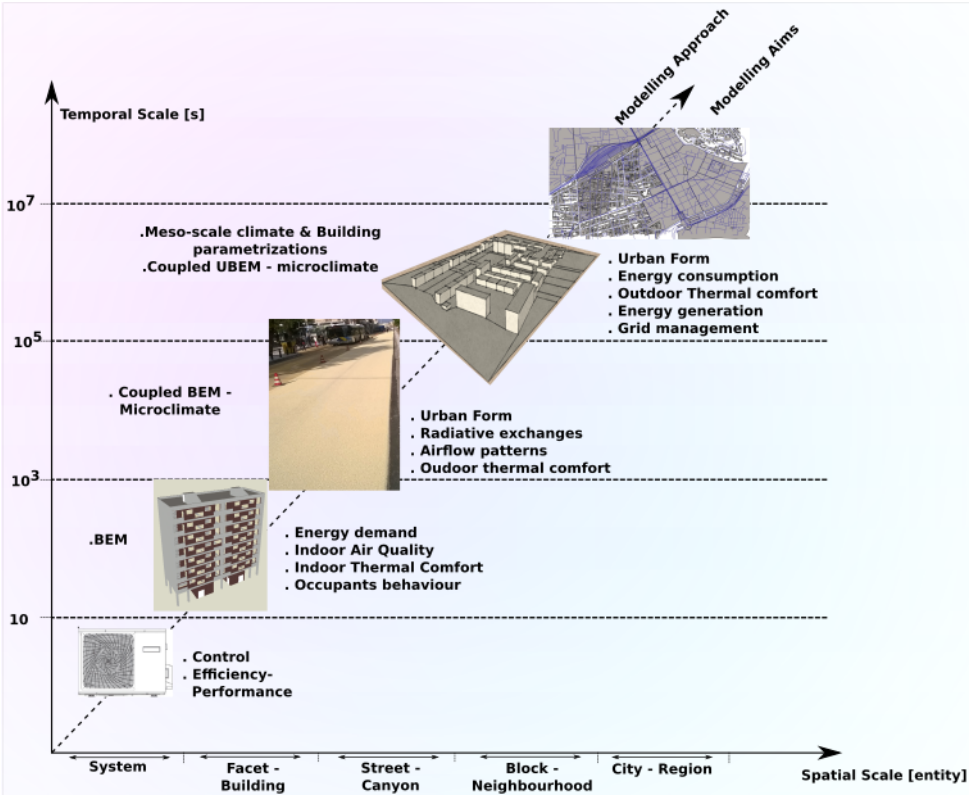

Figure 2.1: Temporal and spatial scales - modeling approaches and aims of the urban canopy layer.

els. Several such systems are unified to create bigger ones-the buildings, the climates of which are often controlled artificially due to the perpetual exchange with the outdoor environment through heat transfer mechanisms. Supporting this basic system, with overground urban infrastructures as roads or pavements and underground ones like distribution networks and pipelines, the establishment of a greater spatial level takes place, namely, the street canyon systems. At the latter scale, the fraction of the incident solar radiation is affected by neighboring elements; the urban facets exchange shortwave and longwave radiation due to different surface properties and the restricted sky view. In such a case, the natural cooling is limited, due to the presence of obstacles blocking the prevailing winds. Assembling such systems together with the urban vegetation, the generation of urban blocks and neighborhoods is established.

The present research aims to study the coupled interactions in the vertical layer of the urban canopy. Horizontally, the spatial scale ranges from the system entity to urban neighborhoods, while the temporal one, from seconds (system's control) to annual studies, as described by Figure: 2.1. Given the heterogeneities and the associated physical phenomena, we conclude that the scale of interest needs to be approached numerically in a fully 3-D context under a coupled indoor-outdoor approach.

2.3 Building Energy Modeling

2.3.1 Physical modeling approaches

In this section, we outline the eminent approaches standing out in the building energy simulation models. Since there is a variety of developed tools serving different fields of building simulation, like the dynamic simulation of building components, dynamic simulation of energy systems and their control, etc., the aim of this study abstains from scrutinizing individual models. We point emphasis on physical models and analyse their respective level of detail for building load calculation, energy modeling, and indoor air quality analysis. We only mention other interesting approaches like the inverse or data-driven modeling [48] or for example approaches based on Artificial neural networks (ANN) [49], [50] but further details are not provided in this manuscript.

To this end, we can categorize the several physical approaches to three main clusters. The nodal, figure: 2.2 (a), the zonal 2.2 (b) and the computational fluid dynamics (CFD) 2.2 (c). Their main common characteristic is the study of heat transfer mechanisms[1] with physical equations, based on the concept of thermal balance approach.

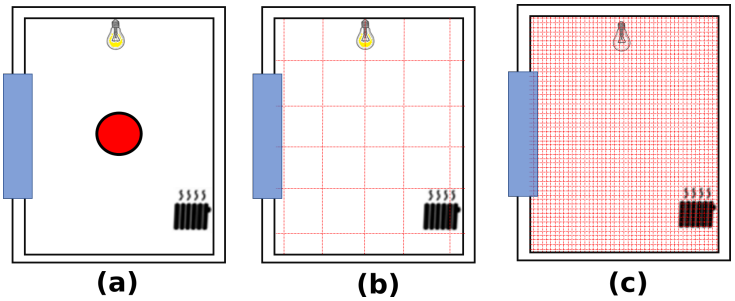

Figure 2.2: Representation of the eminent approaches of physical models in building energy simulation, (a) mono-zone nodal, (b) zonal, and (c) CFD.

The nodal approach considers each building zone as a homogeneous volume characterized by uniform state variables and thus the examined physical parameters are lumped into one node (room, wall, etc.), in which the thermal transfer equations are solved. The solution of the state variable system can be given either by transfer functions (like the response factors method) or by the concept of electrical analogy (RC method). Therefore, this approach is missing detailed outcomes in terms of spatial resolution but it can be extended in time scale and the annual thermal behavior of a building is examined through space-average calculations. The nodal approach is preferred in a wide variety of building simulation packages, including the well-known simulation tools TRNSYS [51], ESP-r[52], and EnergyPlus[53].

The zonal approach can be considered as the intermediate stage between nodal and CFD approaches. It is based on the division of a volume in several structured sub-volumes/cells, in which each cell is governed by thermal and mass balances. Hence, the state variables are computed in every cell, allowing the assessment of their spatial distribution, and thus the computational field is extended from 1-D to 2-D or even 3-D. A big advantage compared to the nodal approach is the ability to study the stratification of air temperature inside the volume,

[1] see Section:2.3.3

while on the other hand the flow profiles must be imported [54], [55]. The zonal approach is widely used in research developed tools [56], [57], [58].

The CFD approach is the more detailed one. The building volume is divided into fine segments, allowing a microscopic study at each element, using the balanced equations of fluid motion (Navier-Stokes). The solution of the physical problem employs a set of equations, where the principal outcome is flow velocity, and once it is calculated, other quantities of interest such as pressure or temperature may be found using dynamical equations. The great advantage of this method is the spatial definition and, if correctly done, its accuracy and application on a wide range of physical problems governed by flow mechanisms. On the other side of the spectrum, as the discretization increases, the simulation time is extended preventing calculations of annual simulations.

In the concept of a spatial scale extension, where the individual building is substituted by dozens, hundreds or thousands, and and by considering that the main aspiration of our research is the assessment of the annual building energy demand, the question of a competent approach selection tends to be gratuitous. Evidently, the nodal approach contains the key features that represent our objectives. Nevertheless, the similar concerns must be appropriately taken into account for the selection of the boundary conditions that enclose the studied elements, that is, the urban environment. In section 2.5.4, we follow the same inductive procedure for the selection of an appropriate approach for studying the building energy demand in regards to the urban microclimate.

2.3.2 Heat and mass transfer phenomena in Buildings

Considering the building as a system, the thermal balance principle can be applied. The heat exchange in buildings is described by three main mechanisms: conduction, convection, and radiation, where each of them contributes in several ways, analysed as follows (Figure:2.3).

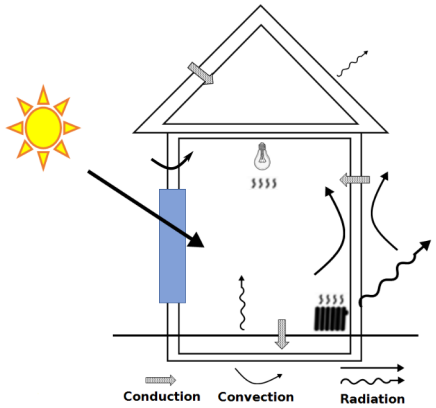

Figure 2.3: Heat transfer balance on a building.

Heat conduction through walls, roofs, and ground floors ($\Rightarrow$). Solar radiation gains through glazing elements by transmission and absorption ($\longrightarrow$). Internal heat gains from people, lighting, and equipment. Latent internal heat gains (losses) through evaporation (condensation) of water involving the latent heat of humidity. Convective ($\curvearrowright$) heat transfer from the building

envelope to the air or from internal surfaces of building elements to indoor air. Heat transfer by convection due to infiltration through cracks or openings and forced mechanical ventilation (fans). Storage in different building elements, both external (walls, roofs, floors) and internal (mass), resulting in the attenuation of internal temperature swing. Convective and radiative share due to artificial heating and cooling by HVAC equipment. Long-wave radiative heat transfer to the upper atmosphere (sky) and clouds; radiative heat transfer between the internal surfaces of building elements, or absorption of solar radiation and light radiation by internal surfaces.

2.3.3 Reduced-Order modeling techniques

2.3.3.1 Conduction

Conduction heat transfer, through slab elements, contributes to the building's thermal balance and consequently to the building loads and thermal responses. Transient (one-dimensional) conduction in a homogeneous slab (surface) is described by the heat diffusion equation:

$$\frac{\lambda}{\rho C_{\mathrm{p}}} \frac{\partial^2 T}{\partial^2 x} = \frac{\partial T}{\partial t} \tag{2.1}$$

where

λ = thermal conductivity [W/m^{2}K]

ρ = density [kg/m^3]

C_{p} = specific heat [J/kg K]

T = temperature at any point [K]

x = distance [m]

t = time [s]

There are several methods available in literature [59] that can perform a solution to equation 2.1, including:

1. Numerical methods such as finite difference and finite element methods, presenting high accuracy but are less computationally efficient.

2. Lumped parameter methods or [RC], representing an intermediate method of accuracy and computational time.

3. Z-transfer theory, including the response factors method, having a high degree of accuracy and are computationally efficient.

We briefly describe the last two methods, as further we will use them to describe the development of building models of the examined software.

RC method: in the RC method, the weight elements are treated based on the analogy between thermal and electrical resistance. This is analog to Ohm's law, with the heat flux replacing the current and the temperature difference replacing the voltage one. The method is taking into account the thermal capacitance of each layer in order to capture the "time delay" and the "Dumping" effects that occur on wall elements [60]. To do so, the thermal capacitance is

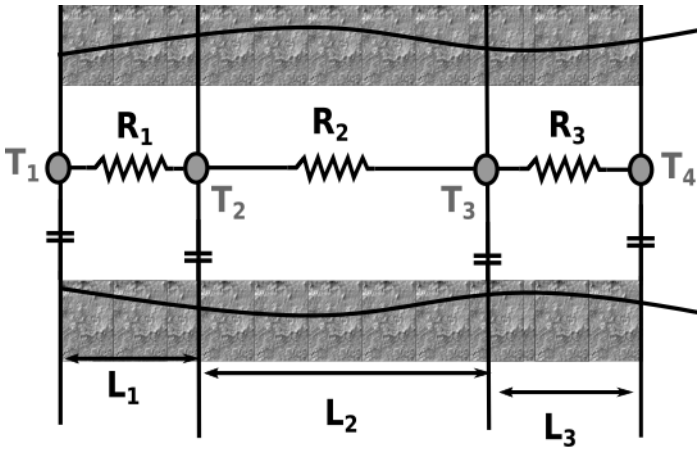

Figure 2.4: Representation of resistance capacitance approach.

usually lumped in the middle of the slab element, such as:

$$C = \rho C_{\mathrm{p}} L \tag{2.2}$$

Thus for a single layer, the *time constant* element will be given:

$$T_{\mathrm{c}} = C\frac{R}{2} \tag{2.3}$$

where

$$R = \frac{L}{2\lambda}$$

which can be used to calculate the requested temperature, as:

$$T_i(t) - T_i(0)\exp(-t/T_{\mathrm{c}}) = \int_0^t T_0(t')\exp[-(t-t')/T_{\mathrm{c}}]dt'/T_{\mathrm{c}}] \tag{2.4}$$

As shown in Figure 2.4, for multilayer slabs, the method treats them as discrete sub-elements where a number of resistances and capacitors are added proportionally to the discretization scheme. In this case, the Time constant element is defined as:

$$T_{\mathrm{c}} = \sum_{i=1}^{4} \rho_i C_{\mathrm{p},i} L_i \left(\frac{1}{h_0} + \sum_{j=1}^{3} \frac{L_j}{\lambda_j} + \frac{L_i}{2\lambda_i} \right) j \tag{2.5}$$

where ρ, C_{p}, L are the density [kg/m^3], specific heat [J/kg K] and thickenss [m] of the materials, and h_0, λ are the external heat film conductance [W/m^{2}K] and the thermal conductivity

[W/mK] (density-depended). From the aforementioned analysis, it springs that the Resistance (R) component describes the steady state properties while the time constant component (T_c) the transient ones. This is an important outcome, since in multilayer insulated walls, the overall R will be equal, no-matter the position of the insulation material, while the T_c will significantly vary. Usually, the method is preferred when the time discretization is small, such in case of thermal system and control simulations.

Response Factors method: this method relates the current heat flux with past and present values of outdoor and indoor surface temperature, through time series coefficients, utilizing a fixed time step ($2\Delta t$) and a triangular unitary excitation (1^oC), Figure: 2.5. These discrete time series coefficients are called *Response Factors*, $R_i(t)$.

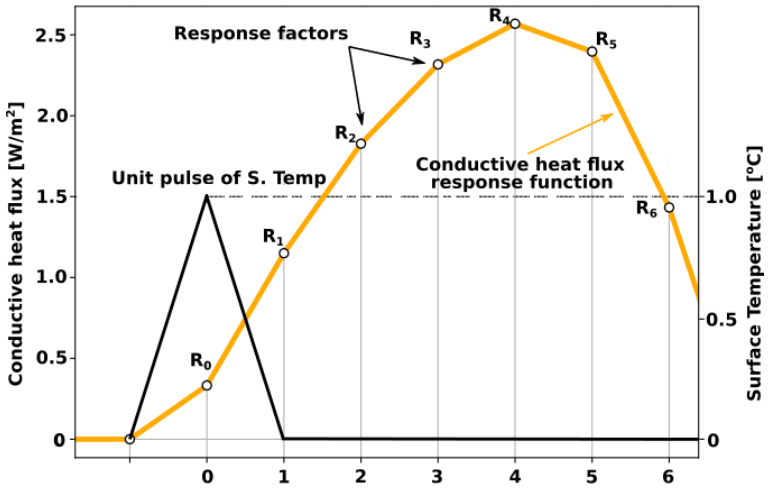

Figure 2.5: Surface temperature unit pulse and the corresponding conductive heat flux response.

More in detail, for a given physical system the relationship between an excitation and the system's response can describe the system's characteristics. If the system complies to linearity[2] and invariability[3], then the superposition [4] method can be applied (such as in Fourier series). Thus, the superposition is the sum of the discrete excitations, where the one can be treated independently from the other. As shown in Figure: 2.6, a continuous time-dependent function, can be analysed in discrete successive terms depending on the size of the time interval. The response of the unitary excitation (1,0,0,0,...), analysed in time-series will be a set of response factors, where the unitary term corresponds to the time of the peak (j=0). As an example, Figure: 2.5 shows the conductive heat flux through a slab element, resulted from the surface temperature input (unitary pulse). In general, the response R(t) of an excitation I(t), at time $j\Delta$ (j = 0,1,2,...,n) will be given in time series form as:

$$R_n = \sum_{j=0}^{\infty} R_j I_{n-j} \tag{2.6}$$

[2]the magnitude of the response is linearly related to the magnitude of the excitation [61]

[3]equal excitations applied at different times always produce equal responses [61]

[4]when a number of changes are taking place simultaneously in any system, each one proceeds as if it were independent of the others, and the total change is the sum of the effects due to the independent changes [61]

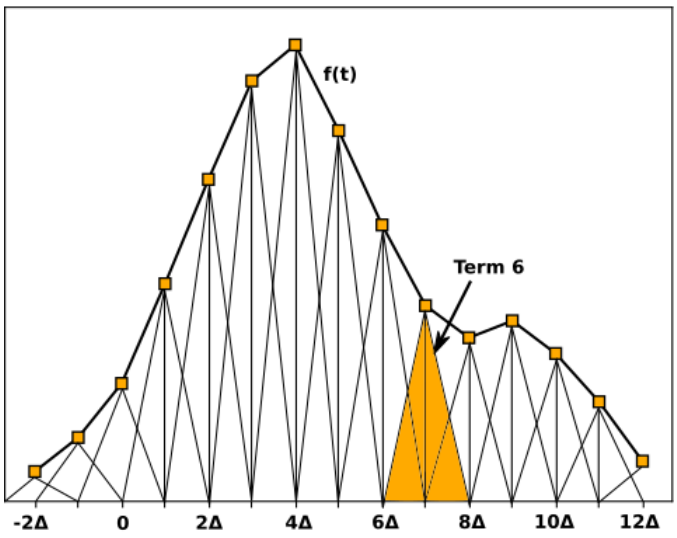

Figure 2.6: Time-series representation of a continuous function f(t); the sixth term of the time-series is depicted.

More precisely, for a multilayer wall, as the one depicted in Figure:2.7, given a unitary excitation of the indoor surface temperature, while keeping the exterior one constant, we can distinguish the overall flux through the wall in two components, the incoming flux X and the outgoing flux Y_{int}. It is proven that $Y_{int} = Y_{out} \equiv Y$ [62] and for a single layer slab the response factors X and Z are identical. Applying the superposition principle, the incoming conductive

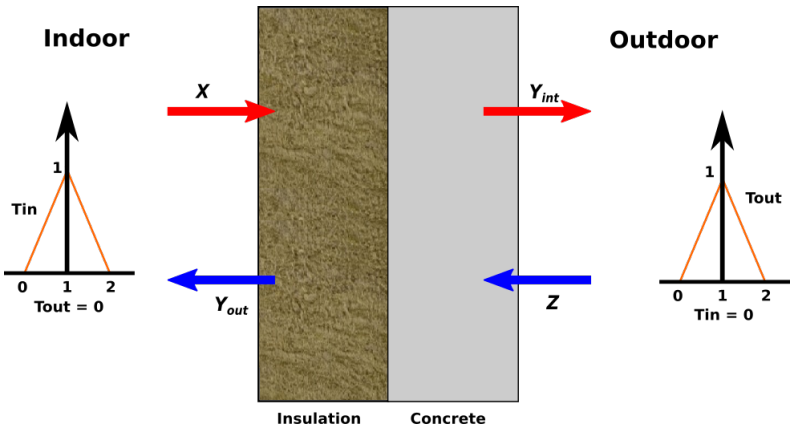

Figure 2.7: Flux response of a multilayer wall for a unitary solicitation for the interior (top) and exterior (bottom) surface temperature.

heat flux through the wall will be given:

$$\overrightarrow{\phi^{n}_{\text{cond},i}} = \sum_{j=0}^{\infty} Y_i^j T_{\text{se},i}^{n-j} - \sum_{j=0}^{\infty} X_i^j T_{\text{si},i}^{n-j} \tag{2.7}$$

This method can be extended as many times as the number of layers in a multilayer wall. Following the similar procedure for the outgoing heat flux through the wall **i**, we can estimate

it from:

$$\overleftarrow{\phi}^{n}_{\text{cond},i} = \sum_{j=0}^{\infty} Y_i^j T^{n-j}_{\text{si},i} - \sum_{j=0}^{\infty} Z_i^j T^{n-j}_{\text{se},i} \tag{2.8}$$

Equations 2.7 and 2.8 are integrated using a summation that tends to infinity. It is proven, that after a certain time step, these responses tend to approximate a constant value, depending on the wall structure. Thus, considering a threshold time range $j = N$ where the impact of the excitation is attenuating, we can assume that:

$$\frac{X_i^{j+1}}{X_i^j} = \frac{Y_i^{j+1}}{Y_i^j} = \frac{Z_i^{j+1}}{Z_i^j} = c \tag{2.9}$$

and using the summation properties, equations 2.7 and 2.8 become:

$$\begin{aligned}\overrightarrow{\phi}^{n}_{\text{cond},i} = {} & Y_i^0 T^n_{\text{se},i} - X_i^0 T^n_{\text{si},i} + \sum_{j=1}^{N} \left(Y_i^j - cY_i^{j-1}\right) T^{n-j\Delta n}_{\text{se},i} \\ & - \sum_{j=1}^{N} (X_i^j - cX_i^{j-1}) T^{n-j\Delta n}_{\text{si},i} + c\phi^{(n-\Delta n)}_{\text{cond},i}\end{aligned} \tag{2.10}$$

$$\begin{aligned}\overleftarrow{\phi}^{n}_{\text{cond},i} = {} & Y_i^0 T^n_{\text{si},i} - Z_i^0 T^n_{\text{se},i} + \sum_{j=1}^{N} \left(Y_i^j - cY_i^{j-1}\right) T^{n-j\Delta n}_{\text{si},i} \\ & - \sum_{j=1}^{N} (Z_i^j - cZ_i^{j-1}) T^{n-j\Delta n}_{\text{se`},i} + c\phi^{(n-\Delta n)}_{\text{cond},i}\end{aligned} \tag{2.11}$$

2.3.3.2 Convection

Thermal convection is the mechanism where energy is transported in a fluid (liquid or gases) by bulk macroscopic motion in addition to conduction. Since we study the heat transfer methods at building level, we are interested in convection mechanisms between indoor or outdoor air and surface elements (walls, roofs, floors), as well as bulk convection through infiltration and ventilation.

Surface Convection The dominant formulae used to calculate the surface convection is the one that corresponds to Newton's Law of Cooling, which associates the convective flux with the temperature difference of a solid surface and a fluid in contact with it. It is given from equation 2.12:

$$\phi_{\text{conv}} = hA(T - T_{\text{s}}) \tag{2.12}$$

where:

h is the convection or film coefficient [W/m^{2}K]

T is the bulk temperature of the air [K]

T_{s} is the surface temperature of the element [K]

Depending on the level of detail of the calculations, the convection coefficient (exterior) can be estimated from empirical average correlations [63] or it can be a constant.

Bulk Convection The bulk convection is the result of energy exchange between two fluid volumes of different temperatures. In building physics, the exchange of outdoor and indoor air through ventilation and/or infiltration results in sensible and latent heat gains. It is estimated using the following relationship 2.13:

$$\phi_{\mathrm{conv}}^{\mathrm{bulk}} = \dot{m}_a C_{\mathrm{p}} (T_o - T_i) = \frac{\dot{Q} C_{\mathrm{p}}}{\upsilon_o} (T_o - T_i) \tag{2.13}$$

where:

$\phi_{\mathrm{conv}}^{\mathrm{bulk}}$ is the sensible heat gain due to infiltration [W]

$\dot{m}_a$ is the mass flow rate of infiltration [kg/s]

C_{p} is the specific heat of air [J/kg K]

T_o is the outdoor air temperature [K]

T_i is the indoor air temperature [K]

$\dot{Q}$ is the volume flow rate of air [m^3/s]

υ_o is the specific volume of air [m^3/kg]

In case of latent heat gains, equation 2.13 is given by:

$$\phi_{\mathrm{conv}}^{\mathrm{latent}} = \dot{m}_a (W_o - W_i) i_{fg} = \frac{\dot{Q}}{\upsilon_o} (W_o - W_i) i_{fg} \tag{2.14}$$

where:

$\phi_{\mathrm{conv}}^{\mathrm{latent}}$ is the latent heat gain due to infiltration [W]

W_o is the outdoor air humidity ratio [kg H_2O vapor/kg dry air]

W_i is the indoor air humidity ratio [kg H_2O vapor/kg dry air]

i_{fg} is the phase change enthalpy [J/kg]

2.3.3.3 Radiation

Radiation is the dominant excitation that affects the surface and zone thermal balance in a building. Shortwave and longwave exchanges are treated differently. We will present these components for the interior incident solar radiation, while the exterior part will be treated in further section, as its calculation requires a spatial scale expansion beyond the building scale.

Indoor Shortwave radiation: estimating the transmitted shortwave radiation in a zone depends on the number, the orientation, and the area of openings and their optical properties; mainly the transmittance and absorption coefficients. Besides, this amount of radiation is partly absorbed and partly reflected in the weight elements of the zone. However, this is a very complex procedure (multiple reflections), and for annual thermal load simulations, it is generally computed in a simplified manner. Assuming that a ratio of the transmitted beam radiation is absorbed by the floor and the rest is reflected diffusely to the rest of the zone's surfaces and that the transmitted diffuse component is uniformly distributed to the vertical surfaces [60], then one can estimate the absorbed solar radiation, as:

$$I_{\text{vert}} = \frac{\sum_{i=1}^{M} I_{\text{d},i} + (1 - a_f) \sum_{i=1}^{M} I_{\text{b},i}}{\sum_{i=1}^{M'} A_j} \tag{2.15}$$

where I_{vert} is the absorbed solar radiation from vertical surfaces [W/m^2], $I_{d,i}$ and $I_{b,i}$ are the transmitted diffuse and direct radiation from window *i* in [W], a_f is floors absorptivity, M, M' are the numbers of windows and interior surfaces and A_j is the area of jth interior surface. In a straightforward manner, the absorbed solar radiation from the floor will be given:

$$I_{\text{floor}} = I_{\text{vert}} + \frac{a_f \sum_{i=1}^{M} I_{\text{b},i}}{A_f} \tag{2.16}$$

Indoor Longwave radiation: estimating longwave radiation is also a complex mechanism, thus, several assumptions must be taken into account. The most used method is the Caroll's [64] mean radiant temperature method, where all of the surfaces are represented as a fictitious one, characterized by the *Mean Radiant Temperature* (mrt). Then the net radiation can be described by the linear formula:

$$I_{\text{LW}} = h_{\text{rad}} A_i (T_i - T_{\text{mrt}}) \tag{2.17}$$

where h_{rad} is the linearized [60] radiation coefficient of a surface in [W/m^{2}K] given by 2.18, A is the area of surface *i* and T_i, T_{mrt} the surface temperature of element *i* and the respective mrt temperature.

$$h_{\text{rad}} = \frac{4\sigma \bar{T}_{\text{ref}}^3}{\frac{1}{F_i} + \frac{1-\epsilon}{\epsilon_i}} \tag{2.18}$$

and

$$F_i = \frac{1}{1 - A_i F_i / \sum_{i=1}^{N} A_i F_i} \tag{2.19}$$

The last set of equations requires the calculation of form factors or *view factors* (Equation:2.19). Since it appears in both sides of 2.19, it must be calculated computationally through an iterative scheme. The $\bar{T}_{ref}$ term denotes the reference temperature, which is approximated by a value of 300 K [60].

2.4 From building to urban scale

2.4.1 Energy balance of urban areas

The principle of energy balance is applicable in various elements of the urban systems such as buildings or urban volumes. Energy balance is the main statement of the conservation of energy and can be used at all spatial and temporal scales. By defining a conceptual volume such as the urban building-soil-air volume, as depicted in Figure: 2.8, the energy balance can

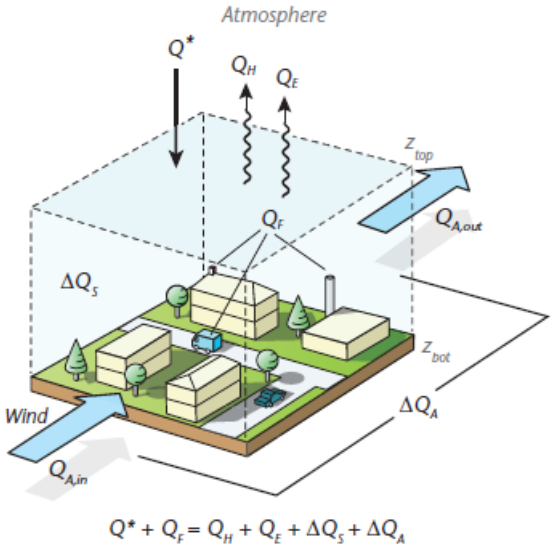

Figure 2.8: Schematic of the fluxes in the urban building-soil-air volume, source:[65].

be written:

$$Q^{\star} + Q_{\mathrm{F}} = Q_{\mathrm{H}} + Q_{\mathrm{E}} + \Delta Q_{\mathrm{S}} + \Delta Q_{\mathrm{A}}, \qquad [\mathrm{W/m^2}] \tag{2.20}$$

where:

$Q^{\star}$ is the net allwave radiation

Q_{F} is the anthropogenic heat flux density which is the associated released heat flux due to human activities

Q_{H} and Q_{E} are the sensible and latent heat flux densities

ΔQ_{S} is the net heat storage change by all the fabric of the city including its construction materials, trees, ground and air contained in the volume

ΔQ_{A} is the net energy added to, or subtracted from, the volume by advection.

In our study, the energy balance method is used for the sub-volumes of the urban canopy as given analytically in section 3.2.6.3, limited to sensible heat flux densities.

2.4.2 Radiation

Solar radiation is the most powerful component of heat transfer mechanisms, as it propagates without the presence of any medium. It drives the climate near earth's ground and regulates the thermal balance of surfaces. The heterogeneities of the urban form provide an uneven distribution of its incident part [66]. Quantifying the amount that reaches the studied urban geometry, is of great importance, since either building energy demand [67] or pedestrian thermal comfort are affected, while at the same time it can significantly affect the potential of zero energy neighbourhoods (nZEN) development [68]. In this framework, the availability of solar radiation must be calculated precisely, taking into account all of the dominant processes of radiation transfer in urban geometries, such as:

- the direct and diffuse components,
- the intricate shadowing events (solar masks),
- the reflected component based on surface optical properties,
- the longwave exchanges between urban surfaces and with the sky

In section 2.3.3.3, we described the radiation exchanges at building level (indoor). Deliberately, we omitted to describe the outdoor radiative exchanges, because the description requires the presence of other urban structures, forcing our study to a different spatial scale, the street canyon one or higher. The latter will be discussed in the next sections.

2.4.2.1 Shortwave radiation

Global radiation, is defined as the sum of the beam and the diffuse solar radiation components on a surface. Beam or direct radiation is the amount of radiation received from the sun without being scattered by the atmosphere, while diffuse is the one received from the sun after its direction has changed by scattering in the atmosphere. Given the definitions, it is straightforward that the calculation of the direct component is a matter of geometrical relationships between a plane surface and the position of the sun relative to that plane [69]. The calculation of direct part, can be found extensively in literature [70], [71]. The diffuse component, requires more complex algorithms and several calculation methods have been developed to describe it. Beam and diffuse, combined with the contribution of the ground reflected one, compose the total incident radiation on a surface, given as:

$$I_{\mathrm{T}} = I_{\mathrm{T,b}} + \underbrace{I_{\mathrm{d,Iso}}}_{\mathrm{a}} + \underbrace{I_{\mathrm{d,cs}}}_{\mathrm{b}} + \underbrace{I_{\mathrm{d,hz}}}_{\mathrm{c}} + I^{*}_{\mathrm{T}} \tag{2.21}$$

Clear sky experimental data proved that the distribution of the incident diffuse radiation is a function of cloudiness and atmospheric clarity. Moreover, it is suggested that the principal components for calculating it in a tilted surface, are composed of:

a) the isotropic part (Eq: 2.21a), received uniformly from the entire sky dome,

b) the circumsolar diffuse (Eq: 2.21b), resulting from forward scattering of solar radiation and concentrated in the part of the sky around the sun,

c) the horizon brightening (Eq: 2.21c), mainly presented in clear skies and concentrated near the horizon.

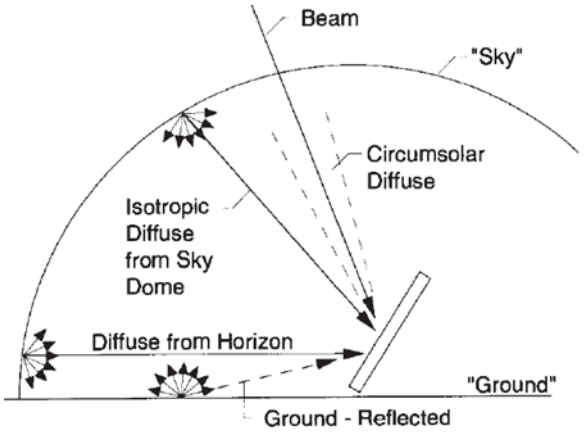

Figure 2.9: Schematic representation of the various parts accounting for the diffuse solar radiation on a tilted surface, source: [70].

2.4.2.2 Sky models

Isotropic sky: the isotropic sky model [72] is based on the assumption that the diffuse radiation is uniformly distributed over the complete sky dome concluding that the sum of the diffuse and ground-reflected radiation is the same regardless the orientation. Thus, the total solar radiation on a tilted surface is the sum of the beam contribution and the diffuse on a horizontal surface. An improved version of the latter, the so-called isotropic diffuse model [73], includes one more component of solar radiation diffusely reflected from the ground, given as:

$$I_{\mathrm{T}} = I_{\mathrm{b}} R_{\mathrm{b}} + I_{\mathrm{d}} \left(\frac{1 + \cos\beta}{2} \right) + I_{\rho_{\mathrm{g}}} \left(\frac{1 - \cos\beta}{2} \right) \tag{2.22}$$

where,

$R_{\mathrm{b}} = \dfrac{\cos\theta}{\cos\theta_z}$, and

$\cos\theta = \cos\theta_{\mathrm{z}} \cos\beta + \sin\theta_{\mathrm{z}} \cos(\gamma_{\mathrm{s}} - \gamma) \sin\beta$

In the above relations, β is the angle between the examined and the horizontal surface, while γ is the surface azimuth. The terms γ_{s}, θ_{z} and θ denote the solar azimuth, zenith and incidence angles respectively [69].

Anisotropic sky - Perez model: most of the developed anisotropic sky models improved the isotropic one by taking into account the circumsolar diffuse and horizon-brightening components on a tilted surface instead of treating only the isotropic one. The Perez model is based on

a more detailed representation of the diffuse components, taking into account the highlighted components of Equation 2.21. It can be written as:

$$I_{\mathrm{d,T}} = I_{\mathrm{d}}\left[(1-F_1)\left(\frac{1+\cos\beta}{2}\right) + F_1\left(\frac{a}{b}\right) + F_2\sin\beta\right] \tag{2.23}$$

where F_1 (Eq: 2.24) the "Circumsolar Brightening Coefficient" and F_2 (Eq: 2.24) the "Horizon Brightening Coefficient". These empirically derived reduced brightness coefficients are functions of sky clearness ϵ and sky brightness Δ parameters as well as of the zenith angle.

$$F_1 = \max\left[0, \left(f_{11}(\epsilon) + f_{12}(\epsilon)\Delta + \frac{\pi\theta_z}{180}f_{13}(\epsilon)\right)\right] \tag{2.24}$$

$$F_2 = \left(f_{21}(\epsilon) + f_{22}(\epsilon)\Delta + \frac{\pi\theta_z}{180}f_{23}(\epsilon)\right) \tag{2.25}$$

The Perez statistically derived coefficients f_{ij} for ranges of ϵ values are given in the following table 2.10:

Range of ε	f_{11}	f_{12}	f_{13}	f_{21}	f_{22}	f_{23}
1.000–1.065	−0.008	0.588	−0.062	−0.060	0.072	−0.022
1.065–1.230	0.130	0.683	−0.151	−0.019	0.066	−0.029
1.230–1.500	0.330	0.487	−0.221	0.055	−0.064	−0.026
1.500–1.950	0.568	0.187	−0.295	0.109	−0.152	0.014
1.950–2.800	0.873	−0.392	−0.362	0.226	−0.462	0.001
2.800–4.500	1.132	−1.237	−0.412	0.288	−0.823	0.056
4.500–6.200	1.060	−1.600	−0.359	0.264	−1.127	0.131
6.200–∞	0.678	−0.327	−0.250	0.156	−1.377	0.251

Figure 2.10: Brightness Coefficients for Perez Anisotropic Sky Model (1990) , source: [74].

Sky clearness ϵ parameter is a function of the hour's diffuse radiation I_{d} and normal incidence beam radiation $I_{\mathrm{b,n}}$ while sky brightness Δ is a function of air mass m, and extraterrestrial normal-incidence I_{on}. The clearness and brightness parameters are given by:

$$\epsilon = \frac{\dfrac{I_{\mathrm{d}} + I_{\mathrm{b,n}}}{I_{\mathrm{d}}} + 1.041\cdot\theta_z^3}{1 + 1.041\cdot\theta_z^3}, \ \theta_z \text{ in radians} \tag{2.26}$$

and

$$\Delta = m\frac{I_{\mathrm{d}}}{I_{\mathrm{on}}} \tag{2.27}$$

The terms **a** and **b** in equation 2.23 determine the angular location of the circumsolar region (the circumsolar radiation is considered to be from a point source at the sun).

$$a = \max(0, \cos\theta) \tag{2.28}$$

$$b = \max(\cos 85, \cos\theta_z) \tag{2.29}$$

where the angle of 85^o represents Perez maximum validation domain. For the determination of the airmass, the empirical relationship of Kasten & Young 1989 [75] is giving a good approximation:

$$m = \frac{\exp(-0.0001184h)}{\cos\theta_z + 0.5057(96.080 - \theta_z)^{-1.634}}, \text{h: the site altitude [m]} \tag{2.30}$$

Thus, the total radiation on a tilted flat surface of the Perez model is:

$$I_{\mathrm{T}} = I_{\mathrm{b}}R_{\mathrm{b}} + I_{\mathrm{d}}\left[(1-F_1)\left(\frac{1+\cos b}{2}\right) + F_1\left(\frac{a}{b}\right) + F_2\sin\beta\right] + I_{\rho_{\mathrm{g}}}\left(\frac{1+\cos b}{2}\right) \tag{2.31}$$

According to [71] and [76], the Perez (1993) model has been found to give the best overall performance when applied to a wide variety of locations and has thus won widespread acceptance.

2.4.2.3 Longwave exchanges

The computation of exterior longwave radiation is a complex phenomenon. The complexity lies in the fact that a surface is exchanging radiative energy with other surrounding surfaces and the sky, leading the problem to intractable solutions. Thus a number of assumptions must be considered. Firstly, we will present the basic law of radiation, which is the one governing the rate at which energy is released from a surface per unit area

$$I_{\mathrm{LW}} = \epsilon\sigma T^4 \tag{2.32}$$

where ϵ is the longwave emissivity, σ is the universal Stefan-Boltzmann constant and T is the absolute temperature of the studied element. Assuming that the surface is opaque, diffuse and isothermal, its properties are governed by the grey body notion and by the fact that the sky is a fictitious surface with an effective temperature T_{sky} The net longwave radiation balance on a surface exposed to the ground and the sky is:

$$I_{\mathrm{LW,i}} = \epsilon\sigma[F_{\mathrm{s-g}}(T_{\mathrm{g}}^4 - T_{\mathrm{s}}^4) + F_{\mathrm{s-sky}}(T_{\mathrm{sky}}^4 - T_{\mathrm{s}}^4)] \tag{2.33}$$

where $F_{\mathrm{s-g}}$ and $F_{\mathrm{s-sky}}$ are the view factors from surface to ground and surface to sky respectively. Equation 2.33 is the most commonly used method in BEM for the calculation of longwave exchanges. This equation is not taking into account the diversity of urban surfaces and assumes that the exchanges with other surfaces can be approximated by the ground temperature. In parallel, the calculation of view factors, is given by geometrical formulas such as:

$$F_{\mathrm{s-g}} = \frac{1-\cos\theta}{2} \tag{2.34}$$

$$F_{\mathrm{s-sky}} = \frac{1+\cos\theta}{2} \tag{2.35}$$

Moreover, the sky and ground temperatures must be computed. We present the eminent approaches for their estimation in the following paragraphs. In many cases it is convenient to express the net longwave radiation in terms of a linear temperature difference, similar to convection (Equation: 2.12). This linearized heat transfer coefficients is given from:

$$h_{\text{r,g}} = \epsilon\sigma \left[\frac{F_{\text{s-g}}(T_{\text{g}}^4 - T_{\text{s}}^4)}{T_{\text{g}} - T_{\text{s}}} \right] \tag{2.36}$$

$$h_{\text{r,sky}} = \epsilon\sigma \left[\frac{F_{\text{s-sky}}(T_{\text{sky}}^4 - T_{\text{s}}^4)}{T_{\text{sky}} - T_{\text{s}}} \right] \tag{2.37}$$

Substituting Equations: 2.36 and 2.37 in 2.33, gives:

$$I_{\text{LW,i}} = h_{\text{r,g}}(T_{\text{g}} - T_{\text{s}}) + h_{\text{r,sky}}(T_{\text{sky}} - T_{\text{s}}) \tag{2.38}$$

The development of three-dimensional models where the urban surfaces are explicitly described, have contributed to the inclusion of the urban surfaces in the longwave radiative exchanges calculation. Under such notion, the view factors from surface to surface are estimated, as shown in section 2.4.2.4, and thus, equation 2.38 is modified to:

$$I_{\text{LW,i}} = \sum_{j=1}^{N_{\text{s}}} h_{\text{rad,e}} F_{\text{i,j}}(T_{\text{s,j}}(t) - T_{\text{s,i}}(t)) + h_{\text{rad,e}}^{'} F_{\text{i,sky}}(T_{\text{sky}}(t) - T_{\text{s,i}}(t)) \tag{2.39}$$

Sky Radiative Temperature: sky radiative temperature constitutes an essential physical parameter taking place in radiative cooling. Since this is not generally measured by standard meteorological stations, it is necessary to be approximated from other measured observations. According to Thermal Analysis Reference Manual (TARP)[77], [78], one can estimate it using formula 2.40. The net thermal radiative flux between a horizontal surface and the sky is given by:

$$I_{\text{LW,sky}} = \epsilon_{\text{sky}} \cdot \sigma \cdot T_{\text{db}}^4 \tag{2.40}$$

with:

T_{db} the absolute dry bulb temperature [K]

ϵ_{sky} the sky emissivity, which according to [77] is given by correlation (2.41)

σ the Stefan-Boltzmann constant [W/m^{2}K^4]

$$\epsilon_{\text{sky}} = [0.787 + 0.764 \cdot \ln(T_{\text{dp}}/273)] \cdot f_{\text{cloud}} \tag{2.41}$$

and

$$f_{\text{cloud}} = 1 + 0.0224 \cdot N - 0.0035 \cdot N^2 + 0.00028 \cdot N^3$$

where:

N is the opaque sky cloud cover [tenths]

T_{dp} the absolute dewpoint temperature [K]

σ the Stefan-Boltzmann constant [W/m^{2}K^4]

Finally, from Equations 2.40 and 2.41 we obtain the desired sky temperature in ^{o}C.

$$\boxed{T_{\text{sky}} = \sqrt[4]{\frac{I_{\text{LW,sky}}}{\epsilon_{\text{sky}}}} - 273.15} \tag{2.42}$$

Ground Temperature: ground temperature is an important physical parameter affecting heat transfer of ground surfaces. Additionally, it is related to heat transfer in underground installations such as geothermal exchange systems.
The ground temperature varies in response to atmospheric fluctuations. The surface of the Earth absorbs solar energy and emits longwave radiation, while at the same time, air temperature and precipitation are also modifying its thermal behavior through convection and conduction mechanisms. These solicitations are impacting the temperature in depths close to the surface. Thus a mathematical formula [79],[80], following an harmonic function can estimate the typical annual cycles of monthly average ground temperature:

$$T_{\text{g,s}}(t) = T_{\text{a}} - T_{\text{amp}} \cos(\omega t - \phi) \tag{2.43}$$

with:

T_{a} the annual average air temperature [K]

T_{amp} the annual amplitude of the monthly average air temperature

t, ω, ϕ the time coordinate, angular frequency and phase in [s], [$\frac{rad}{\text{s}}$], [rad] respectively.

In a certain depth z at time t, the ground temperature can be estimated by the heat conduction equation:

$$\left.\begin{array}{c} \rho C \dfrac{\partial T(z,t)}{\partial t} = \nabla[\lambda \nabla T(z,t)] \\ T(z,0) = T_{\text{a}} \end{array}\right\} \xRightarrow[(2.44)]{(2.43)} \tag{2.44}$$

where:

ρ the soil density [kg/m^3]

C the specific heat capacity [J/kg $\cdot$ K]

λ the soil thermal conductivity [W/mK].

Considering the soil as a semi-infinite medium of a constant thermal diffusivity with its surface exposed to the variable ambient temperature, the solution of (2.44) at depth z when a steady cyclic pattern is established, is given by:

$$T_{\mathrm{g}}(z,t) = \bar{T}_{\mathrm{a}} - T_{\mathrm{amp}} \cdot \exp\left[-z\sqrt{\frac{\omega}{2\alpha}}\right] \cos\left[\omega t - \phi - z\sqrt{\frac{\omega}{2\alpha}}\right] \tag{2.45}$$

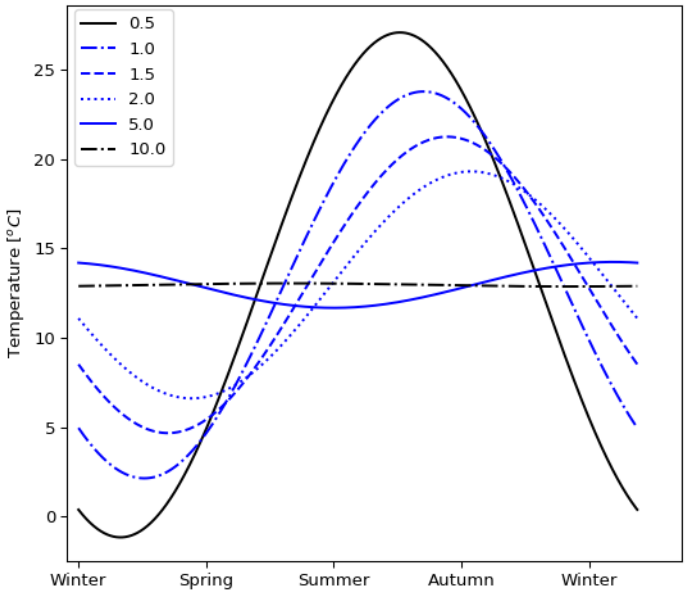

Figure 2.11: Ground temperature representation for various depths.

In the last equation, the term α expresses the ground thermal diffusivity in [m^2/s]. Figure 2.11 shows the ground temperature distribution for various depths using a standard meteorological file for the city of La Rochelle. The selected thermal properties correspond to standard soil characteristics. One can conclude that as the depth increases, the annual fluctuations tend to disappear. When a threshold value of around 10m is reached, then the soil temperature tends to approximate the annual average air temperature (T_{a}).

2.4.2.4 Multiple reflections

In urban geometries the reflected component of solar radiation, is of great importance, as it can modify the surface thermal balance of the studied elements and their surroundings. Eventually the building thermal loads are affected [81]. Moreover, the last years, cool material applications in buildings and open spaces (pavements, sidewalks) have been established. For outdoor applications the impact of the reflected shortwave radiation in surrounding buildings is of great importance [82]. The following sections present various approaches developed to serve different microclimate modeling spatial scales.

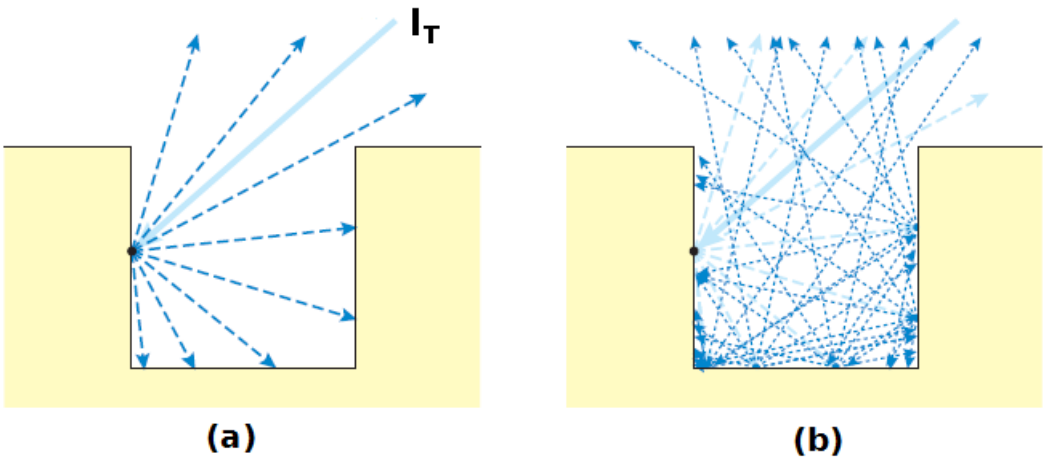

Figure 2.12: Schematic representation of (a) first reflection and (b) second reflection of beam component from a canyon facets, source: [65].

Radiosity method: the amount of the incident energy on a building surface varies depending on the albedo as well as the albedo of other neighboring surfaces. In deep and narrow canyon formations, solar trapping effect leads to an increased energy consumption for cooling [83]. To this end, the reflected shortwave irradiance must be considered, especially in dense geometries. A possible way to estimate it is the radiosity method. The radiosity J of a surface, is defined as the rate at which radiation leaves the surface due to emission and reflection in all directions per unit area of the surface. The amount of irradiance received by a surface after reflection, considering the air as a non-participating medium, is the sum of the solar incident irradiance $I_{0,\mathrm{SW,i}}$ (beam and diffuse) and the interchange irradiance $I^*_{\mathrm{SW,i}}$ (Equation 2.46).

$$I_{\mathrm{AR,SW,i}} = I_{0,\mathrm{SW,i}} + I^*_{\mathrm{SW,i}} \quad \text{with} \quad I_{0,\mathrm{SW,i}} = I_{\mathrm{b,SW,i}} + I_{\mathrm{d,SW,i}} \tag{2.46}$$

Assuming that the urban geometry with sky forms an enclosure (closed cavity) [84] and that the sky is a hemisphere with infinite radius, the shortwave radiosity of the surface can be expressed by formula 2.47.

$$J_{\mathrm{SW,i}} = \rho_{\mathrm{SW,i}}(I_{0,\mathrm{SW,i}} + I^*_{\mathrm{SW,i}}) \tag{2.47}$$

By substituting 2.46 to 2.47, the shortwave irradiance after reflection is given by:

$$I_{\mathrm{AR,SW,i}} = \frac{J_{\mathrm{SW,i}}}{\rho_{\mathrm{SW,i}}} \tag{2.48}$$

Equation 2.48 requires the creation of matricial systems which can be solved by matrix inversion. Hopefully, when urban scenes are represented, the corresponding matrices are sparse and thus the calculation is executed in reasonable time. The interchange flux component, can be

calculated by including the other surfaces of the scene, given by the following formula:

$$I^{*}_{\mathrm{SW,i}} = \sum_{j=1}^{N} F_{\mathrm{ij}} I_{\mathrm{SW,j}} \tag{2.49}$$

The calculation of view factors between all surfaces is required which is detailed in the next section.

Calculation of View Factors: in order to compute the radiation exchange between any two surfaces, the concept of a view factor must be introduced. A view factor is defined as the fraction of the radiation leaving surface **i** and is intercepted by surface **j**. Again, we assume that our scene forms an enclosure and that urban surfaces are diffuse emitters and reflectors having a uniform radiosity. For the outdoor surfaces $\mathrm{A_i}$, and $\mathrm{A_j}$ with distance R and θ_{i}, θ_{j} the polar angles with the normals $\mathbf{n}_{\mathrm{i}}$, $\mathbf{n}_{\mathrm{j}}$, the view factors of surface **i** can be determined by the well known relationship:

$$F_{\mathrm{ij}} = \frac{1}{A_{\mathrm{i}}} \int_{A_{\mathrm{i}}} \int_{A_{\mathrm{j}}} \frac{\cos\theta_{\mathrm{i}} \cos\theta_{\mathrm{j}}}{\pi R^2} dA_{\mathrm{i}} dA_{\mathrm{j}} \tag{2.50}$$

of for surface **j**:

$$F_{\mathrm{ji}} = \frac{1}{A_{\mathrm{j}}} \int_{A_{\mathrm{i}}} \int_{A_{\mathrm{j}}} \frac{\cos\theta_{\mathrm{i}} \cos\theta_{\mathrm{j}}}{\pi R^2} dA_{\mathrm{i}} dA_{\mathrm{j}} \tag{2.51}$$

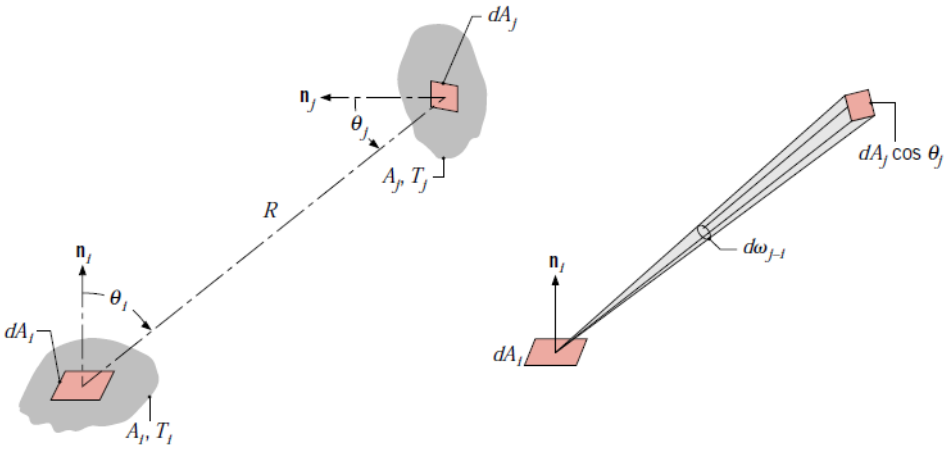

Figure 2.13: View factor associated with radiation exchange between elemental surfaces of area $\mathrm{dA_i}$ and $\mathrm{dA_j}$, source: [85].

Combining equations 2.50 and 2.51 the reciprocity relation and the summation rule can be determined and reduce the simulation time.

$$A_{\mathrm{i}} F_{\mathrm{ij}} = A_{\mathrm{j}} F_{\mathrm{ji}} \tag{2.52}$$

$$\sum_{j=1}^{N} F_{\mathrm{ij}} = 1 \tag{2.53}$$

Simplified Radiosity method (SRA): the Simplified Radiosity method has its origin in the method of image processing of digital elevation methods (DEMs). It was introduced in [86] to calculate the reflected solar radiation component in urban environments, while reducing significantly the simulation time. The method employs a street canyon, for which the angle of elevation of the opposing canyon wall (or its urban horizon angle $\boldsymbol{u}$ in Figure: 2.14) produces the same obstruction view factor as the real skyline. More in detail, the direct sky irradiance for

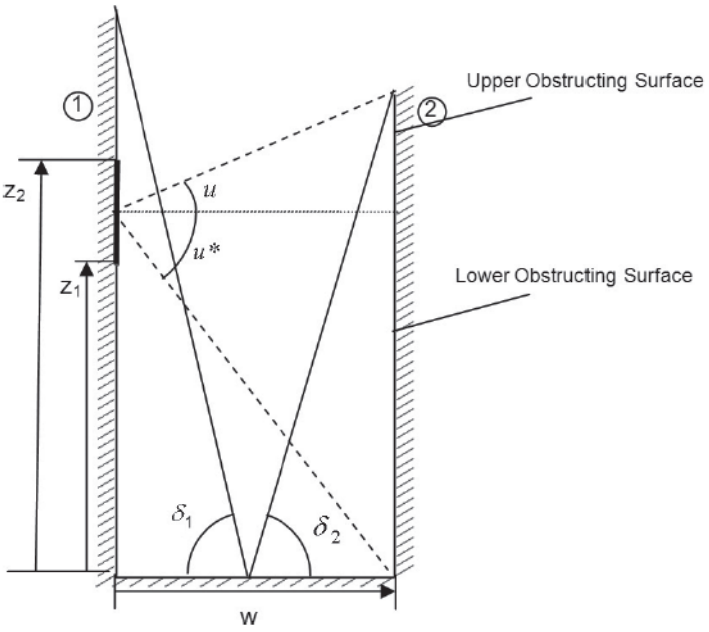

Figure 2.14: Geometry of a notional canyon for the diffuse reflection calculation, source: [87].

a set of **p** sky patches, each of which subtends a solid angle $\boldsymbol{\Phi}$ and has a radiance $\boldsymbol{R}$ is given by:

$$I_{\mathrm{d}} = \sum_{i=1}^{p} R\Phi\sigma\cos\theta \tag{2.54}$$

where $\boldsymbol{\sigma}$ is an equivalent sky view factor [0,1] defined as the proportion of the plane that can be seen by patch **p** and $\boldsymbol{\theta}$ is the mean angle of incidence [87].

Assuming the radiant external environment as two hemispheres, one above the horizontal plane and another one below it [88], discretized into **p** patches each, the reflected irradiance will be given:

$$I_{\mathrm{AR,T}} = \sum_{i=1}^{2p}(R^{\star}\Phi\omega\cos\theta)_{\mathrm{i}} = \sum_{i=1}^{2p}(R^{\star}\Phi(1-\sigma)\cos\theta)_{\mathrm{i}} \tag{2.55}$$

where ω is the obstruction view factor and $R^{\star}$ is the surface radiance. Now, from equation 2.46 and substituting equations 2.54, 2.55, the radiance of the surface will be given as:

$$R = \Big(I_{\mathrm{b}} + I_{\mathrm{d}} + I_{\mathrm{AR,T}}\Big)\rho/\pi \tag{2.56}$$

Equation 2.56 is leading to the following matrix system:

$$I_{\mathrm{d}} = \boldsymbol{A} \cdot \boldsymbol{I_{\mathrm{T}}} + \boldsymbol{B} \cdot \boldsymbol{R} \tag{2.57}$$

which can be solved with a matrix inversion after reformulating it or iteratively since matrix-vector multiplications are relatively inexpensive for sparse matrices.

Absorptive Efficiency method: this method assumes an infinite long canyon, where the roof has the sky view factor of a horizontal surface with an unobstructed horizon. It is based on the absorptive 'efficiency' definition. This unitless quantity relates the albedo of the canyon with its aspect ratio and it is evaluated by comparing the absorptive ability of the surface facets to that of the canyon as a whole (in 2-D) [65]. Assuming a canyon of unit length like the one of Figure: 2.12a, the overall albedo is given by:

$$\alpha_{\mathrm{sur}} = \frac{W\alpha_{\mathrm{floor}} + H(\alpha_{\mathrm{wall\ 1}} + \alpha_{\mathrm{wall\ 2}})}{2H + W} \tag{2.58}$$

with α the albedo and W, H the canyon width and walls height. The absorptive efficiency will be given from the following relation:

$$R_{\mathrm{c}} = \frac{1 - \alpha_{\mathrm{top}}}{1 - \alpha_{\mathrm{sur}}} \tag{2.59}$$

with

$$\alpha_{\mathrm{top}} = \frac{I_{0,\mathrm{SW},\downarrow}}{I_{0,\mathrm{SW},\uparrow}} \tag{2.60}$$

This expression shows that the deeper and narrower the canyons are, the higher the absorptive efficiency is.

2.4.3 Airflow

The airflow in urban environments is a driving force for the development of local microclimates, as the vertical stratification of the atmospheric sub-layers is mainly affected by the turbulent exchanges between the surface and the atmosphere. This flow of air in the atmosphere, or simpler the wind, is ideally assumed to be parallel to the earth's surface and its mathematical description is given from a 3-D vector; $\vec{u} = (u, v, w)$, where u, v, w are the respective components in each direction (x,y,z). Nevertheless, the presence of obstacles in its prevailing direction acting as drag forces combined with radiative, thermal and latent fluxes of the urban environment, are modifying the characteristics of the flow. The following sections, deal with the circulation patterns around isolated buildings and building arrays while in parallel the wind distribution and characteristics in urban canyons and the general wind profiles in urban areas are analysed and discussed.

2.4.3.1 Isolated buildings circulation

Buildings affect the airflow distribution around them due to the generation of pressure perturbations. The airflow around buildings can be divided into four characteristic zones [89], visualized in Figure: 2.15:

- the undisturbed zone (A)
- the displacement zone (B),
- the cavity zone (C) and
- the wake zone (D)

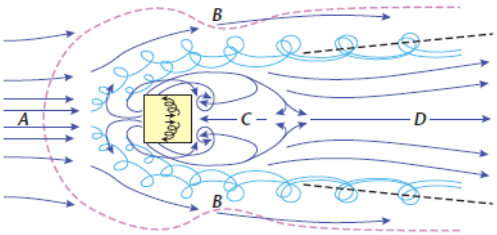

Figure 2.15: Airflow patterns around an isolated cubic building, source: [65].

The undisturbed zone, is the zone area where the prevailing wind is approaching the building. At the displacement zone the streamlines are displaced in all directions, over the roof, down the front and around the building due to pressure perturbations. A positive pressure is created on the upstream side while negative on the roof, lee and lateral sides. This phenomenon is observed at a threshold point in the front side of the building, at around the two thirds of the building height, called stagnation point. Vortices generation at the corner and the roof top occur while in parallel air circulates in the reverse direction. The cavity zone (has an approximate length 2.5-3 times the building height) is the area behind the building (part of the wake zone) where the streamlines are separated, leaving a suction zone in the lee of the building. At this place, a recirculation zone is formed by both an along-wind roll due to flow over the roof, plus two horizontally-oriented rolls due to lower pressure behind each side wall [65].

2.4.3.2 Building arrays flow patterns

Considering a higher spatial scale rather than an isolated building, the airflow of urban form can be described by some general patterns. Those patterns are primarily influenced by the wind direction and the urban form spacing.

For a prevailing wind perpendicular to building position, as shown in Figure: 2.16, the airflow regime can be distinguished into three types:

- the isolated flow (a),
- the wake interference flow (b) and
- the skimming flow (c)

which they depend on height-to-width ratio of the canyon.

To this end, when the buildings (regardless of building shape) are well apart (H/W greater than 0.05), the flow can be described by the concept of isolated buildings, as the flow fields do not interact. The *isolated roughness flow* occurs when an area is characterized by widely spaced buildings. In this area, the space ratio (H/W) is lower than the critical value of 0.35

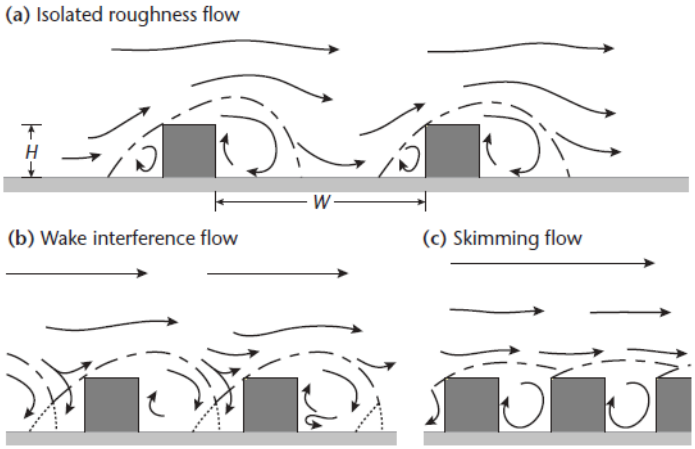

Figure 2.16: Airflow patterns around building arrays of increasing height-to-width ratio, source: [90].

(0.4 for cubic and 0.3 for row) and the concept of the urban canyon is almost non-existent. The airflow pattern is much like those of isolated buildings with small lateral wake interactions. At denser formulations ($0.35 < \text{H/W} < 0.65$ or H/W up to approximately 0.7 for cubic and 0.65 for row buildings), the flow pattern is described as *wake interference flow*. At this flow type, the vortex (cross-canyon vortex) in the cavity behind the upwind building is reinforced by the flow down the windward face of the next building [91]. At highly dense areas ($\text{H/W} > 0.65$), described as street canyons, a vortex circulation flow occurs inside it, while the above-roof flow pass by buildings roof-top, generating the so-called *skimming flow*.

The flow pattern characterization, as described above, seem to depend only on the height-to-width ratio. Oke [91], proposed threshold lines where the flow regime is described by the overall canyon geometry characteristics (a combination of length-to-width and height-to-width ratios).

The flow pattern regimes differ for prevailing winds along the canyon. In this case (angle $< 30^o$), the flow is channeled along the canyon and the vortex vanishes, while for an intermediate wind angle (approximately $< 45^o$) a helical flow occurs along the canyon [92].

2.4.3.3 Urban wind profiles

The representation of wind profile in urban areas requires the development of mathematical idealizations to describe the mean horizontal wind in the ISL[5] around a city or city region, as it is assumed to be independent of the horizontal position. In general, the wind speed inside the city at a certain height is reduced compared to a rural area and this is caused due to the different roughness induced by the urban structures, as shown in Figure 2.17.

Under statically neutral conditions, the mean wind speed tends to become zero close to the ground due to frictional drag causes, while the pressure gradient forces cause the wind to increase with height. Considering that surface stress (represented by the friction velocity $u_\star$[6]),

[5]Inertial sublayer, part of the ABL where shear-dominated turbulence creates a logarithmic velocity profile and variation of turbulent fluxes with height is small [65]

[6]$u_\star = \frac{\tau}{\rho} = \frac{\text{surface shearing stress}}{\text{atmospheric density}}$

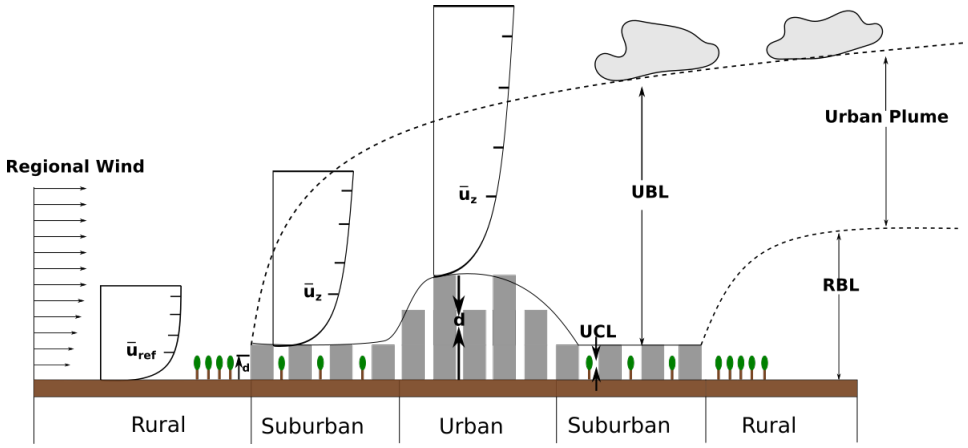

Figure 2.17: Schematic representation of two-layer urban atmosphere classification combiend with the vertical wind profiles, adapted from: [90] and [93].

and surface roughness (represented by the aerodynamic roughness length, z_0) are relevant [94], the mean wind at height z is given:

$$\bar{u}_z = \frac{u_\star}{k} \ln\left(\frac{z}{z_0}\right) \tag{2.61}$$

where k is the universal von Karman constant, independent from the flow and the surface. The last equation (2.61) can be given also in a similar formula, by speculating the displacement distance d (Figure: 2.17):

$$\bar{u}_z = \frac{u_\star}{k} \ln\left(\frac{z-d}{z_0}\right) \tag{2.62}$$

The displacement distance is approximately the building height, for cases of packed buildings where they act as a displaced surface of a given roughness. Equation 2.62 can be extrapolated for two heights in order to give the wind profile in a height of interest z based on a height z_{ref} where data are available:

$$\frac{\bar{u}_z}{\bar{u}_{z_{\text{ref}}}} = \frac{\ln\left(\frac{z-d}{z_0}\right)}{\ln\left(\frac{z_{\text{ref}}-d}{z_0}\right)} \tag{2.63}$$

The *logarithmic wind* profile (figure:2.17), as expressed in equations 2.62 and 2.63 can be extended to unstable (non-neutral) diabatic conditions by relating the momentum flux (Φ_M) with the height and the Obukhov length L from Businger-Dyer Relationships [95]. Other similar expressions, as equation 2.63 have been suggested after street-canyon pollution modeling [96]. An alternative empirical form of 2.62 is the *power law* wind profile expression, given by:

$$\bar{u}_{z_1} = \bar{u}_{z_2}\left[\frac{z_1-d}{z_2-d}\right]^{\alpha} \tag{2.64}$$

where $\bar{u}_{z_2}$ represents the observed wind speed at a suitable reference height (z_2), while $\bar{u}_{z_1}$ is the wind speed at the place of interest given a specific height. The exponent α it is estimated either by field and laboratory studies [97], [98] or it can be related to roughness length through the following formula [99]:

$$\alpha = 0.096 \log_{10} z_0 + 0.016(\log_{10} z_0)^2 + 0.24 \tag{2.65}$$

The power law wind profile, Equation: 2.64, is preferred by engineers as the friction velocity, the roughness length, and the displacement height are not readily obtained.

The *exponential law* [100], [101] developed for wind within vegetation canopies can be also applied in the urban canopy layer.

$$\langle \bar{u} \rangle_z = \langle \bar{u} \rangle_{z_e} e^{a(z/H-1)} \tag{2.66}$$

where H is the canopy height and a is the attenuation coefficient which relates the canopy top to the mixing length within the canopy. Wind tunnel experiments [102] indicated that the attenuation coefficient is linearly approximated $a = 9.6\lambda_f$ with the packing density and can fit adequately to urban areas. The best correlation was obtained for a λ_f value of around 0.1.

2.5 Urban Building Energy & Microclimate modeling

2.5.1 Introduction

In his research article, Reinhart [103] characterized the Urban Building Energy modeling as a nascent field. Some years later, indeed, the scientific committee of the International Building Simulation Conference (IBPSA2019), highlighted that for the first time, the UBEM submitted articles exceeded the ones of BEM, proving the increased interest of this research field. At the same time, the increasing trend of studying the UHI, as shown in Figure:2.18, put in prior place these two scientific fields.

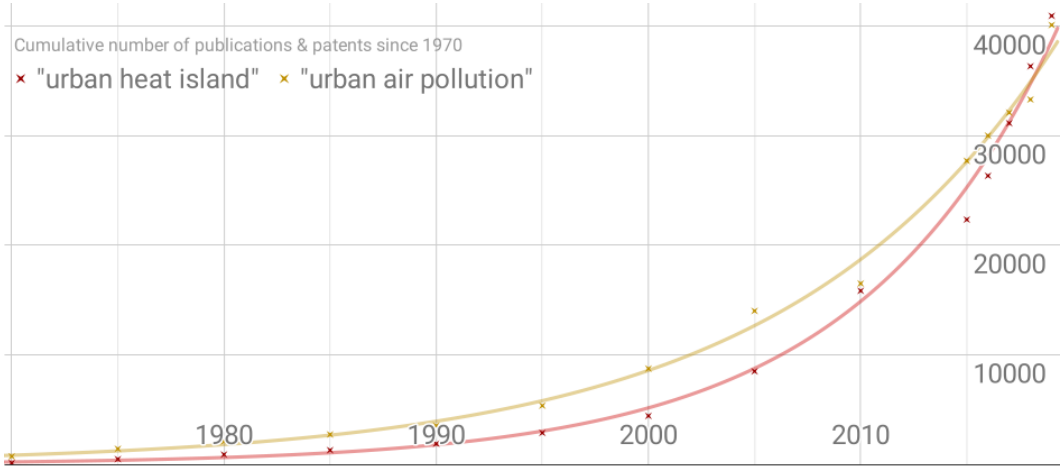

Figure 2.18: Increasing trend of UHI studies, adapted from google scholar.

The urban energy modeling is a multidisciplinary research topic, placing together a vast variety of scientific fields. The main studied principle is the building energy demand, which is

correlated to the operating systems at a local or central scale. In parallel, energy generation and storage as well as energy conversion and distribution aspects have emerged the need for holistic approaches. In order to support the decision process, optimization techniques, and frameworks of better assessing the possible solutions and their applicability are emerging in parallel with the modeling approaches. Moreover, as all of these aspects are interconnected with the urban environment, reciprocal phenomena occur, and thus the urban microclimate's contribution cannot be neglected in such studies. Santamouris [104], in the dawn of the previous decade, highlighted the importance *to account for the local microclimate the effect of neighboring buildings when conducting energy simulations*. Allegrini, in the article: [105], stated that *there is a strong interaction between the local microclimate and the buildings. They should ideally be modeled in a coupled way rather than the microclimate being a predetermined boundary condition.* Robinson, in the concluding chapter of the book [71], emphasized *the acute need for closely conducted interdisciplinary research* towards fully coupled models of urban modeling.

In this framework, triggered by the apothegms from the experts in this research field, we orient the following discussion towards the analysis of the existing approaches and methods in urban energy and microclimate modeling, the tools required to conduct a numerical investigation and the possible ways to couple them.

2.5.2 Approaches & methods

Urban energy modeling can be defined as the analysis of the energy performance of neighborhoods [103], meant to study various scales, ranging from several dozens to thousands of buildings. In this context, lots of efforts to cluster this multidisciplinary and multiscale field have been conducted. Some research articles, are pointing emphasis to the urban building stock, and investigate the eminent modeling approaches from this point of view [106]. Those can be analysed based on their general methodological philosophy, and thus two fundamental classes can be derived; the bottom-up and the top-down approaches [107]. A further refinement of these two governing approaches is held by [108], by analysing the bottom-up approach to statistical and engineering methods. An extension on the latter, has been proposed in the work of [109], by including the intelligent computer systems method or more in detail, as suggested in [110], the neural networks, the support vector machines, and the gray models' methods.

From another point of view, Allegrini [105] examines the urban energy modeling from the systems perspective. He classifies the modeling approaches to district energy systems, renewable energy modeling, and urban microclimate. Another way to study the urban building energy modeling is the combination of the aforementioned clusters and their examination as a unified system. In the research article of [111], a vast variety of modeling approaches in relevance with energy systems is covered and assessed, such as building simulation, district networks simulation, urban climate studies, micro- and macrosimulation of transportation, and optimization engines. To this end, other refinements such as temporal and spatial scaling are also examined [112], while another interesting analysis can be achieved by also including sociological, economical, geographical, and targeting audience aspects [113].

Concerning urban microclimate, the notion of bottom-up and top-down can be respectively interpreted as an up-scaling and a downscaling approach. The latter requires multi-scale modeling of urban climate using the nesting technique. More in detail, from a Globar or Regional model (25km), the methodology descends stepwise to a mesoscale (1km) and then to an urban

or building scale model respectively. Characteristic examples of the downscaling method can be found in [114], [115], [116]. The up-scaling method follows the opposite procedure. It is frequently used to estimate the urban air pollution and emergency preparedness situations [117]. However, such a process is not generally preferred for the study of UHI effect or for its mitigation strategies. On the contrary, for the UHI investigation, another methodological discretization has to be considered. According to [118], two main approaches are used to study the UHI effect. The observational approach which is using field measurements, thermal remote sensing and prototype experiments, and the small-scale modeling. The latter, is not able to account for all the phenomena that simultaneously contribute to the phenomenon. Thus, it can be extended up to city scale by various coupling schemes. Particularly, it is usually adjusted to different parametrized schemes dealing with the building, the urban canyon, or the urban canopy. The following sections provide an analytical review of the prominent models, developed to support both the urban energy and urban climate modeling.

2.5.3 Urban building energy models

As previously discussed, several approaches and methods exist to model urban energy demand. In this section, we will present the most influential models that meet our objectives. We are mainly focused on bottom-up approaches and specifically to engineering methods. Thus the following review contains only the tools that correspond to this goal. We orient our discussion towards three key elements:

- the building energy model,
- the boundary conditions (including solar-based manipulations), and
- energy systems modeling.

The last two items can give an estimation of the potential interactions with neighboring elements. At the same time, the programming language and the compatibility with external connections for cosimulation are discussed.

TEASER (Tool for Energy Analysis and Simulation for Efficient Retrofit) [119], is a design-driven ROM for fast assessment of the energy efficiency potentials of building stocks. It integrates statistical information of building stock archetypes and international standards to enrich acquired basic data in order to generate dynamic simulation models for BPS. TEASER is characterized by an open structure to enable multiple data sources. The building energy model is based on the RC method, taking into account the thermal effects on exterior elements, interior and windows, encompassing phenomena such as convection and solar absorption, using an equivalent air temperature [120]. The tool offers different discretization schemes giving various RC-combinations for single zone or multizone buildings, while for higher scale energy simulations considers archetype buildings based on statistical data. It is integrated into Python programming language allowing co-simulation through an FMI standard. Furthermore, it can be linked to several Modellica libraries [121] for the description of local energy systems, like static AHU model with heat recovery unit or centralized such as CHP (connected to a heating grid that is primary-supplied by waste heat from a lignite power plant). It uses standard boundary conditions (typical datasets of meteorological variables). The tool aims to provide individual, dynamic BPS for multiple buildings.

The IDEAS [122] (Integrated District Energy Assessment by Simulation) district energy simulation tool is a multiscale simulation model for the integration, interaction, control, and feedback of buildings, district systems, and multidisciplinary energy systems. IDEAS is built as an object-oriented tool, composed of three main simulation elements. The building energy library uses the key objects to simulate the heat transfer mechanisms in buildings resulting in a transient building energy model based on the finite volume method using the heat balance approach [123]. The outdoor conditions and thus the respective phenomena correspond to standard meteorological files used in BEM. The thermal building system library embeds a vast variety of energy systems and components, suitable for building energy calculations, but the development of control sequences with dynamics of similar time scales can not be performed [124]. The occupancy model corresponds to Markov chains allowing lighting and occupancy schedules, while the building management system allows on/off control on space heating and window blinds. The electricity library can simulate the renewable photovoltaic production, electrical energy storage, and distribution of buildings and districts. The electrical grid corresponds to an unbalanced three-phase AC radial grid. The tool is implemented in the Modelica modeling language.

CitySim [125] is another well-known software for simulating and optimising urban resource flows. The tool combines a custom GUI with developed thermal simulation engines such as a building thermal model, a sophisticated algorithm of radiation exchanges as well as behavioral, plant, and equipment models. More in detail, the building thermal model is based on the RC method, taking into account the dominant heat transfer phenomena occurring at the zone-building scale. The radiation model accounts for direct, diffuse, and inter-reflected components based on the SRA method, as well as radiative exchanges of the urban surfaces. Occupancy schedules and appliances are based either on stochastic models using Markov chains, or on deterministic profiles. The HVAC system model is limited for the ideal representation of air's psychometric state while the energy conversion systems is consisted of simplified curve regression equations. Its open structure allows coupling the tool with other models such as transport simulation models. The import data correspond to xml file format and the solver is operating in the C++ computing language.

CityBES [126] is a web-based platform to simulate the energy performance of a city's building stock. The building energy model corresponds to the EnergyPlus simulation engine through the OpenStudio software development kit. It uses an open data standard as CityGML source data to represent and exchange 3-D city models or 2-D geoJSON file formats. In its initial state, the outdoor conditions are described by standard meteorological files, where radiative exchanges or inter-reflections are not taken into account [127]. HVAC systems, indoor lighting, plug-loads, service water heating, and building operation schedules are systematically applied to the CityBES framework through EnergyPlus [128]. District energy systems are not included and the integration language corresponds to C++.

City Energy Analyst (CEA) is a computational framework for the analysis and the optimization of energy systems in neighborhoods and city districts [129], based on statistical and analytical calculation methods. Overall, the simulation tool covers various thermal procedures and building energy-related topics, though most of them are implemented in a simplified manner, allowing simulations up to city scale. More in detail, the tool consists of resource potential modules, system technologies at local and central scale, decision support analysis, and multi-criteria assessment. The thermal zone module is based on a simplified RC model of three nodes.

The solar radiation module corresponds to the hemispherical view-shed algorithm taking into account shading effects [130]. The thermal network model is based on a simplified representation of heat exchangers estimated at nominal conditions. The model is established in Python v2.7 programming language.

SimStadt [131] is a modular platform for simulation of thermal energy demand and photovoltaic potential at an urban scale. It consists of preprocessing workflow steps (Geometry, Physics, Usage) which derive simulation relevant parameters from the CityGML model, building physics and usage libraries [132]. The boundary conditions correspond to readily available qualified weather databases. A dynamic simulation model is not yet implemented on the tool (it is planed), thus calculation of hourly building energy demand is not allowed and building representation is limited to building archetypes of four different LoDs. In contrast, a monthly energy balance is applied to each building, allowing to estimate space heating and cooling demands of a given case study. Energy systems are not integrated into the tool. The DHW and electrical demands are calculated through statistical methods on an annual basis. The tool offers three available radiation models, depending on the desired level of detail. A simplified one of an isolated building based on the Hay sky model, a ray-casting algorithm, coupled with the first one for the consideration of the solar masks or a detailed one using the SRA method, coupled with the Perez sky model to allow solar masks and multireflection calculations. It has an open structure allowing linking the platform to other simulation tools, for the integration of district networks (e.g., Stanet software). It is integrated with Java programming language.

DIMOSIM [133] (District Modeller and Simulator) is a bottom-up simulation tool of the feasibility, conception, and operation of district energy systems, by considering and implementing a wide range of phenomena for the transient analysis. It can simulate various local and district heating systems and their management, renewable generation, storage, and ICTs for intelligent energy management, retrofit strategies while in parallel it supports control optimization modules at district and/or building level. More in detail, the tool consists of a rather detailed RC thermal zone model, taking into account the key elements of thermal transfers, applied in a detailed or simplified manner, a solar radiation algorithm accounting for solar masks and the principal radiation components, as well as multiple energy systems, and distribution modules. The representation of the outdoor conditions is similar to the majority of BES tools corresponding to standard meteorological input files. It contains an electrical and thermo-hydraulic grid module based on different LoD including simplified steady-state, transient, and plug flow sub modules. Occupancy schedules and behavioral models are derived from a mixture of statistical and stochastic data based on national surveys. DIMOSIM is developed as an object-oriented Python v.3 package in a modular way, allowing readily external connections and co-simulation procedures. Analytically, we will examine some key modules of this tool in the next chapter.

2.5.4 Urban climate models

As stated in the introductory section the UHI modeling operates on an extended spatial scale, ranging from micro to city-scale applications. The microclimate models can follow the similar categorization that we presented in Section: 2.3 where we described the eminent BES approaches: the CFD, the zonal, and the nodal.

The cluster of CFD models solves the continuity and the Reynolds-averaged Navier Stokes (RANS) equations, in which the Large Eddy Simulations (LES) approach can be applied to

represent accurately the small-scale turbulence. The most commonly used turbulence models of RANS employ the k-ϵ[7] and the Eddy Diffusivity methods [134]. A characteristic example of these types of models is the well-known tool ENVI-met. It is a 3-D numerical microclimate model based on the RANS equations, with a nonhydrostatic, obstacle-resolving model and advanced parameterizations for simulation of surface-plant-air interactions in urban environments [135]. The tool provides a spatial resolution ranging from 0.5-10 m with times steps varying from the finest of 10 s to 1 hour. Additionally, it has features not commonly available in other CFD dispersion codes such as a vegetation module. The required inputs correspond to meteorological and thermophysical parameters as well as domain characteristics. It employs a structural grid, thus complex building formations are not compatible with the package. Although it is commonly accepted that CFD packages are accurate enough, their weakness is due to the extensive computational cost [136]. Because of this, it is difficult to couple them with other simulation models, for example, to account for solar heat gains at urban surfaces or anthropogenic heat from building HVAC systems in an extended temporal scale (annual).

The zonal models are operating in the urban canopy layer by meshing the urban environment in structural or unstructured sub-cells. These models are capable to study the heterogeneities of the built environment, as they evaluate the distribution of the dominant physical variables in 3-D. Although they are less accurate than CFD models, they can assess the air temperature and airflow patterns by solving mass, pressure, and energy balance equations. The airflow distribution is usually assigned using the urban wind profiles presented in section 2.4.3.3. In most of this type of model, latent phenomena are either not considered or included in a simplified manner. These models take into account 3-D geometries, and thus they are efficient in linking them with other simulations tools such as solar radiation models. Zonal models are usually preferred for strong coupling effects of urban microclimate and building energy demand since the calculation time is still acceptable, contrary to CFD tools. Examples of zonal models can be found in [137], [138], [139].

The last category, nodal models, has gained popularity recently. They are distinguished in single or multi-layer models. Usually, nodal models are using a horizontal average approach to describe the atmospheric state, so they simplify the urban environment to just one effective dimension (the z-one). Each vertical layer can be represented as a homogeneous layer described by one node. A characteristic example of a multi-layer urban canopy model is CIM (Canopy Interface Model) [140]. It is a 1-D meteorological model solving the diffusion equation in one-dimension and calculating vertical profiles of meteorological variables such as wind speed, wind direction, and air temperature. It is differentiated from other canopy models by introducing a 1.5-order turbulent closure scheme and resolving locally the turbulent kinetic energy taking into account the obstacles of the urban canopy. The model can be used as an intermediate tool between a micro-climatic and a meso-scale model.

Nodal single layer tools are the most representative models for studying the urban climate. Usually, the urban canopy is represented by one node where an ideal street canyon formulation occurs. The latent and sensible heat fluxes are estimated through parametric schemes. Then, the urban canopy model is connected with the second node of an atmospheric model, standing for the UBL. The main assumption is that the urban system is a black-box where inputs and outputs are serving the energy balance budget and exchanges occur through its top. Nodal models utilize several parametrization schemes (canyon-based). Characteristic examples of this type of models

[7] turbulent energy k and its dissipation rate ϵ

are the Single-Layer Urban Canopy model [141] the UWG (Urban Weather Generator)[142], the TEB (Town Energy Balance Model) [143] and the urban VGS model [144].

The urban boundary layer or meso-scale models, such as the MM5 [145](Fifth-Generation Penn State/NCAR Mesoscale Model) or its substitute the Weather Research and Forecasting WRF [146], were designed with the objective to serve both atmospheric research and operational forecasting needs. Therefore, they operate in a huge range of spatial scale (25km to 1km) [147], [148]. They are based on the Monin-Obukhov similarity theory (MOST), the atmosphere is assumed to be Boussinesq, either hydrostatic like in URBMET [149] or nonhydrostatic as in Meso-NH atmospheric simulation system [150]. Most of them are often coupled with an energy balance scheme at the surface as in the SURFEX [151], the SM2U [152] or ISBA [153] models. An extensive assessment of the meso scale models can be found in [154]. This model category is out of the scope of our research, but we mention them because they established the notion of multi-scale modeling for studying coupled phenomena and several types of UHI effect.

2.6 Coupled models & approaches

2.6.1 BEM - microclimate

The link between rising energy demand and local climatic phenomena is demonstrated in various studies. Considerable attention has been concentrated on the cooling period when the impact of the UHI effect is intensified. Thus, various numerical approaches and studies have emerged, aiming to the estimation of the potential energy loss capture, caused by the local phenomena.

The asynchronous (chaining) coupling method which combines a Building Energy Simulation (BES) model with a microclimate code is mainly preferred. Sun [155] applied this method by developing a parametrized urban canopy scheme using the TEB-ISBA coupled model to generate hourly UHI magnitudes across 15 climate zones in the United States. The obtained air temperature was then used to generate modified weather data as import to EnergyPlus. The authors found that the modified air temperature led to an average of 17% increase in building cooling energy use and an average of about 17% decrease in building heating energy use over the studied climate locations, while individual results per climate zone revealed the detrimental and beneficial role of UHI. Gobakis [156] followed a similar coupling approach between a BES and a microclimate model to study the impact of different convective heat transfer coefficients to a building settlement in the University campus of Chania. They showed that cooling demand could vary up to 25% between standalone and coupled models. Castaldo [157], performed a chaining coupling scheme between ENVI-met and EnergyPlus, intending to evaluate the impact of the local microclimate on building thermal-energy performance and renewable production under various UHI mitigation scenarios. Therefore, two representative days (summer-winter) were simulated with the microclimatic tool and based on various interpolations, an annual modified meteorological file was extracted for usage in the thermal simulation building model. The authors concluded that the implemented scenarios could reduce building energy need for HVAC up to 10% under the referenced conditions. Similar studies using the chaining method with identical or similar simulation tools can be found in [158], [159], [82], [160], [161], [162]. The afore-mentioned approaches seem capable to serve the concept of Net zero energy buildings (NZEB), however, they are either temporally limited due to the time expensive microclimate

simulations (CFD) or spatially restrained, as they account just for the building scale. Moreover, the chaining coupling schemes could give a general estimation about the actual environmental conditions but crucial information is lost due to the non-dynamic character of the methodology.

To this end, another effort to minimize the uncertainties of building energy simulation has been conducted by Bouyer [163]. In his study, a synchronous coupling between the CFD code FLUENT, the thermoradiative tool Solene and a multizone building nodal network model has been realized. On the one hand, the exchanged variables were the convective heat exchange coefficients, the mass rate of moisture, and the air temperature, on the other hand, surface temperatures, the global radiation, and latent fluxes. The study revealed that solar irradiance is the most crucial parameter on the building energy consumption, but also that longwave radiative and convective fluxes must not be neglected. Similar outcomes were highlighted by Malys [164] and have led to another type of microclimate model, the so-called Solene-Microclimat model. In its current version, the CFD code has been substituted by the CFD code Saturne [165]. The tool was validated for a street canyon configuration in [166]. Similarly, Allegrini [167] examined the variations on energy demand between a stand-alone building and buildings integrated into a street canyon by coupling a 2D CFD code and a BES tool for a moderate climate in Basel, Switzerland. He showed an increase in space cooling demand while space heating decreases in the case of the street-canyon configuration. He suggested that neglecting the UHI effect leads to an important underestimation of the cooling demand.

2.6.2 UBEM - microclimate

In order to extend the boundaries of the simulation domain, a novel series of coupled models have emerged. Mauree [168], applied a one-way coupling scheme between CitySim and CIM to study the impact on energy demand when the urban climate is taken into account for the EPFL campus. The coupling variables correspond to surface and air temperature. The methodology induced a three-step offline coupling procedure. They demonstrated that the wind speed and air temperature deviations compared to a typical dataset could lead to a reduction of the simulating heating demand error by a factor of 2 compared to record data. Similarly, Allegrini [169] used a one-way coupling scheme between CitySim and the CFD model OpenFOAM. The coupling variable was the building surface temperatures simulated with the UBEM which was then used as boundary conditions in the CFD model. The study aimed to assess the impact of different albedo surfaces on the local urban microclimate for a building site in Switzerland. Maiullari [170] developed an asynchronous coupling scheme to link the UBEM CEA with the microclimate code Envimet. The study intended to include microclimatic data in the computation of space cooling and heating consumption in a rehabilitated area in Zurich for the coldest and hottest days. The authors highlighted that microclimate consideration lead to significant variations of total space heating and cooling consumption. In all of the aforementioned studies, the commonly used method of chaining coupling was used and dynamic feedback was not captured.

An interesting effort at this scale has been conducted by Gros [171]. In this study, a coupling scheme between a reduced-order building model, an urban dispersion tool, and a thermoradiative code has been tested. The integration of the various sub-models was held with the zonal approach. From the outcomes of this work, the microclimate code EnviBatE emerged. In this model, a 3-D representation of buildings and microclimate has been taken into account while

the model was used to assess the reciprocal effects of building energy demand and urban canopy conditions. Latent phenomena were neglected, but the implemented approach was very efficient in terms of execution time, and the dominant phenomena occurring at this scale were considered. Further details on this approach are given in the next Chapter.

2.6.3 Urban climate - energy systems

The waste anthropogenic heat released by the operating energy systems constitutes one of the major factors that contribute to the development of the UHI effect, as presented in section 1.3.1. Earlier studies indicated that the heat released by air-conditioning systems has a significant impact on the urban environment and should be taken into account in a more complete study of the urban canopy climate and cooling energy demands [172].

To this end, particular attention has been paid to the feedback of AC systems on outdoor air temperatures. De Munck [173] demonstrated a coupling scheme between a meso-meteorological model and a single layer-module to account for the built environment, to estimate Paris air temperature increase due to air conditioning units. The study was conducted for six days representing the anticyclonic conditions of the 2003's heatwave. The outcomes revealed a maximum increase in the ambient temperature of 2 ^{o}C for a potential future doubling of air conditioning waste heat released to the atmosphere. Similarly, Salamanca [174] integrated a meso-scale with a multilayer urban canopy and a simplified building energy model for the city of Houston (nested area of 110km). The results obtained from a 2-day simulation period found an increase in night temperatures of up to 2 ^{o}C. A different approach was presented by Wen [175]. In this study the authors developed a mathematical nested urban box model, to correlate the atmospheric stability with the possible air temperature increase due to the rejected heat of the AC units in the lower level of the atmosphere. In this method, the potential heat rejection was introduced as a parameter to the model, given statistical data obtained from the city of Wuhan. They estimated that the air temperature increase could reach 2.6 ^{o}C and 0.2 ^{o}C under inversion and normal conditions respectively. Concerning the district scale, a synchronous "ping-pong" scheme was developed from Hsieh [176] based on a BES and a computational fluid dynamics (CFD) code. The maximum air temperature increase due to the rejected heat from window type AC unit was estimated at 1.89 ^{o}C, given a fixed COP value, for a case study in Taipei.

According to Sailor [177], a dynamic linking of an urban atmospheric model and a building energy model is required for the estimation of the anthropogenic heat and the rejected heat of AC units in the urban environment. The aforementioned studies give an estimation of the amplitude of the UHI and the systems' feedback in air temperatures. However, various simplifications must be considered depending on the examined spatial scale. In some cases, buildings are parametrized, while in others, the study is either temporally limited (hours) and the seasonal behavior can not be assessed or the rejected heat is introduced as a ratio without considering the local characteristics of the studied area.

2.7 Existing limitations & models selection

So far, we have progressively investigated the preponderant physical phenomena and the eminent approaches employed to represent them; from building to neighborhood scale. More-

over, we presented the implemented modeling techniques and the tools used to capture the interactions between buildings, energy systems, and urban microclimate at these scales.

The accurate representation of all of the physical phenomena and their reciprocal effects, is a major challenge, due to the complex interactions. The most obvious complexity of the urban canopy layer is its 3-D, multi-faceted, and multi-layered structure. The heterogeneity of the landscape and the differentiation of the urban elements (different thermal and optical characteristics) are difficult to be parameterized, as frequently the particular overwhelms the general. Based on this consideration, the notion of local microclimate modeling has gain space compared to previously applied techniques. However, to our knowledge, a unified tool, capable to estimate the building energy demand and the microclimate conditions by the utilization of district energy systems is non-existent. Our objective is deeply rooted in the latter argument. Triggered by the three main pillars: buildings - microclimate - energy systems, we present a new methodology of synchronous coupling schemes between an UBEM and a microclimate model. The selected models, Dimosim and EnviBatE have the corresponding capabilities for the neighborhood scale studies. Detailed descriptions of all of the physical processes inside and outside the building are not necessary for the prediction of the annual energy consumption at the neighborhood scale. Then, most of the building models, as shown in section 2.5.3, employ an RC zone approach. The LoD is variable depending on the objectives of each tool. Dimosim consists of a structural detailed RC model. As a further matter, solar radiation acting as the dominant stimuli of building cooling demand must be given with the main components in detail (total, reflected, and longwave exchanges). EnviBatE is taking into account all of the aforementioned components. In addition, the urban airflow calculation is often a major issue, affected by the accurate but time-consuming CFD simulations. The zonal method adapted at the neighborhood scale in EnviBatE can be a possible solution to tackle this. Additionally, the integration of centralized energy solutions, such as a cooling network, to microclimate studies has not been so far investigated. Dimosim contains modules of district energy systems in various LoDs. Finally, both tools are integrated into the same programming language allowing loosely communication between them.

The adapted methodology can be characterized as multi-scale. The starting point corresponds to the system scale and concludes to the neighborhood one (Figure: 2.1). In parallel, it is established on a multidisciplinary way, since the development of the different employed methods has brought together different specialists such as engineers (systems modeling), building physicists (building thermal model), architects (solar model), meteorologists (urban pollution modeling) and urban planners (morphology and space use). In the next chapters, the developed simulation models and coupling strategies, as well as their integration in a real case study are presented in detail.

Applications

Chapter 3

Developed Simulation Tools and Methods

Contents

3.1 District Model Simulator (DiMoSim)

DIMOSIM [133] is an integrated simulation tool for the analysis of feasibility, conception and operation of district energy concepts. It consists of (a) building and thermal zone models, (b) thermal and electric network models and (c) a variety of energy system components for the various scales (sensor, emitters, hydronic distribution, production, storage and control). It has been developed progressively in CSTB (Center Scientific et Technique du Bâtiment / Sophia-Antipolis), in the framework of several national and european projects [178], [179], [180], [181], [182], initially in Matlab programming language, later as an object-oriented Python 2.7 package (the last version of the tool has been updated to Python 3) with continuous integration and deployment capabilities. This structure allows the implementation of new sub-models in the core code that can be performed either in parallel or independently from the existing simulation package. In the following sections, we will present some of the basic modules that are strongly connected with the objectives of our work.

3.1.1 Thermal Zone model

The thermal zone model corresponds to an RC[1] model in order to account for the fundamental physical mechanisms occurring at zone level with respect to computational efficiency. The developed RC model is based on a state-space formulation in order to allow fast calculations for various parametric studies, while at the same time it retains the sensitivity to the typical design parameters used in building energy simulation, adapted to the urban scale.

The heat transfer mechanisms considered in the thermal zone model are:

- Transient heat conduction through envelopes, roofs and floors as well as internal walls and masses.
- Steady state heat conduction through windows.
- Exterior convective heat exchanges of envelopes, roofs and windows.
- Absorbed shortwave radiation of building envelopes, roofs and windows.
- Longwave radiant heat exchange of envelopes, roofs and window elements taking into account the view factors to sky and ground.
- Interior convective heat exchanges of interior surfaces and windows.
- Radiative gains in the interior surfaces from occupants, equipment and solar radiation.
- Ventilation heat fluxes.
- Thermal bridges.
- The intermediate floors are represented as thermal mass or adjacent envelope between zone (in case of a multi-zone description of the building).

[1] see sections: 2.3.3.1, 2.3

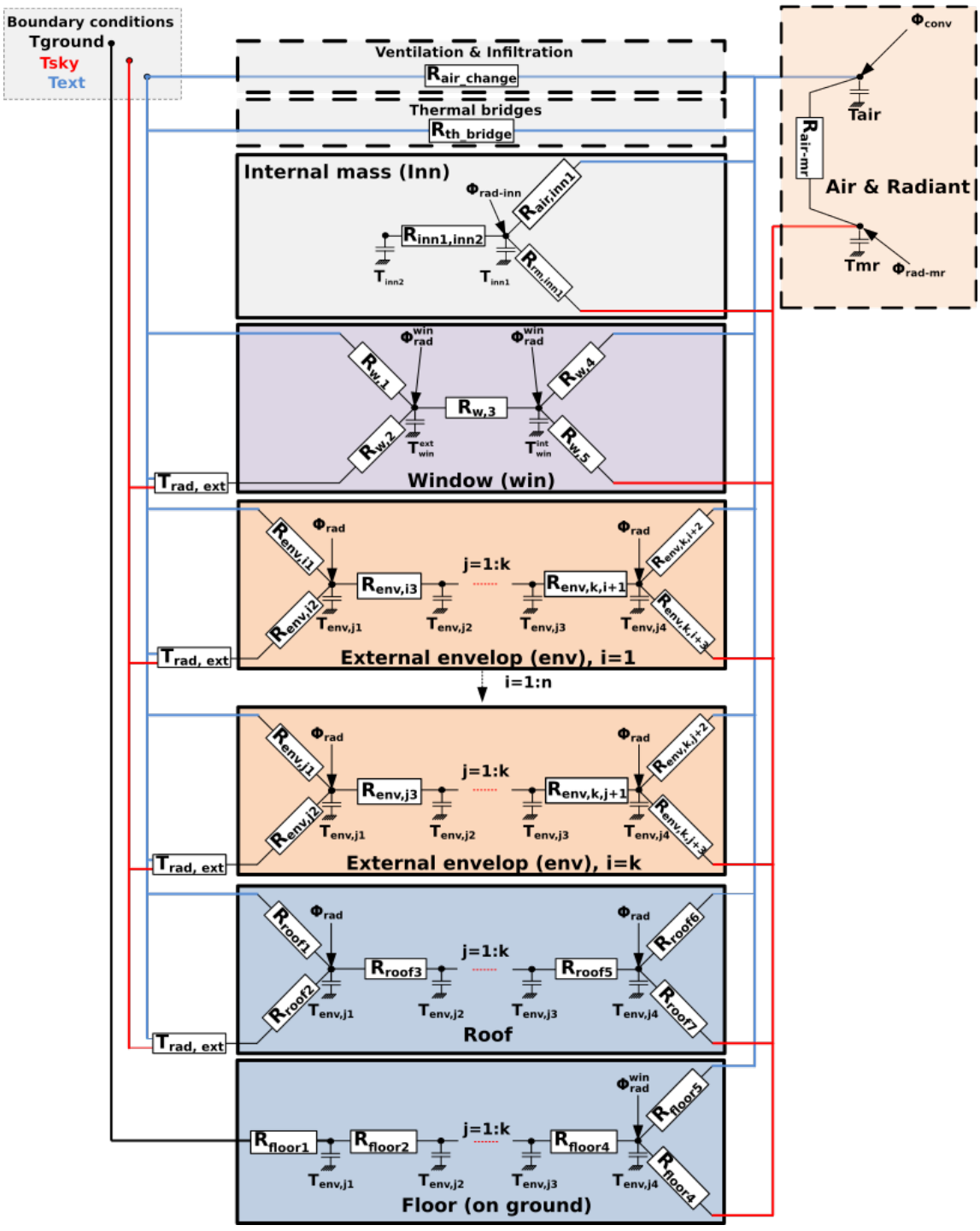

Figure 3.1: Layout of the thermal zone model, adapted from [182].

More in detail, as shown in Figure: 3.1, the wall envelope model (identical for roofs) consists of a minimum of four capacitors and three resistances (Figure: 2.4) representing external surface, first mass layer, second mass layer and internal surface and can be easily extended to a higher discretization scheme. The number of envelope layers and discretization of each layer can be adjusted by the user. It can either be applied to each individual façade or to all façades, as

an aggregated envelope. Windows are represented as a two node model with two thermal capacitors on the external and internal surfaces. The absorbed shortwave radiation is calculated in a specific radiation module for each façade, considering solar close and far masks and is injected to the outer surface of the wall. On the internal surface, radiative gains from occupants, equipment and solar radiation are injected proportionally to the areas of the walls. The combined ventilation-infiltration module calculates the heat flux to or from the zone given either simple mechanical ventilation system or a ventilation system with heat recovery. Thermal bridges are estimated from the number of floors, the position of the insulation and the perimeter of the zone footprint considering a global thermal bridge coefficient. Finally, the model includes an internal mass module, in which all adjacent and internal walls or floors are represented allowing to consider the thermal inertia.

3.1.1.1 State-space formulation

In this section we present the state-space formulation of the implemented model. For illustration purposes in this report, we consider a simple thermal zone of a rectangular shape, consisted of six boundaries, four-walls with an opening at their center, a roof and a ground floor. Each wall is subdivided into four layers, representing two plaster layers at the exterior and interior side, a mass and an insulation layer in the middle. The aforementioned description corresponds to the default parameters of the model, concluding to a $R_{31}C_{18}$ default model.

The state space equation-form of our linear and first-order system is given by the equation 3.1, where X is the state vector of the variables, U is the input vector shaped $[12 \times 1]$, **A** is the constant state matrix of shape $[18 \times 18]$ and **B** is the constant input matrix shaped $[18 \times 12]$. **C** is the vector of heat capacities.

$$\begin{aligned} \boldsymbol{C}\dot{X}(t) &= \boldsymbol{A}X(t) + \boldsymbol{B}U(t) \\ \dot{X}(t) &= \frac{\boldsymbol{A}}{\boldsymbol{C}}X(t) + \frac{\boldsymbol{B}}{\boldsymbol{C}}U(t) \end{aligned} \tag{3.1}$$

The full state response, is given by equation 3.2, using the Euler exponential technique. It consists of two components: the first is a term similar to the system homogeneous response X(t) = $e^{\boldsymbol{A}t}$X(0) that is dependent only on the system initial conditions X(0). The second term is in the form of a convolution integral, and consists the particular solution for the input U(t), with zero initial conditions.

$$X(t) = X(t - dt)\boldsymbol{A_d} + \boldsymbol{B_d} \cdot U(t) \tag{3.2}$$

where:

$$\boldsymbol{A_d} = e^{\boldsymbol{A/C}dt} \tag{3.3}$$

$$\boldsymbol{B_d} = (\boldsymbol{A/C})^{-1}(e^{\boldsymbol{A/C}dt} - e^{\boldsymbol{A}/C0})\boldsymbol{B} \tag{3.4}$$

The convergence of the integration factors and the state transition matrix (Equations: 3.3, 3.4) is evaluated in the initialization step of the simulation. The analytical representation of the state space system is given in 3.5, 3.6, 3.7, 3.8 and 3.9 as follows:

$$C = \left[(\rho C_p)_{\text{air}} V_{\text{z}},\ \ 1,\ \ 1,\ \ 1,\ \ [C_{\text{srt}} L \rho C_{\text{p}} A]_{\text{inn}},\ \ [(1 - C_{\text{srt}}) L \rho C_{\text{p}} A]_{\text{inn}}\ \ [L \rho C_{\text{p}} A]_{\text{i}}^{\text{j}}\ \ \cdots\ \ [L \rho C_{\text{p}} A]_{\text{i}}^{\text{j}}\ \ \right]^T \tag{3.5}$$

$$\dot{X}(t) = \left[\dot{T}_{\text{air}}^{\text{z}}\ \ \dot{T}_{\text{mrt}}^{\text{z}}\ \ \dot{T}_{\text{s,win}}^{\text{ex}}\ \ \dot{T}_{\text{s,win}}^{\text{int}}\ \ \dot{T}_{\text{s,inn}}^{\text{int}}\ \ \dot{T}_{\text{core}}^{\text{int}}\ \ \dot{T}_{\text{s,i,j}}^{\text{ex}}\ \ \cdots \dot{T}_{\text{s,i,j}}^{\text{int}}\right]^T \tag{3.6}$$

$$X(t - \Delta t) = \left[T_{\text{air}}^{z}\ \ T_{\text{mrt}}^{z}\ \ T_{\text{s,win}}^{\text{ex}}\ \ T_{\text{s,win}}^{\text{int}}\ \ T_{\text{s,inn}}^{\text{int}}\ \ T_{\text{core}}^{\text{int}}\ \ T_{\text{s,i,j}}^{\text{ex}}\ \ \cdots\ \ T_{\text{s,i,j}}^{\text{int}}\right]^T \tag{3.7}$$

- V_{z} the volume of the thermal zone [m^3]
- the subscript *air* signifies the air properties
- the subscript *inn* signifies the inner mass properties
- the subscript *core* signifies the inner mass core properties
- the constant C_{srt} signifies the inner mass surface share ratio
- $i \in [1, .., 6]$ the number of exterior boundaries and
- $j \in [1, 4]$ the number of wall layers enumerated from exterior to interior
- t is the actual time step

$$
A = \begin{bmatrix}
a_{00} & 0 & 0 & a_{03} & a_{04} & 0 & \cdots & 0 & a_{09} & 0 & \cdots & 0 & a_{0i} \\
0 & a_{11} & 0 & a_{13} & a_{14} & 0 & \cdots & 0 & a_{19} & 0 & \cdots & 0 & a_{0i} \\
- & - & - & - & - & - & - & - & - & - & - & \vdots & 0 \\
0 & 0 & a_{22} & a_{23} & 0 & \vdots & \vdots & \vdots & \vdots & \vdots & \vdots & 0 & \cdots \\
a_{30} & a_{31} & a_{32} & a_{33} & 0 & \vdots & \vdots & \vdots & \vdots & \vdots & \vdots & 0 & \cdots \\
- & - & - & - & - & - & - & - & - & - & - & - & - \\
a_{40} & a_{41} & 0 & 0 & a_{44} & a_{45} & 0 & \vdots & \vdots & \vdots & \vdots & 0 & \cdots \\
0 & \vdots & \vdots & 0 & a_{54} & a_{55} & 0 & \vdots & \vdots & \vdots & \vdots & 0 & \cdots \\
- & - & - & - & - & - & - & - & - & - & - & - & - \\
0 & \vdots & \vdots & \vdots & \vdots & 0 & a_{66} & a_{67} & 0 & \vdots & \vdots & 0 & \cdots \\
0 & \ddots & \vdots & \vdots & \vdots & 0 & a_{76} & a_{77} & a_{78} & 0 & \vdots & \vdots & \vdots \\
0 & \vdots & \vdots & \vdots & \vdots & \vdots & \vdots & a_{87} & a_{88} & a_{89} & 0 & \vdots & \vdots \\
a_{90} & a_{91} & 0 & \vdots & \vdots & \vdots & \vdots & 0 & a_{98} & a_{99} & 0 & \vdots & \vdots \\
- & - & - & - & - & - & - & - & - & - & - & - & - \\
a_{i0} & a_{i1} & 0 & \vdots & \vdots & \vdots & \vdots & \vdots & \vdots & \vdots & \vdots & 0 & a_{ii}
\end{bmatrix}
\begin{matrix}
\\ \\ - \\ \vdots \\ \\ - \\ \\ \\ - \\ \\ \\ - \\ \\ - \\ 0 & a_{i,i-1}
\end{matrix}
\tag{3.8}
$$

where

- Indoor Air Temperature node

$$a_{00} = \underbrace{-h_{\mathrm{c}}^{\mathrm{in}} A_{\mathrm{inn}}^{t}}_{a_{04}} - \underbrace{h_{\mathrm{r}}^{\mathrm{in}} A_{\mathrm{w}}^{t}}_{a_{03}} - \sum_{b=1}^{N_b} \underbrace{h_{\mathrm{c}}^{\mathrm{in}} A_{\mathrm{b}}^{i}}_{a_{0i,..,0i+4}} - C_{\mathrm{Bdg}}$$

- Indoor Mean Radiant Temperature node

$$a_{11} = - \underbrace{h_{\mathrm{c}}^{\mathrm{in}} A_{\mathrm{inn}}^{t}}_{a_{14}} - \underbrace{h_{\mathrm{r}}^{\mathrm{in}} A_{\mathrm{w}}^{t}}_{a_{13}} - \sum_{b=1}^{N_b} \underbrace{h_{\mathrm{c}}^{\mathrm{in}} A_{\mathrm{b}}^{i}}_{a_{1i,..,1i+4}}$$

} for $i = [9, 13, .., 29]$

- Exterior window node

$$a_{22} = - \underbrace{h_{\mathrm{c}}^{\mathrm{ex}} A_{\mathrm{w}}^{t}}_{b_{20}} - \underbrace{h_{\mathrm{r}}^{\mathrm{ex}} A_{\mathrm{w}}^{t} F_{\mathrm{w}}^{\mathrm{sky}}}_{b_{21}} - \underbrace{h_{\mathrm{r}}^{\mathrm{ex}} A_{\mathrm{w}}^{t} F_{\mathrm{w}}^{\mathrm{gr}}}_{b_{22}} - \underbrace{U_{\nu_{\mathrm{w}}}^{\mathrm{ex}} A_{\mathrm{w}}^{t}}_{a_{23}}$$

- Interior window node

$$a_{33} = - \underbrace{h_{\mathrm{c}}^{\mathrm{in}} A_{\mathrm{w}}^{t}}_{a_{30}} - \underbrace{h_{\mathrm{r}}^{\mathrm{in}} A_{\mathrm{w}}^{t}}_{a_{31}} - \underbrace{U_{\nu_{\mathrm{w}}}^{\mathrm{in}} A_{\mathrm{w}}^{t}}_{a_{32}}$$

- Inner mass surface node

$$a_{44} = - \underbrace{\frac{\lambda_{\mathrm{inn}}}{L_{\mathrm{inn}}} A_{\mathrm{inn}}}_{a_{45}} - \underbrace{h_{\mathrm{c}}^{\mathrm{in}} A_{\mathrm{inn}}}_{a_{40}} - \underbrace{h_{\mathrm{r}}^{\mathrm{in}} A_{\mathrm{inn}}}_{a_{41}}$$

- Inner mass core node

$$a_{55} = - \underbrace{\frac{\lambda_{\mathrm{inn}}}{L_{\mathrm{inn}}} A_{\mathrm{inn}}}_{a_{54}}$$

- Exterior node of a wall for: $i \in [6, 10, .., 26]$, $j = i + 1$

$$a_{ii} = -\underbrace{\frac{1}{R_{1,i}}}_{a_{ij}} - \underbrace{h_{\mathrm{c}}^{\mathrm{ex}} A_{\mathrm{b}}^{i}}_{b_{i0}} - \underbrace{h_{\mathrm{r}}^{\mathrm{ex}} A_{\mathrm{i}} F_{i}^{\mathrm{sky}}}_{b_{i1}} - \underbrace{h_{\mathrm{r}}^{\mathrm{ex}} A_{i} F_{i}^{\mathrm{gr}}}_{b_{i2}}$$

- Exterior node of ground floor

$$a_{ii} = -\underbrace{\frac{1}{R_{1,i}}}_{a_{ij}} - \underbrace{h_{\mathrm{gr}}^{\mathrm{ex}} A_{b}^{i}}_{b_{i2}}$$

- 1st mass layer node of a wall for: $i \in [7, 11, .., 27]$

$$a_{ii} = -\underbrace{\frac{1}{R_{1,i}}}_{a_{ii-1}} - \underbrace{\frac{1}{R_{2,i}}}_{a_{ii+1}}$$

- 2nd mass layer node of a wall for: $i \in [8, 12, .., 28]$

$$a_{ii} = -\underbrace{\frac{1}{R_{2,i}}}_{a_{ii-1}} - \underbrace{\frac{1}{R_{3,i}}}_{a_{ii+1}}$$

- interior node of a wall for: $i \in [9, 13, .., 29]$

$$a_{ii} = -\underbrace{\frac{1}{R_{3,i}}}_{a_{ii+1}} - \underbrace{h_{\mathrm{c}}^{\mathrm{in}} A_{i}}_{a_{i0}} - \underbrace{h_{\mathrm{r}}^{\mathrm{in}} A_{i}}_{a_{i1}}$$

where:

$$\left.\begin{aligned} R_1 &= \frac{1}{A_{\mathrm{b}}^{i}}\left[\frac{L_1}{\lambda_1} + \frac{L_2}{2\lambda_2}\right] \\ R_2 &= \frac{1}{2A_{\mathrm{b}}^{i}}\left[\frac{L_2}{\lambda_2} + \frac{L_3}{\lambda_3}\right] \\ R_3 &= \frac{1}{A_{\mathrm{b}}^{i}}\left[\frac{L_3}{2\lambda_3} + \frac{L_4}{\lambda_4}\right] \end{aligned}\right\} \text{in [K/W]}$$

with:

- h_{c},h_{r} the convective and radiative heat exchange coefficients
- A the area of the examined surface
- C_{Bdg} is a constant of thermal bridge share
- F^{sky}, F^{gr} the view factors of a surface to sky and ground respectively
- $U_{\nu_{\mathrm{w}}}$ is the window U-value
- λ is the thermal conductivity of a layer

- L is the thickness of a layer
- R is the thermal resistance of a layer

$$B = \begin{bmatrix}
C_{\text{Bdg}} & 0 & 0 & 0 & 0 & 1 & 0 & 0 & 0 & 0 & 0 & 0 \\
0 & 0 & 0 & 0 & 0 & 0 & 0 & 0 & 0 & 0 & 0 & 0 \\
h_{\text{c}}^{\text{ex}} A_{\text{w}}^{t} & h_{\text{r}}^{\text{ex}} A_{\text{w}}^{t} F_{\text{w}}^{\text{sky}} & h_{\text{r}}^{\text{ex}} A_{\text{w}}^{t} F_{\text{w}}^{\text{gr}} & 0 & 1 & 0 & 0 & 0 & 0 & 0 & 0 & 0 \\
0 & 0 & 0 & C_{\text{w}}^{\text{r}} & 1 & 0 & C_{\text{w}}^{\text{r}} & 0 & 0 & 0 & 0 & 0 \\
0 & 0 & 0 & C_{\text{in}}^{\text{r}} & 0 & 0 & C_{\text{in}}^{\text{r}} & 0 & 0 & 0 & 0 & 0 \\
0 & 0 & 0 & 0 & 0 & 0 & 0 & 0 & 0 & 0 & 0 & 0 \\
h_{\text{c}}^{\text{ex}} A_{\text{b}}^{t} & h_{\text{r}}^{\text{ex}} A_{\text{b}}^{t} F_{\text{i}}^{\text{sky}} & h_{\text{r}}^{\text{ex}} A_{\text{b}}^{t} F_{\text{i}}^{\text{gr}} & 0 & 0 & 0 & 0 & 1 & 0 & 0 & 0 & 0 \\
0 & 0 & 0 & 0 & 0 & 0 & 0 & 0 & 0 & 0 & 0 & 0 \\
0 & 0 & 0 & 0 & 0 & 0 & 0 & 0 & 0 & 0 & 0 & 0 \\
0 & 0 & 0 & C_{\text{r}}^{\text{b,tr}} & 0 & 0 & C_{\text{r}}^{\text{b,tr}} & 0 & 0 & 0 & 0 & 0 \\
h_{\text{c}}^{\text{ex}} A_{\text{b}}^{t} & h_{\text{r}}^{\text{ex}} A_{\text{b}}^{t} F_{\text{i}}^{\text{sky}} & h_{\text{r}}^{\text{ex}} A_{\text{b}}^{t} F_{\text{i}}^{\text{gr}} & 0 & 0 & 0 & 0 & 0 & 1 & 0 & 0 & 0 \\
0 & 0 & 0 & 0 & 0 & 0 & 0 & 0 & 0 & 0 & 0 & 0 \\
0 & 0 & 0 & 0 & 0 & 0 & 0 & 0 & 0 & 0 & 0 & 0 \\
0 & 0 & 0 & C_{\text{r}}^{\text{b,tr}} & 0 & 0 & C_{\text{r}}^{\text{b,tr}} & 0 & 0 & 0 & 0 & 0 \\
h_{\text{c}}^{\text{ex}} A_{\text{b}}^{t} & h_{\text{r}}^{\text{ex}} A_{\text{b}}^{t} F_{\text{i}}^{\text{sky}} & h_{\text{r}}^{\text{ex}} A_{\text{b}}^{t} F_{\text{i}}^{\text{gr}} & 0 & 0 & 0 & 0 & 0 & 0 & 1 & 0 & 0 \\
0 & 0 & 0 & 0 & 0 & 0 & 0 & 0 & 0 & 0 & 0 & 0 \\
0 & 0 & 0 & 0 & 0 & 0 & 0 & 0 & 0 & 0 & 0 & 0 \\
0 & 0 & 0 & C_{\text{r}}^{\text{b,tr}} & 0 & 0 & C_{\text{r}}^{\text{b,tr}} & 0 & 0 & 0 & 0 & 0 \\
h_{\text{c}}^{\text{ex}} A_{\text{b}}^{t} & h_{\text{r}}^{\text{ex}} A_{\text{b}}^{t} F_{\text{i}}^{\text{sky}} & h_{\text{r}}^{\text{ex}} A_{\text{b}}^{t} F_{\text{i}}^{\text{gr}} & 0 & 0 & 0 & 0 & 0 & 0 & 0 & 1 & 0 \\
0 & 0 & 0 & 0 & 0 & 0 & 0 & 0 & 0 & 0 & 0 & 0 \\
0 & 0 & 0 & 0 & 0 & 0 & 0 & 0 & 0 & 0 & 0 & 0 \\
0 & 0 & 0 & C_{\text{r}}^{\text{b,tr}} & 0 & 0 & C_{\text{r}}^{\text{b,tr}} & 0 & 0 & 0 & 0 & 0 \\
0 & 0 & h_{\text{gr}}^{\text{ex}} A_{\text{b}}^{t} & 0 & 0 & 0 & 0 & 0 & 0 & 0 & 0 & 0 \\
0 & 0 & 0 & 0 & 0 & 0 & 0 & 0 & 0 & 0 & 0 & 0 \\
0 & 0 & 0 & 0 & 0 & 0 & 0 & 0 & 0 & 0 & 0 & 0 \\
0 & 0 & 0 & C_{\text{r}}^{\text{b,tr}} & 0 & 0 & C_{\text{r}}^{\text{b,tr}} & 0 & 0 & 0 & 0 & 0 \\
h_{\text{c}}^{\text{ex}} A_{\text{b}}^{t} & h_{\text{r}}^{\text{ex}} A_{\text{b}}^{t} F_{\text{i}}^{\text{sky}} & 0 & 0 & 0 & 0 & 0 & 0 & 0 & 0 & 0 & 1 \\
0 & 0 & 0 & 0 & 0 & 0 & 0 & 0 & 0 & 0 & 0 & 0 \\
0 & 0 & 0 & 0 & 0 & 0 & 0 & 0 & 0 & 0 & 0 & 0 \\
0 & 0 & 0 & C_{\text{r}}^{\text{b,tr}} & 0 & 0 & C_{\text{r}}^{\text{b,tr}} & 0 & 0 & 0 & 0 & 0
\end{bmatrix} \tag{3.9}$$

with

- C_{w}^{r}, C_{in}^{r}, $C_{\text{r}}^{\text{b,tr}}$ are coefficients holding for the radiative shares of windows 3.10, inner mass 3.11 and boundaries 3.12.
- h_{gr} is the heat exchange coefficient 3.13 with the ground.

$$C_{\text{w}}^{\text{r}} = \frac{A_{\text{w}}^{\text{Tot}}}{A_{\text{opaque}} + A_{\text{w}}^{\text{Tot}}} \tag{3.10}$$

$$C_{\text{in}}^{\text{r}} = \frac{A_{\text{inn}}^{\text{Tot}}}{A_{\text{opaque}} + A_{\text{w}}^{\text{Tot}}} \tag{3.11}$$

$$C_{\text{r}}^{\text{b,tr}} = \frac{A_{\text{b}}^{\text{Tot}}}{A_{\text{opaque}} + A_{\text{w}}^{\text{Tot}}} \tag{3.12}$$

$$h_{\text{gr}} = \frac{\lambda_{\text{gr}}}{D},\ D = \text{depth} \tag{3.13}$$

$$U = \begin{bmatrix} T_{\text{air}}^{t} \\ T_{\text{sky}}^{t} \\ T_{\text{gr}}^{t} \\ \phi_{\text{trans}}^{\text{w}} \cdot C_{\text{blind}} \\ \phi_{\text{abs}}^{\text{w}} \cdot C_{\text{blind}} \\ C_{\text{g}}^{\text{c}} \cdot \phi_{\text{gains}}^{\text{int}} + \phi_{\text{hvac}}^{\text{c}} + \phi_{\text{vent}} \\ C_{\text{g}}^{\text{r}} \cdot \phi_{\text{gains}}^{\text{int}} + \phi_{\text{hvac}}^{\text{r}} \\ \phi_{\text{gains,1}}^{\text{sol}} \\ \vdots \\ \phi_{\text{gains,gr}}^{\text{sol}} \end{bmatrix} \tag{3.14}$$

with

- C_{blind}, is a coefficient of blind position.
- C_{g}^{c}, C_{g}^{r}, constants expressing the convective and radiative shares of internal gains.
- $\phi_{\text{trans}}^{\text{w}}$, $\phi_{\text{abs}}^{\text{w}}$ are the solar fluxes transmitted 3.15 / absorbed 3.16 through/by windows.
- ϕ_{gains}, ϕ_{hvac}[2], ϕ_{vent}[3] are the heat fluxes due to internal gains, hvac equipment (convective and radiative) and ventilation losses.

$$\phi_{\text{trans}}^{\text{w}} = A_{\text{w}}[I_{\text{b}}^{\text{trans}} C_{\text{b}}^{\text{sr}} + I_{\text{d}}^{\text{trans}} C_{\text{d}}^{\text{sr}}] \tag{3.15}$$

$$\phi_{\text{abs}}^{\text{w}} = aA_{\text{w}}[I_{\text{b}} C_{\text{b}}^{\text{sr}} + I_{\text{d}} C_{\text{d}}^{\text{sr}}] \tag{3.16}$$

and

[2] see section:3.1.3
[3] see section:3.1.4

- $C_{\mathrm{b}}^{\mathrm{sr}}$ is the sun ratio coefficient depending on window's horizontal and vertical shadings calculated as a function of shading depth characteristics.
- $I_{\mathrm{b}}^{\mathrm{trans}}$ is the beam transmitted component depending on the transmission coefficient, the beam on plane and the angle of incidence.
- The *angle of incidence* is the angle between surface normal and direction of incident beam radiation.
- $I_{\mathrm{d}}^{\mathrm{trans}}$ is the diffuse transmitted component depending on window's transmittance, the diffuse component on plane and a coefficient adapted from [183].

3.1.2 Solar Radiation model

The implemented solar radiation model employs hourly measured data imported from the meteorological file, combined with sky models and simplified mask algorithms.

More in detail, the estimation of the total tilted surface radiation requires the knowledge of the fraction of the total horizontal radiation into its beam, diffuse, and ground reflected components, as analytically presented in section: 2.4.2.1. The beam and diffuse components are initially given by the meteorological file and then, these are projected onto the tilted surfaces, multiplied by mask coefficients. The direct solar mask module, as shown in Figure: 3.2, determines at which time steps the sunbeam is obscured, given the shading mask for each boundary or thermal zone, the sun height and azimuth, calculated through [184]. The shading mask is calculated either at the center of the thermal zone or at the center of each boundary. The second option, requires the calculation of the center point, its azimuth, and inclination. The diffuse mask model estimates the sky view factor in order to take into account the visible sky vault as given in [185]. Both components are then projected onto the titled surfaces. The ground and sky diffuse components are calculated through the integration of the PV-lib module [186], where the Perez 1990 [74] model is applied. The method follows the procedure as exactly described in section 2.4.2.1.

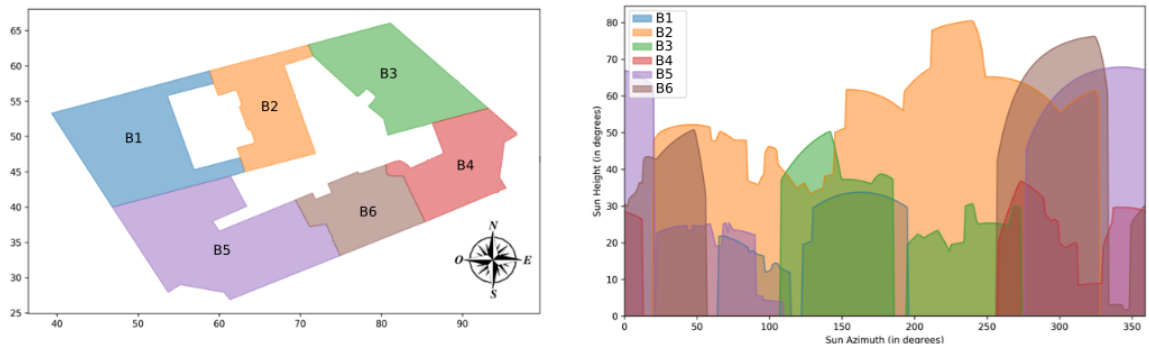

Figure 3.2: Mask calculation between buildings, where the south is located at 180 on x-axis, adapted from: CSTB.

3.1.3 Emitter model

The emitter model (as any object in Dimosim), is based on a fourfold procedure. Initially, the generic object named "object generator" completes possible missing parameters. Later, the so-called "sizer" object is used, with the objective to estimate a nominal heating (3.17) and cooling (3.18) power, depending on the thermal characteristics of the corresponding thermal zone,

$$\phi_{\text{heat}}^{\text{nom}} = U_{\text{v,z}}(T_{\text{sp}}^{\text{h}} - T_{\text{air}}^{\text{min}}) + \phi_{\text{vent}}^{h} \ [W] \tag{3.17}$$

or

$$\phi_{\text{cool}}^{\text{nom}} = U_{\text{v,z}}(T_{\text{air}}^{\text{max}} - T_{\text{sp}}^{\text{c}}) + \phi_{\text{vent}}^{\text{c}} + \frac{I_{\text{b}}^{\text{max}} A_{\text{w}}}{3} + \phi_{\text{gains}}^{\text{int}} \tag{3.18}$$

with:

- $U_{\text{v,z}}$ the aggregated (boundaries and windows) zone's U-value [W/K]
- T_{sp} the set-point temperature for heating and cooling [K]
- ϕ_{vent} the ventilation flux for heating and cooling given by equation: 3.19, with the ΔT term given for the min/max air temperature and the respective set-points
- I_{b} the max beam radiation from the imported meteorological file [W/m^2]
- $\phi_{\text{gains}}^{\text{int}}$ the internal gains given either from the occupation scenario or as a constant value [W]

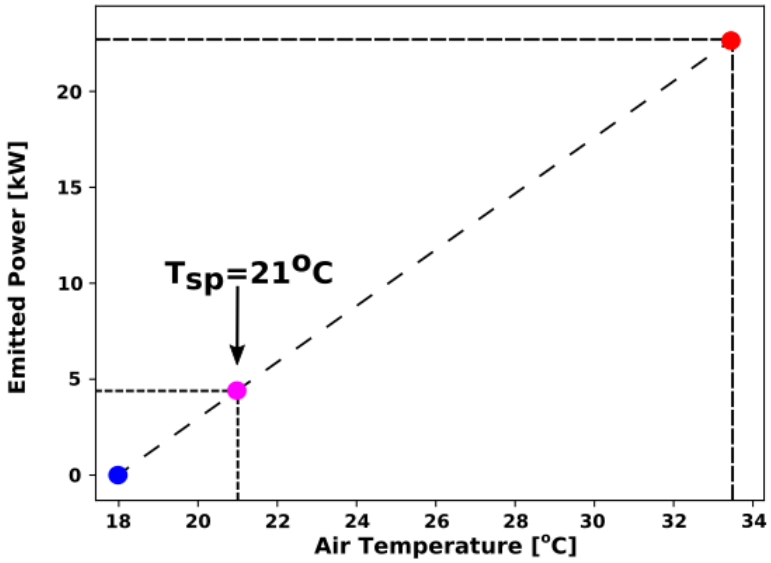

Figure 3.3: Estimated power for a given heating set-point temperature (21^{o}C) based on the interpolation scheme between the extreme values.

while the initialisation function is responsible for the matrix creation and the initial values completion.

Once the nominal heating and cooling demands are calculated, then for every time step inside the time loop, depending on the emitter type (radiators, split-systems, etc) and the emitter control, the calculation of the emitted power, as well as the determination of the radiative and convective shares are acquired. In case of ideal control, the calculation is based on the thermal characteristics of the thermal zone, through an iterative scheme between the maximum and minimum heating or cooling power. The state space zone model calculates the extreme indoor air temperatures and a linear interpolation (Figure: 3.3) is executed between the obtained values. Given the set-point temperature and the linear fit, the determination of the actual power of the emitter is established. In a third calculation of the zone state space system, the actual power is injected in order to update all states of the model.

3.1.4 Ventilation model

The energy gains or losses to the thermal zone due to the ventilation flow stream are evaluated in the combined ventilation-infiltration module. Two types of ventilation systems are implemented: simple mechanical extract ventilation and mechanical ventilation with heat recovery. The calculation is based on equation 3.19,

$$\phi_{\text{vent}} = \frac{\dot{m}_{\text{vent}}}{dt} C_{p_{\text{air}}} (1 - f_0)(T_{\text{air}} - T_{\text{z}}), \ [W] \tag{3.19}$$

where:

- $\dot{m}_{\text{vent}}$ is the supplied mass flow rate [kg/s] given in 3.20
- f_0 is the efficiency of the system defined as the ratio of heat that can be recovered by using exhaust air (0 if no heat recovery)
- K_1 is the air change rate [1/h]
- V_{z} is the zone air volume [m^3]
- ρ_{air} is the air density given by [187]

$$\dot{m}_{\text{vent}} = K_1 V_{\text{z}} \rho_{\text{air}} \tag{3.20}$$

3.1.5 Generator model

The generator model represents a multi-scale object allowing to consider different levels of system's energy generation. At zone level, the generator can represent an individual energy system providing heating/cooling needs and/or DHW production. At building level, the generator can act either as a standalone collective system delivering heat to one or several thermal zones, or to be connected to a network and deliver heat to the building through either a building or a thermal zone substation. This generator type is connected to a district level thermal grid, which is linked to a centralized energy production system. The building substation is mainly represented by a heat exchanger transferring the heat from the primary circuit (thermal grid) to the secondary one (building loop). At this level, depending on the selected distribution type,

the connections and thus the hydronic-loops may differ. In the context of this thesis, two main elements will be studied. The individual energy generation at the zone level and the centralized energy production at the district level.

3.1.5.1 Individual energy generation - Zone level

The local generator corresponds to an individual energy system, delivering the thermal output to a single thermal zone, which is then injected directly as thermal flux through an emitter, as shown in Figure 3.4. The integrated generator models at this level (Zone Generator), represent

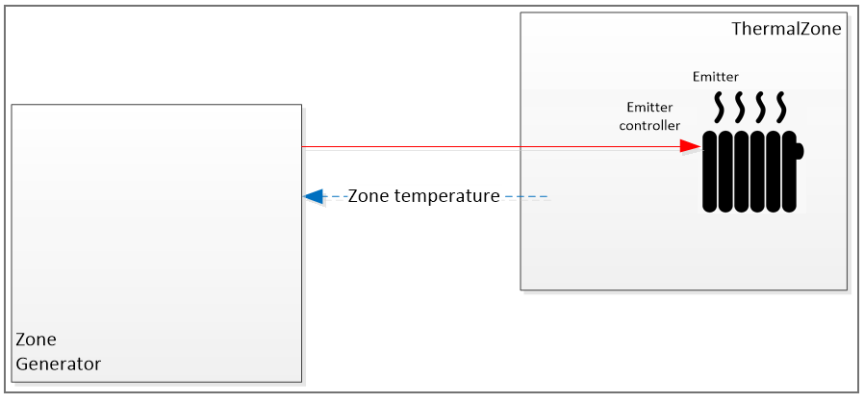

Figure 3.4: Schematic representation of a local independent energy system, source: CSTB.

either an electric convector or an air-to-air heat pump (split air conditioner). Moreover, an ideal system at this level, as the one shown on figure 3.4, has been integrated, providing to the linked emitter the desired power. This type of system is not representative of any real technology, but allows simulating a district with ideally operating generators, meaning that without any consideration of the nominal specifications of the generator, it is possible to reach all temperature set-points (the latter does not exist if the necessary power exceeds the nominal one calculated in the sizing procedure).

3.1.5.2 centralized energy generation - Building & Zone substation

Based on a centralized energy generation, the distributed heat from the thermal network is initially transferred to the building substation, which is represented as a heat exchanger (Figure: 3.5). The main pump circulates hot water up to the zone substation level, while the control valve allows to control the supply temperature in the building circuit. Thus, the building level distribution module is dissipating heat to the zone substation. The latter is used to deliver heating/cooling and domestic hot water to a single thermal zone. This model is composed of two steady state heat exchanger models for heating/cooling and DHW that are activated through control valves. The heat exchange coefficients of both heat exchangers are defined as a second order polynomial from a dataset, depending on the primary and secondary flow rates [188]. At each time step, depending on the current flow rates, the polynomial is employed to establish the correct heat exchange coefficient.

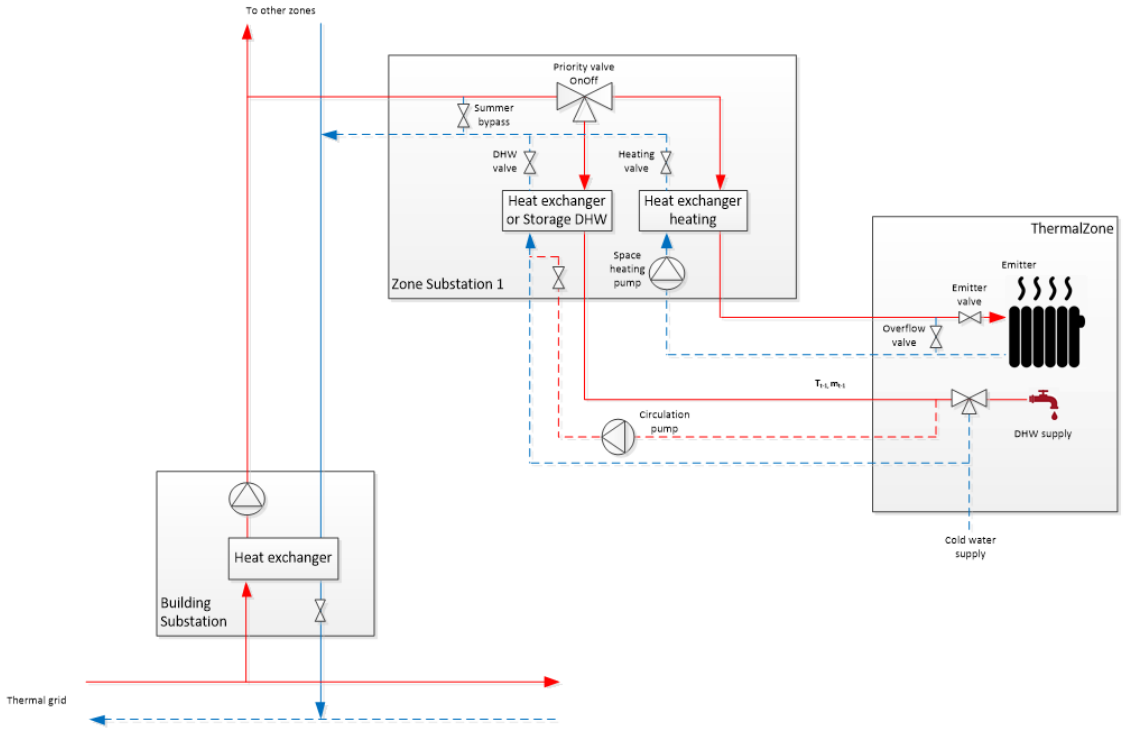

Figure 3.5: Schematic representation of a centralized energy generation scheme with building & zone substations, source: CSTB.

3.1.6 Thermal network model

The thermal network model consists of three main elements. Initially, the network generation module generates either an existing network configuration or future possible installations and it is responsible for the creation of the nodes. The network configuration module sets the characteristics of the tube model. Both modules are executed in a pre-processing mode, while the third element, the tube model, calculates the temperature (and the pressure when hydraulic model is considered) at each node and it is part of the time loop of the core model. Three types of thermal network models are available in the tool:

1. Steady state model
2. Transient nodal model (one node or multiple nodes)
3. Plug-Flow model

The steady state model has been used in this thesis, presented further in section:3.1.6.2, due to its convenience and time efficiency, although the steady state conditions are not satisfied in real case applications. However, it is sufficient for basic energy demand and consumption calculations.

3.1.6.1 Network generation & configuration

The network generation module is operating with a twofold objective. At the initialization phase it allows:

- importing standardized file formats of existing network configurations, checking and recovering the possible missing branches or
- generating automatically the network path based on street information or user defined data.

A complete set of import data is realized when the coordinates of the central thermal station are defined. At a second step, the initial network graph is discretized in order to allow the creation of intermediate nodes where the buildings are connected to them. In parallel, the minimum tube length is preferred, concluding to superfluous node reduction based on the shortest path bridging (spanning tree algorithm) protocol. The entire procedure is depicted in Figure: 3.6 for the *"Geraniums district"*[4] located in the city of La Rochelle, France. The thermal grid is generated based on road paths imported from geojson file.

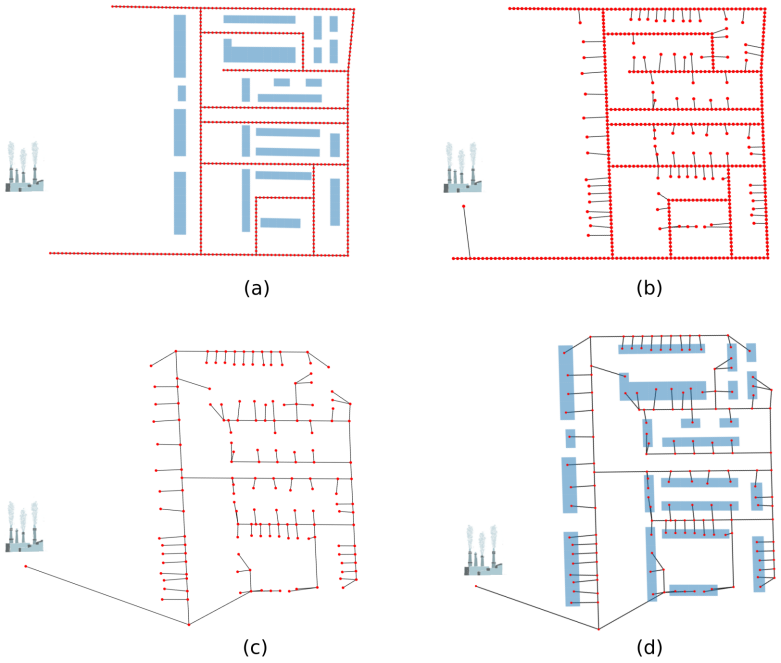

Figure 3.6: Network generation procedure. Data import (a), node generation (b), superfluous nodes elimination (c), final outcome with building substation-nodes (d).

The different configurations of available networks in the tool are:

- *Two-tube model*
- *Four-tube model*

The two-pipe model is the most common configuration of the tool, consisted of supply and return tubes, allowing a district heating, cooling or reversible simulation. It is limited to one type at a time, thus it can be extended to the four-tube model in case of parallel applications (simultaneous heating and cooling needs). A three-pipe model is planned in the forthcoming version of the tool. This will allow to model a thermal network with two supply pipes at different

[4]see: section 5.3.3.4

temperatures. This configuration is pertinent when considering districts composed of buildings that operate at different temperatures.

3.1.6.2 Network steady state model

The description of a thermal network model is mainly based on the interconnection of two principal phenomena. The thermal grid is connected to the building and zone substations, as presented in section (3.1.5.2) through a network of tubes. In the model speculation, each of them is represented by a nodal description. At these nodes, the fluid that transfers the heat enters with a reference temperature and leaves with a modified one, corresponding to the supply and return temperatures. In parallel, the pressure differences (pressure drop) are calculated for estimating pump consumptions. Hence, thermal and hydraulic phenomena are considered in order to represent an integrated network model.

To calculate the return temperatures in the afore-mentioned nodes, we consider that the network consists of discrete segments. In each of these segment points, since the substations are represented as heat exchangers, the heat flow can be determined by the logarithmic mean temperature difference, and thus:

$$\phi_{\text{ex}} = 1 - \exp\left[\frac{UA}{\dot{m}C_{p_{\text{fl}}}}\right] \tag{3.21}$$

where the UA is the overall heat transfer coefficient, U, multiplied by the heat transfer area A of the heat exchanger. The latter, is considered as the fraction of the nominal mass flow rate with density and maximum velocity. The overall heat transfer coefficient is estimated from 3.22, where the fouling resistances are neglected:

$$\frac{1}{U} = R_{\text{in}} + R_{\text{tb}} + R_{\text{out}} \tag{3.22}$$

where:

- the R_{in} term is the inside convection resistance, given by 3.23, with $N_u \propto Re,\, Pr$ the Nusselt number depending on flow characteristics and thus on Prandlt and Reynolds numbers [189],
- the R_{out} term is the outside convection resistance, given by 3.26 and
- the $R_{\text{tb}} = R_{\text{cop}} + R_{\text{ins}}$ term is tube's conductive resistance (copper-based and insulation-polyethylene high-density), given by 3.24 and 3.25.

$$R_{\text{in}} = \frac{1}{h_{\text{in}} A_{\text{in}}} = \frac{1}{\frac{N_{\text{u}} k_{\text{fl}}}{d_{\text{tb}}^{\text{in}}} \pi d_{\text{tb}}^{\text{in}} L_{\text{tb}}} \tag{3.23}$$

$$R_{\text{cop}} = \frac{\ln(d_{\text{tb}}^{\text{out}} - d_{\text{tb}}^{\text{in}})}{2\pi\lambda_{\text{tb}} L_{\text{tb}}} \tag{3.24}$$

$$R_{\text{ins}} = \frac{\ln(d_{\text{ins}}^{\text{out}} - d_{\text{tb}}^{\text{out}})}{2\pi\lambda_{\text{ins}} L_{\text{tb}}} \tag{3.25}$$

$$R_{\text{out}} = \frac{1}{h_{\text{out}} A_{\text{out}}} = \frac{1}{h_{\text{out}} d_{\text{tb}}^{\text{out}} \pi L_{\text{tb}}} \tag{3.26}$$

Hence, the outlet temperature of a tube segment can be calculated in a matricial system consisted of the length (L), UA and flow matrices, from equation: 3.27.

$$T_{\text{out}} = T_{\text{in}}(1 - \phi_{\text{ex}}) + T_{\text{amb}} \tag{3.27}$$

In the latter, T_{in} is the segment's supply temperature, ϕ_{ex} is the return flow of the tube segment and T_{amb} is the ground temperature. The grid's return temperature is the dot product of the corresponding segments return temperature and flow divided by the total return flow. In this steady-state model, transient effects have been represented by adding a storage volume at each building connection or in the central production system.

3.2 EnviBatE

EnviBate [171] stands for environment and buildings. It is a research numerical package, developed by the *University of La Rochelle (LaSiE)*, conceived to study the interactions between buildings and local microclimate. It is an already coupled model, as it comprises of a thermal surface and reduced-order thermal building models, a simplified module of the urban canopy and a sophisticated solar radiation algorithm. These sub-models are finally integrated in a unique zonal model, where buildings and outdoor environment communicate through interfaces, the urban surfaces. The final integration has been carried out in Python programming language (2.7v). The following sections provide details regarding the various submodules of the tool and the implemented physical mechanisms used to describe these interactions.

3.2.1 Generation of urban meshes

As already stated, the tool is consisted of various sub-modules and each of them corresponds to a different calculation domain. At the end, all of them are integrated in a unique final zonal mesh that accounts for buildings, outdoor surfaces and outdoor air cells. More in detail, EnviBatE, is using a fine triangulated mesh (Figure 3.7b) for the calculation of solar radiation, a hexahedral structure grid for the airflow calculation (Figure 3.7a) and an unstructured zonal outdoor mesh (Figure 3.7c) where the coupled phenomena are computed.

The imported layout data, obtained either by two / three-dimensional vector databases or from three-dimensional modeling engines, correspond to the starting point of the methodology. The layout data are then fully attributed in an XML file format and parsed to a three-dimensional finite element mesh generator, GMSH [190]. At this step, given the characteristic length of precision for the zonal sub-grid generation, the initial mockup is meshed and extruded up to the canopy level. At the next step, the physical volumes are divided into building thermal zones or canopy cells. In parallel, the physical surfaces are clustered to urban surfaces (roads, sidewalks, greenery, etc.), building facades or roofs, where the physical properties are attributed. The process is completed with the generation of the solar sub-mesh and the attribution of windows, given a window to wall ratio. At the same time, an indexation module ensures the correspondence of every physical surface or volume between the various sub-meshes. An alternative option has been developed, in which the published python library pygmsh (MIT license) is used, and the aforementioned methodology is performed automatically without requiring the manual intervention of the user.

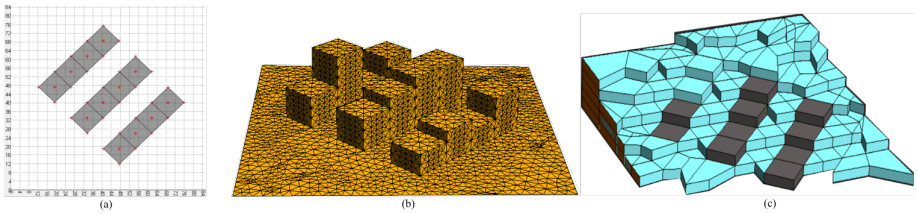

Figure 3.7: The airflow grid (a), triangulated solar mesh (b) and the integrated zonal mesh (c).

3.2.2 Solar radiation model

The integrated solar radiation model of EnviBatE combines SOLENE [191] simulation package enhanced with modules based on the radiosity method. The first is called internally for the computation of beam and diffuse components as well as the estimation of view factors. The second one is used for the calculation of the shortwave inter-reflected component and the longwave irradiance exchanges.

3.2.2.1 Calculation of beam, diffuse & reflected components

Beam and diffuse components are calculated at the barycenter of each triangle, through the triangulated mesh presented in figure 3.7b. The calculation requires further import layouts. A simple layout (non-triangulated) of building horizontal surfaces and vegetation elements which serves the role of the solar masks and a second one representing the sky vault. The last is considered as a hemisphere of infinite radius with the scene located at its center (Figure: 3.8), divided in 4^n discrete triangulated segments [192].

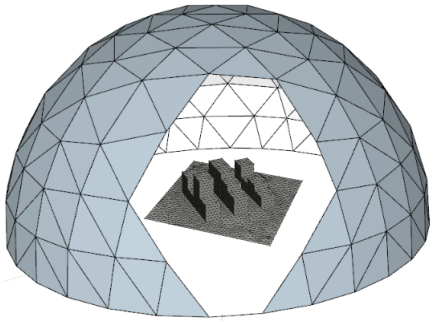

Figure 3.8: Sky dome division in triangulated patches with the scene at its center.

The tool considers the sun as a spherical point source where the celestial geometry determines its position based on the solar declination angle [193], the solar altitude and solar azimuth. Suns' energy is estimated by a statistical radiance model [191], [194]. The sky dome can be seen as a source of diffuse energy with a non-uniform luminance distribution. The luminance is described by the "all weather" Perez model [195].

More in detail, in order to take into account the presence of the masks in an urban geometry, each surface is considered as an observer looking vertically at the sky. The urban geometry is then projected to the sun path in order to determine at each time step (1h) whether the sun is visible or not from this surface, using an algorithm of hidden surfaces [192]. Thus, if the sun is

visible, the beam component can be determined from equation: 3.28,

$$I_b = I_0 R_b \tag{3.28}$$

where R_b, is the geometric factor expressing the ratio of beam radiation on the tilted surface to that on a horizontal surface at any time. It is estimated from 2.22, and I_0 is the incident beam radiation on a horizontal surface. The same procedure is followed in the diffuse mask model, executed independently from the previous one.

In the integrated model of EnviBatE, the direct and diffuse components are calculated under clear sky conditions. In order to reduce the simulation time, the executables of Solene are called in a daily basis. In order to take into account the nebulosity, daily average Perez coefficients are introduced in the calculation of the diffuse component. In parallel, the beam component is weighted with a cloud cover coefficient. To do so, a simulation of a squared horizontal surface is carried out, and its outputs are used to generate a coefficient which is based on the direct component of the meteorological data:

$$C_{\text{neb}} = \min\left[\max\left[0, \frac{I_{\text{b,meteo}}}{I_{\text{b,sqr}}}\right], 1\right] \tag{3.29}$$

Once the direct and diffuse components are estimated, the total incident solar radiation received by a surface is given as:

$$I_{0,\text{SW,i}} = \sum_{n=1}^{N_{\text{trn}}} C_{\text{neb}} \cdot I_{\text{b,SW,i}} + I_{\text{d,SW,i}} \tag{3.30}$$

where N_{trn} expresses the number of sub-triangles that constitute an urban surface. Given the total amount of incident radiation received at each surface, the calculation of the reflection component is held by the radiosity method for each urban surface, as presented in section: 2.4.2.4.

3.2.2.2 Calculation of exterior longwave radiation

The longwave radiation is an important mechanism of heat transfer in buildings. The urban surfaces (building surfaces, roads, sidewalks, urban greenery) radiate to sky and receive an amount of radiative heat flux from surrounding surfaces. Due to its complexity, several assumption must be made:

- the urban surfaces are assumed to be opaque ($\tau = 0$), diffuse (isotropic radiation) and isothermal with a uniform irradiation
- the sky is assumed to be a fictive surface with an effective sky temperature[5]

Taken into consideration the afore-mentioned assumptions, the net longwave radiation received by a surface, can be estimated by the formula:

$$I_{\text{LW,i}} = \epsilon\sigma \sum_{j=1}^{N_s} F_{\text{i,j}}(T_{\text{s,j}}^4(t) - T_{\text{s,i}}^4(t)) + \epsilon\sigma F_{\text{i,sky}}(T_{\text{sky}}^4(t) - T_{\text{s,i}}^4(t)) \tag{3.31}$$

[5]see Section: 2.4.2.3

According to [64] and considering relatively small differences between the surface temperatures, the outdoor surfaces can be handled as a fictitious single surface where:

$$\left(T_{\mathrm{s,j}}^4(t) - T_{\mathrm{s,i}}^4(t)\right) = 4T_{\mathrm{mrt}}^3(T_{\mathrm{s,j}}(t) - T_{\mathrm{s,i}}(t)) \tag{3.32}$$

where T_{mrt} is the mean radiant temperature, defined as the temperature of a black enclosure exchanging heat by radiation with the given surface at the same rate as the actual surroundings. In the model this is taken as the average surface temperature of the considered surfaces according to [196]. Equation 3.32 can be linearized by introducing a radiation heat transfer coefficient:

$$h_{\mathrm{rad,e}} = 4\sigma T_{\mathrm{mrt}}^3 \tag{3.33}$$

Then, equation 3.31 reduces to:

$$I_{\mathrm{LW,i}} = \sum_{j=1}^{N_{\mathrm{s}}} h_{\mathrm{rad,e}} F_{\mathrm{i,j}}(T_{\mathrm{s,j}}(t) - T_{\mathrm{s,i}}(t)) + h_{\mathrm{rad,e}}^{'} F_{\mathrm{i,sky}}(T_{\mathrm{sky}}(t) - T_{\mathrm{s,i}}(t)) \tag{3.34}$$

3.2.3 Airflow model

In order to calculate the wind distribution in urban areas, EnviBatE is coupled with the airflow model QUIC-URB [197]. In this section, a brief description of QUIC system and QUIC-URB are presented, as well as the physical and mathematical background of the model. Further in this section we highlight the established methodology to integrate the wind velocities in the core model.

3.2.3.1 Presentation of QUIC dispersion modeling system

QUIC stands for Quick Urban & Industrial Complex. It has been developed in Los Alamos National Laboratory with the objective of fast response urban transport and dispersion modeling. The model computes the three-dimensional wind patterns and pressure fields as well as the dispersion of airborne contaminants [198] around clusters of buildings. It consists of QUIC-URB[197], QUIC-PRESURE [6] [199], QUIC-PLUME [7] [200],[201] and QUIC-GUI [202] corresponding to wind and pressure models, a dispersion model and a graphical user interface respectively.

3.2.3.2 Calculation of the wind velocity components

QUIC-URB uses empirical algorithms and mass conservation to estimate the wind velocities around buildings using a zonal approach [197]. The wind field distribution is calculated using the eulerian approach, as shown in Figure: 3.9, based on a structural grid (hexahedral in 3-D). Building footprints are depicted either as simple cubes (including stacked polygons), or cylindrical or ellipsoidal shapes. Urban vegetation can also be considered.

[6] based on Poisson equation : $\frac{\partial}{\partial x_i}\left(\frac{\partial \bar{P}}{\partial x_i}\right) = \rho\frac{\partial}{\partial x_i}\left(\nu\frac{\partial^2 \bar{U}_i}{\partial x_j \partial x_j} - \frac{\partial(\bar{U}_i\bar{U}_j)}{\partial x_j} - \frac{\partial(\overline{\partial u_i' \partial u_j'})}{\partial x_j}\right)$

[7] based on Lagrangian approach: $\frac{D\vec{u}}{Dt} = \frac{du}{dt} + \frac{d\nu}{dt} + \frac{dw}{dt}$

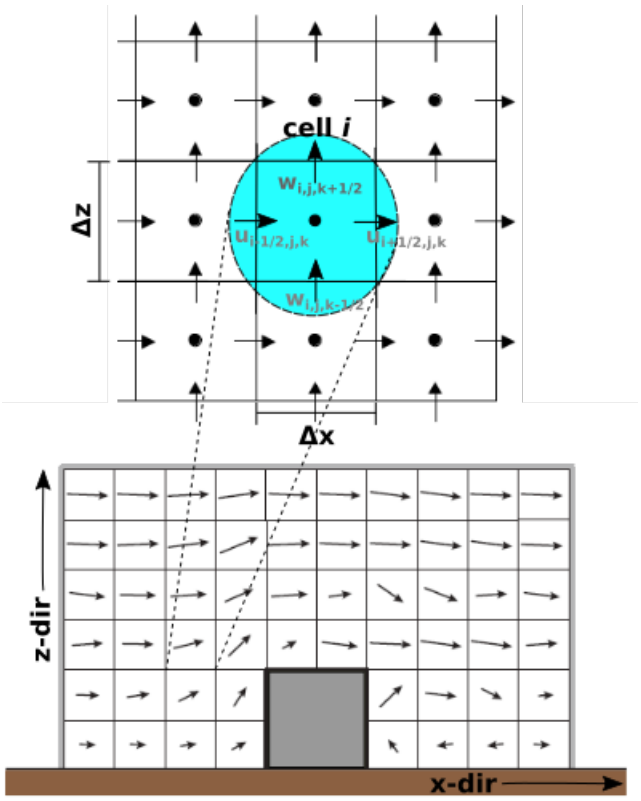

Figure 3.9: Schematic representation of wind-field calculation using the eulerian approach, adapted from:[65]-[198].

Initially, a uniform wind field representation is prescribed (u_0, ν_0, w_0) based on an incident flow u_{in}, given from the power-law velocity profile 2.64. The urban space around buildings is divided in sub-domains where empirical wakes and cavities are defined, as presented in section 2.4.3.1. Then, the flow patterns associated with building geometries are invoked, similarly to those of section: 2.4.3.1. More in detail, the flow regime is determined by estimating the length-to-height ratio S/H (Figure: 3.10). If $S/H > 2$ the flow regime is treated as *isolated roughness flow*, while for cases where $S/H < 2$, the geometry is treated as street canyon, where the *skimming flow* is taking place. In the last case, the initial velocity field is given by Rockle's formulation:

$$u_0 = -u(H)\frac{d}{0.5S}\left(\frac{S-d}{0.5S}\right) \tag{3.35}$$

$$w_0 = -\frac{1}{2}u(H)\left|1-\frac{d}{0.5S}\right|\left(1-\frac{S-d}{0.5S}\right) \tag{3.36}$$

where according to Figure: 3.10, $u(H)$ is the mean wind velocity at the top of the upwind building, w is the vertical velocity , S and d are the distances between buildings and downwind from the upwind building respectively. The flow above buildings is described by the equation 2.63

where the displacement height and the roughness length are given by the following formulas:

$$d = 0.8 \frac{\sum_{i=1}^{N_b} W_i L_i H_i}{\sum_{i=1}^{N_b} W_i L_i} \tag{3.37}$$

$$z_0 = 0.2 \frac{\sum_{i=1}^{N_b} W_i L_i H_i}{L_x L_y} \tag{3.38}$$

$$\tag{3.39}$$

with N_b the number of buildings, L_x and L_y the lengths of the computational domain in x and y directions.

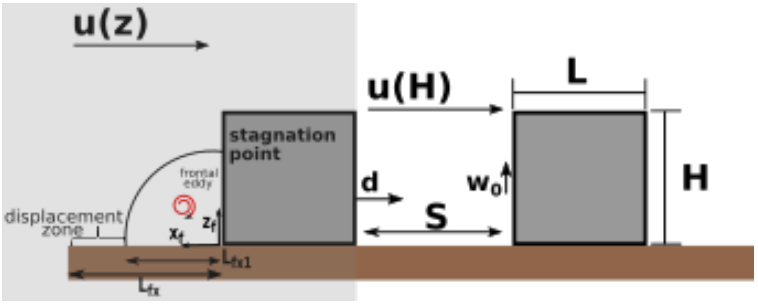

Figure 3.10: Schematic representation of frontal area parameters (colored / isolated building) and multiple building parameterization scheme, adapted from [203].

In case of isolated roughness flow, the length of the frontal eddy and cavity zones, L_f and L_r, are parametrized using the modified formulas of [204] and [205], as proposed by [206] after wind tunnel validation experiments. These are presented below:

$$L_{f1} = \frac{0.6 \frac{W}{H}}{1 + 0.8 \frac{W}{H}}, \text{ frontal eddy} \tag{3.40}$$

$$L_f = \frac{1.5 \frac{W}{H}}{1 + 0.8 \frac{W}{H}}, \text{ displacement zone} \tag{3.41}$$

$$L_c = \frac{1.8 \frac{W}{H}}{\left(\frac{L}{H}\right)^{0.3} \left(1 + 0.24 \frac{W}{H}\right)}, \text{ cavity zone} \tag{3.42}$$

Since QUIC-URB solution is based on the equation of mass conservation [207], pressure gradients and vorticity generation are neglected. The last terms are taken into account by a simple vortex parametrization applied to the front eddy region through trigonometric relations for the streamwise 3.43 and spanwise 3.44 velocities,

$$u_0 = u_0(H)\left(0.6\cos\left(\frac{\pi z_f}{0.5H}\right) + 0.05\right) \left(-0.6\sin\left(\frac{\pi x_f}{L_{fx1}}\right)\right), \text{ streamwise velocity} \tag{3.43}$$

$$w_0 = u_0(H)\left(-0.1\cos\left(\frac{\pi x_f}{L_{fx1}}\right) - 0.05\right), \text{ spanwise velocity} \tag{3.44}$$

with x_f, z_f the varying length and height (Figure : 3.10-colored) of the vortex region [203].

QUIC-URB was compared with a Reynolds-averaged Navier-Stokes (RANS) computational fluid dynamics (CFD) model, and a Large Eddy Simulation (LES) CFD code against time-averaged wind measurements obtained in downtown Oklahoma City during the Joint Urban 2003 Field Campaign [208]. The authors suggested that the model performed only slightly worse than the two CFD codes, and given the fact that the simulation time was 2-3 orders of magnitude faster, it is clear that it captures the major flow features for a fraction of the computational cost.

3.2.4 Outdoor Thermal Surface model

The thermal surface model constitutes the key element where the surface temperature calculation is used to couple the outdoor air temperature with the indoor thermal load derived from a thermal zone calculation. To do so, the thermal balance equation 3.45 is used, to compute both the interior and exterior surface temperatures. The solution requires the calculation of the conductive and convective heat fluxes (3.45: terms 1,2), while at the same time the longwave and the incident total shortwave irradiances (3.45: terms 3,4) must also be computed.

$$\underbrace{\phi^t_{\text{cond, i}}}_{1} + \underbrace{\phi^t_{\text{conv, i}}}_{2} + \underbrace{I^t_{\text{LW, i}}}_{3} = \underbrace{I^t_{\text{SW, i}}}_{4} \tag{3.45}$$

For the calculation of the conductive heat flux, the response factors method is selected. This method relates the current heat flux with past and present values, through time series coefficients, utilizing a fixed time step (1h) and a triangular unitary excitation (1^oC). Analytically, is presented in section: 2.3.3.1.

$$\phi^t_{\text{cond, i}} = \sum_{n=0}^{\infty} Y_{\text{i}}^n T_{\text{si,i}}^{t-n} - \sum_{n=0}^{\infty} Z_{\text{i}}^n T_{\text{se,i}}^{t-n}, \text{ for building surfaces} \tag{3.46}$$

or

$$\phi^t_{\text{cond, i}} = \sum_{n=0}^{\infty} Y_{\text{i}}^n T_{\text{g}}^{t-n} - \sum_{n=0}^{\infty} Z_{\text{i}}^n T_{\text{se,i}}^{t-n}, \text{ for ground surfaces} \tag{3.47}$$

For ground surfaces (roads, pavements, etc), the calculation requires the definition of the soil temperature. The latter, is computed through equation: 2.45. It can be noticed that the greater

the thickness of the soil, the number of response factors is increasing. Therefore, a depth of 50 cm (Figure: 2.11-black solid line) was chosen to limit the number of response factors and keep consistent with the storage capacities of the programming environment.

The convective heat flux is calculated by the Newton's Law of Cooling formula, describing heat transfer between a solid surface and a fluid (air) in contact with it (equation: 3.48), for a standard convection coefficient:

$$\phi^t_{\text{conv, i}} = h_{\text{c,i}}(T^t_{\text{a,k}} - T^t_{\text{s,i}}) \tag{3.48}$$

in which the air temperature term ($T^t_{\text{a,k}}$) is equal to the air temperature of the adjacent air cell. In case of multiple adjacency, the term is weighted by the surface ratio:

$$\phi^t_{\text{conv, i}} = h_{\text{c,i}}\left(\frac{A_{\text{i,k}}}{A_{\text{i}}}T^t_{\text{a,k}} - T^t_{\text{s,i}}\right) \tag{3.49}$$

where $A_{\text{i,k}}$ is the surface percentage in contact with the air cell k.

The longwave irradiance term $I^t_{\text{LW, i}}$ is given by equation 3.34 and the total incident irradiance $I^t_{\text{SW, i}}$, considering multiple reflection is calculated from 2.48. The longwave reflections between urban surfaces are neglected.

3.2.5 Building Energy model

The study of the annual energy consumption at district scale, given the actual computational skills, requires a reduced-order model describing the physical processes inside and outside the building.

The integrated BEM is based on the nodal approach combined with the weighting factors method [209], [62]. This calculation method has its origin in a more elementary one: the response factors[8] [209]. By analogy, the identical procedure used to compute the conductive heat flux can be extended to estimate the thermal needs of a zone. Thus, the weighting factors can be globally defined as the thermal responses of a volume cell (thermal zone) to unitary impulses applied on a given excitation [210]. The implemented approach takes into account the thermal solicitations of solar irradiance I_{SW}, outdoor surface temperatures T_{se} and setpoint temperature T_{SP} for every studied building zone, and calculates the thermal responses given either free-floating conditions or indoor setpoint temperature. Then, it calculates the outdoor derivative flux from the given solicitations and the corresponding weighting factors FP$_i$. In this context, the thermal balance of a building volume cell can be achieved by employing the following relation:

$$P^t = \rho C_{\text{p}} V \frac{dT^t_{\text{sp}}}{dt} + \rho C_{\text{p}} D_V (T^t_{\text{sp}} - T^t_{\text{a,k}}) - Q^t_{\text{int}} + \sum_{i=1}^{N_{\text{w}}} A_{\text{i}} h_{\text{ci,i}} (T^t_{\text{si,i}} - T^t_{\text{sp}}) \tag{3.50}$$

where:

P is the power needed to keep the set-point temperature T^t_{sp} at time t [W]

[8] see section:2.3.3

V is the volume of the building cell [m^3]

D_V the ventilation air mass flow [m^3/s]

$T^t_{\text{a,k}}$ the temperature at time t of the canopy cell indexed k in contact with the building cell [^{o}C]

$T^t_{\text{si,i}}$ is the inside surface temperature of wall i of the building cell [^{o}C]

T^t_{sp} is the set-point temperature of of the building cell (thermal zone) [^{o}C]

A_{i} is the area of the wall i [m^2]

$h_{\text{ci,i}}$ is the inside convective heat transfer coefficient [W/m^{2}K]

Q^t_{int} internal heat gain due to occupant metabolism and household appliances [W]

In equation 3.50, the conductive heat flux term requires the computation of the interior surface temperature T_{si}. However, this step has been overpassed by applying the weighting factors method and the convolution technique as follows. The interior surface temperature T_{si} variation is driven by the intensity of an excitation E, equal to:

$$T^t_{\text{si,i}} = \sum_{n=0}^{\infty} T^n_{\text{si},E,\text{i}} E^{t-n} \tag{3.51}$$

where $T^n_{\text{si},E,\text{i}}$ is the interior surface temperature of the wall element i, n hours after the generation of the unitary excitation E. It can be defined as the product of the convolution of the given excitation, because the weighting factors represent for the cell what the response factors are to the wall (equation: 2.6):

$$T^n_{\text{si},E,\text{i}} = \sum_{n=0}^{\infty} WF^n_{\text{i}} E^{t-n} \tag{3.52}$$

By substituting equation 3.52 to 3.51 and speculating k number of excitations, the interior surface temperature of the wall element i will be given:

$$T^t_{\text{si,i}} = \sum_{k=0}^{K} \sum_{n=0}^{\infty} WF^n_{\text{i,k}} E^{t-n}_{\text{k}} \tag{3.53}$$

Hence, the conductive heat fluxes of N_{w} number of walls, yield a thermal load in the zone due to the discrete excitations on interior surface temperatures, equal to:

$$Q^t_E = \sum_{k=0}^{K} \left[\sum_{n=0}^{\infty} \left(\sum_{i=0}^{N_{\text{w}}} A_{\text{i}} h_{\text{c,i}} T^n_{\text{si},E_{\text{k,i}}} \right) E^{t-n}_{\text{k}} \right] \tag{3.54}$$

Thus, the power to maintain the set-point temperature will be finally given by substituting the aforementioned methodology to equation 3.50.

$$\begin{aligned} P^t =& \rho C_{\text{p}} V \frac{dT^t_{\text{sp}}}{dt} + \rho C_{\text{p}} D_V (T^t_{\text{sp}} - T^t_{\text{a,k}}) - Q^t_{\text{int}} - Q^t_{\text{SW}} - Q^t_{T_{\text{sp}}} \\ & - \sum_{i=1}^{N_{\text{w}}} A_{\text{i}} h_{\text{ci,i}} T^t_{\text{sp}} - \sum_{j=1}^{N_{\text{w}}} Q^t_{T_{\text{si,j}}} \end{aligned} \tag{3.55}$$

3.2.5.1 Indoor Thermal Surface model

The indoor thermal surface model follows the thermal balance method, using equation 3.45, as indicated in section 3.2.4. The modified equations for the indoor environment are as follows.

The conductive heat flux equation (3.46) becomes:

$$\phi^t_{\text{cond,in, i}} = \sum_{n=0}^{\infty} Y_{\text{i}}^n T_{\text{se,i}}^{t-n} - \sum_{n=0}^{\infty} Z_{\text{i}}^n T_{\text{si,i}}^{t-n} \tag{3.56}$$

The convective heat flux equation 3.48 is given:

$$\phi^t_{\text{conv,in, i}} = h^{\text{int}}_{\text{c,i}} (T^t_{\text{sp,i}} - T^t_{\text{si,i}}) \tag{3.57}$$

In order to estimate the transmitted solar radiation through the windows, the window to wall ratio and the transmissivity must been taken into account. Equation 2.48 gives the incident solar radiation in the corresponding exterior wall, after the inter-reflection calculation. Then the transmitted radiation is:

$$I_{\text{tr,zone}} = \frac{1}{A_{\text{g}}} \sum_{i=0}^{N_{\text{win}}} A_{\text{win,i}} \tau_i I_{\text{AR,SW,i}} \tag{3.58}$$

where the $I_{\text{AR,SW,i}}$ component is calculated through the methodology presented in section 2.4.2.4. The indoor longwave radiation is computed as presented in section 2.3.3.3 from equation 2.17, where the mean radiant temperature is substituted by the mean surface temperature of the walls multiplied by the view factor.

3.2.6 Integrated tool

3.2.6.1 Integration of Airflow model

As already discussed in sections: 3.2.1, 3.2.3.2 the airflow model is using a hexahedral grid to compute the wind velocities in each grids' center. These outcomes are used to calculate the air mass flow in each interface of the grid. To do so, an interpolation between the center points of two adjacent grids is used, as depicted in Figure: 3.11. Mathematically, the computation is described in equations 3.59 - 3.61 for the three wind speed components respectively. The adapted interpolation scheme preserves the mass conservation in each airflow mesh with an error less than 0.2% [211].

$$Du_{x,y,z} = \frac{u_{x,y,z} + u_{x-1,y,z}}{2} dydz \tag{3.59}$$

$$Dv_{x,y,z} = \frac{u_{x,y,z} + u_{x,y-1,z}}{2} dxdz \tag{3.60}$$

$$Dw_{x,y,z} = \frac{u_{x,y,z} + u_{x,y,z-1}}{2} dxdy \tag{3.61}$$

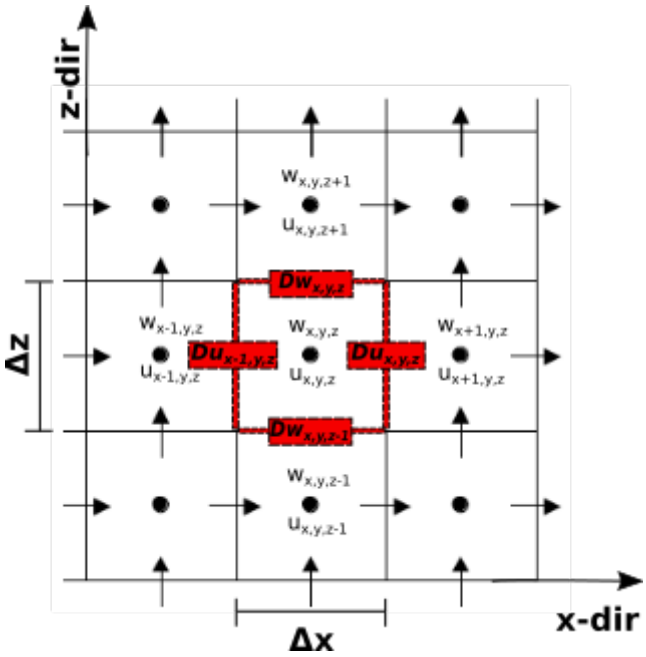

Figure 3.11: Schematic representation of air mass flow calculation through each interface of a centred cell for x and z components.

3.2.6.2 Meshes Adaptation

A crucial step towards the integrated tool is the indexation and adaptation of the various sub-meshes to a unified zonal model. Since the triangulate discretization used in the solar sub-mesh is perfectly matched with the zonal division (one zonal planar surface is subdivided in various triangles based in Delaunay algorithm [212]), each surface constitutes from several triangles. Nevertheless, the discretization scheme of the QUIC structured grid, is more complex to be matched with the unstructured zonal surfaces.

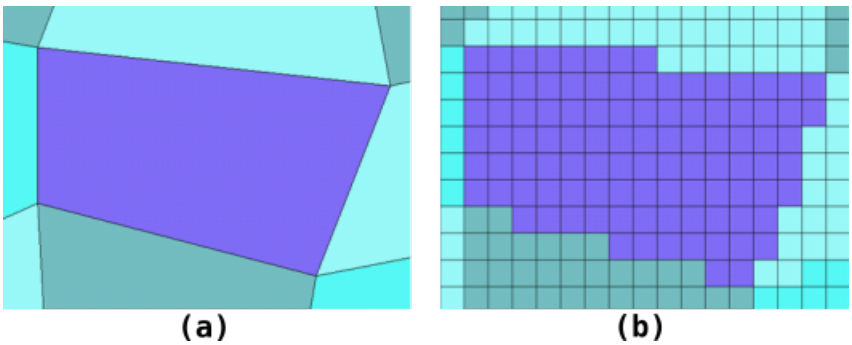

Figure 3.12: Representation of an unstructured zonal mesh (a) and the corresponding structured QUIC meshes (b) on a XY plane, source: [171].

To this end, the urban canopy is divided in numerous sub-cells (volumes) shaped like prisms or hexahedra, as shown in figure 3.12a, represented by five or six facets in 3-D - the interfaces. The corresponding QUIC mesh is formed by numerous of sub-facets, enumerated as N_{fqx}, N_{fqy}

and N_{fqz} in the x,y,z axis respectively (Figure 3.12b). Since the air mass flow in each QUIC-interface is calculated from 3.59, 3.60, 3.61, the overall air mass flow of the corresponding zonal cell will be given as:

$$Q_n = \rho\left[\sum^{N_{\text{fqx}}} Du_{x,y,z} + \sum^{N_{\text{fqy}}} D\nu_{x,y,z} + \sum^{N_{\text{fqz}}} Dw_{x,y,z}\right] \tag{3.62}$$

In parallel, the zonal mesh (comprised of N_{inf} number of interfaces) is governed by the mass conservation principle:

$$\sum_{n=1}^{N_{\text{inf}}} Q_{\text{n}} = 0 \tag{3.63}$$

Due to the interpolation scheme that has been adapted for the calculation of the air mass flow in each QUIC-cell, the airflow budget for the canopy cells (zonal mesh) might be unbalanced. In order to verify the mass balance, an iterative correction process is taking place by redistributing the residuals proportionally to the surface of each canopy cell.

3.2.6.3 Zonal mesh & canopy model

The calculation of the outdoor air temperature through the zonal model approach has been previously applied in [138] and [213] by splitting the urban canopy to equal sub-volumes. In EnviBatE, the developed approach, aiming to study the coupled outdoor-indoor phenomena, extrudes the urban canopy cells according to the form of each thermal zone. This option allows the representation of a variety of urban structures instead of rectangular polygons of building blocks in which the spatial characteristics are explicitly considered. The size of the canopy or thermal zone cells is defined either manually from the user or by setting a characteristic length corresponding to the preferred discretization accuracy. Each urban facet (wall, roof, etc.) is acting as the interface between the indoor and the outdoor environment. Thus, thermal and mass exchanges occur through these elements. As the urban canopy is divided in various sub-cells, each of them is represented by one central node, which is driven by the notion of the thermal balance. The outdoor canopy cell temperature at each time step is computed through equation 3.64:

$$\rho C_{\text{p}} V_{\text{k}} \frac{dT_{\text{k}}}{dt} = \sum_{n=0}^{N_{\text{n}}} \phi_{\text{k,n}} + \phi_{\text{s}} \tag{3.64}$$

where C_{p} is the specific heat of air, V_{k} is the cell volume, ρ is the air density, $\phi_{\text{k,n}}$ is the heat flux through the face n given by equation3.65 and ϕ_{s} is the heat production in the cell given by equation 3.66.

$$\phi_{\text{k,n}} = \begin{cases} C_{\text{p}} Q_{\text{n}} (T_{\text{a,j}} - T_{\text{a,k}}), & \text{in contact with canopy cells} \\ h_{\text{ce,i}} A_{\text{i}} (T_{\text{se,i}} - T_{\text{k}}), & \text{in contact with building cells} \end{cases} \tag{3.65}$$

$$\phi_s = \begin{cases} 0 & \text{in contact with canopy cells} \\ \rho C_{\text{p}} D_V (T_{\text{a,k}} - T_{\text{sp}}), & \text{in contact with building cells} \end{cases} \tag{3.66}$$

with Q_{n} and D_V the air mass flow rate through each interface and the ventilation airflow respectively.

The final integration of the model is expressed by a linear differential equation (3.67). More in detail, the analytical formation of the system is given in 3.68, where **X**(t) is a vector of:

- power, ***P***, calculated through 3.55, shaped equal to the number (N_{z}) of thermal zones,
- surface temperatures, T_{s}, of ground and building surfaces shaped equal to their number, calculated by the analytical expression of 3.45 and
- outdoor air temperature, T_{a}, calculated through 3.64 with a shape equal to the number (N_{c}) of the canopy cells

$$C \cdot X(t) = D(t) \tag{3.67}$$

$$\overbrace{\begin{bmatrix} 1 & c_{02} & \cdots & \cdots & \cdots & c_{0N_{z+s+c}} \\ \vdots & \ddots & \ddots & \ddots & \ddots & \vdots \\ c_{N_{z1}} & \cdots & \cdots & \cdots & \cdots & 1 \\ \hline 0 & \cdots & c_{N_{z+1}N_{z+1}} & \cdots & \cdots & c_{N_{z+1}N_{z+s+c}} \\ \vdots & \ddots & \vdots & \ddots & \ddots & \vdots \\ 0 & \cdots & \cdots & \cdots & \cdots & c_{N_{z+s}N_{z+s+c}} \\ \hline 0 & 0 & \cdots & c_{N_{z+s+1}N_{z+s+1}} & \cdots & c_{N_{z+s+1}N_{z+s+c}} \\ \vdots & \vdots & \vdots & \vdots & \ddots & \vdots \\ 0 & 0 & \cdots & \cdots & \cdots & c_{N_{z+s+c}N_{z+s+c}} \end{bmatrix}}^{\boldsymbol{C}} \cdot \overbrace{\begin{bmatrix} P_0^t \\ \vdots \\ P_{\mathrm{N_z}}^t \\ \hline T_{\mathrm{s,N_{z+1}}}^t \\ \vdots \\ T_{\mathrm{s,N_{z+s}}}^t \\ \hline T_{\mathrm{a,N_{z+s+1}}}^t \\ \vdots \\ T_{\mathrm{a,N_{z+s+c}}}^t \end{bmatrix}}^{\boldsymbol{X(t)}} = \overbrace{\begin{bmatrix} d_0^t \\ \vdots \\ d_{\mathrm{N_z}}^t \\ \hline d_{\mathrm{s,N_{z+1}}}^t \\ \vdots \\ d_{\mathrm{s,N_{z+s}}}^t \\ \hline d_{\mathrm{a,N_{z+s+1}}}^t \\ \vdots \\ d_{\mathrm{a,N_{z+s+c}}}^t \end{bmatrix}}^{\boldsymbol{D(t)}} \tag{3.68}$$

C is the matrix of the resistances and $D(t)$ is the vector of input variables

N_{z}, N_{s}, N_{c} are the number of zones, surfaces and air cells respectively,

c_{ij} are the intrinsic factors of zones and surfaces, determined from the response and weighting factors. From $c_{\mathrm{N_{z+s+1}N_{z+s+1}}}$ to end correspond to air cells intrinsic coefficients,

d_i expresses the potential variable terms over time, according to scenarios such as, ventilation rates, temperature set points, or incident solar irradiation values.

3.3 Generic Coupling Methodology

The coupling methodology is based on a cosimulation approach[9]. This process requires the concurrent representation of building footprints in both tools, as either the building model is simulated twice or it constitutes the basic point where the link between the indoor and the outdoor environment is based on. Thus, the boundary conditions (boundary temperatures), the simulation parameters (exchange coefficients, etc.), the imported layouts (building footprints) and the remaining import data such as occupancy schedules and setpoint temperatures must be identical in both tools. Figure 3.13, presents the initialization phase and the pre-processing flowchart of the adapted methodology. Additionally, a unique identification method of the exchanged physical parameters must be established. This is a crucial step towards the realization of the coupled model, presented in the following section.

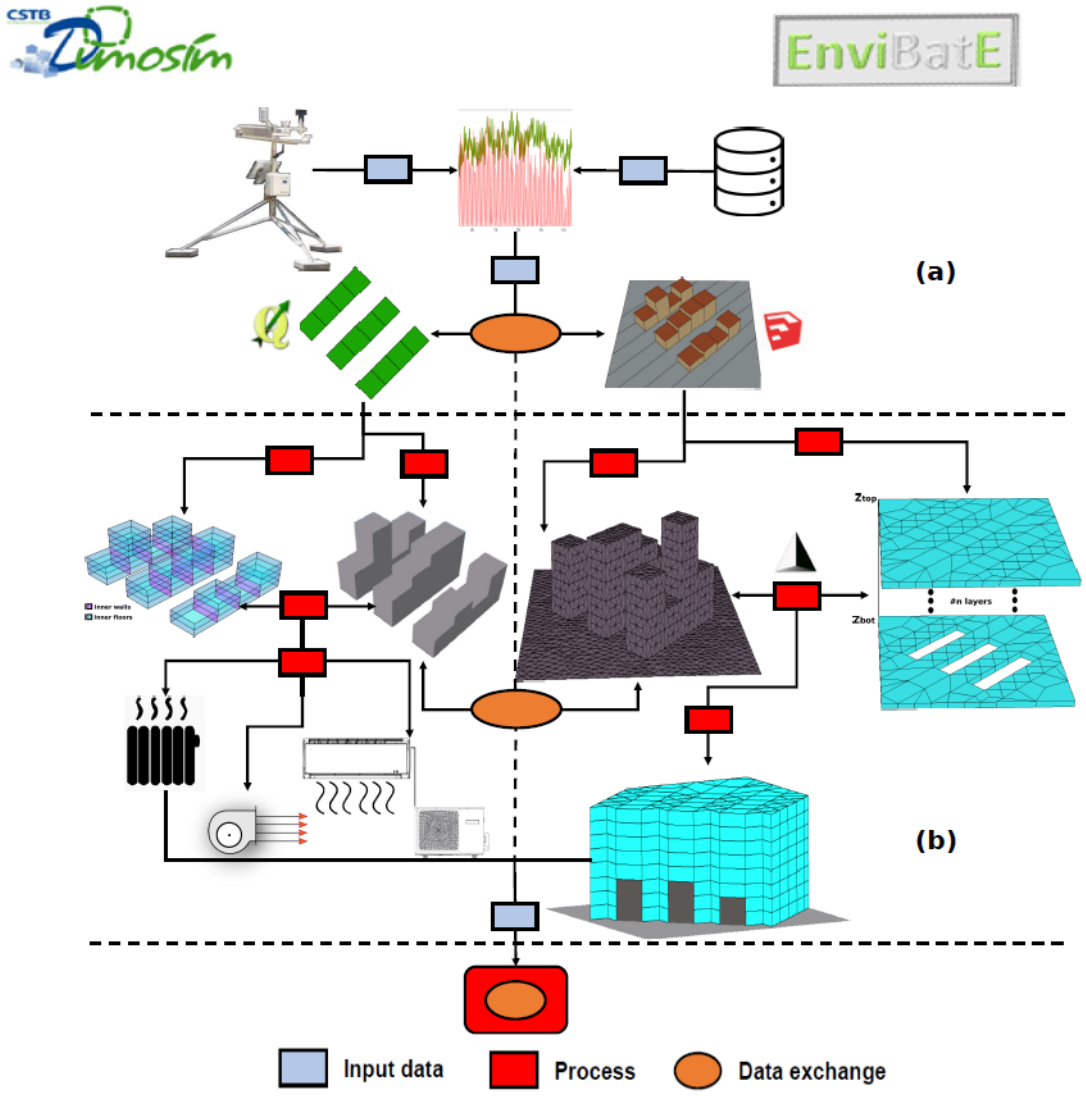

Figure 3.13: Initialization and pre-processing flowchart of the coupling methodology.

[9] see Section: 4.2

3.3.1 Geometrical Manipulations

The examined tools use different types of data sources to introduce building footprints. Dimosim is characterized by an open structure that allows the import of multiple data sources like databases (BD Topo, OpenStreetMap) or standardized information models (shapefiles or geojson), while EnviBATE employs a 3-D modeling engine, CERMA plugin (t4su) embedded into SketchUP [214] software. Although both tools support self-defined file formats; their generation is difficult to adjust at district scale requirements.

To enhance the import data flexibility and to establish a robust and precise communication between the tools, a bidirectional process capable to transform data types is implemented. The representation of either existing layouts or potential district configurations is where the bidirectional sense lies. Figure: 3.13a, shows a characteristic canyon geometry based on building archetypes. The initial file is generated by a 3-D modeling engine. Given a characteristic geolocation point of the hypothetical area where the district belongs, the transformation module detects the building footprints and heights, and then generates an identical mock-up in geojson format, ensuring the correct position with respect to the preferred coordinate system.

On the other hand, in presence of a real district, it is more convenient to extract geometry data from databases. In that case, the opposite procedure is followed. Figure: 3.14a shows a reference district in the city of La Rochelle extracted with QGIS software [215] from GIS data in a geojson format. The developed transformation module, creates automatically buildings and open spaces to the intended text file with high accuracy (Figure: 3.14b). Following the opposite procedure, the mock-up is transformed again in its initial state (geojson format). For visual representation, we plot in Figure: 3.14c, the geojson file (geo-location included) generated after the last transformation, where the method's efficiency is depicted. Apart from building

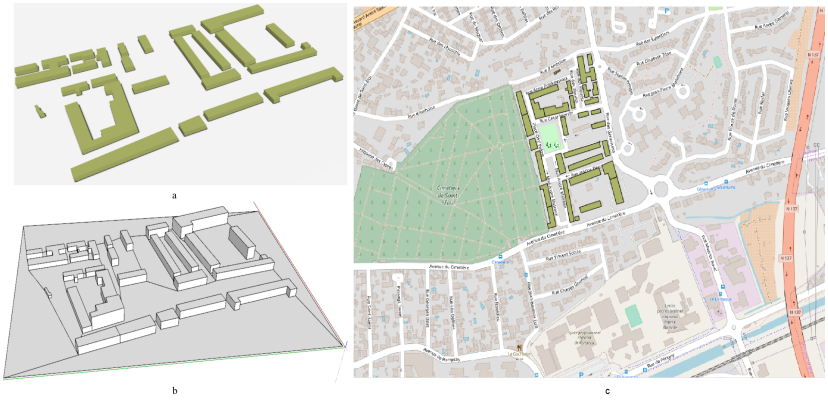

Figure 3.14: 3-D representation of the district in QGIS (a) and (b) in SketchUp after the first transformation. (C) corresponds to the opposite procedure.

configurations, a similar approach could be used to extract layout data for a potential district heating/cooling network configuration[10].

Moreover, a preparatory step towards the online coupling schemes is established with the objective to facilitate and stabilize the exchange procedure. The solar exposed boundaries (building surfaces) combined with ground floor surfaces are indexed in both tools. Initially, during the

[10]see section: 5.3.3.4

layout data transformation, each building object is indexed with a characteristic number representing the building id. Given the simulation parameters (floor height), and after the generation of the thermal zones and the solar exposed boundaries (Figure: 3.13b), each of the aforementioned elements are enhanced with a specific id according to the following formula:

$$\text{Building ID} \dashrightarrow \quad \text{Thermal Zone ID} \dashrightarrow \quad \text{Surface ID} \dashrightarrow \begin{cases} \cdot \text{ Azimuth} \\ \cdot \text{ Area} \\ \cdot \text{ Center point} \end{cases}$$

where: azimuth is the surface orientation for vertical elements, the second index is the area of the surface, and the third one corresponds to the center point of the surface coordinates. This process allows a unique id of every surface, neglecting the possible errors when matching the building surfaces during the data exchange. Additionally, postprocessing is facilitated enabling a convenient way of data visualisation from both tools.

3.3.2 Boundary Conditions

The cosimulation of two different BES models, except for common building layouts, requires the implementation of identical boundary conditions, including meteorological data and heat exchange coefficients (radiative, convective). The boundary conditions for both tools correspond to annual weather files, enabling various types (epw, tmy, etc.) of import files. As it happens, the standard meteorological files do not usually contain data regarding sky and ground temperatures. Therefore, the common used meteorological file, is enhanced with those boundary temperatures allowing the calculation of radiative exchanges with the sky and the ground (in Dimosim) and the conductive (both tools)/convective exchanges with the ground (in EnviBatE). The calculation methods presented in sections: 2.4.2.3 and 2.4.2.3 are employed for the calculation of the sky radiative and the soil temperatures respectively.

3.3.3 Neighborhood numerical mock-up

To facilitate the presentation of the implemented coupling strategies, a neighborhood numerical mock-up is generated following the flowchart presented in the previous sections. More in detail, the case study is based on an urban canyon settlement composed of 16 buildings (divided in 43 thermal zones) of various heights randomly selected, Figure:3.15. The urban geometry

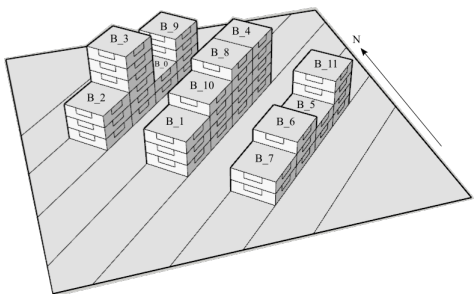

Figure 3.15: Illustration of the implemented case study.

has a maximum aspect ratio of 1.8 [H/W] formation, depicting a discontinuous row of mid-rise

high-density urban canyon, following the urban typologies classification of [216] and [217]. The adapted morphology is representative for the majority of the metropolitan European cities.

Table 3.1: Thermal and optical properties of buildings composing the urban neighborhood.

Building Characteristics / Thermal and Optical Properties		
Floor Height	3	[m]
Floor Surface	100	[m^2]
Window to wall ratio	0.20	[-]
Roof albedo	0.30	[-]
Roof U-value	0.78	[W/m^2K]
Wall albedo	0.30	[-]
Wall U-value	0.34	[W/m^2K]
Floors U-value	0.15	[W/m^2K]
Window Type	Double glazing	[-]
Window U-value	2.50	[W/m^2K]
Window transmittance	0.79	[-]
Window absorptance	0.08	[-]
Set point cooling / heating	28 / 19	[^oC]
Infiltration rate	0.70	[ACH]

Each thermal zone is 3m height and the floor surface is 100m^2. The building surfaces and all of the thermal zones are descretized evenly in both tools. Window to wall ratio is assumed to be 0.2. The thermal transmittance is 0.34, 0.78 and 2.5 [W/m^2K] and the solar reflectance is 0.3, 0.2 and 0.08 for wall elements and floors, roofs and windows respectively (Table:3.1). Interior insulation of polystyrene has been added, as it is the most common application in French building stock. Constant infiltration rate of 0.7 [ACH] is selected. The set point temperatures are forced to be 28 and 19 [^oC] for the cooling and heating season respectively. The selection is established to represent buildings constructed after 2000s, characterized as medium insulated buildings.

Table 3.2: Characteristics of the simulated district.

District Characteristics / Thermal and Optical Properties		
District surface	7056	[m^2]
Orientation	45 from N	[^{o}]
L/W	4	[-]
H/W	1.8 max	[-]
Pavements albedo	0.50	[-]
Pavements U-value	3.20	[W/m^2K]
Canyon VF max	0.43	[-]
Canyon VF min	0.15	[-]
Vegetation	None	[-]

The orientation of the domain is 45^o (from N counter clockwise). The outdoor space is formed by concrete pavements presenting a thermal transmittance of 3.2 [W/m^2K], while the

optical properties are tabled in 3.2. Outdoor air cells are adapted to the thermal zone's distinction in order to ensure that one zone is in contact with an outdoor air cell (one on one alignment). The spatial resolution of the solar mesh corresponds to a maximum value of 2 m, discretizing each building surface to at least 44 sub-surfaces (triangles), while the sky is divided in 256 patches. The airflow calculation has been performed with an hexahedral mesh composed of cubes of 1(dx) x 1(dy) x 3(dz) m to reach a final 86 x 86 x 36 grid domain at each axis respectively. Those various sub models constitute different programming objects which are finally integrated to a unified zonal model.

Every thermal zone is equipped with a split air conditioning unit, providing the necessary thermal loads. This type of systems are the commonly used and preferred ones, as an instant and low-cost solution for individual usage. We speculate that the rejected flux of the system is distributed to the adjacent air cells, weighted by the surface ratio. The mode of the system is reversible to account both for heating and cooling period. The fuel type is set to electricity.

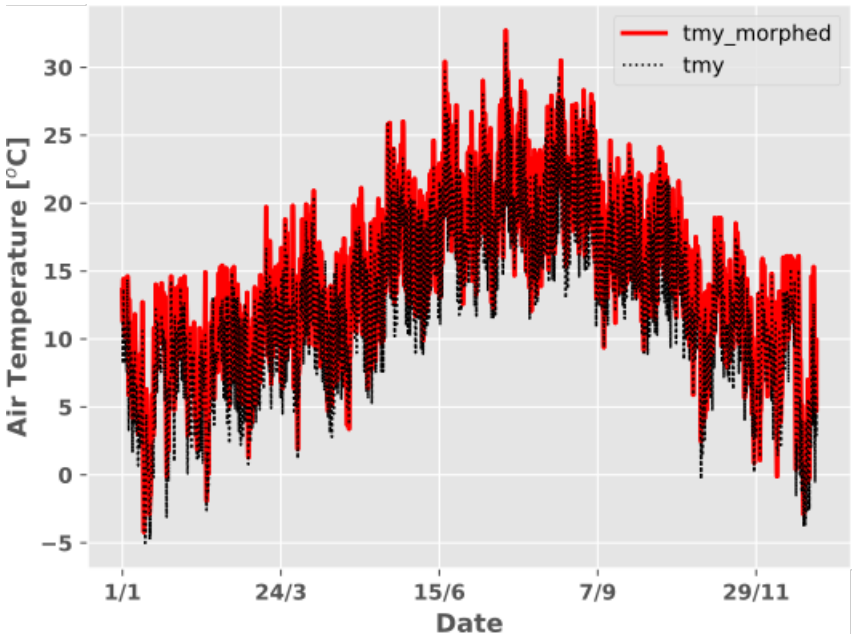

Figure 3.16: TMY and morphed air temperature dataset.

Table 3.3: Characteristics of the TMY and TMY morphed meteorological files.

Meteo_file	**Air Temperature [^{o}C]**		
Type	Average	Max	Min
TMY	13.0	31.9	-5.0
TMY_morphed	14.6	32.7	-4.2

Regarding the input boundary conditions, the meteorological data correspond to La Rochelle's typical meteorological year interpolated with CCWorldWeatherGen [218] to 2050 according to the A2 future scenario of forcing agents given in the IPCC Special Report [219]. This option enables the study of the potential cooling energy demand and its impact, as the cooling needs due to the typical meteorological file are low, corresponding to 179 cooling degree hours (CDH).

Figure 3.16 presents the annual distribution of the air temperature given from the TMY[11] and the morphed TMY meteorological files and Table 3.3 shows the average, maximum and minimum air temperatures. Both extreme temperatures increase by 0.8 ^{o}C in the morphed file, while the annual average air temperature rise corresponds to 1.7 ^{o}C.

[11] obtained from TRNSYS weather database

Chapter 4

Development of Different Coupling Strategies

Contents

Graphical abstract

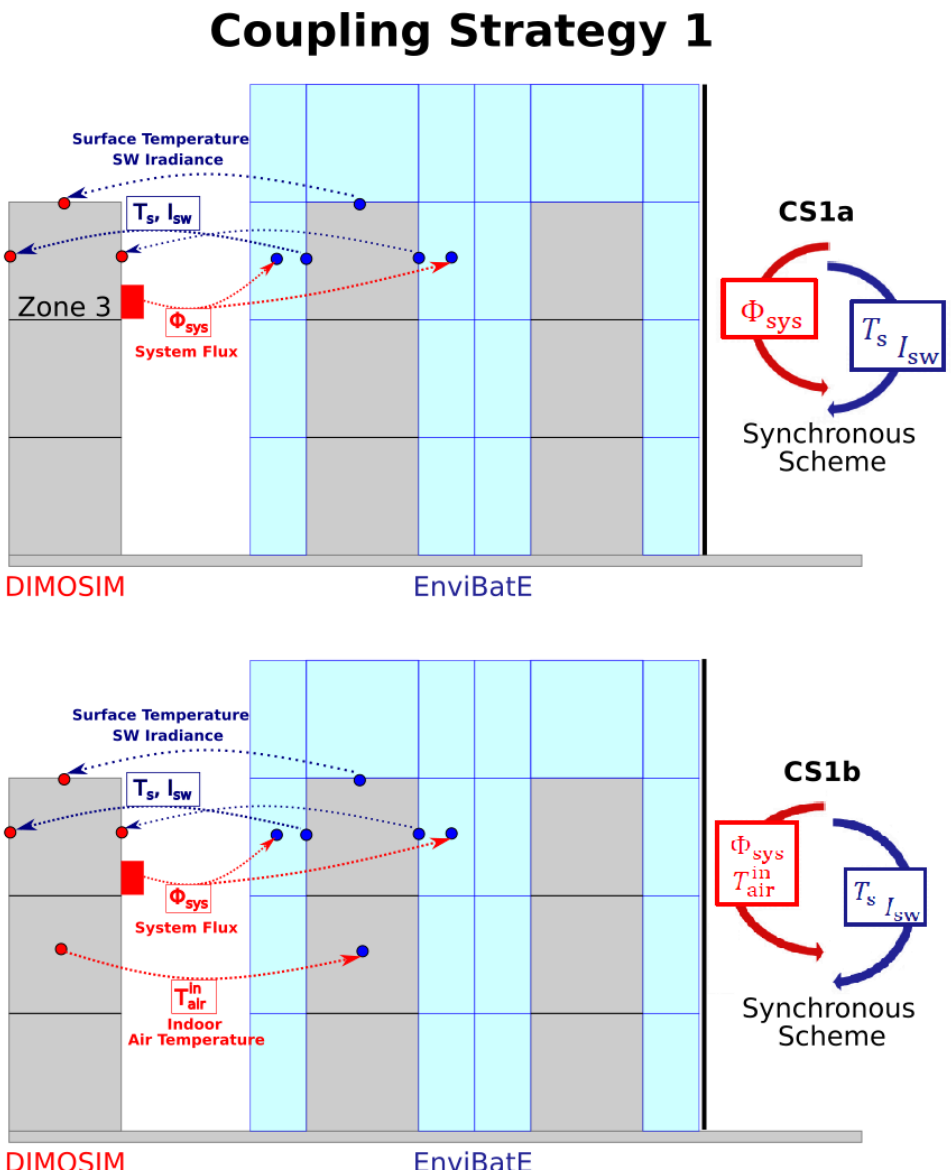

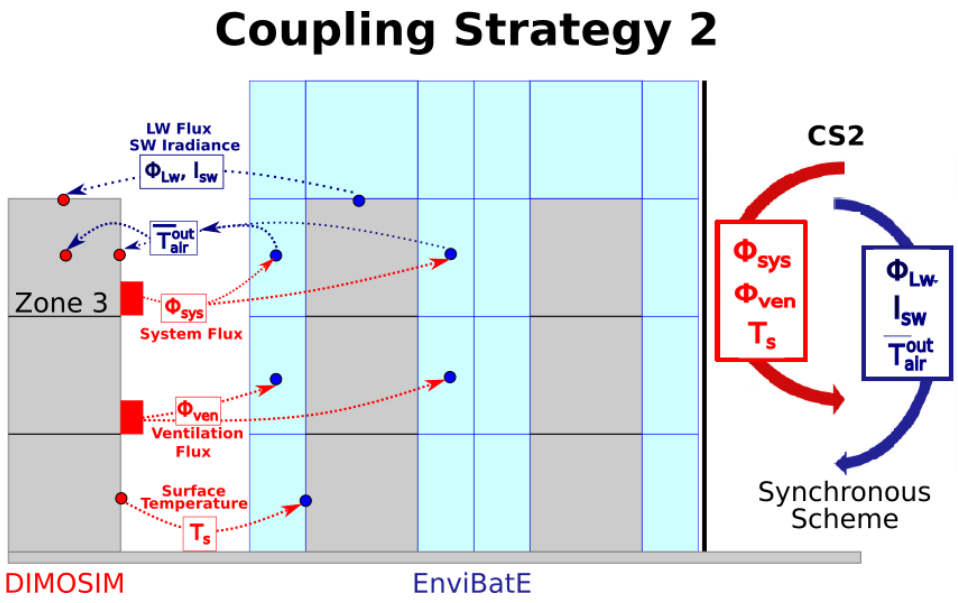
Coupling Strategy 2
LW Flux
SW Iradiance
Φ_Lw, I_sw
T_air^out
Zone 3
Φ_sys
System Flux
Φ_ven
Ventilation Flux
Surface Temperature
T_s
CS2
Φ_sys
Φ_ven
T_s
Φ_Lw,
I_sw
T_air^out
Synchronous Scheme
DIMOSIM
EnviBatE

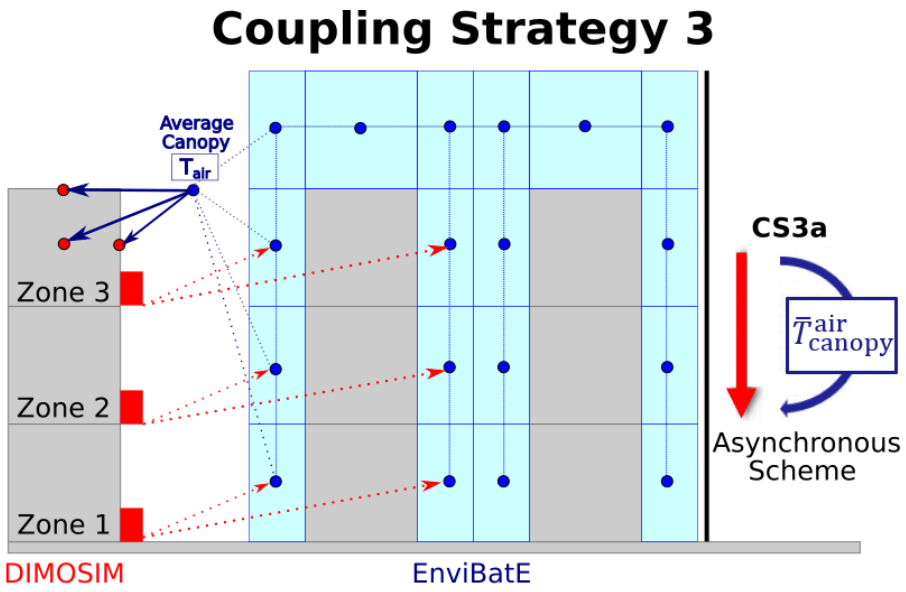
Coupling Strategy 3
Average Canopy
T_air
Zone 3
Zone 2
Zone 1
CS3a
T̄^air_canopy
Asynchronous Scheme
DIMOSIM
EnviBatE

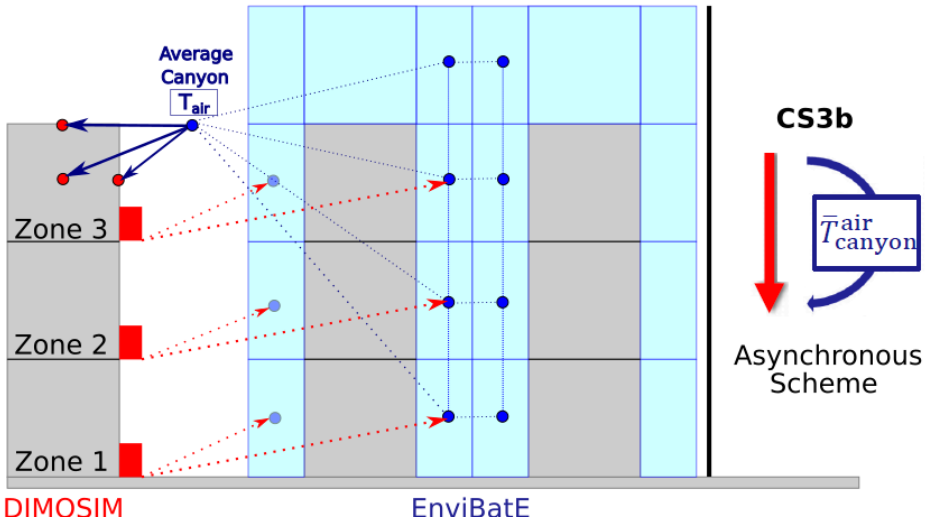
Average Canyon
T_air
Zone 3
Zone 2
Zone 1
CS3b
T̄^air_canyon
Asynchronous Scheme
DIMOSIM
EnviBatE

Table 4.1: Physical models and considered phenomena for the implemented coupling schemes.

Schemes \ Models	SW			LW			Airflow	BEM		Systems		
	I_b	I_d	I^*	Ground	Sky	Surf.	Flow field	WF	RiCj	Emitter	Generator	Waste Heat
Std_Dimosim	√	√	¬	√	√	¬	¬	¬	√	√	√	¬
CS3	√	√	√	√*	√*	¬	¬	¬	√	√	√	¬
CS3a	√	√	√	√*	√*	¬	¬	¬	√	√	√	¬
CS3b	√	√	√	√*	√*	¬	¬	¬	√	√	√	¬
CS1a	√	√	√	¬	√	√	√	√	√	√	√	√
CS1a_NF	√	√	√	¬	√	√	√	√	√	√	√	¬
CS1a_ThR**	√	√	√	¬	√	√	¬	√	√	√	√	¬
CS1b_Ta	√	√	√	¬	√	√	√	√	√	√	√	√
CS2	√	√	√	¬	√	√	√	¬	√	√	√	√
CS2_NF	√	√	√	¬	√	√	√	¬	√	√	√	¬
* // ** // NF	View Factors from EnviBatE // Thermoradiative used as reference // No Flux											

4.1 Introduction

This chapter seeks to investigate the coupling alternatives between the UBEM (Dimosim) and the microclimate model (EnviBatE), in order to study the interactions between buildings, urban microclimate and energy systems. In this context, different coupling strategies have been implemented, divided into two main categories [220], [221]:

- the synchronous or online scheme, and
- the asynchronous or offline scheme

depending on the exchanged physical parameter. In this classification, when the coupling variable does not require a bidirectional exchange (e.g., solar irradiance) it can be handled offline. On the contrary, an online coupling process is preferred when dynamic effects influence the thermodynamic integrity of the system. The latter requires that the models run in sequence (cosimulation) and thus, two main methods are identified in the literature:

- the "ping-pong" method in which each model uses the results of the other model in the previous time step, and
- the "onion" method in which the models iterate within one-time step until satisfactory convergence.

The main objective of this work is the development of a multi-scale model to account simultaneously for local and central energy systems, urban building energy demand and local microclimate assessment. In this chapter, the key objectives are triggered by a fourfold aim, the assessment of:

- the impact of local microclimate in urban building energy demand,
- the impact of ACs waste heat to outdoor air temperature,
- the feedback of ACs waste heat to energy demand, and
- the deviations between different coupling methods

The developed methodology is initially based on the cosimulation of the building model. At this step, the system's waste heat calculated in the UBEM is ejected in the microclimate model, while in parallel, the surface temperature calculated in the microclimate model is imposed on the UBEM, under a ping-pong coupling scheme. According to [222], a detailed evaluation of a dynamic system can be achieved through an integrated approach. Based on the latter, we implemented a second coupling scheme where the key objects of the microclimate model were decoupled and the matrix systems were reformatted to employ them in the UBEM. Particularly, following the similar coupling method (ping-pong) we integrated the solar radiation model (Solene), and the zonal model in the UBEM, in which the exchanged variables were the outdoor air temperature and the system's waste heat. Further on, an asynchronous coupling scheme of the outdoor air temperature was used to identify the possible discrepancies between the implemented coupling methods. Finally, in order to quantify the sensitivity of each method under various boundary conditions and different building insulation capacities, the developed synchronous coupling schemes were lumped in a parametric study.

4.2 Development of a Cosimulation platform

The synchronous coupling procedure requires the development of a cosimulation platform capable to manage the communication of the tools for extended temporal conditions (annual simulation) and large data exchanges. The realization is established through an inter-process communication defined as socket. Socket programming allows a low-level networking interface communication between connected parts. The developed methodology designates the simulation tools to a server (Dimosim) - client (EnviBatE) bonds, by setting a Transmission Control Protocol (TCP), an interface address (localhost) and a port to listen on (Figure: 4.1). Then, the binding process is used, associating the socket with the provided network interface and port number.

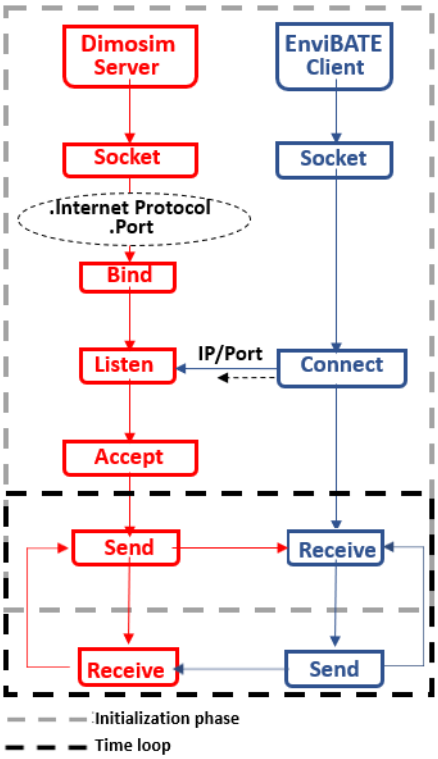

Figure 4.1: Schematic representation of the implemented networking interface communication.

In the initialization stage, the potential exchanged variables are equipped with a unique id[1], allowing to confirm their identification and the appropriate matrix position in each tool. Additionally, the implemented platform is used to arrange the exchanged variables automatically, avoiding additional iterations inside the time loop. Thus, the exchanged objects (variables, id, position) of Dimosim are sent for each time step of the specified simulation period to EnviBatE and vice-versa through this network communication. The procedure is established with a low computational cost [order of μs].

[1] see Section: 3.3.1

4.3 Synchronous Coupling Schemes

4.3.1 General methodology

The synchronous coupling procedure is based on a ping-pong coupling scheme, as shown in Figure: 4.2. For each time-step (1h) of the simulation, the calculated variable in Dimosim, is sent through the cosimulation platform to EnviBatE. At the same time, the latter considers in its calculation the received variable and proceeds to it. When it is finished, the respective variables are imposed on Dimosim in order to perform the calculation of the next time-step. This repeated exchange, which is managed automatically by the developed cosimulation platform, lasts until the end of the simulation.

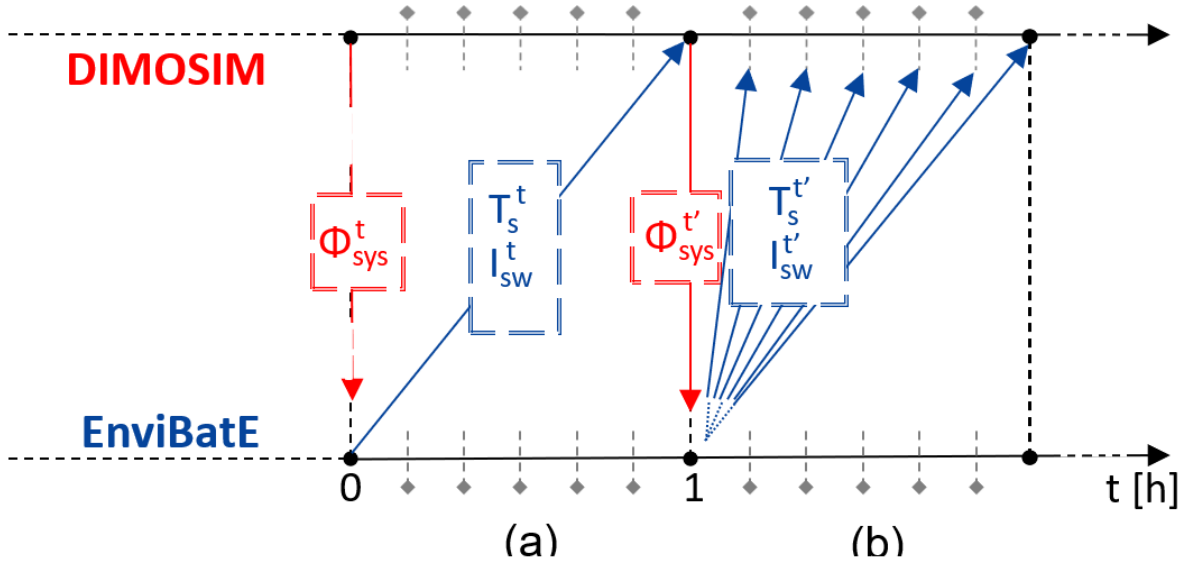

Figure 4.2: Schematic representation of the implemented on-line coupling scheme.

Nevertheless, the thermal calculation of an energy system like an air-source heat pump requires a further discretization of the simulation time-step. In this case, the variable X corresponds to the average value of the six previous time steps (Figure: 4.2b). This option is preferred to avoid the implementation of a different coupling method (e.g., onion), in which the computing resource implications due to the required iterations will be a major drawback (in terms of calculation time).

4.3.2 Surface Temperature Coupling Scheme - CS1a

The building model represents the common object of both tools, allowing us to act as the starting point of the synchronous coupling schemes. Since in EnviBatE the surface temperature[2] is strongly coupled with the outdoor air temperature of the adjacent air cells, it can be considered as the parameter which tracks the environmental impact on the studied element (thermal zone). In its calculation includes:

[2] see sections: 3.2.4, 3.2.6

- the solar irradiance (shortwave) which takes into account the direct, diffuse and multi-reflected components. The longwave exchanges are also considered using the view factors from surface to sky and from surface to surface and it is an outcome of the coupling procedure with Solene tool (contribution to: term 1, 3, 4 of equation: 3.45)
- the outdoor air temperature through convective exchanges, which takes into account the airflow calculated in each interface of the zonal mesh and is an outcome of the coupling procedure with QUIC-URB (contribution to: term 2 of equation: 3.45),

that are missing from Dimosim. On the contrary, EnviBatE lacks information about the operating HVAC system. The indoor environment of the building model is considered to maintain a temperature set point for the entire simulation period. This restriction does not allow to estimate the actual energy demand of the studied thermal zone, instead, the outcomes are limited to perpetual system use. In parallel, it deters it from assessing the environmental impact of the operating energy system. The latter, is of great importance, as it can modify the outdoor conditions at the local scale and thus the respective energy demand of the adjacent buildings or the outdoor thermal comfort at the pedestrian level. In order to tackle the aforementioned particular limitations of the tools, the general methodology presented in section: 4.3.1 has been implemented. The exchanged variables of Figure: 4.2 correspond to:

- $\Phi^t_{sys,i}$, is the system flux ejected to the ambient environment from thermal zone i at time step t
- $T^t_{s,j}$, is the surface temperature of surface j at time step t and
- $I^t_{sw,j}$, is the incident shortwave solar irradiance received from surface j at time step t.

4.3.2.1 Modification of governing matrix systems

More in detail, we assume a thermal zone **i** which is in contact with the outdoor environment (zonal cell **k**) through the wall surface **j** (Figure:4.3). A split air conditioning unit is operating in it. We perform an initial calculation in Dimosim at time step **t**. The emitter module calculates the heating or cooling load of thermal zone **i** in order to satisfy the current set point. The air conditioning system generates a heat flux (ϕ_{system}), which is linked with the outdoor environment. This additional flux is sent to EnviBatE and injected to the canopy cell **k** (Eq.: 3.64, 4.1). It is equal to Equation: 4.2 or 4.3 for heating and cooling periods respectively, considering the thermodynamic cycle.

In EnviBatE, the thermal balance of an outdoor cell is described from Eq: 3.64, where ϕ_s for a zonal cell adjacent to a building zone is modified and presented in Equation: 4.1. This term expresses the heat flux produced in the cell. A similar approach has been implemented in [213] for a street canyon.

$$\phi_{\text{s}} = \rho C_{\text{p}} D_V (T^t_{e,k} - T^t_{\text{ind}}) + \phi_{\text{system}} \tag{4.1}$$

$$\phi_{\text{system}} \equiv \Phi^{\text{heat}}_{\text{cond}} = -\phi_{\text{emitter}} \cdot \frac{\text{COP} - 1}{\text{COP}} \tag{4.2}$$

or

$$\phi_{\text{system}} \equiv \Phi^{\text{cool}}_{\text{evap}} = \phi_{\text{emitter}} \cdot \frac{\text{COP}}{\text{COP} - 1} \tag{4.3}$$

where:

COP is the coefficient of performance, calculated using either the thermodynamic cycle or a polynomial model for the thermodynamic process, depending on the examined thermal system.

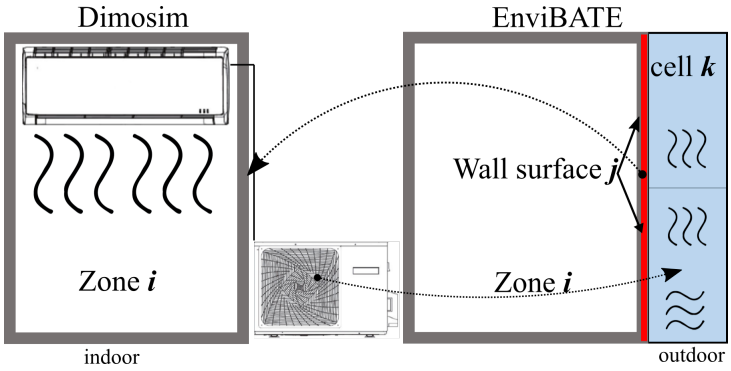

Figure 4.3: Schematic representation of the exchanged variables.

The calculations of air temperature at cell **k** and exterior surface temperature of wall surface **j** at time step **t**, are influenced by this added heat flux. The next time step **t'** we are imposing in Dimosim the surface temperature of wall surface **j** calculated the previous time step in EnviBatE. To do so, the exterior node of the wall model in Dimosim is turned off, as well as the respective thermal exchanges. Mathematically, our system for the surface temperatures, can be expressed by the governing equation 3.1, or in matrix form by the set of systems: 3.5, 3.6, 3.7, 3.8, 3.9, and 3.14.

The first order solution of the linear system using the matrix exponential [223], [224] as an integrating factor gives:

$$\boldsymbol{x}(t) = \boldsymbol{\Phi}(t)x(0) + \boldsymbol{\Phi}(t)\int_0^t \boldsymbol{\Phi}(t-\tau)\boldsymbol{B}u(\tau)d\tau$$

where $\boldsymbol{\Phi}(t) = e^{\boldsymbol{A}t}$ is the Matrix exponential, calculated using the following properties:

$$e^{\boldsymbol{A}t} = \boldsymbol{I} + \boldsymbol{A}t = \frac{\boldsymbol{A}^2t^2}{2!} + \frac{\boldsymbol{A}^3t^3}{3!} + ...$$
$$e^{\boldsymbol{A}0} = \boldsymbol{I}$$
$$e^{-\boldsymbol{A}t} = [e^{\boldsymbol{A}t}]^{-1}$$
$$\int_0^t e^{\boldsymbol{A}t}dt = \boldsymbol{A}^{-1}[e^{\boldsymbol{A}t} - \boldsymbol{I}],\ if\ \boldsymbol{A}^{-1}\ exists$$

If we apply in the diagonal matrix of heat capacities an increased value by three orders of magnitude at the exterior node of the building model, then $\mathbf{\Phi}(t) \rightarrow 1$ and $\boldsymbol{B} \rightarrow 0$. In this way, the surface temperature sent at each time step from EnviBatE is imposed to Dimosim's matrix system. The remaining elements of the matrix are not influenced by this approach since in the total matrix system every one of the remaining variables is treated independently.

4.3.2.2 Coupling efficiency

The proposed coupling scheme has been tested for the case study described in section 3.3.3. In the following sections, we provide the respective outcomes. However, we highlight in this section the efficiency of the developed coupling scheme. On the face of it, an index to illustrate the efficiency of the methodology, is the variance between the surface temperature calculated in EnviBatE with the one processed in Dimosim after the exchange. Figure 4.4 correlates the surface temperature of a referenced roof (B_3) calculated in EnviBatE against the one processed in Dimosim for every time step. The correlation reveals a perfect matching, leading the coefficient of determination (R^2) to a value of 100% association between them. The same behavior is observed for all of the exchanged surface temperatures. This verification step allows us to further investigate the outcomes of the coupled simulations.

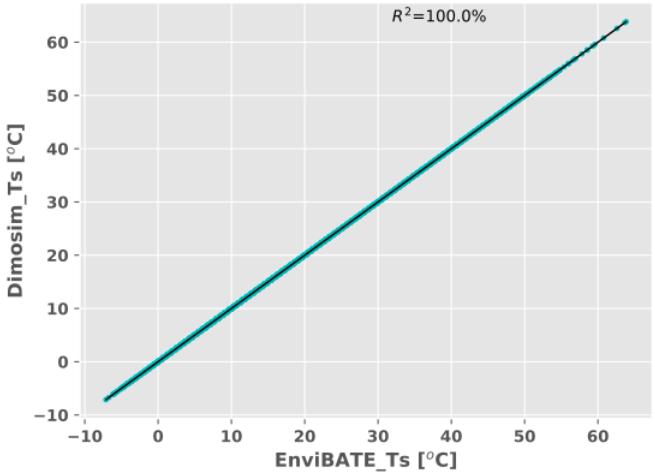

Figure 4.4: Correlation between the calculated surface temperature in EnviBatE and the processed one in Dimosim for a reference roof surface.

4.3.3 Surface Temperature & Indoor Air Temperature Coupling Scheme - CS1b

The indoor environment of EnviBatE is governed by a constant set-point temperature depending on the simulation period (heating/cooling). The calculation of the power required to maintain the set-point temperature as well as the calculation of the exterior surface temperature is employing the solicitation of the indoor air temperature. Moreover, the combined infiltration-ventilation module exchanges with the outdoor environment given this constant temperature, forcing the exchange to depend only on the ventilation rate or the occupancy schedule. This

approximation affects the calculation of the bulk convection, and thus, the outdoor air and the exterior surface temperatures.

Based on the previous coupling scheme we extend the approach by adding a fourth exchanged variable. It corresponds to the calculated indoor air temperature of every thermal zone in Dimosim's building model. The exchanged variables of the synchronous coupling scheme (Figure: 4.2) have been modified as:

- $\Phi^{t}_{\text{sys},i}, T^{\text{ind},t}_{\text{air},i}$, are the system flux ejected to the ambient environment and the indoor air temperature of thermal zone i at time step t
- $T^{t}_{s,j}$, is the surface temperature of surface j at time step t and
- $I^{t}_{sw,j}$, is the incident shortwave solar irradiance received from surface j at time step t.

This is the only change between the previous scheme (4.3.2) and the actual one. Moreover, the implementation of this coupling scheme aims to extend the capabilities of the individual models. The coupling schemes can offer a step-up on each tool, considering three main axes:

- examination of model responses in enhanced coupled phenomena,
- potential extension of tools individual capabilities,
- consideration of the above in respect to execution time.

4.3.3.1 Coupling efficiency

The correlation of the calculated and imposed surface temperatures is identical with the one presented in Figure: 4.4, revealing again a perfect matching. At this time, a huge alteration

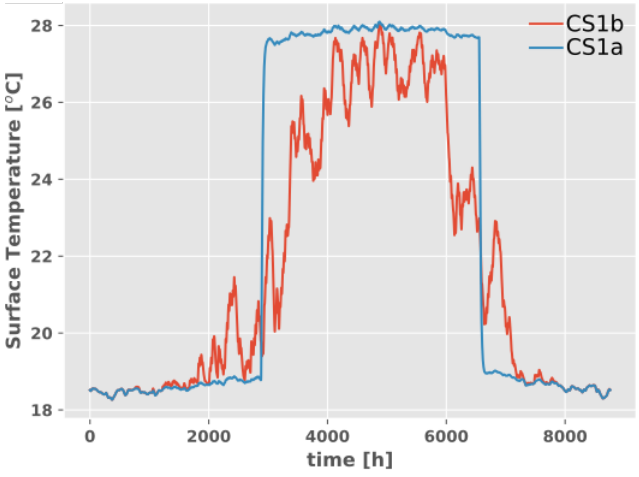

Figure 4.5: Comparison of surface temperature distribution for an intermediate floor.

lies on the surface temperature distribution of intermediate floors, as well as the indoor air temperatures, obtained in EnviBatE. Figure 4.5, presents the surface temperature distribution of an intermediate floor simulated under the coupling scheme CS1a (the thermal behavior is identical with the standalone model) and the actual one CS1b. It is evident that the surface temperature

distribution of the intermediate floors in the standalone simulation (or the previously presented coupling scheme) is influenced mainly from the indoor air temperature. The latter is evident in the ”reversed well”, where the set-point temperature of heating period reverts to the cooling selected one. On the other hand, the CS1b distribution is much smoother, with respect to the hourly modified indoor air temperature.

The similar trend is observed for the indoor air temperature. Figure 4.6 shows the distribution of the indoor air temperature for a reference zone (B3_Z5). In the CS1a scenario, as in the standalone simulation, the thermal zone is assumed to be under the specified set-point temperatures all around the year. This assumption has an impact also on the obtained power outcomes. By imposing the indoor air temperature from Dimosim, the indoor air temperature varies hourly, depending on the indoor conditions of the respective thermal zone.

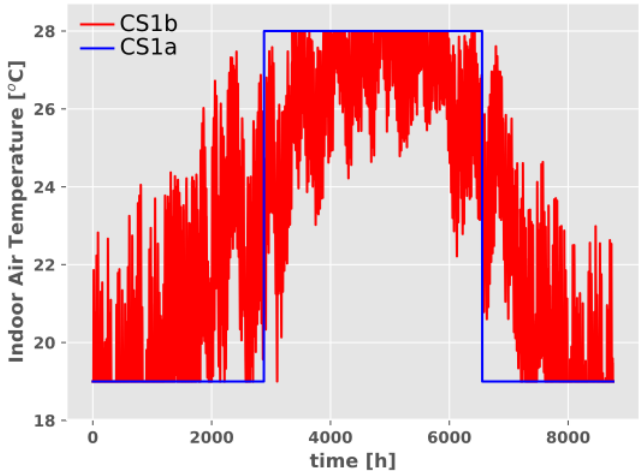

Figure 4.6: Comparison of indoor air temperature for a reference thermal zone.

4.3.4 Outdoor Air Temperature Coupling Scheme - CS2

The methodology of coupling the exterior surface temperature was triggered by the fact that this variable incorporates the microclimate footprint. On the other hand, the coupling methodology requires the concurrent simulation of the building model in both tools. Although the considered physical phenomena at the thermal zone level are similar for both tools, the implemented approaches are different. This assumption influences both outcomes and simulation time, as the building model is simulated twice. Moreover, as presented in section: 2.6.3, the evaluation of the impact of energy systems waste heat to the outdoor environment is studied by coupling schemes based on the air temperature variable. Thus, towards the development of an integrated tool, we built a new coupling strategy that combines the key modules of each tool to a unique new coupled model.

To accomplish this, we assume Dimosim and specifically its thermal zone module as the core model of the building environment and we enhance it with the microclimate modules of EnviBatE. More in detail, we are using the same coupling method (ping-pong) to integrate into Dimosim’s building model the radiative and airflow modules. In this way, the considered physical phenomena remain untouched and the building is simulated once. This time the exchanged variables of Figure:4.2 correspond to:

- √ $T_{air,i}^{ind,t}$ the indoor air temperature of thermal zone i at time step t
  √ $T_{s,j}^{t}$ the exterior surface temperature of wall element j of thermal zone i at time step t
  √ P_{i}^{t} the cooling or heating power of thermal zone i at time step t (optional)
  √ $D_{v,i}^{t}$ the ventilation losses of thermal zone i at time step t
  √ $\Phi_{sys,i}^{t}$ the system flux ejected to the ambient environment from thermal zone i at time step t
- √ $I_{sw,j}^{t}$, is the incident shortwave solar irradiance received from surface j at time step t,
  √ $\Phi_{lw,j}^{t}$, is the longwave radiative flux received from surface j at time step t, taking into account the urban scene,
  √ F_{j}^{sky}, is the sky view factor of surface j,
  √ $T_{air,k\rightarrow K}^{out,t}$, is the average outdoor air temperature of zonal cells $k \rightarrow K$ adjacent to the studied thermal zone at time step t.

4.3.4.1 Modification of governing matrix systems

As the building model is now simulated only once, we need the corresponding variables ($T_{air,i}^{ind,t}$, $T_{s,j}^{t}$, $D_{v,i}^{t}$, $\Phi_{sys,i}^{t}$) calculated in Dimosim, to impose them in the matrix system of EnviBatE. At a first step, the radiative exchanges with the ground are turned off in Dimosim (term b_{22} of the state matrix 3.8), since the model will be enhanced with the respective calculation from EnviBatE, which considers the longwave exchanges with other surfaces of the urban scene. Moreover, the sky view factors calculated from EnviBatE are imposed on Dimosim's building model to enable a more precise calculation of the radiative exchanges with the sky. As a second step, the matrix system of EnviBatE must be reformed.

The initial matrix system of EnviBatE is expressed by a linear differential equation: 3.67 or analytical from matrix: 3.68. In this system, the unknown variables corresponding to power and building surface temperatures are eliminated. Conversely, the variables that express the outdoor air temperature and the surface temperatures of the urban scene remained unchanged. However, the calculation of the convective exchanges with the building surfaces and the combined ventilation/infiltration module have been reformed and imposed to the vector of the input variables. Moreover, a supplementary matrix system has been developed for the calculation of the longwave exchanges of building surfaces, based on the first term of Equation: 3.34. Thus, the received/loss energy from surface **i** to surface **j** ($I_{LW}^{i\rightarrow j}$) can be estimated from the following system:

$$\begin{bmatrix} -A_1 h_r \sum F_{1,j} & A_1 h_r F_{1,2} & \cdots & A_1 h_r F_{1,j} \\ A_2 h_r F_{2,1} & -A_2 h_r \sum F_{2,j} & \cdots & A_2 h_r F_{2,j} \\ \vdots & \vdots & \ddots & \vdots \\ A_i h_r F_{i,1} & A_i h_r F_{i,2} & \cdots & -A_i h_r \sum F_{i,j} \end{bmatrix} \cdot \begin{bmatrix} T_1 \\ T_2 \\ \vdots \\ T_i \end{bmatrix} \tag{4.4}$$

where:

A is the wall surface [m^2],

$F_{i,j}$ is the view factor of surface i to surface j and

h_r is the linearized radiative heat exchange coefficient given by 3.33, and

T_i is the surface temperature of wall i.

Once the calculations are performed, the average outdoor air temperature of the cells adjacent to the thermal zones is transferred to Dimosim together with the radiative energy of each surface. The latter is then imposed in Dimosim's input vector **U** (3.14). In parallel, the input meteorological air temperature has been substituted by a vector of air temperatures with a length equal to the number of thermal zones. In this coupling scheme, the microclimate footprint is considered by the local air temperature in terms of conductive, convective, and radiative heat exchanges. Additionally, the COP of the system and the respective thermal output of the evaporator/condenser are calculated based on the local outdoor air temperature. The integration of the airflow, the solar radiation, and the zonal model to Dimosim constitutes the development of a new microclimate module of the tool.

4.4 Asynchronous Coupling Schemes

As examined in Section 2.6, a commonly used method to estimate the impact of the urban microclimate to building energy demand, is the usage of asynchronous coupling schemes or "Chaining" method [225].

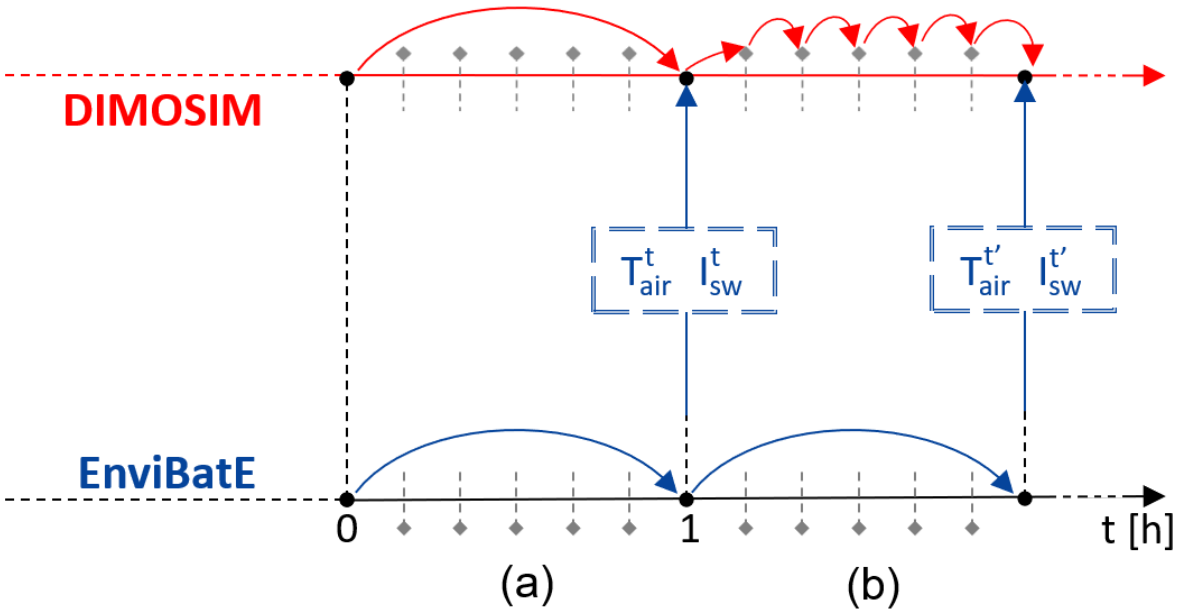

Figure 4.7: Schematic representation of the implemented off-line coupling scheme.

The methodology of the asynchronous coupling schemes is based on the unidirectional exchange of a parameter from model to model, as shown in Figure: 4.7. The schematic representation depicts the developed simulation models, executed in sequence and the one (EnviBatE) is

sending the requested variable to the other at every time-step. This methodology can be applied either as already described, or when the individual models are executed separately, and then, the calculated variables of the one are introduced as inputs to the other. In general, the method is efficient when the coupled variable is independent of external sources. For instance, solar radiation can be considered as an independent one, since it is predetermined for a solar exposed boundary, given its dependency on geometry factors.

4.4.1 Incident Solar irradiance Coupling Scheme - CS3

Sections 3.1.2 and 3.2.2 dealt with the calculation methods of solar irradiance in Dimosim and EnviBatE respectively. In this section, the asynchronous method was used to impose the incident solar radiation from EnviBatE to Dimosim, availing our study with a twofold benefit. On the one hand, serves as the first step towards the integration of the urban environment to the UBEM, on the other hand, offers a detailed representation of solar-based parameters, such as the calculation of the direct and diffuse components in a fine triangulated mesh. Moreover, the computation of the view factors for every urban surface allows us to consider the inter-reflections and the longwave exchanges between the urban surfaces. Figure: 4.8 shows the relative difference of the sky view factors for each wall of the implemented urban geometry between Dimosim and EnviBatE.

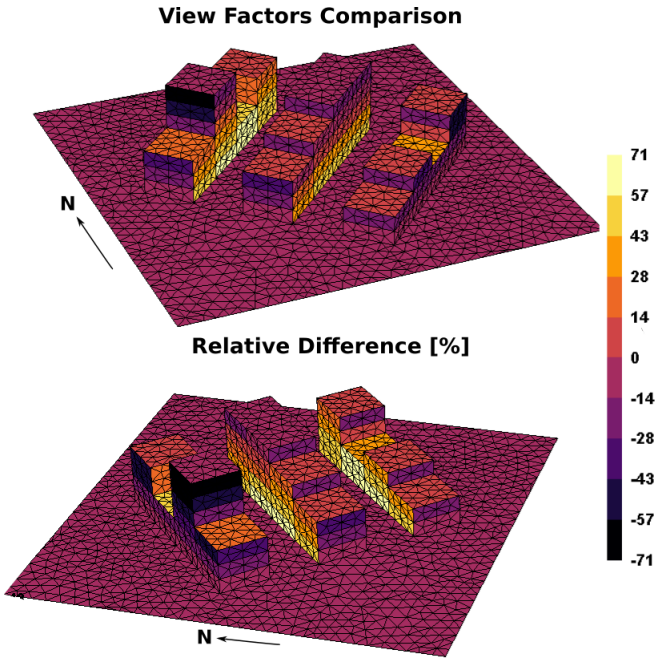

Figure 4.8: Relative difference of the sky view factors between Dimosim and EnviBatE.

In this study, two alternative options were tested for the integration of the solar irradiance to Dimosim. The one described in the previous section, depicted by Figure: 4.7 and a second one where the solar data were imported from a file in the initialization phase of Dimosim. When the second option is preferred, the developed indexation module, described in Section 3.3, was employed. In our study, the second option was selected due to its convenience, as both approaches vary only in execution time.

4.4.2 Outdoor Air Temperature Coupling Schemes - CS3a CS3b

The impact of the urban microclimate on building energy demand is frequently examined through the chaining method. As an example, an offline coupling of outdoor air temperature to a BEM emerges from the generation of a new meteorological file which then is used as an input to the BEM[3], without requiring the simultaneous feedback of the receptor. Nevertheless, the building is interconnected with the outdoor environment and so the calculation misses the feedback of building emissions to the ambient environment.

In this study, the aforementioned option was deployed in order to investigate the possible discrepancies between the synchronous and the asynchronous coupling schemes. To this end, a further chaining method is proposed. Apart from solar radiation, the outdoor air temperature obtained by a coupled simulation (CS: 4.3.4) allows us to generate a modified meteorological file. The modified data are then used as an input to Dimosim. Given the case study presented in Section 3.3.3, we performed annual simulations for two cases:

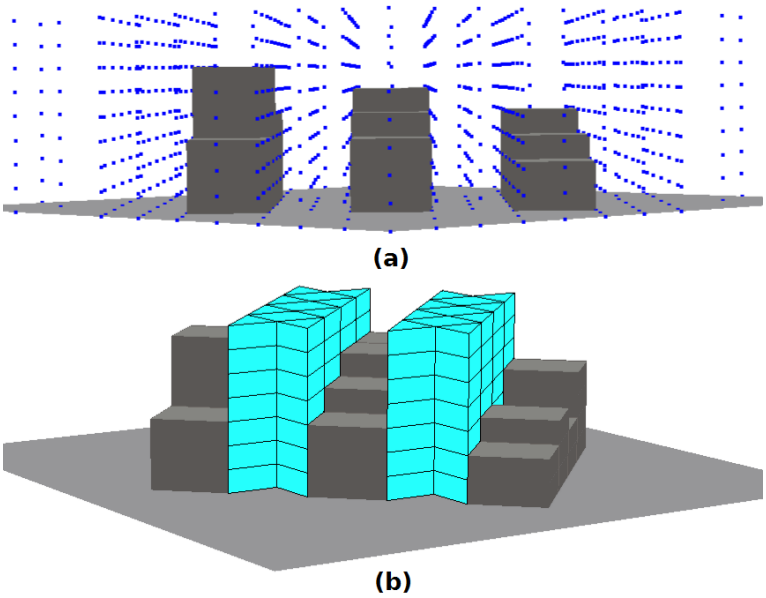

Figure 4.9: Air cells (cyan) used for the generation of the modified meteorological file.

i. $\bar{T}_{\text{canopy}}$(CS3a): Obtain the average air temperature from the zonal cells that form the urban canopy (entire mock-up), Figure:4.9a. This option allows us to lump all the exterior nodes in one, imitating the one-node representation of canopy models.

ii. $\bar{T}_{\text{canyon}}$(CS3b): Obtain the average air temperature from the zonal cells corresponding to street canyons and they are adjacent to the examined thermal zones, Fig: 4.9b. This option is a parallelism of coupled building energy and microclimate models.

[3]see Section:4.4.2

4.5 Assessment of thermal and microclimate performance

This section aims to quantify the thermal and microclimate performance of the case study presented in Section: 3.3.3, based on the developed coupling strategies.

The evaluation of energy demand is based on the comparison between the fully coupled schemes and the coupled standalone simulations. More in detail, the coupling strategies CS1a and CS1b were compared against a coupled thermoradiative simulation (CS1a_ThR). In the latter, the airflow model has been put aside and the outdoor zonal cells are forced to the boundary conditions given by the meteorological file. The coupling strategies CS2 and CS3b were compared against the coupling strategy CS3a (Offline_SW) in which the standalone model of Dimosim was enhanced with the solar irradiance calculated in EnviBatE. These options allow to consider similar building energy models in the comparisons.

The evaluation of the ACs waste heat feedback in building energy demand, as well as the impact on outdoor air temperature, requires a different strategy. The comparison is held between the presented synchronous coupling schemes (CS1a and CS2) and the similar ones where the feedback of the system is not rejected in the urban canopy (symbolized with a "NF" as an ending in the forthcoming analysis[4]).

Finally, to quantify the potential discrepancies in building energy demand between synchronous and asynchronous coupling schemes, the CS2 coupling strategy was compared against the CS3b asynchronous scheme, in which a new meteorological file was generated based on the outcomes of an annual simulation of CS2.

4.5.1 Evaluation of Energy Demand

4.5.1.1 CS-1a Coupling Scheme surface temperature

In order to illustrate the impact of the local microclimate conditions on building energy demand, we compare the results of two annual simulations. The tested schemes, correspond to

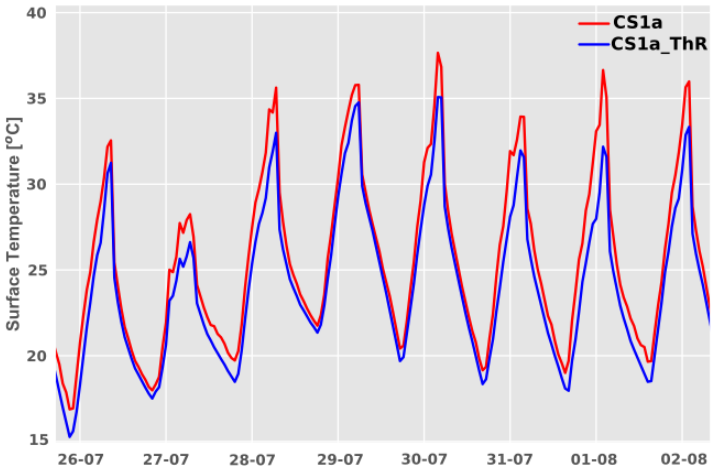

Figure 4.10: Surface Temperature comparison between coupled microclimate and thermoradiative models.

[4]see Table: 4.1

CS1a and CS1a_ThR as presented in section 4.3.2. The outcomes of the thermal zones that form each building, were accumulated and the comparison is held at the building scale. Table 4.2[5] presents the cooling and heating demand per building for the implemented coupling schemes.

Table 4.2: Annual cooling and heating demand per building for the CS1a coupling scheme.

	Thermal Demand [kWh/m^2/y]					
	Cooling			Heating		
Index	CS1a_ThR	CS1a	RD [%]	CS1a_ThR	CS1a	RD [%]
B_0	3,3	3,6	9,5	79,2	80,0	1,0
B_1	19,4	20,4	5,0	57,1	57,6	0,9
B_2	17,1	17,9	4,5	63,0	63,7	1,1
B_3	27,5	28,3	2,7	142,7	143,5	0,6
B_4	22,1	23,0	4,3	133,5	134,3	0,7
B_5	6,7	7,5	10,4	47,1	47,4	0,7
B_6	14,6	15,6	6,1	59,6	60,0	0,6
B_7	14,5	15,4	6,1	40,1	40,5	0,9
B_8	14,8	15,6	5,5	97,3	97,9	0,6
B_9	21,6	22,5	4,1	137,5	138,7	0,9
B_10	13,8	14,6	6,0	83,2	83,7	0,6
B_11	24,2	25,4	4,6	88,1	88,7	0,7
Total	199,6	209,8	4,9	1028,3	1035,9	0,7
Average	16,6	17,5	5,1	85,7	86,3	0,7

At first glance, the assumption taken in section 4.3.2 proves to be correct. The surface temperature, acting as the carrier of the outdoor environment, transfers its impact on the indoor one. More in detail, Figure 4.10 presents a snapshot of the surface temperature comparison

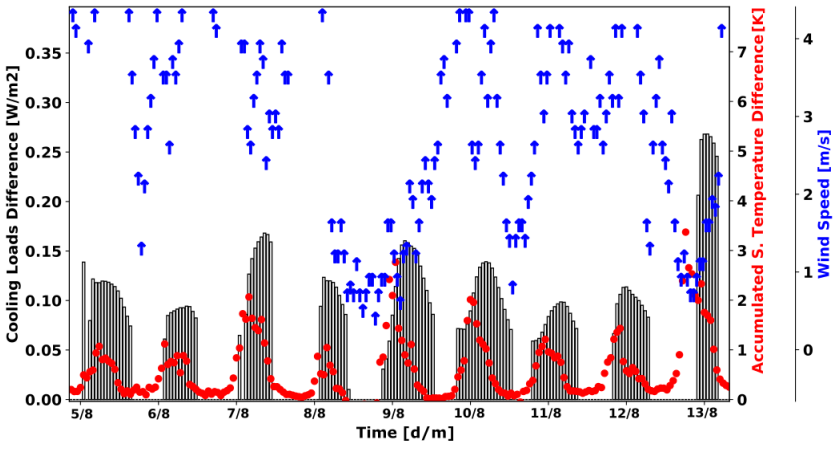

Figure 4.11: Accumulated surface temperature difference against total cooling loads difference between coupled microclimate and thermoradiative models.

between the coupled microclimate and thermoradiative models for a northern oriented building

[5]for visual representation of building indices see Figure: 3.15

surface (B_5) during a representative summer week. The surface temperature increase causes a respective increase in cooling loads. The latter is verified also from Figure: 4.11. In this diagram, the accumulated surface temperature difference (of the surfaces that enclose a thermal zone) between the referenced scenarios, has been plotted against the cooling load difference (black boxes) for building B_5, where the maximum relative difference in cooling demand is observed. The general trend shows that the higher the accumulated temperature difference, the higher the corresponding cooling demand difference. Moreover, the surface temperature increase is correlated with wind speed conditions. In the presence of low wind speed, the building heat discharges affect intensively the local outdoor conditions, causing feedback on the calculated surface temperature and the cooling demand respectively. In this coupling scheme, the impact of the local microclimate on building energy demand is studied through coupled convective and conductive heat transfer mechanisms, depending on the insulation capacity of the building envelope.

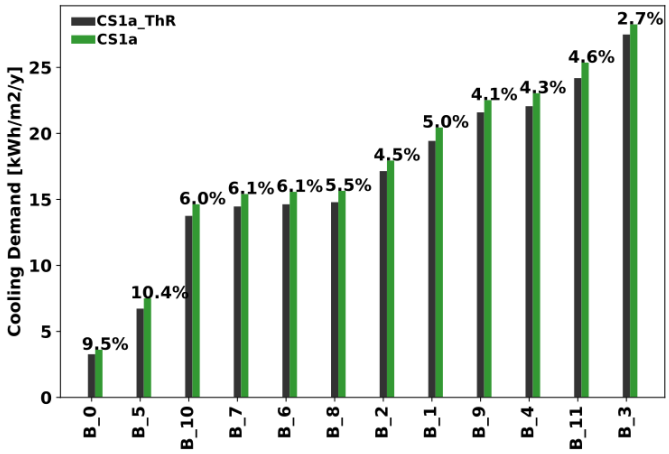

Figure 4.12: Annual cooling demand for thermoradiative (ThR) and fully coupled model (CS1a) for each building.

The cooling loads and their respective relative difference between the two scenarios are plotted for each building in Figure 4.12. The average cooling demand increase of the entire cooling season is 5.1%, while the peak reaches 10.4% in B_5. The 2-storey buildings are significantly affected and exhibit the maximum relative differences, while buildings located in the middle of the canyon formation, exhibit also an increase on cooling demand ranging between 5.5% and 6.0%.

The neighborhood cooling demand deviation is plotted in Figure: 4.13 for the entire cooling period. In this plot, the relative difference of the cooling demand for every time-step of the cooling period is depicted in terms of heatmap representation. Evidently, the higher differences are observed early in the morning and late in the evening where the peak increase reaches approximately the value of 27%. Conversely, during the midday hours the differences are limited (<5%). At this period, both simulation scenarios present a rise in cooling demand, as the incident and transmitted solar radiation combined with the increased outdoor air temperature are dominating the energy regime of the buildings. During the evening or even late at night, the buildings release additional heat in the local air cells. The observed lag is correlated with the inertia of the building envelope and it is captured by the coupled model for the entire cooling

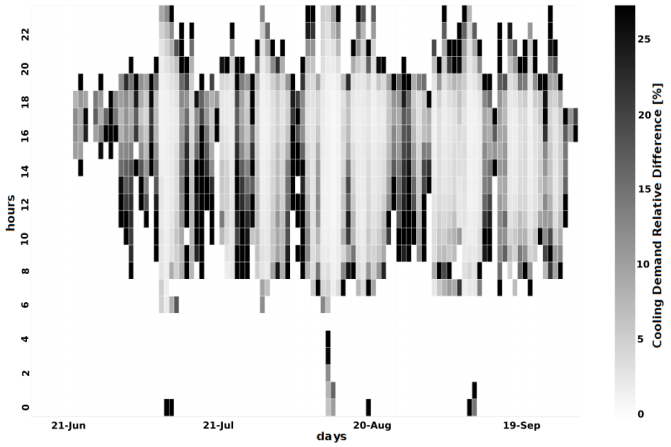

Figure 4.13: Impact of microclimate (relative difference/hour) on neighborhood cooling demand in CS_1a coupling strategy.

period. This outcome reveals the model's capability to represent the canopy overheating.

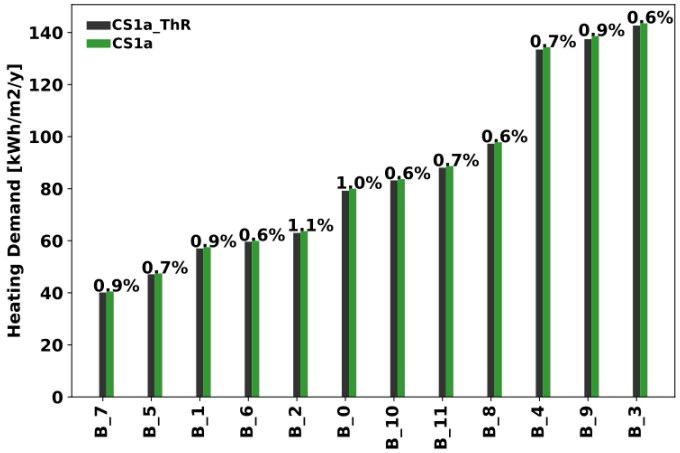

Figure 4.14: Annual heating demand for thermoradiative (ThR) and fully coupled model (CS1a) for each building.

On the contrary, the heating demand exhibits a slight increase. The average increase is 0.7%, while the peak is way much smoother compared to the cooling one, reaching 1.1% (B_2), although in terms of absolute values the deviation is approximately similar to the cooling one. At a first step, one can speculate that this is caused due to systems rejected flux, as the condenser rejects cold flux to the adjacent air cells. However, the trend and the outcomes are similar even when comparing the CS1a_NF and the CS1a_ThR coupling schemes where the system flux is neglected. This observation requires further investigation. For this purpose, we plot in Figure: 4.15 the outcomes obtained from the CS1a_NF and CS1a_ThR scenarios for a representative (coldest) week of the year. The plot shows the heating demand difference as a function of surface and air temperature (both meteorological and mean zonal) difference. It is evident that the heating demand is mainly observed during the night hours. When the surface temperature difference is positive, meaning that the microclimate simulation presents a higher surface temperature than the thermoradiative one, the average zonal air temperature is higher

than the boundary one (meteorological file) and correspondingly the heating demand is lower (e.g., time-steps 25-40). The opposite trend is observed under reversed thermal behavior, showing the impact of the local microclimate conditions when conducting building energy demand studies. A similar agreement of this event has been recently reported in [226].

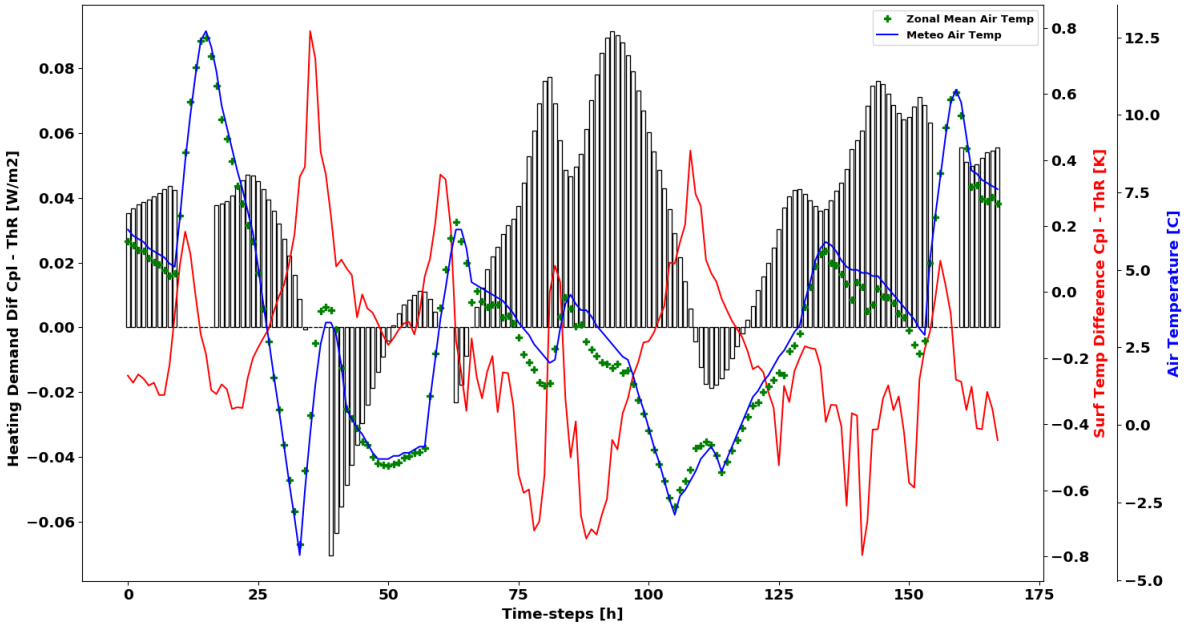

Figure 4.15: Heating demand difference as a function of surface temperature difference and air zonal temperature for a referenced zone during a representative heating week between CS1a_NF and CS1a_ThR scenarios.

4.5.1.2 CS-1b Coupling Scheme surface & air temperature

The coupling strategy CS1b presents an almost identical behavior with the coupling strategy CS1a. The percentage increase in both cooling and heating demand is trivial compared to the previous aforementioned coupling scheme. Nevertheless, this enhanced coupled model can also capture the microclimate impact on both simulation periods.

More in detail, during the cooling period the average cooling demand increase is 4.7% between the coupled microclimate and thermoradiative models. It is reduced by 0.2% compared to the previous scheme (CS1a). At building level (Figure: 4.16), the analysis presents a similar trend, where either the outcomes per building are identical or a tiny deviation of approximately 0.1% - 0.2% is observed.

During the heating period, the outcomes present also an identical behavior with the previously implemented coupling scheme, as shown in Figure: 4.17. At this period, the average heating demand percentage increase is also 0.7%.

The CS1 category of coupling strategies, presents almost identical outcomes due to:

- similar coupling variables,
- the addition of the fourth exchanged variable (indoor air temperature) does not affect the calculation of the thermal demand because when the energy system is operating the

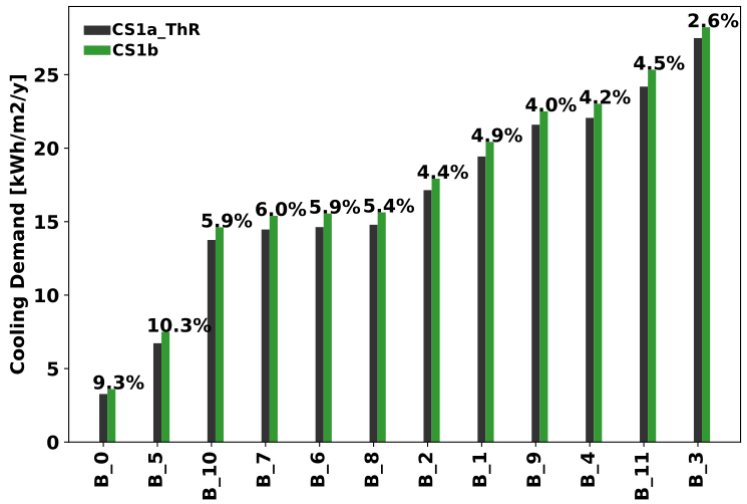

Figure 4.16: Annual cooling demand for thermoradiative (ThR) and fully coupled model (CS1b) for each building.

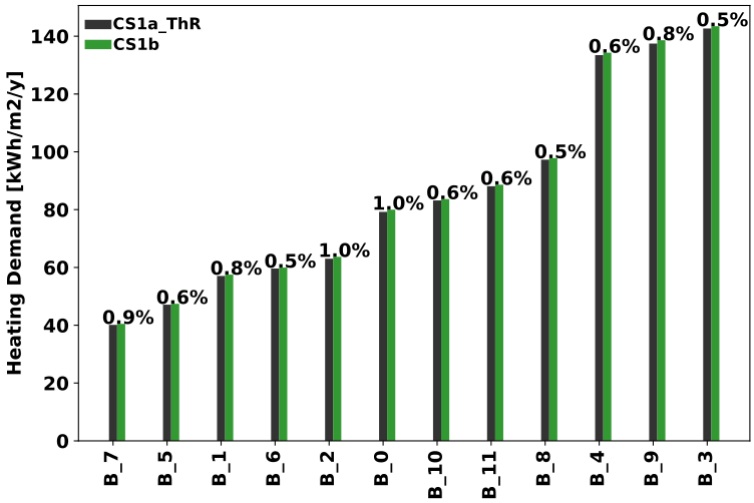

Figure 4.17: Annual heating demand for thermoradiative (ThR) and fully coupled model (CS1b) for each building.

indoor set-point temperature is constant and identical in both coupling schemes. Thus, neither the exhaust flux of the ventilation system has changed nor the calculated surface temperature.

The impact of the modified indoor air temperature is mainly affecting the coupled model when the energy system is turned off. The following section (4.5.3) highlights the altered behavior of the model and its impact on the outdoor environment. However, this coupling scheme pluralizes EnviBatE with the representation of the indoor environmental conditions.

4.5.1.3 CS-2 Coupling Scheme outdoor air temperature

The coupling variable of CS2 corresponds to the outdoor air temperature of the zonal cells adjacent to the thermal zones, while the system flux is also considered. To quantify the impact

of the microclimate to building energy demand we compare the synchronous coupling scheme: 4.3.4 with the respective asynchronous scheme CS3 (4.4.1) which considers a standalone simulation enhanced with the solar outputs calculated in EnviBatE. Both coupling schemes consider the same building model (the one of Dimosim) as well as the same radiation inputs (the latter is kept identical in all of the coupling schemes).

Table 4.3: Annual cooling and heating loads per building and their respective relative difference (RD) for the integrated coupling scheme.

	Thermal Demand [kWh/m^2/y]					
	Cooling			Heating		
Index	CS3	CS2	RD [%]	CS3	CS2	RD [%]
B_0	2,8	5,3	47,0	82,1	84,2	2,5
B_1	18,4	23,0	20,0	58,7	61,5	4,6
B_2	16,5	20,0	17,5	64,3	68,4	5,9
B_3	27,3	29,2	6,5	144,2	150,6	4,3
B_4	21,5	25,6	16,0	135,4	140,6	3,7
B_5	5,9	9,9	40,5	49,3	50,8	2,9
B_6	13,9	18,4	24,6	61,1	63,7	4,1
B_7	13,7	18,0	23,5	41,1	43,6	5,7
B_8	14,2	18,4	23,1	99,7	102,8	3,1
B_9	21,1	24,8	14,8	138,9	145,3	4,4
B_10	12,8	17,5	26,7	85,8	88,3	2,8
B_11	23,6	27,4	13,9	89,3	94,0	5,0
Total	191,7	237,5	19,3	1049,9	1093,8	4,0
Average	16,0	19,8	19,2	87,5	91,2	4,1

In this context, the energy demand during the cooling period presents significant deviations between the coupled and the standalone model. The amount of difference between the implemented scenarios is much higher than the coupling schemes presented in the aforementioned analysis. Higher deviations occur for low rise buildings (Table: 4.3). The percentage difference is almost doubled reaching 47%, while for others fluctuates at around 20% (Figure: 4.18). The minimum one is observed at building B_3 (highest building of the scene), revealing the stratification of the outdoor air temperature and its impact. The total difference during the entire cooling season is approximately 19% which in terms of absolute values accounts for 46 kWh/m^2.

The observed significant deviations (compared to CS1) can be explained by the choice of the exchanged variable. The air temperature is affecting the convective heat exchanges between the envelope and the outdoor air temperature. This deviation causes alterations on the calculated surface temperature which then affects the conductive heat flux through walls and the radiative exchanges with the other surfaces. Besides, the ventilation module is taking into account the air temperature of the air cells adjacent to each thermal zone rather than a constant input value obtained by the meteorological file. In addition, the impact of the systems waste heat is more intense[6]. In this coupling scheme, all of the heat transfer mechanisms are considered in the

[6]see section: 4.5.2.2

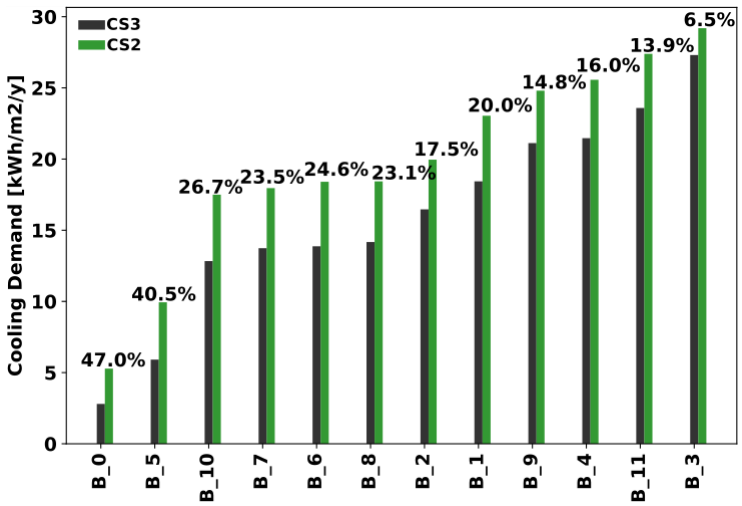

Figure 4.18: Annual cooling demand for CS3 (Std) and fully coupled model (CS2).

same building model.

The district cooling demand is described by a similar increased percentage difference, as shown in Figure: 4.19. The latter fluctuates up to approximately 75%. However, the severe increase in the neighborhood cooling demand is found again late in the evening and early in the morning as already discussed in Section: 4.5.1.1. Both Figures: 4.18 and 4.19 reveal that when the coupling variable corresponds to the outdoor air temperature, the impact of the local microclimate is more intense.

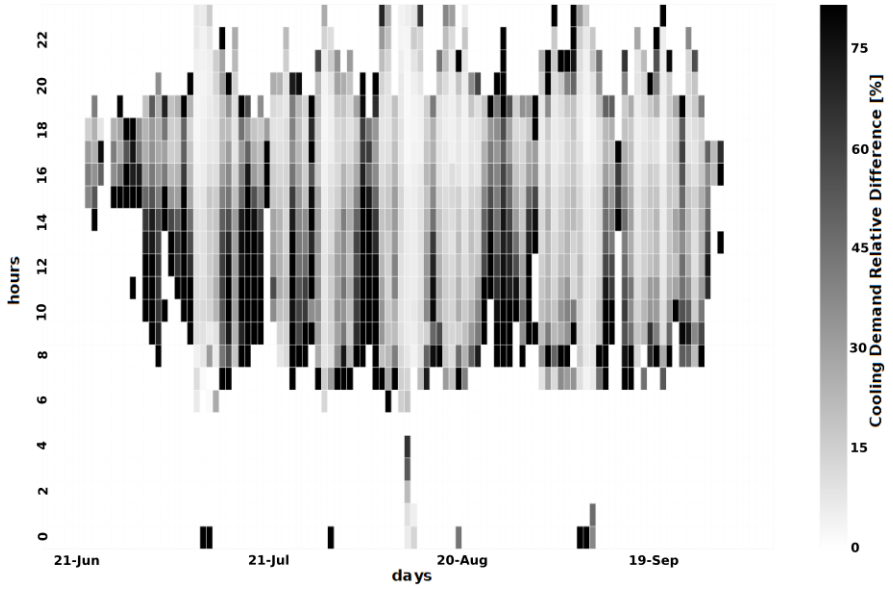

Figure 4.19: Impact of microclimate (relative difference/hour) on neighborhood cooling demand in CS_2 coupling strategy.

On the other hand, the heating demand presents a decent difference, but this is less intense compared to the cooling one. The trend is following the previous coupling strategy. The total

amount of difference during the entire heating period is reaches 4%. The corresponding absolute difference is 43.9 kWh/m^2, slightly lower than the cooling one.

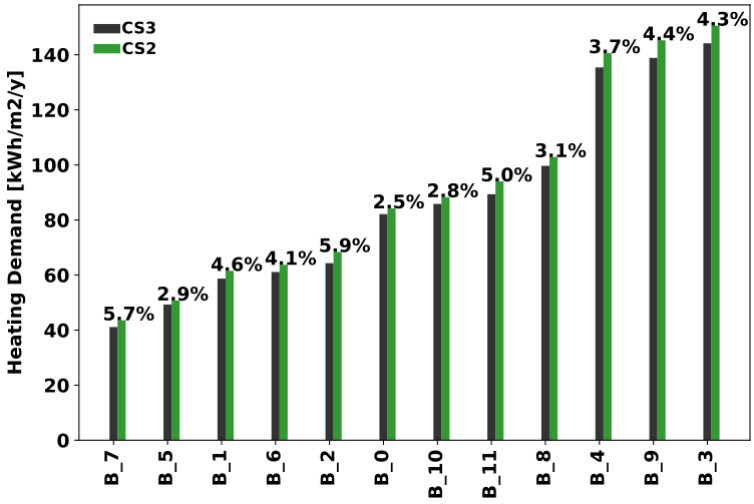

Figure 4.20: Annual heating demand for CS3 (Std) and fully coupled model (CS2) for each building.

Figure: 4.21 shows again the heating demand difference as a function of the surface temperature difference and air zonal temperature for a referenced zone during a representative heating week. Although the general trend of the figure is similar to Figure: 4.15, particular attention must be paid in the intensity of the dependent variable (heating demand). At this time, the mean outdoor zonal temperature is the forcing agent of heating demand discrepancies. When this variable exceeds the value of the meteorological temperature, then the coupled model underestimates the heating demand. This is evident in the time-steps range 50-65 in which the fluctuation of the outdoor air temperature causes a respective one in the energy demand.

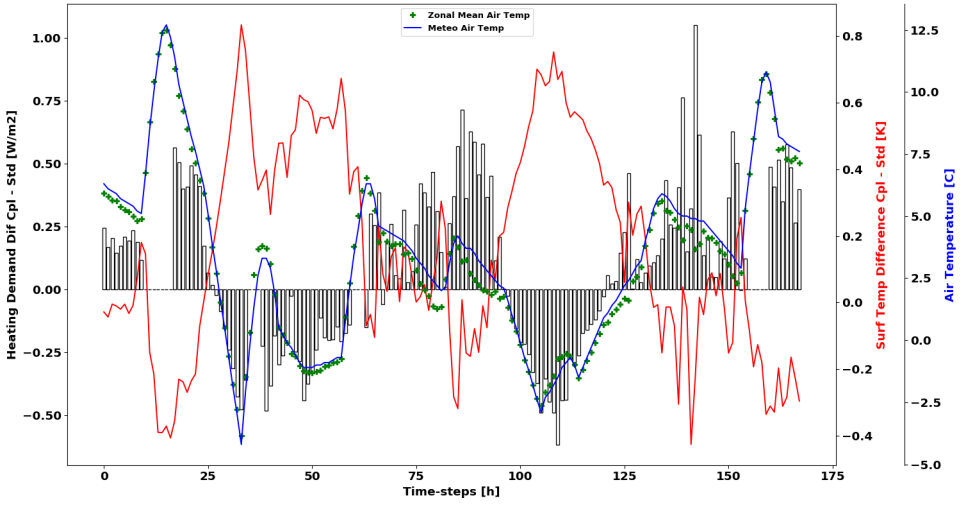

Figure 4.21: Heating demand difference as a function of surface temperature differences and air zonal temperature for a referenced zone during a representative heating week between CS2 and CS3 scenarios.

4.5.1.4 CS-3 Coupling Scheme single-node air temperature

In this final simulation set, the CS3 scenario has been compared with the Offline_Canopy and Offline_Canyon. At first glance, the simulation outcomes exhibit deviations on cooling and heating demand for both modified files. The trend is similar for both scenarios, while higher deviations are observed at $\bar{T}_{\text{canyon}}$ generated file. Table 4.4, presents the detailed simulation results, classified per building and scenario. Each raw contains accumulated data for the thermal zones that constitute each building, while each column classifies the selected scenarios and it is split into sub-columns for cooling (left) and heating (right) periods. The RD column presents the percentage difference between the standalone (CS3) simulation and the referenced chaining scenario.

Table 4.4: Annual cooling (left) and heating (right) demand per building and their respective relative difference (RD) for the referenced scenarios.

	Thermal Demand [kWh/m^2/y]									
Index	CS3		CS3a		RD [%]		CS3b		RD[%]	
B_0	2,8	82,1	3,2	83,2	13,6	1,3	3,6	83,8	21,5	2,0
B_1	18,4	58,7	19,9	60,0	7,3	2,1	20,8	60,6	11,4	3,2
B_2	16,5	64,3	17,8	65,7	7,6	2,1	18,7	66,4	11,9	3,1
B_3	27,3	144,2	29,7	146,8	8,0	1,8	31,2	148,1	12,5	2,7
B_4	21,5	135,4	23,7	137,8	9,2	1,7	25,0	139,0	14,3	2,6
B_5	05,9	49,3	06,7	50,3	11,4	1,9	7,2	50,8	17,6	2,9
B_6	13,9	61,1	15,2	62,4	8,8	2,1	16,1	63,1	13,6	3,1
B_7	13,7	41,1	14,8	42,0	7,3	2,2	15,5	42,5	11,5	3,3
B_8	14,2	99,7	15,7	101,6	10,0	1,9	16,8	102,6	15,5	2,8
B_9	21,1	138,9	23,1	141,0	8,5	1,5	24,3	142,1	13,2	2,3
B_10	12,8	85,8	14,2	87,4	9,7	1,9	15,1	88,3	15,0	2,8
B_11	23,6	89,3	25,6	91,2	8,0	1,9	26,9	92,1	12,4	3,0
Total	191,7	1049,9	209,6	1069,4	8,5	1,8	221,2	1079,4	13,3	2,7
Aver	16,0	87,5	17,5	89,1	8,6	1,8	18,4	89,5	13,0	2,2

Even though the amount of the relative difference for cooling loads is significant, presenting a maximum of 21.5% (canyon) and 13,6% (canopy) for building B_0 (Fig:4.22), the absolute difference is of the order of 0.6 and 0.4 kWh/m^2 respectively. Concerning the annual heating loads, the highest relative difference is observed at building B_7 (Fig:4.23) with a value of 2.2% and 3,3% for the canopy and canyon modified files respectively. At this time, the absolute difference is doubled for the canyon scenario, reaching 1.8 kWh/m^2. The maximum absolute difference occurs in building B_3 both for cooling and heating periods.

Regarding the district energy demand, Table:4.4 presents the total annual cooling and heating outcomes. The neighborhood absolute annual difference between the canyon and the standalone simulations is 59 kWh/m^2, presenting equal deviations of 29.5 kWh/m^2 for both seasons. In terms of a relative difference the respective outcomes are 13.3% and 2.7% for the cooling and heating periods respectively. The canopy case comparison presents slightly lower deviations, reaching 8.5% and 1.8% or in terms of absolute values 17.9 kWh/m^2 and 19.9 kWh/m^2 for the aforementioned periods.

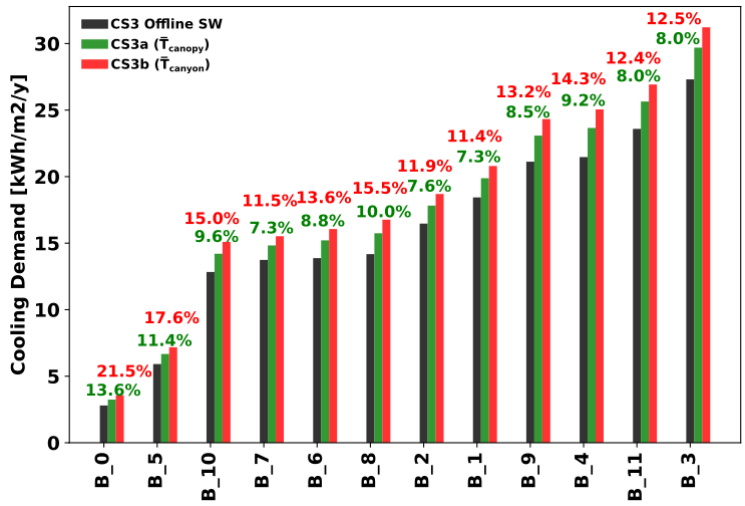

Figure 4.22: Annual cooling demand for CS3 (black), modified canopy CS3a (green) and canyon CS3b (red) for each building.

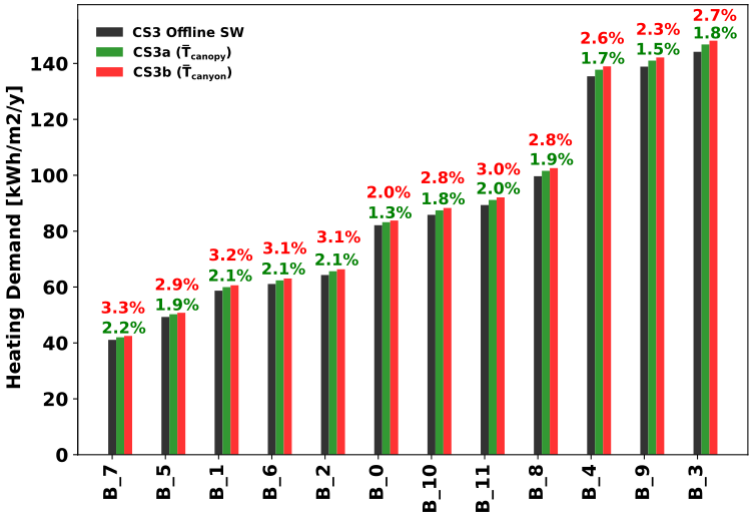

Figure 4.23: Annual heating demand for CS3 (black), modified canopy CS3a (green) and canyon CS3b (red) for each building.

Another interesting finding lies in the deviations of synchronous and asynchronous coupling methods when coupling with the same variable. In this context, the simulation outcomes of the synchronous coupling scheme (CS2) have been compared with the respective ones of the CS3 coupling strategy. We can observe that the asynchronous canyon scheme underestimates the cooling demand by 7.1% while the corresponding difference for the heating one is 1.9%. In parallel, the asynchronous canopy scheme underestimates by 11.7% and 6.9% the cooling and heating demands respectively. Besides, the variability of the outcomes based on the coupling approach, proves that the air temperature-based coupling affects significantly the building thermal behavior compared to the surface temperature one.

4.5.2 Evaluation of ACs waste heat feedback to energy demand

4.5.2.1 CS-1a Coupling Scheme surface temperature

In order to evaluate the feedback of systems wasted heat to building energy demand, a different simulation set has been established. The coupled simulation of the surface temperature scheme (CS1a - Cpl_Ts) is compared with a similar one where the system flux is not considered.

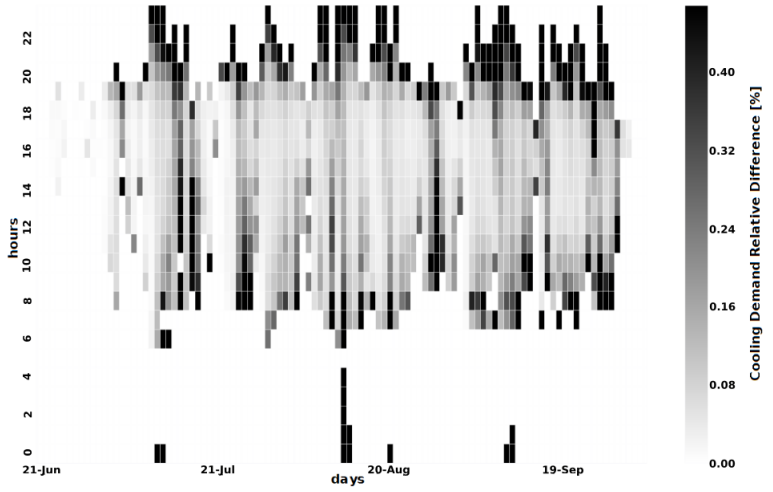

Figure 4.24: Impact of energy systems (relative difference/hour) on neighborhood cooling demand of CS_1a.

Figure: 4.24, presents a heatmap with the neighborhood percentage difference in cooling demand. As we can observe, this coupling scheme can not capture the feedback of the systems rejected heat as the maximum percentage difference is approximately 0.4%. However, it is evident that the additional demand occurs generally after 8 pm. During daytime hours the difference is trivial. The rejected heat of the systems is modifying the outdoor air temperature[7] and consequently the surface temperature of the adjacent zone. However, this slight surface temperature increase is not affecting the thermal performance of the examined zones (or buildings).

4.5.2.2 CS-2 Coupling Scheme outdoor air temperature

In order to study the impact of the additional system flux of the CS2 coupling scheme, one more simulation scenario is launched, in which we kept the general coupling scheme presented in section: 4.3.4 and we modify it without ejecting the flux of the systems to the adjacent air cells. The comparison between the two scenarios (CS2 and CS2_NF) is depicted in Figure: 4.25 representing the cooling (a) and heating (b) periods respectively.

The cooling demand presents an average increase of approximately 1.2%. Again, the maximum percentage difference occurs in low rise buildings reaching 2.2% and 2.3%. The minimum difference corresponds to 0.7%. The absolute difference of the penalty increase for the cooling period is 2.7 kWh/m^2. Figure: 4.26 shows the temporal distribution of the percentage difference

[7] see section: 4.5.3

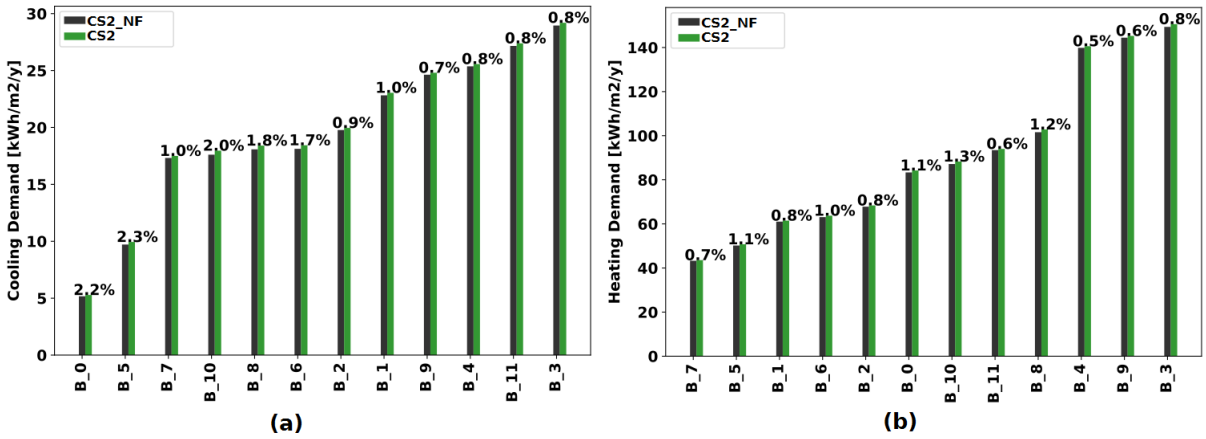

Figure 4.25: Annual feedback of system flux on cooling (a) and heating (b) demand for each building.

in cooling demand for the entire district due to systems rejected heat. The minimum difference is observed mainly during the daytime hours varying up to 1%, while the maximum appears during the evening (after 8 pm) reaching approximately 2%.

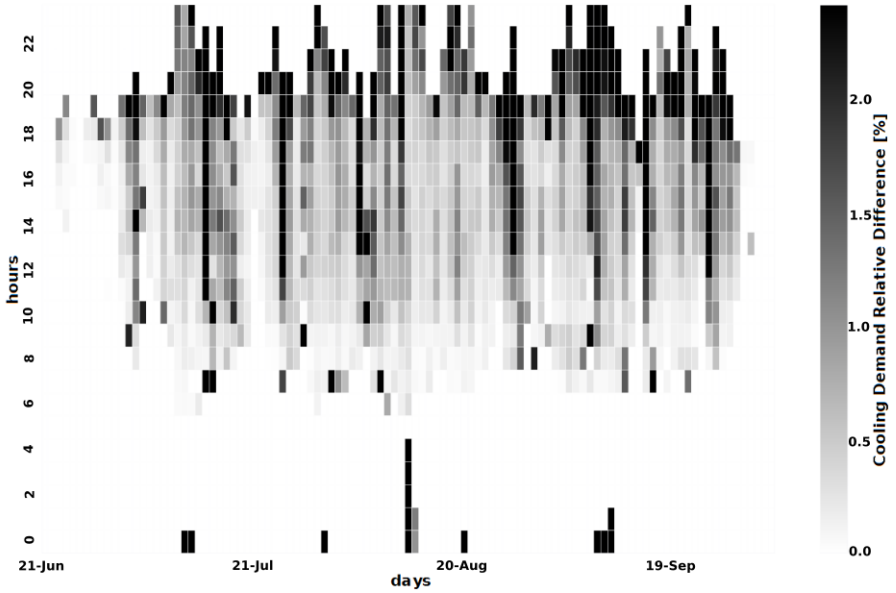

Figure 4.26: Impact of energy systems (relative difference/hour) on neighborhood cooling demand of CS_2.

The range of heating demand rise varies from 0.5% to 1.3% for the minimum and maximum percentage difference respectively. The average difference is 0.9% while the corresponding absolute value is almost seven times higher than the cooling one, reaching 18.5 kWh/m^2 for the entire heating season.

4.5.3 Evaluation of local Air Temperature due to ACs

The evaluation of the local air temperature due to ACs rejected heat has been studied under the synchronous coupling schemes. To do so, two coupled annual simulations were launched. The first one corresponds to the coupled schemes presented in section: 4.3, while the second one is similar but the waste heat is not imposed on the matrix system of EnviBatE.

4.5.3.1 CS-1a Coupling Scheme surface temperature

The impact of systems flux on ambient air is captured in both cooling and heating periods. More in detail, during the cooling period, the air temperature of the canyon derived from the coupled simulations is increasing and most of the canyon cells present a 0.2 - 0.5^{o}C increase of air temperature. The maximum absolute difference occurs in late July during the afternoon and varies from 0.1^{o}C to 1.4^{o}C (Figure 4.27). At this time step, the meteorological air temperature

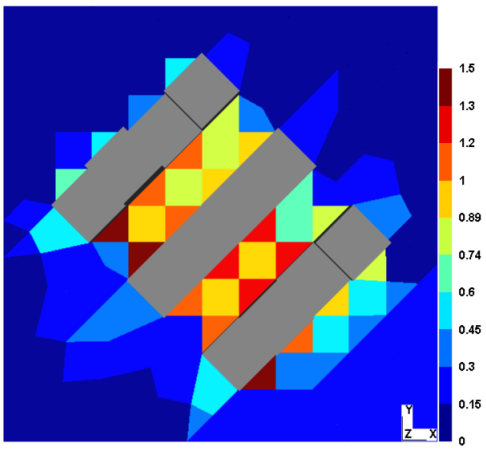

Figure 4.27: Maximum impact of ACU (CS1a scenario) on air temperature during the cooling period ($h = 0 - 3m$).

is 32.7^{o}C while the dominant wind direction is NNW'n (north-northwestern) perpendicular to canyons direction and the wind speed is 0.7 m/s. Figure 4.28 depicts the streamlines of the flow

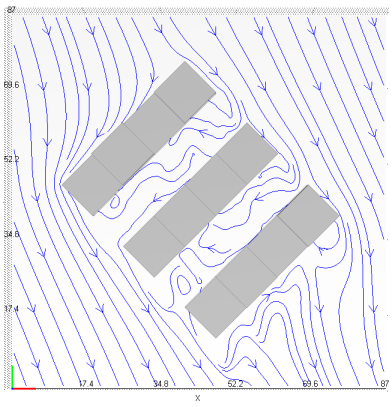

Figure 4.28: Streamlines for a dominant wind of 340^o.

at the pedestrian level, showing the diluted curves next to the building where the maximum deviation occurs.

The same trend is observed also for the heating period. The range of difference is higher since the heating loads and the respective ejected flux for a heating-dominated city (La Rochelle) are higher. The maximum air difference is observed in late December inside the canyon with an absolute value of 1.94^{o}C (Figure 4.29). At this time step, the meteorological temperature is

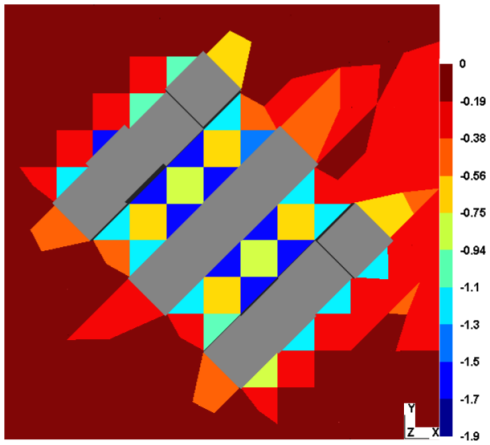

Figure 4.29: Maximum impact of ACU (CS1a scenario) on air temperature during the heating period ($h = 0 - 3m$).

-2.9^{o}C and the wind speed is 0.1 m/s. The wind direction is western, representing the dominant wind direction of the area. Figure 4.30 shows again the streamlines of the wind flow, proving that the systems flux remains trapped at these cells, as the advection is really weak at this moment.

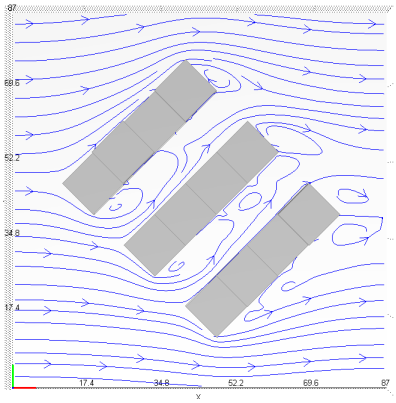

Figure 4.30: Streamlines for a dominant wind of 270^o.

4.5.3.2 CS-1b Coupling Scheme surface & indoor air temperature

The results of this coupling scheme, in terms of maximum air temperature difference, are almost similar to the ones presented in the previous section. Figures 4.31 and 4.32 show a similar trend. Nonetheless, the outdoor air temperature distribution exhibits small deviations. It

is observed mainly in the air cells adjacent to the ventilated thermal zones. The difference occurs due to the deviation of the indoor air temperature (and respectively the ventilation losses) and the slight modification of the surface temperature. The amount of this difference is fluctuating from 0.05 to 0.5^{o}C (Figure:4.33) and it is mainly observed at the air cells of 0-3m height.

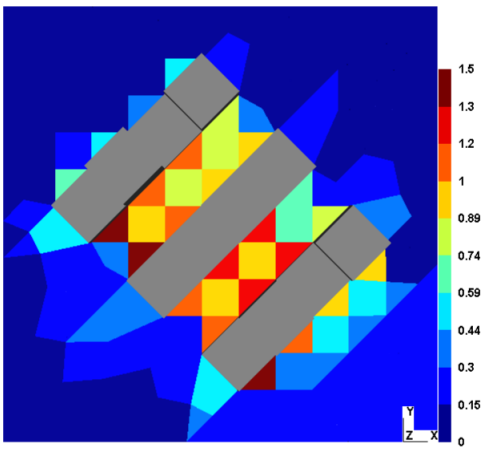

Figure 4.31: Maximum impact of ACU (CS1b scenario) on air temperature during the cooling period ($h = 0 - 3m$).

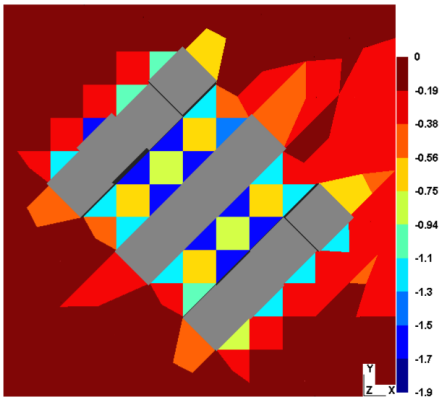

Figure 4.32: Maximum impact of ACU (CS1b scenario) on air temperature during the heating period ($h = 0 - 3m$).

Concerning the heating period, the range of temperature difference remains similar. The maximum difference is 0.65 ^{o}C (Figure:4.34) observed in the air cells of height 6-9 m. This difference is correlated to the specific heating needs of each studied thermal zone.

The results obtained from this coupling scheme show the variation of outdoor air temperature when considering explicitly the indoor thermal conditions rather than assuming fixed conditions for each zone of the simulated area. Moreover, the detailed representation slightly affects the energy demand. On the other hand, the simulation tools keep the advantages of the previous coupling procedure and an added value is gained, corresponding to better representation of the building elements and the interior air temperature nodes.

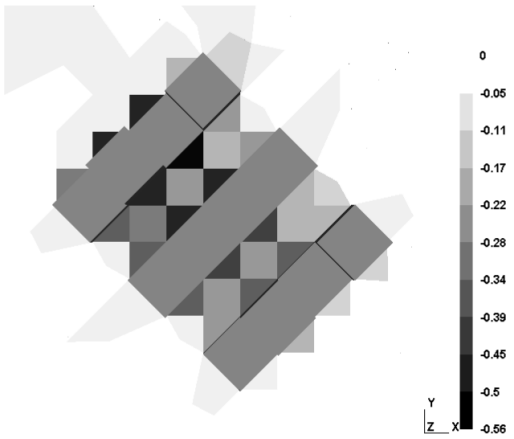

Figure 4.33: Maximum outdoor air temperature deviation between CS1b and CS1a scenarios during the cooling period ($h = 0 - 3m$).

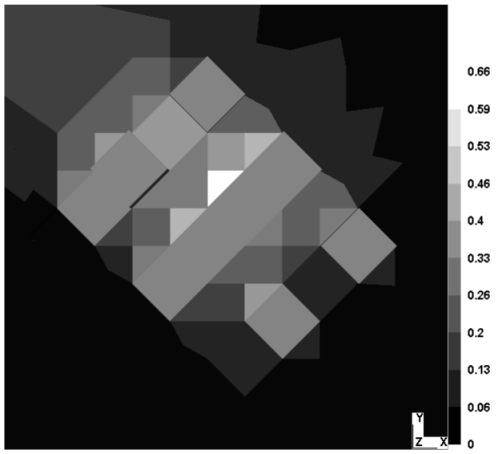

Figure 4.34: Maximum outdoor air temperature deviation between CS1b and CS1a scenarios during the heating period ($h = 6 - 9m$).

4.5.3.3 CS-2 Coupling Scheme outdoor air temperature

The implemented coupling scheme is capable, one more time, to capture the impact of the energy systems to ambient air temperature. The results obtained by this coupling scheme slightly deviate from the ones presented in the previous sections. The alteration on outdoor air temperature is mainly influenced by the coupling variable. The maximum average difference of air temperature between the various coupling scenarios is reaching 0.4^oC and 0.2^oC for the cooling and heating periods respectively. Moreover, although the maximum air temperature difference during the heating period occurs at the same time step as in the previous coupling schemes, the respective one for cooling differs. Further investigation is needed.

During the cooling period, the maximum air temperature difference is almost 1.97^oC, when the system rejected heat is considered, as shown in Figure 4.35. The meteorological dry bulb temperature at this time step is 30.4^oC while the prevailing wind is a NW'n (318^o) with a value of 0.5 m/s. The actual wind speed in the cell of the highest difference is less than 0.2 m/s (Figure:4.36) leading to overheating phenomena.

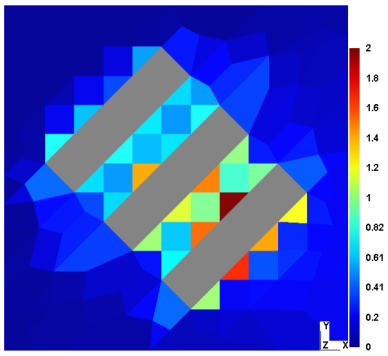

Figure 4.35: Maximum impact of ACU (CS2 scenario) on air temperature during the cooling period ($h = 0 - 3m$).

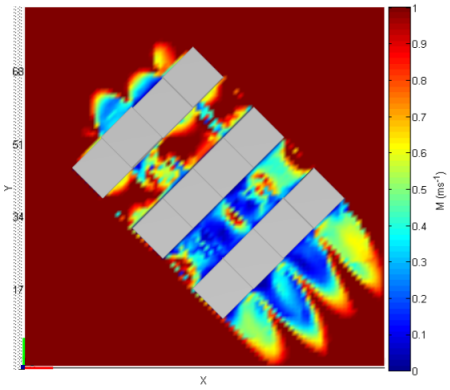

Figure 4.36: Wind speed distribution scaled to 0-1 values during the time step of maximum system flux impact ($h = 1.5m$).

The observed discrepancy is attributed to the dynamic behavior of the model and thus to the ejected ventilation and system fluxes. When the system flux is rejected, the outdoor air temperature is affected and thus the ventilation heat losses. The corresponding maximum air temperature difference of the time step where the previous coupling schemes assessed it, is less than 0.3^oC.

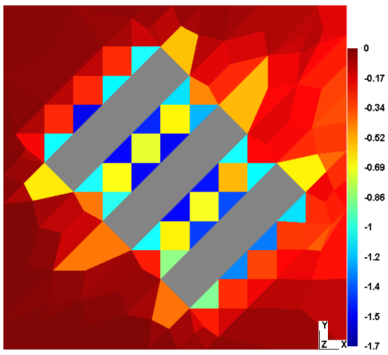

Figure 4.37: Maximum impact of ACU (CS2 scenario) on air temperature during the heating period ($h = 0 - 3m$).

A similar trend is captured for the heating period. Some minor alterations between the coupled scenarios are still found, but this time the maximum air temperature difference occurs at the same time step. The absolute maximum air temperature difference corresponds to 1.7^oC, while the previous coupling schemes record it to 1.9^oC.

4.6 Parametric Study

In this section, the presented synchronous coupling schemes have been lumped for different climate types and building thermal characteristics. The climate types, according to Köppen-Geiger classification map, [227], [228] correspond to:

1. Mediterranean **Csa** temperate climate with dry and hot summers (Athens) with wind gusts during the summer period (Athens)
2. Mediterranean **Csa** temperate climate with dry and hot summers (Seville)
3. Oceanic **Cfb** or Marine West Coast Climate characterized as temperate, humid with warm summers (La Rochelle)
4. Continental **Dfc** or hemiboreal climate characterized of cold, humid seasons with cool summers (Stockholm)

The meteorological data correspond to typical meteorological files[8]. Building thermal characteristics were obtained from RAGE classification [229] and they are clustered in two main typologies, in order to represent the existent building stock:

1. Buildings constructed between 1968-1974
2. Buildings constructed between 1990-2000

In this classification, four different types of buildings were considered, Single Family Houses, Terraced Houses, Multi-Family Houses and Apartement Blocks. The thermophysical properties correspond to average values of thermal conductivity and layer thickness for walls, roofs, floors, ground floors and windows concluding to medium-well and poorly insulated buildings. The properties of medium-insulated buildings are given in Table: 3.1, while the poor-insulated ones are characterized by thermal transmittance values (U_v) of 1.59, 2.08, 2.5 and 4.2 [W/m^{2}K] for walls, roofs, ground floors and windows respectively. Four different models are considered: the CS3 (★), the CS2 (■), the thermoradiative CS1a (CS1a_ThR) (▼), and the fully coupled CS1a (▲) (Table:4.1). The selection is established in order to depict a representative model for each of the cases mentioned in this chapter, as well as to compare the thermal behavior between the standalone models and the coupled ones.

The objective of the parametric study is to identify the models sensitivity under different boundary conditions and different building characteristics. Moreover, the selection of ACU as the operating energy system, will impact differently the model's response. The remained simulation parameters were identical for both scenarios as given in Tables: 3.1 and 3.2. This option was selected for comparison purposes, however some of the selected parameters are ideal and might affect the simulation results (e.g., the selection of interior insulation which is not generally preferred in warm climates, the infiltration rate, etc.).

[8] obtained from Energy+ [53]

4.6.1 Assessment of energy demand

In this section, the simulation outputs are compared in terms of average cooling and heating thermal demand, as shown in Figures: 4.38 and 4.39. Although the district configuration remains identical, the simulation outcomes, exhibit different thermal behavior depending on:

- insulating capacity of building envelope,
- type of coupling scheme,
- climate conditions

To this end, it is evident the energy increase between poorly and medium-well insulated buildings for all of the climate types. Both cooling and heating demands present significant variations when the insulation capacity changes. This is captured by all of the considered models.

More in detail, during the cooling period the meteorological file of Seville presents the highest cooling demand. The maximum percentage difference is observed when the air temperature is considered as the coupling variable for poor-insulated buildings. The CS2 coupled model deviates by almost 13% from the respective standalone, presenting an absolute value of around 30 kWh/m^2/zone. At the same time, the CS1a model presents a percentage difference of almost 9% compared to the respective standalone CS1a_ThR. Notably, the standalone models differ significantly for poorly insulated buildings and the same trend is inherited to the coupled ones. For medium-well insulated buildings, the percentage difference is 10.3% and 2.9% between coupled and standalone simulation for air and surface temperatures coupling variables respectively.

The simulation outcomes for the meteorological file of Athens, present slightly decreased cooling demand but the general trend remains similar to the one of Seville. The percentage differences approximate the respective values of Seville, reaching 13% and 8.7% for poor-insulated buildings between the coupled and standalone models, while the well-insulated ones present deviations of approximately 10% and 2%. The previously described trend is depicted also for the meteorological files of La Rochelle (typical) and Stockholm. The cooling demand is very low for both cities, reaching a maximum of 2.7 kWh/m^2/zone and 0.47 kWh/m^2/zone respectively. Thus, the percentage difference is high but in terms of absolute values, it corresponds to a maximum of 0.45 kWh/m^2/zone.

All of the aforementioned outcomes reveal common highlights:

- when the coupling variable corresponds to air temperature, the combined impact of microclimate and system waste heat is higher compared to standalone simulations,
- poorly insulated buildings are more sensitive to the microclimate conditions, presenting increased thermal demand that leads to increased heat rejection and thus increased system feedback
- under poor insulation capacity, the deviation between the coupled models diminishes.

During the heating period, the building insulation capacity affects significantly the simulation outcomes. The outcomes of Stockholm's meteorological file, present more than double energy demand compared to La Rochelle case, with an average value of almost 260 kWh/m^2/zone

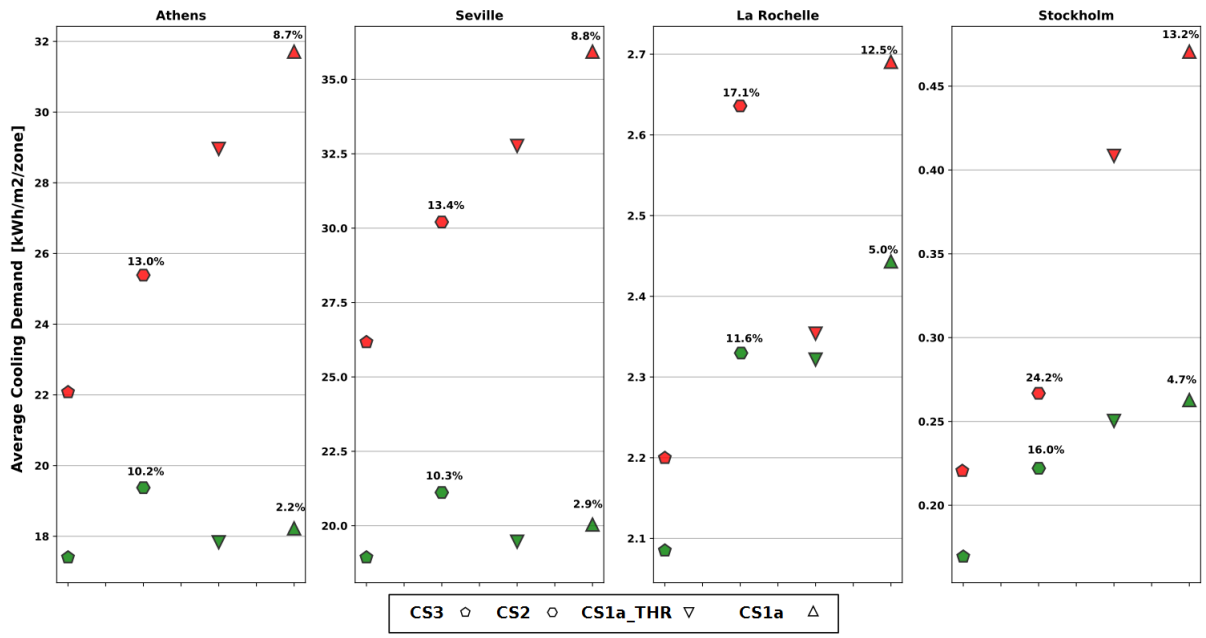

Figure 4.38: Average cooling demand for four cities, two building thermal characteristics (green: well; red poor insulation) and three coupling schemes.

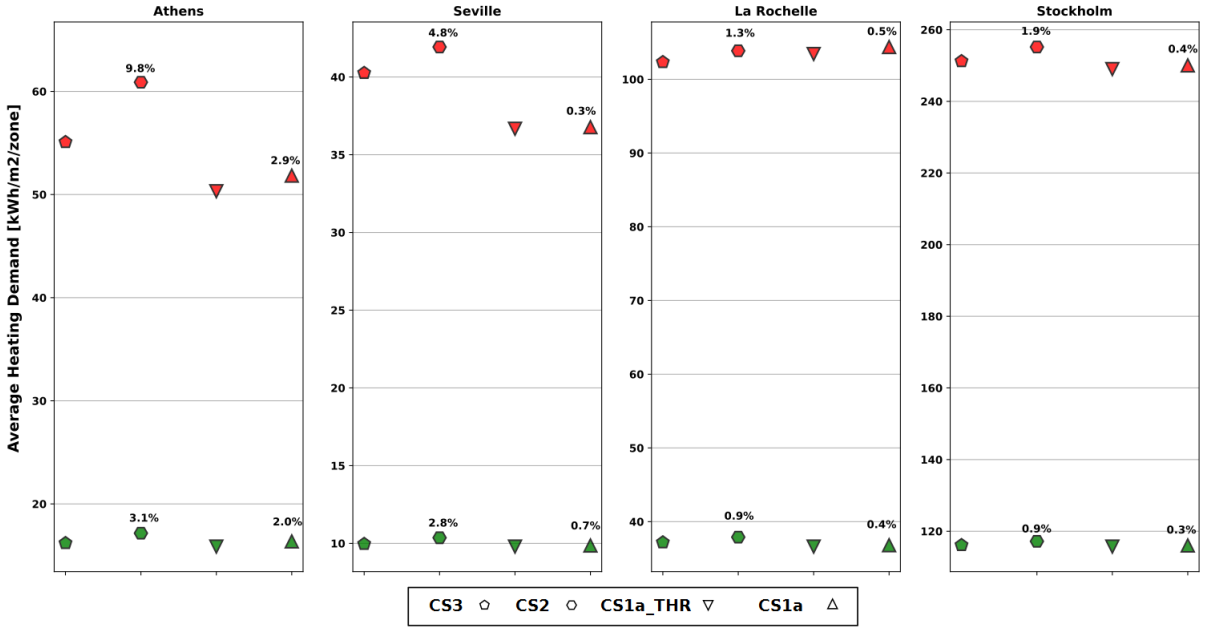

Figure 4.39: Average heating demand for four cities, two building thermal characteristics (green: well; red poor insulation) and three coupling schemes.

while for La Rochelle the respective average demand is almost 105 kWh/m^2/zone. For Mediterranean climates, Athens presents a heating average demand of around 60 kWh/m^2/zone, while the respective one for Seville approximates the 42 kWh/m^2/zone. During the heating period, both poorly and medium-well insulated buildings present a compact thermal behavior in terms

of percentage difference. This is due to:

- increased energy demand compared to the cooling one
- the impact of both microclimate and system waste heat affects significantly the cooling energy demand

However, a key observation in Figure: 4.39 is the severe increase in the heating demand of the CS2 model in the case of Athens. This energy rise is associated to the wind speed conditions of the meteorological file. The wind speed values of the meteorological file are null for many time steps of the simulation time. The developed model considers only the advection mechanism of air circulation, and thus under null wind speed, the waste flux of the system is trapped. This outcome shows the necessity for further developments of the model. A buoyancy model needs to be integrated, in order to tackle the potential overheating incidents. Moreover, it will allow to extend our studies regarding the implementation of different energy systems, such as mounting chillers in the roof-top of the buildings.

4.6.2 Assessment of microclimate parameters

In this section, we point emphasis to the potential air temperature increase of the zonal cells adjacent to thermal zones, as a function of the rejected heat flux of the air-conditioning units during the cooling period. An additional simulation scenario was considered, corresponding to the CS2_NF model. Figure 4.40 shows the maximum local air temperature rise (first occurrence if repeated) during the cooling period as a function of the rejected heat from the ACU. In the case of Athens, the maximum air temperature rise for medium insulated buildings is 2.0 ^{o}C for an injected heat flux of 12.0 W/m^2, while the corresponding one for poorly insulated ones is 3.6 ^{o}C for approximately 18 W/m^2. In Seville, which is also governed by a Mediterranean climate, the maximum air temperature rise is 3.3 ^{o}C for 13.6 W/m^2 corresponding to medium insulation capacity, while for the poor one exacerbates to 5.3 ^{o}C for a rejected flux of 24.25 W/m^2. For the typical climate file of La Rochelle, the maximum air temperature rise is much less, reaching 0.9 ^{o}C, for a rejected flux of 9.3 W/m^2. In the case of poorly insulated buildings, the temperature increase is 1.2 ^{o}C corresponding to an additional heat flux of 11.9 W/m^2. For the Stockholm case study, the temperature increase is low, with values of approximately 0.1 ^{o}C and 0.2 ^{o}C, representing the limited cooling needs of the city. The rejected fluxes from the evaporator are 4.6 W/m^2 and 5.9 W/m^2 for medium and poor insulation capacities respectively.

An interesting finding is that the maximum air temperature difference occurs under different boundary conditions, even for the similar meteorological file. As an example, in the case of Seville, the maximum temperature rise is observed for a 0.0 m/s and 0.2 m/s wind speed values for medium and poorly insulated buildings. At the same time, the meteorological dry bulb temperature is 36.4^{o}C and 34.2 ^{o}C, found both late in the afternoon during mid-July. In Athens, the peak zonal air temperature difference corresponds to a boundary temperature of 31 ^{o}C and 30 ^{o}C, while at the same time the meteorological wind speed was 0.1 m/s for both cases, found again in the afternoon during mid-July. For the meteorological file of La Rochelle, the same tendency exists. The boundary climate data correspond to 30.5^{o}C and 0.69 m/s for medium insulated buildings, while for the poor ones the respective values are 29.3^{o}C and 0.8 m/s. In the case of Stockholm, the meteorological dry bulb temperature corresponds to 26.4^{o}C and 25.6^{o}C and the wind speed is 1.3 m/s and 1.5 m/s for medium and poor insulating capacity respectively.

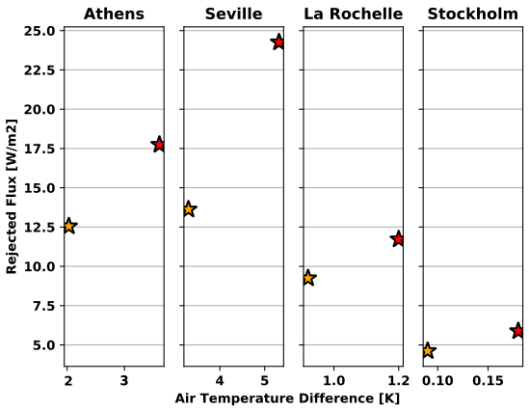

Figure 4.40: Correlation of rejected flux per floor area and temperature rise for medium (orange) and poor (red) insulated buildings.

There is no regular variability between the injected heat flux and the air temperature rise. The latter is strongly dependent on dry bulb temperature and wind speed conditions. An effort to correlate the wind speed conditions with the potential overheating is given in Figure 4.41. The outdoor air temperature difference of all of the zonal cells is plotted against the boundary wind speed (well-insulated buildings scenario) for the meteorological file of Seville. An interesting finding is the estimation of a threshold value. Above it, the advection is dominant and no matter the added fluxes from buildings or systems, the air temperature is stabilized. We estimate this threshold value at around 5.1 m/s. Above this wind speed limit value, the air temperature presents very slight modifications, less than 0.25 K, while for a wind speed value lower than 1.8 m/s, the air temperature presents severe fluctuations. This is a very interesting remark because on the one hand designates the conditions in which the potential buoyancy model has to be implemented, on the other hand, it can be used as an index for the efficiency of cool material implementations.

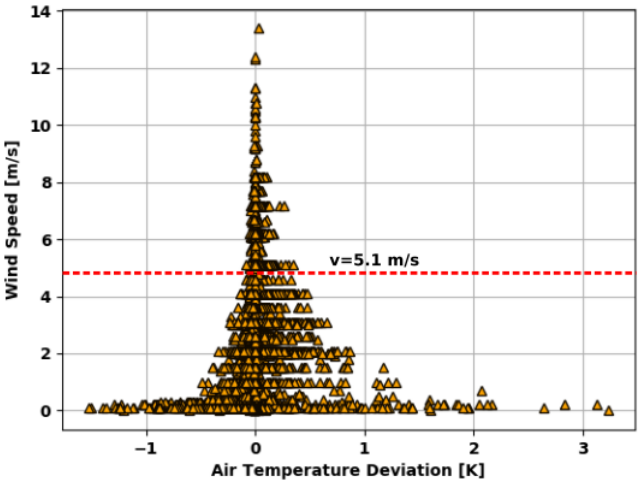

Figure 4.41: Correlation between wind speed and temperature deviation in Seville.

4.7 Chapter Conclusions

This chapter presented the development of various coupling strategies between an UBEM (Dimosim) and a microclimate model (EnviBatE). We clustered the coupling methods to synchronous and asynchronous, depending on the examined variable. The synchronous coupling schemes were established with the employment of the ping-pong approach, while the asynchronous ones were based on the chaining method. For comparison purposes, we selected a physical variable (outdoor air temperature) to quantify the variability between them.

More in detail, the synchronous coupling methodology was distinguished to building-based and microclimate-based coupling variables, while in parallel the rejected heat from the operating energy systems (ACU) was taken into account in all of the coupling schemes. The consideration of the exterior surface temperature of wall elements as the coupling parameter which tracks the microclimate footprint enabled us to assess the impact of local microclimate to building energy demand studies. Furthermore, the concurrent exchange of the afore-mentioned parameter enhanced with the indoor air temperature verified the amelioration of the individual model capabilities. Although both coupling schemes assessed the impact of the energy systems to local microclimate, the quantification of their feedback on building energy demand was limited. The conception of an integrated tool led us to a further synchronous coupling scheme, in which the outdoor urban scene was linked to the UBEM, without requiring the concurrent simulation of the building model. The consideration of the outdoor air temperature as the coupling variable enabled us to assess the impact of the energy systems and the respective feedback on building energy demand.

Furthermore, the asynchronous coupling scheme of the incident solar irradiance availed our study with a twofold benefit. On the one hand, served as the first step towards the integration of the urban environment to the UBEM, on the other hand, offered a detailed representation of solar-based parameters, such as the calculation of the direct and diffuse components in a fine mesh. Moreover, the integration of the view factors allowed us to consider the inter-reflections and the radiative exchanges between the urban surfaces. The asynchronous coupling scheme of the air temperature enabled us to quantify the potential discrepancies between online and offline coupling methods. To this end, the comparison between synchronous and asynchronous coupling strategies showed a significant difference in cooling demand. The respective annual energy demand diverges from 0.1% to 2.2% for a case study of an oceanic climate with warm summers, using a morphed tmy meteorological file.

In order to study the sensitivity of the implemented coupling methods and their response to different boundary conditions and different types of buildings, a parametric study was conducted. We conclude that the building model is more sensitive when coupling with the air temperature due to the bulk convection, especially for medium-well insulated buildings. In the case of buildings with poor insulation capacitance, the coupling scheme of the exterior surface temperature, is decent, especially for heating-dominated cities. Moreover, the parametric study revealed a crucial limitation of the model. The latter stands for the airflow model which considers only the advection mechanism. Nevertheless, all of the implemented methods are coherent for the need of microclimate integration in building energy demand studies, especially for the cooling period. Given the present documented and the future estimated temperature increase, we conclude that the assessment of cooling energy divergence between standalone and coupled simulations, shows the necessity of microclimate integration to building energy simulations.

Finally, in order to provide an estimation regarding the computational cost of the developed models, we present in Figure: 4.42 the annual thermal demand as a function of the execution time for the implemented case study of section: 4.5.1.1. We must mention that the quantification of the execution time for the asynchronous coupling schemes does not include the computational cost needed to generate the import data. The simulations were performed with an Intel(R) Xeon(r) CPU @2.80GHz, 4 Core(s) processor.

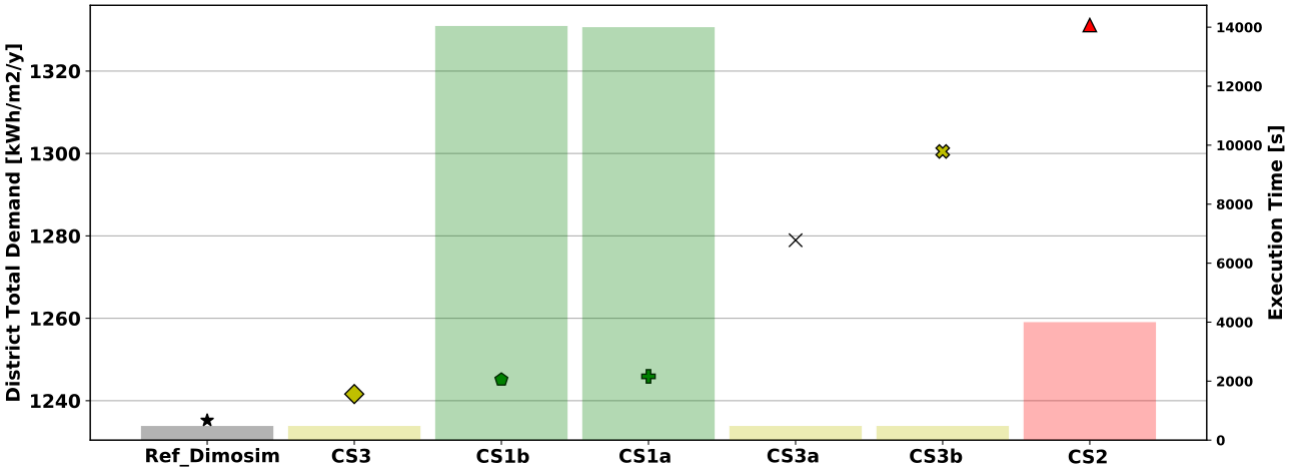

Figure 4.42: Annual energy demand (markers) of the implemented coupling schemes as a function of execution time (bars).

Chapter 5

District energy systems & local microclimate - Case study of Geraniums District

Contents

5.1 Introduction

In this chapter, the developed integrated model has been used to evaluate the thermal footprint of a residential district in the city of La Rochelle, covering a total floor area of 63800 m^2. The scope of this study is to assess the energy demand of the district at different scales, from local to neighbourhood level, by comparing the application of individual and centralized energy systems, with respect to the local microclimate. Specifically, we study the potential capability of a district energy network (DEN) to counterbalance the local UHI effect. In addition, we inspect if the energy penalty of the district network, due to the thermal losses of the piping circuit and auxiliaries, can be balanced by the reduction of heat discharges of the individual systems and, by extension, their feedback to building energy consumption. Furthermore, we investigate the implications under future climate conditions as well as a possible extensive installation of cool materials in the referenced area.

5.2 Physical characteristics of the district

5.2.1 Audit of the site

The studied district is situated in the Geranium area, approximately 2 km away from the city center, in the north-eastern part of the city of La Rochelle, as shown in Figure: 5.1. The

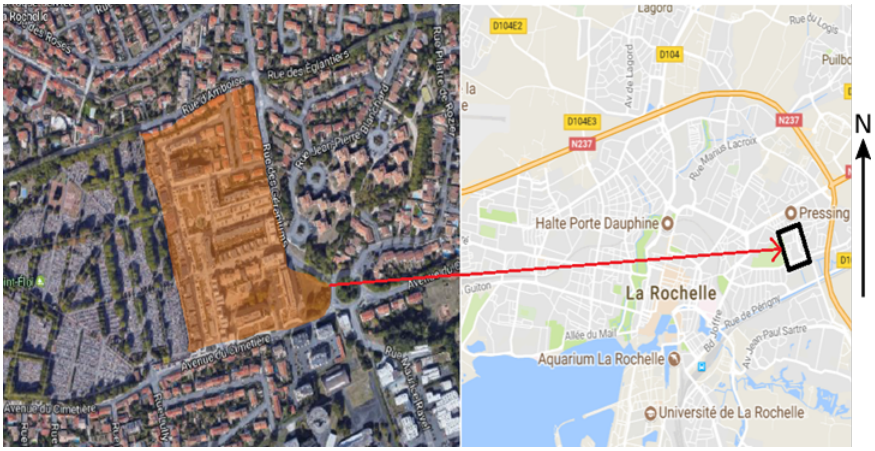

Figure 5.1: Location of the studied district in La Rochelle.

built area forms a polygon with an approximated surface of 63800 m^2. The building stock is a mixture of existing and new buildings with mainly residential usage. The buildings present significant variations of heights. The district borders on the Geraniums cemetery to the West and it is thus unprotected from the dominant western winds that occur in the area and exposed to solar irradiance, especially during the summer period. The rest of the borders are enclosed by traffic axes. It is characterized as a residential area, as commercial buildings are non-existent according to cadastral data. The outdoor space is composed of asphalt roads and concrete sidewalks, while a small amount of them is sparsely vegetated.

5.2.2 Building characteristics

The total number of buildings corresponds to 87. It is divided by 3m floor heights, giving a total number of 232 thermal zones, as shown in Figure:5.2. The maximum building height is

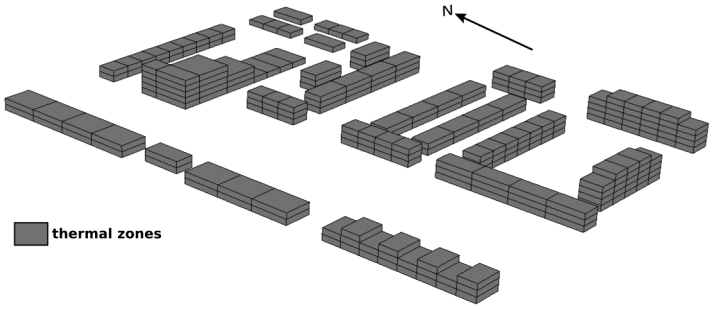

Figure 5.2: 3-D Visualization of buildings and thermal zone division.

15m, corresponding to building blocks, while the minimum match with single-floor detached houses of 3m.

The building stock has been separated into two main categories, buildings constructed before the 1970s and newer ones constructed after the 2000s, as depicted in Figure: 5.3. The

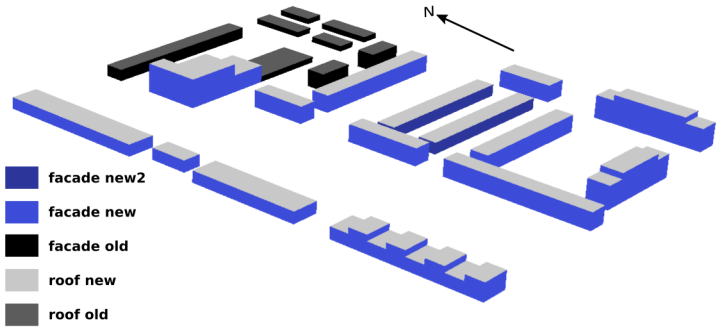

Figure 5.3: 3-D Visualization of the buildings according to the thermal properties of the exterior boundaries.

external boundaries have been divided into four layers, representing two plaster layers at the exterior and interior sides, a mass and an insulation layer between them, as presented in section 3.1.1.1. Tables: 5.1 and 5.2 summarize the envelope characteristics and the material thermal properties respectively.

The total building envelope area is 37236 m^2, analysed to 23406 m^2 of vertical surfaces and 13830 m^2 of roof and ground floor surfaces. The maximum zone area is 400 m^2 corresponding to single-floor old apartments, while for the building blocks the respective area ranges between 100 and 300 m^2. The glazed area is almost 4681 m^2 resulting to glazing ratio of 0.2.

Interior floors and inner wall mass elements have been kept identical for both building types. Figure 5.4 visualizes the interior element division. The rest of the imported data required to perform the simulations, such as: occupancy schedules, internal gains due to appliances and lighting, ventilation/infiltration, and setpoint temperatures for each thermal zone are difficult to be gathered at this scale, especially when they are not provided by national databases. Hence,

Table 5.1: Envelope properties of the buildings.

Construction Element	**U value** [W/m^{2}K]	**Materials** [outer to inner]	**Thickness** [mm]	**Albedo** [%]
Gfloor old	2.5	P-C-MW-P	10 - 200 - 1.7 - 10	-
Gfloor new	0.4	P-C-MW-P	10 - 200 - 6.4 - 10	-
Roof old	2.08	P-MW-C-P	10 - 4.2 - 200 - 10	26
Roof new	0.33	P-MW-C-P	10 - 8.1 - 200 - 10	20
Wall old	1.59	P-C-MW-P	10 - 200 - 8.6 - 10	30
Wall new	0.36	P-C-MW-P	10 - 200 - 73 - 10	30
Wall new 2	0.36	P-C-MW-P	10 - 200 - 73 - 10	22
Inner mass	1.0	C	10	-

Table 5.2: Construction material thermal properties.

Element	**Density** ρ [kg/m^3]	**Specific Heat** C_p [J/kgK]	**Thermal Conductivity** λ [W/mK]
plaster [P]	950.0	840.0	0.16
concrete [C]	2240.0	840.0	0.92
mineral wool [MW]	45.0	1030.0	0.03

Table 5.3: Windows thermal and optical properties.

Window Type	**U value** [W/m^2]	**Transmission** [%]	**Absorption** [%]
Single glazed-wooden frame	3.25	78.9	8
Doubled glazed-aluminium frame	2.5	78.9	8

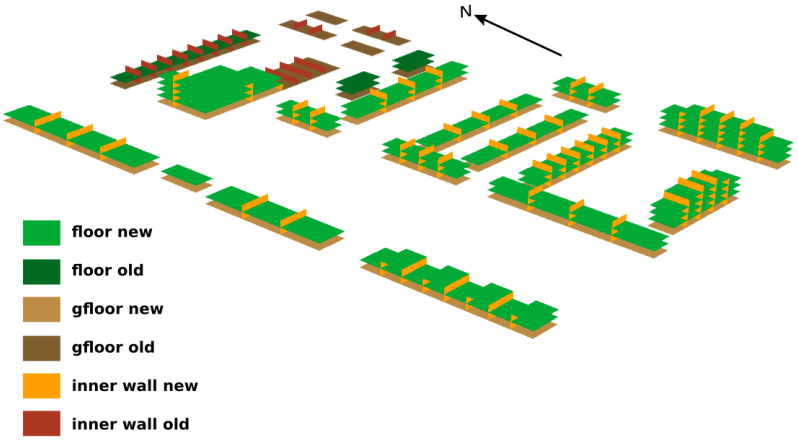

Figure 5.4: 3-D visualization of the interior thermal zone elements.

they have been defined conventionally based on the methodology developed in the building thermal regulation (RT2012), in accordance with those presented in Section: 3.3.3.

5.2.3 Outdoor characteristics

The generated outdoor space has a surface of 207995 m^2. It has been expanded almost four times from the core of the district area, mainly in the x-direction (considering north in the y-direction) by 300 m, in order to generate the hypothetical district energy network and its energy HUB. It consists of asphalt roads, concrete pavements and soil spaces, as shown in Figure: 5.5. The thermal characteristics of the materials used for the outdoor space are presented in Table: 5.4. Vegetation is taken into account only in solar calculations, considering a monthly constant transmission factor of poplar trees.

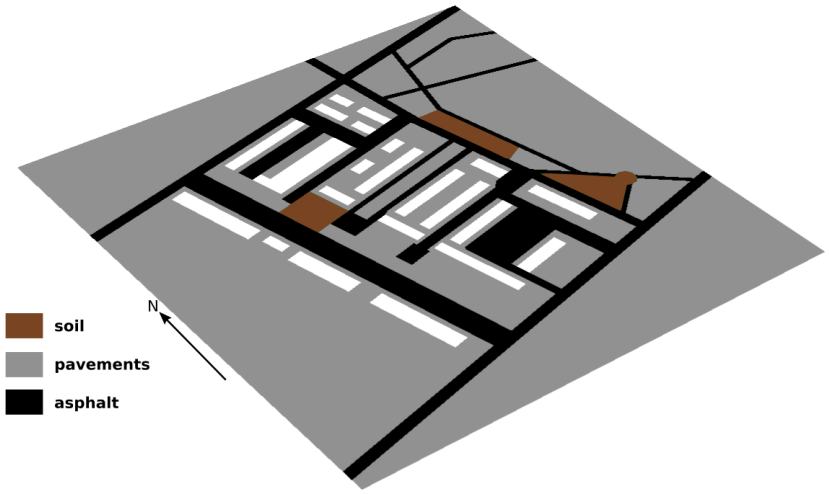

Figure 5.5: Visualization of neighborhood's open space generated mock-up.

Table 5.4: Thermal properties of the exterior surface of outdoor materials.

Element	**Thickness** **d** [mm]	**Density** ρ [kg/m^3]	**Specific Heat** C_p [J/kgK]	**Thermal Conductivity** λ [W/mK]
soil	200	1600.0	1000.0	1.0
concrete	200	2300.0	920.0	0.92
asphalt road	400	2300.0	920.0	1.75

5.3 Simulation work-flow

5.3.1 Implemented Scenarios

The study includes two main scenarios. Each of them considers an individual and a centralized energy system. In the case of an individual system, each thermal zone is equipped with a split air conditioning unit (AC) where the system's flux is released in the adjacent canopy cells, weighted by the surface ratio. The centralized energy system corresponds to a district energy network (DEN). We speculate that the district generator is far away from the core of the district and thus it can be considered as zero on-site emitter of waste heat.

The aforementioned generic scenarios have been integrated into different climate scenarios. The first simulation set represents the base case, where the district energy demand and microclimate performance have been evaluated under the standard meteorological file for both energy providing options. In order to assess the sensitivity of the district in a potential warmer climate, described by intense cooling needs, the modified meteorological file has been used, representing the Extreme scenario.

Table 5.5: Albedo modifications implemented in the Extreme cool simulation scenario.

	Solar Reflectance [%]						
	Roof old	**Roof new**	**Wall old**	**Wall new**	**Wall new 2**	**Pavements**	**Road**
Init	26	20	30	30	22	40	15
Cool	60	70	50	50	50	66	35

Finally, we inspect the impact of cool (highly reflective) materials as a possible mitigation strategy against urban overheating in the extreme scenario. In this case, an extensive application of cool materials has been set for both building elements and open spaces, in addition to the distinct energy alternatives. The solar reflectance has been modified for each surface according to Table: 5.5. In the following post-processing analysis we consider by default the abbreviations of each simulation scenario as presented in Table: 5.6.

Table 5.6: Implemented simulation scenarios of the Geraniums district case study.

Simulation Scenario	**Meteorological data**	**Abbreviation**	
Normal	La Rochelle TMY-1995	AC_Std	DEN_Std
Extreme	La Rochelle TMY-2050	AC_2050	DEN_2050
Extreme - Cool materials	La Rochelle TMY-2050	AC_2050_cool	DEN_2050_cool

5.3.2 Boundary conditions

The meteorological data correspond to a typical meteorological year of La Rochelle. Besides, a modified meteorological file was generated using Meteonorm software, presenting slight differences with the one employed in Chapter 4. The modified file represents the extreme conditions of 2050 according to the A2 future scenario. More in detail, Figure: 5.6 shows the monthly average total solar irradiance of the standard and the morphed meteorological files. The maximum standard total solar irradiance on tilted surface corresponds to 929 W/m^2 found on 21/08 at 12:00 pm, while for the morphed one is slightly increased to 991 W/m^2, found on the same date.

In parallel, Figure: 5.7 presents the comparative dry bulb temperature of the used annual meteorological files. The maximum air temperatures correspond to 31.9 ^{o}C and 35.6 ^{o}C, found on 20/7 at 4:00pm, while the average air temperature during the cooling period is 18.8 ^{o}C and 20.9 ^{o}C representing the standard and the extreme meteorological files respectively. Sequentially, the minimum air temperature is found on 12/01 with a value of -5 ^{o}C for the standard file while at the same time for the extreme scenario is -3.1 ^{o}C. The average air temperature during

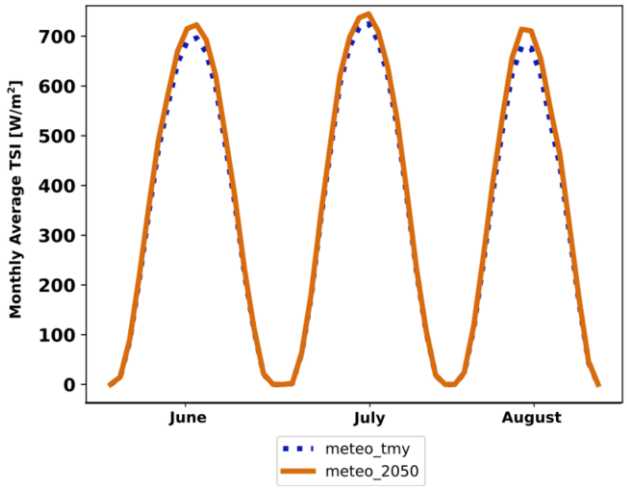

Figure 5.6: Monthly average total solar irradiance of the used meteorological files during the cooling period.

the heating period is 8.1 °C and 9.5 °C respectively. The annual average of the typical file is 12.9 °C and 14.6 °C for the projected one.

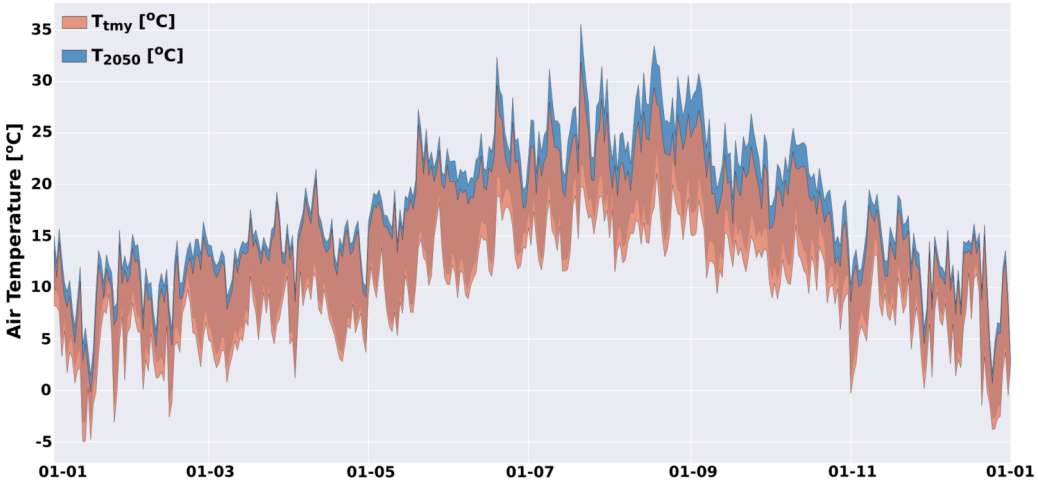

Figure 5.7: Dry-bulb temperature of the used meteorological files.

An efficient way to relate the meteorological variables to cooling and heating energy demand is the calculation of the cooling and heating degree hours[1] (equations: 5.1, 5.2), given as the

[1]

$$\mathbf{CDH}(T_{\mathrm{B}}) = \sum_{j=1}^{N} (T_{\mathrm{met}} - T_{\mathrm{B}})^{+} \tag{5.1}$$

$$\mathbf{HDH}(T_{\mathrm{B}}) = \sum_{j=1}^{N} (T_{\mathrm{B}} - T_{\mathrm{met}})^{+} \tag{5.2}$$

integral of temperature difference over a time period for a supplied base temperature. Table:5.7 summarizes the results for base temperatures equal to 26°C and 19°C.

Table 5.7: Cooling and heating degree hours for the given base temperatures of the standard and projected meteorological files.

Location	Meteo_file	CDH (T_B=26°C)	HDH (T_B=19°C)
La Rochelle	TMY-1995	179	45392
La Rochelle	TMY-2050	952	39661
Relative Difference	**-**	**81.2 [%]**	**12.6 [%]**

The wind speed and direction of the standard meteorological file for the cooling and heating periods are presented in Figure: 5.8, in terms of windrose representation. The dominant wind directions are W-NW'n and W-SW'n during the cooling and heating periods respectively, representing an air circulation from the sea towards the mainland.

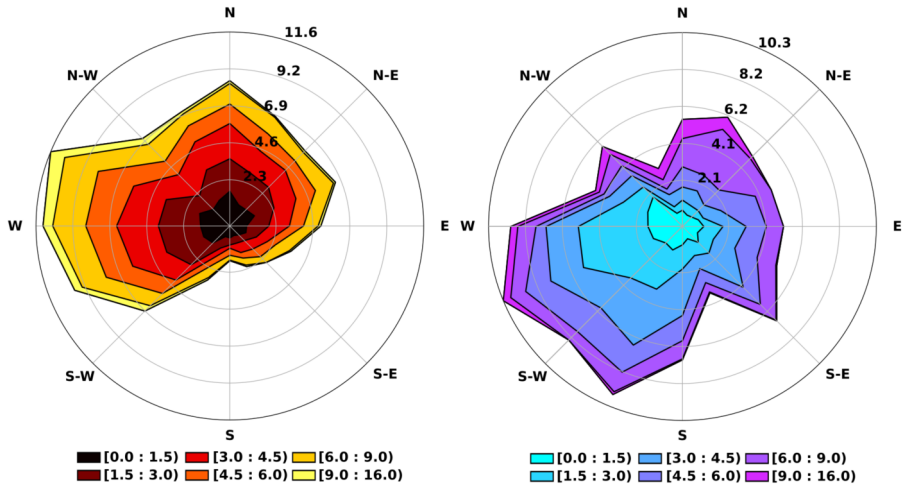

Figure 5.8: Windrose infilled representation of the tmy meteorological file during the cooling (left) and heating (right) period.

5.3.3 Generated numerical mock-ups

5.3.3.1 Solar mesh

The calculations of solar irradiance have been performed in a fine triangulated mesh. The district is composed of 2197 surfaces. For the generation of the solar mesh, only the solar exposed boundaries were employed, resulting in a total number of 1481 surfaces. The mesh has been refined by splitting into 16821 triangles, as shown in Figure: 5.9. For building roofs, a characteristic division length of 10 m is preferred, while it is halved to 5 m for the rest of horizontal elements and building walls. This option was chosen for improving computational efficiency because most of the roofs have an even height. Hence, it is unnecessary to subdivide them into finer facets. The generated mask file enumerates 270 faces, taking into account only vertical elements, including urban vegetation.

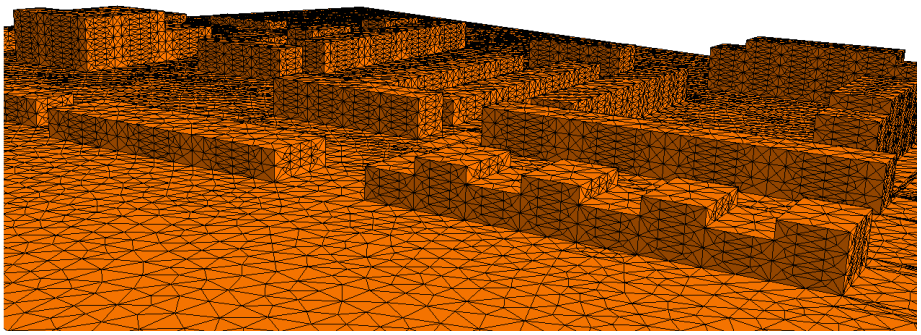

Figure 5.9: 3-D Visualization of the generated triangulated surface mock-up.

5.3.3.2 Airflow mesh

The generated airflow computational grid is based on a hexahedral staggered grid, composed of cubes of 1(dx) x 1(dy) x 3(dz) m. The final grid domain is set at 457 x 456 x 27 m, at each axis respectively leading to 5.626.584 calculation points, as shown in Figure: 5.10. The calculations

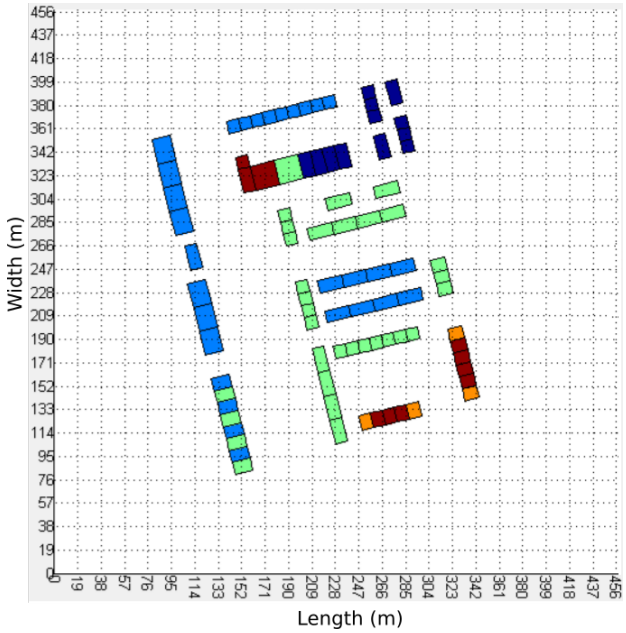

Figure 5.10: Visualization of the airflow structural grid.

have been performed for 36 wind directions given a reference value of 3 m/s. In a further step, the extracted outcomes for both wind speed and direction were adapted according to the meteorological data.

5.3.3.3 Zonal mesh

The aforementioned sub-meshes have been integrated into a final zonal mesh. The last consists of 5112 air cells divided into 6 horizontal layers. The upper boundary is at 18 m, expanded by one layer (3 m) over the highest building. Each layer consists of 852 air cells, in

contact with the ground and the building surfaces. Those air cells constitute the urban canopy. The air cells in contact with the thermal zones are forced to have similar dimensions with the adjacent roofs or walls (Figure: 5.11), representing a hexahedral shape. The rest of the canopy cells were meshed based on the Delaunay algorithm given a characteristic length of 10 m.

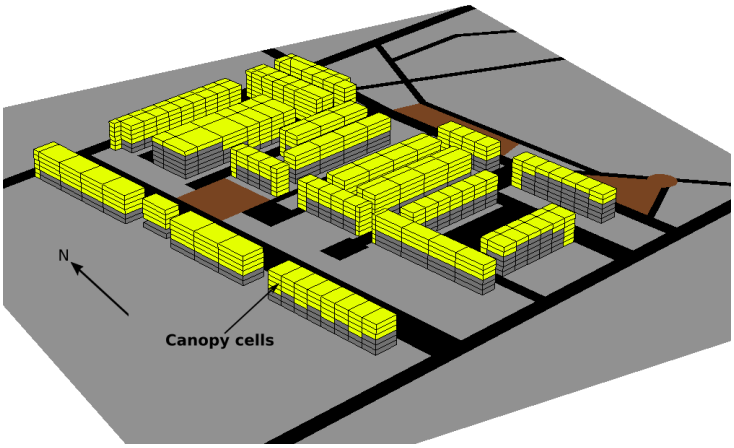

Figure 5.11: 3-D visualisation of the zonal mesh for a part of the air cells (yellow boxes) in contact with building elements.

5.3.3.4 District energy network characteristics

The district energy network consists of a steady-state[2] network model in which thermal and hydraulic phenomena are considered. In order to calculate the temperature inside the tubes, the thermal losses to the ground are taken into account, depending on tube diameters, thermal insulation, and ground temperature.

The network path has been generated using road footprints from the imported SketchUp file, considering that the tubes circuit is constructed below them. To do so, the middle points of each road segment have been used. The optimized network path has been realized with the methodology presented in section: 3.1.6.1. In addition, each building has been equipped with a local substation, providing heat to the different thermal zones. The building substations, the calculation nodes, and the network's path are depicted in Figure 5.12, while Table: 5.8 provides their characteristics. The piping circuit composes of copper-based tubes enhanced with polyethylene high-density insulation ($\lambda = 0.028$ [W/mK]). The energy hub corresponds to an ideal central generator applied both for cooling and heating period. The nominal heating and cooling supply temperatures have been set to 55°C and 12°C for the respective seasons.

Table 5.8: Characteristics of the implemented DEN.

DES	Model	# Nodes	Length (m)	# B. Substations
Network	Steady-State	164	3387.0	87

[2]see: section 3.1.6.2

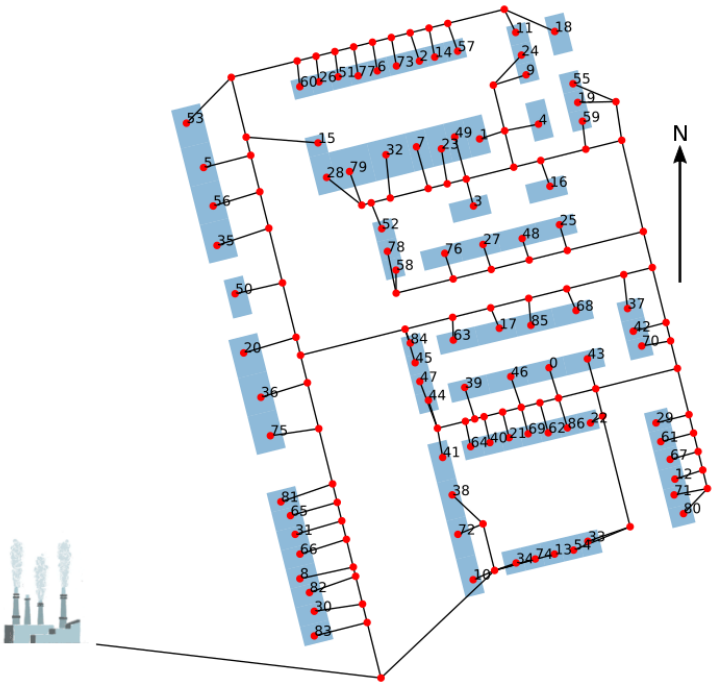

Figure 5.12: Visualization of the generated DEN.

5.4 Simulation Results

In this section, the simulation outcomes of the implemented scenarios are presented, divided into two main categories; the energy and the microclimate assessment. The energy analysis is subdivided initially at two different scales, the zone and the building level in which the data are obtained from local substations, while further district level comparative outcomes are provided including the network's thermal losses. The energy analysis is based on cumulative frequency diagrams at zone level and 3-D visualization images of the absolute values for individual buildings. In addition, comparative 3-D plots quantify the absolute and relative differences at various scales. The microclimate assessment is based on the CDH (cooling degree hours) and HDH (heating degree hours) indicators, by speculating an outdoor thermal comfort temperature of 26 ^{o}C and 19 ^{o}C during the cooling and heating periods respectively. In parallel, 3-D visualization images of several microclimate parameters are provided, as well as comparative results between the implemented scenarios.

5.4.1 Base Scenario

5.4.1.1 Energy Analysis

Zone level: we present in this section the simulation outcomes for the energy demand of the district at the zone level under the basic meteorological scenario. In Figure: 5.13, the cumulative frequency of annual heating loads is depicted for every thermal zone of the district. The diagram can be analysed in two main parts, the part corresponding to well-insulated buildings (85% of the building stock) and the rest of it (15%) in which the poorly insulated ones are depicted. As we can observe, the well-insulated buildings present a minimum of heating needs

at around 14.8 kWh/m^2, while the corresponding maximum reaches approximately the value of 76.1 kWh/m^2, depending on the characteristics of each thermal zone. The respective extreme values when the DHN (district heating network) is considered, are almost equal, exhibiting minimum and maximum values of 14.7 kWh/m^2 and 75.5 kWh/m^2 respectively, showing the small deviations of zone's thermal performance during the heating period, when the impact of the rejected flux in the local environment is not considered. These maximum values can be char-

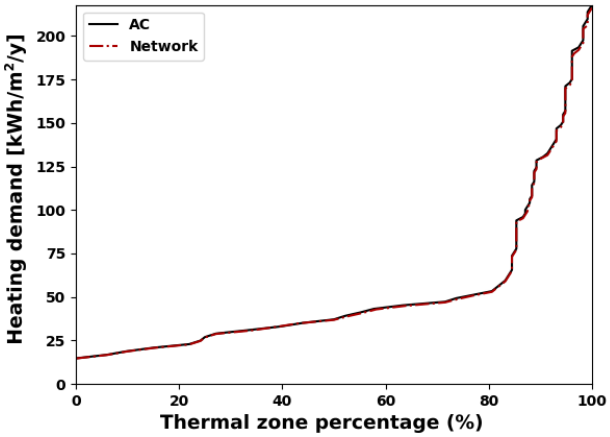

Figure 5.13: Cumulative frequency of energy demand at zone level during the heating period for the standard scenario.

acterized as the turning point of the diagram, as both slopes are increasing rapidly after them. The annual heating needs for poor-insulated buildings are exacerbated up to 217.8 kWh/m^2 for the AC case and 216.1 kWh/m^2 for the network one, presenting almost four times higher heating needs than the well-insulated ones. The observed variations between thermal zones of similar insulation capacity lie on the specific characteristics of each zone, such as incident solar radiation, orientation, and their respective position inside the district.

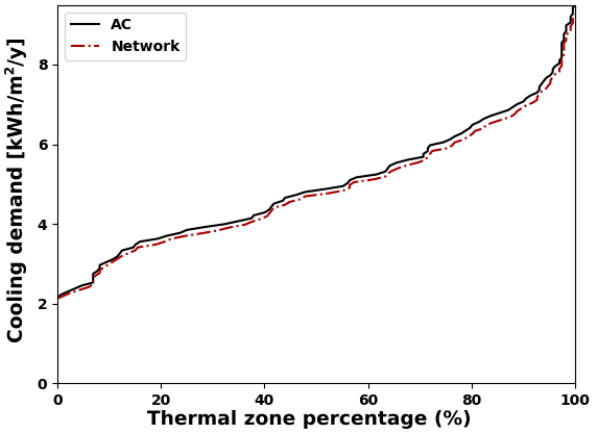

Figure 5.14: Cumulative frequency of energy demand at zone level during the cooling period for the standard scenario.

Similar behavior can be found during the cooling period, however, the curves are increasing progressively during this period, due to the actual low cooling needs of the district under this

scenario. For the AC_Std scenario, the annual cooling needs of the well-insulated buildings range between 2.2 kWh/m^2 and 6.7 kWh/m^2 while for the poor ones, the cooling needs range between 6.7 kWh/m^2 and 9.5 kWh/m^2. The respective outcomes of the DEN_Std scenario are 2.1 kWh/m^2 and 6.6 kWh/m^2 for the well-insulated buildings, while for the poor-insulated ones they are slightly decreased, ranging from 6.6 kWh/m^2 to 9.3 kWh/m^2.

Building level: at the building level, the outcomes of the building substations have been compared and visualized between the two tested scenarios, pointing emphasis to the cooling needs. This option is selected due to the limited differences during the heating period between the two scenarios, as has been shown already from the zonal comparison. We must notice that the building division is established vertically. Figure: 5.15 visualizes the absolute values per building for the AC_Std scenario. The minimum cooling loads occur at single-zone buildings and the maximum ones to the 15m building blocks. Moreover, the buildings consisting of façades oriented towards the south-western direction present higher cooling needs compared to others with similar characteristics (insulation level), due to the increased transmitted solar gains through windows. The annual minimum cooling demand is 3.26 kWh/m^2 while the maximum corresponds to 31.3 kWh/m^2.

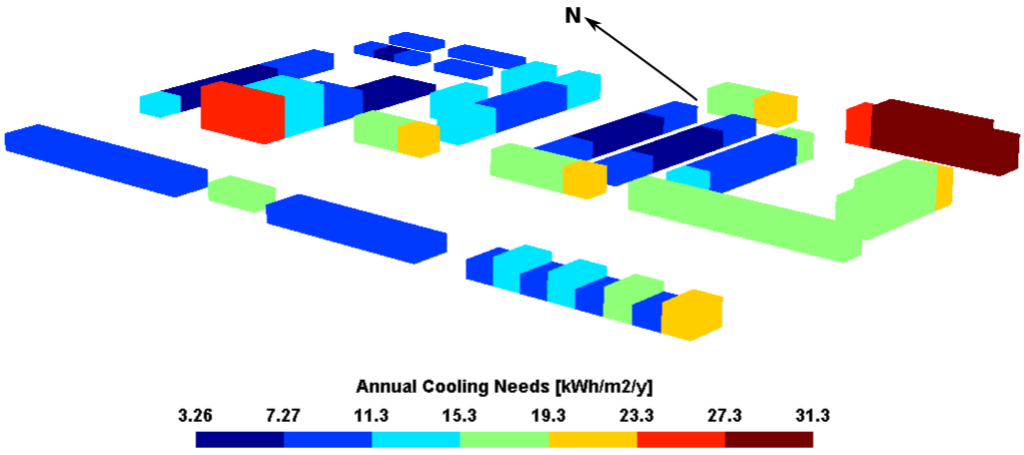

Figure 5.15: 3-D visualization of cooling needs per building for the AC_std scenario.

As expected, the DEN_std scenario presents lower values of cooling needs, as the rejected flux from the AC units is eliminated. Figure: 5.16, shows the respective accumulated outcomes per building. The minimum cooling needs are 3.13 kWh/m^2 and the maximum ones 30.7kWh/m^2, following the similar thermal behavior with the AC_std scenario. Depending on the number of zones, the cooling load difference ranges from 0.14 kWh/m^2 to 0.72 kWh/m^2. In general, the maximum absolute difference is due to:

- The amount of exposed surfaces per building
- The formation of the district and the respective position of each building inside it.

As an example, the continuous mid-rise blocks in the middle of the district are blocked from the west from a neighboring building, and their formation corresponds to a characteristic example of a canyon geometry. The dominant west winds during the cooling period are blocked and the

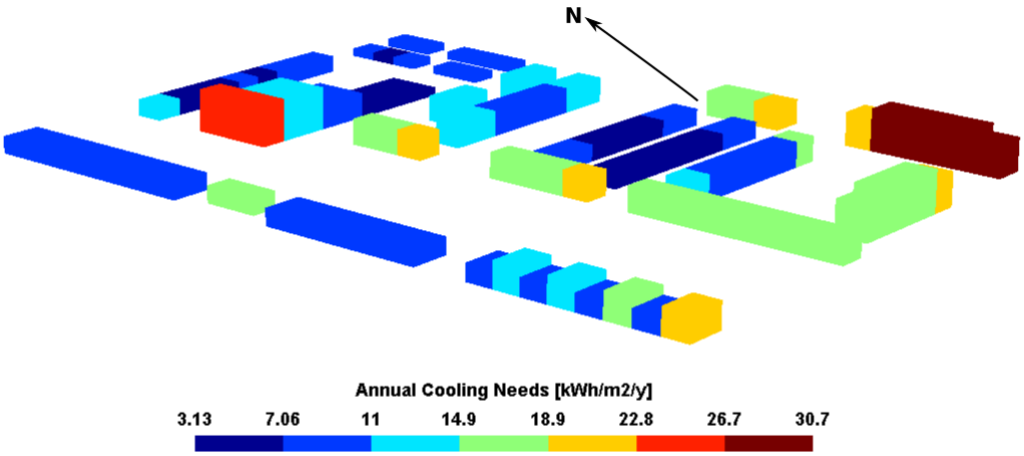

Figure 5.16: 3-D visualization of cooling needs per building for the DEN_std scenario.

rejected flux from the AC units is trapped at this point, transforming it to a hot spot. This is proven from Figure:5.17. In this image, we visualize the relative difference per building be-

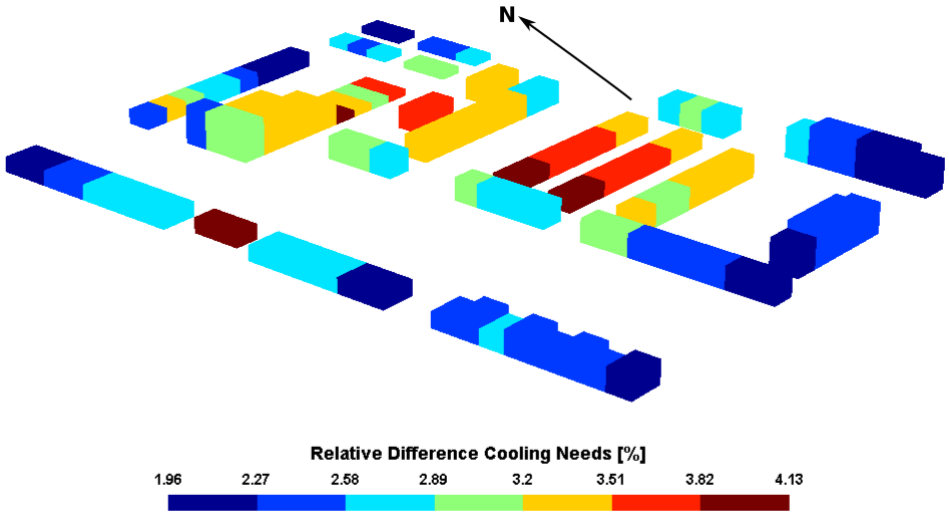

Figure 5.17: 3-D visualization of the relative difference in cooling needs per building for the implemented scenarios.

tween the implemented scenarios. The dark red color depicts the maximum relative difference in cooling needs. Two more buildings exhibit significant deviations apart of the already mentioned canyon formation. The first one is located at the western borders of the district, receiving the rejected flux from the neighboring building blocks, while the second one is a poor-insulated single-zone apartment. The latter, presents a higher deviation on cooling loads because its thermal behavior is mainly influenced by convective exchanges, as the presence of the tall building next to it leads to limited solar gains (Fig: 5.18) and air-circulation (Fig: 5.20) in the referenced one. Thus, the rejected flux from the adjacent block increases locally the air temperature and the respective cooling demand.

5.4.1.2 Microclimate Analysis

In this section, we present the microclimate analysis based on the simulation outcomes of the basic meteorological scenario. In Figure: 5.18, we plot the accumulated total incident irradiance at each surface of the district during the cooling period. In the upper part of the figure the building façades facing the north-east direction are plotted, while the lower part depicts the south-western oriented ones. The maximum incident solar irradiance is 709 kWh/m^2 found on roofs and horizontal surfaces of the outdoor environment, while the south-western façades receive a heat flux ranging from 615 kWh/m^2 to 709 kWh/m^2. On the contrary, the north-

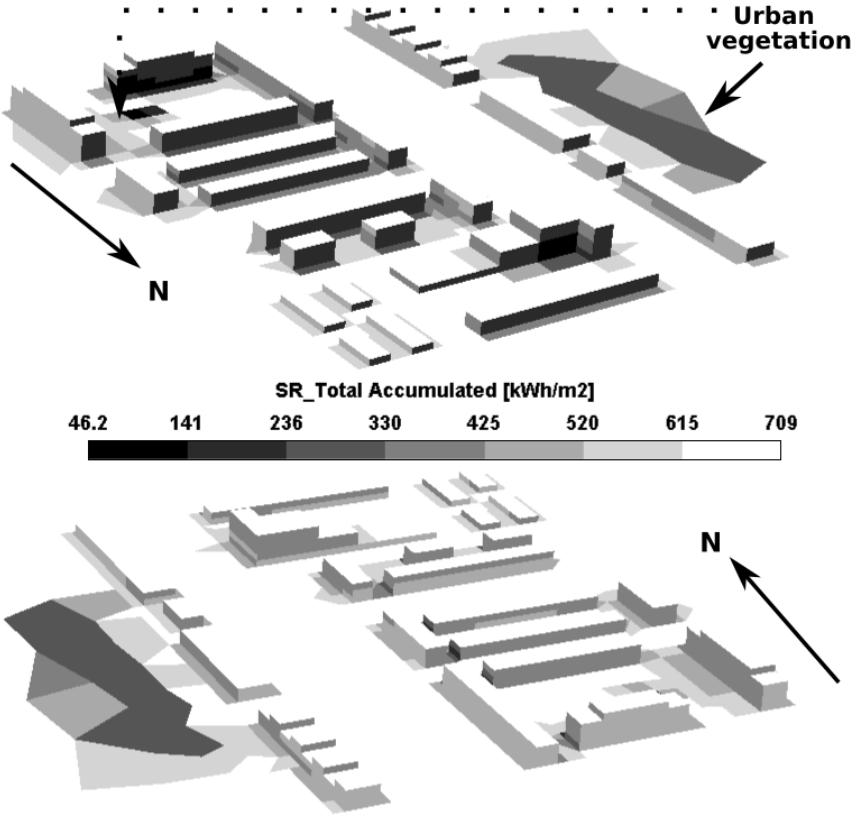

Figure 5.18: 3-D visualization of the accumulated incident solar irradiance for the std scenario during the cooling period.

oriented façades receive a lower amount of the incident solar irradiance, ranging from 141 kWh/m^2 to 236 kWh/m^2 depending on their height and their specific location inside the district. A small ratio of building surfaces is shadowed by neighboring obstacles, presenting the smallest amount of received solar gains which are in between 46.2 kWh/m^2 and 141 kWh/m^2. It is evident on the diagram the impact of urban vegetation on the incident solar irradiance. As pointed in Figure: 5.18, the impact of urban greenery can reduce solar exposure by almost a factor of three. We must mention that the plotted outputs incorporate also the incident reflected component on every surface. The latter can explain some small differences in the surfaces of the same buildings that are characterized by a different color scale. This is due to the different view factors of each sub-surface.

Further on, Figure: 5.19 shows the impact of the rejected flux on the local environment,

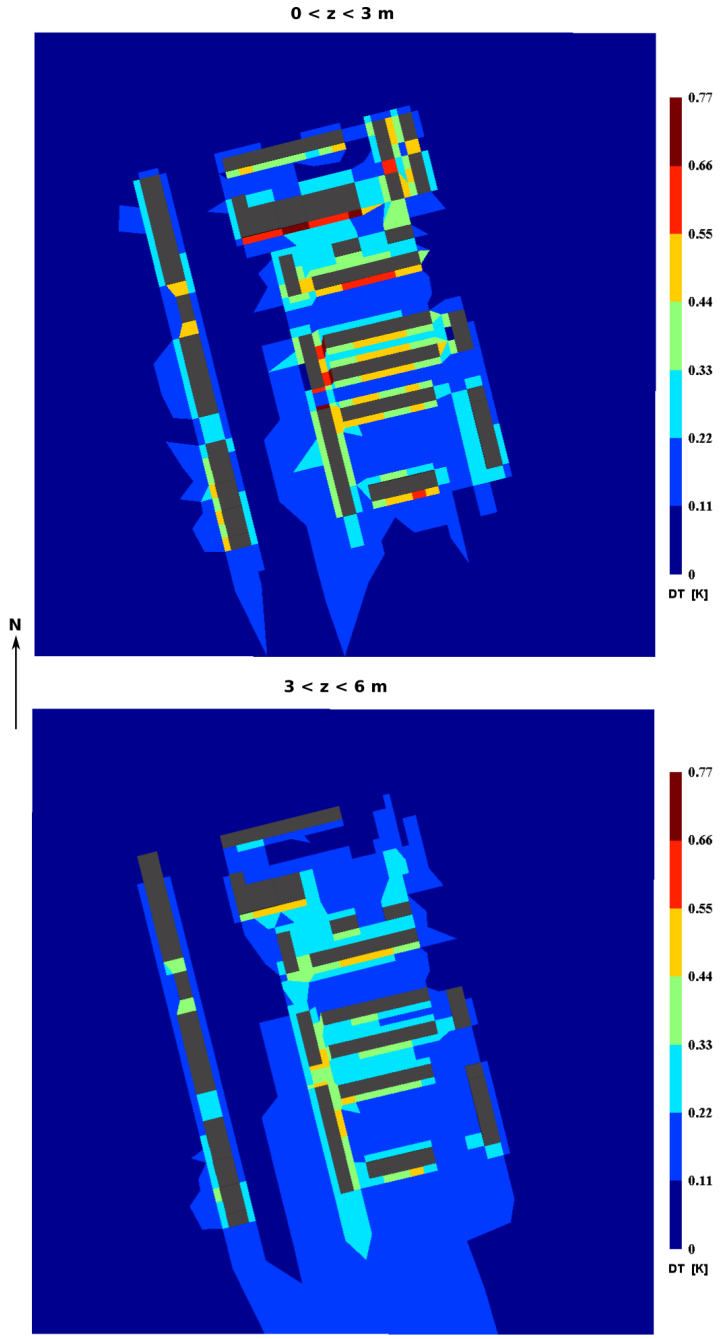

Figure 5.19: 3-D visualization of the air temperature difference [K] between the AC_Std and the DEN_Std simulation scenarios for two horizontal canopy layers during the hottest time step of the meteorological file.

when the AC units are operating. The plot is based on the time step where the highest meteorological temperature is recorded[3]. As we can observe, the higher deviations occur at street canyon formations with values ranging from 0.4 K to approximately 0.8 K. These can be found at the air cells at the pedestrian level ($0 < z < 3$ m). These air cells, receive the rejected flux

[3] see Section: 5.3.2

of the AC units as well as heat fluxes from the road and building surfaces, and thus the impact on them is higher. At this time step the meteorological temperature is 31.9 ^{o}C and the wind speed is 1.3 m/s coming from the north (36^o). The maximum impact of the AC units is recorded four hours later, at 8:00 pm, and the corresponding deviation reaches the 1.8^{o}C. The wind speed from the meteorological file corresponds to 0.7 m/s and has a northern direction too (3^o). The corresponding meteorological temperature is 29.3 ^{o}C.

In Figure: 5.20 we plot the streamlines and the wind velocity contour at the pedestrian level for a referenced wind speed (4.2 m/s) and wind direction (292^o). The values comply with the windrose diagram presented in section: 5.3.2 and represent the average wind speed and dominant wind direction during the cooling period. This figure combined with Figure:5.18 can be used as a first step in order to identify the possible hot spots inside the district. In the left plot, it is evident the areas were the streamlines are diluted. The reduced wind circulation

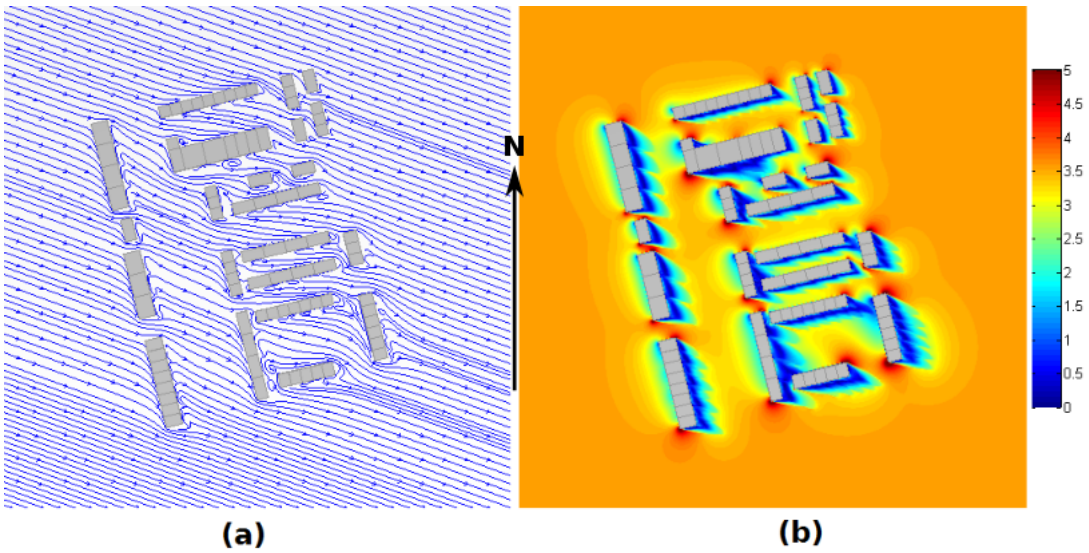

Figure 5.20: Visualization of streamlines (a) and wind speed contour (b) for the dominant wind direction and the average wind velocity of the meteorological file during the cooling period.

is depicted on the right side of the diagram with blue color, characterized by low wind speed values ($<$1m/s) in the lee side of the buildings.

Finally, in order to give an indirect estimation of the impact of the selected energy system on outdoor thermal comfort conditions, we calculate and visualize the difference in CDH for each outdoor air cell at the pedestrian level for the entire cooling period. The maximum difference is almost 58 CDH, found in the air cells in contact with buildings, as shown in Figure: 5.21. Most of the air cells, present a small difference deviating between 0 and 16.6, while the majority of cells that are adjacent to buildings present values between 16.6 and 24.9. Moreover, an effort to estimate the environmental footprint of the district is held. The average air temperature of all canopy cells is computed in order to evaluate the respective CDH and HDH of the district. The results are presented in Table: 5.9 and compared against the respective ones from the meteorological file. As we can see there is a slight difference between the two scenarios leading to a 2.8% increase of the CDH when the AC units are used against the centralized solution of the DEN. The same slight increase is also observed during the heating period. Notably,

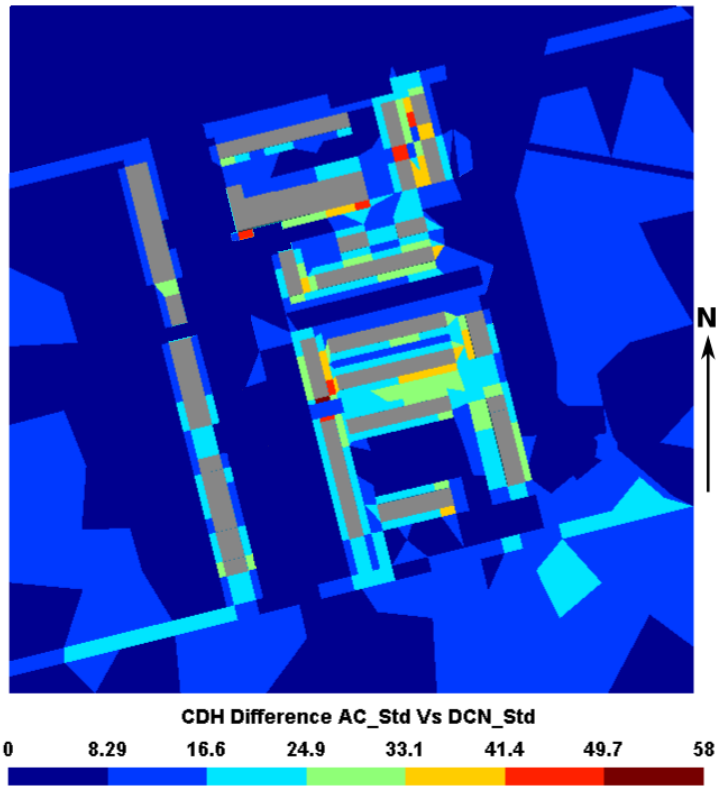

Figure 5.21: Visualization of the CDH difference between the AC_Std and DEN_Std simulation scenarios.

Table 5.9: Cooling and heating degree hours for the given base temperatures of the AC_Std and DEN_Std simulation scenarios. Coloured red: the reference meteorological ones.

Simulation scenario	**CDH (T_B=26°C)**		**HDH (T_B=19°C)**	
AC_Std	543	179	42384	45392
DEN_Std	528		42305	
Relative Difference [%]	**2.8**		**0.2**	

the deviation of the calculated ones with the respective meteorological outcomes is evident especially during the cooling period.

5.4.2 Extreme Scenario

5.4.2.1 Energy Analysis

Zone level: in this section, the simulation results are analysed at the zone level for the different implemented scenarios. We plot again, in Figure: 5.22 the cumulative frequency against the heating demand for every thermal zone of the district. As we can observe, the well-insulated buildings present a better thermal behavior than the poor-insulated ones, as the 85% of the stock exhibits heating needs ranging from 11.5 kWh/m^2 to 65.5 kWh/m^2 for the DEN_2050 scenario. In parallel, the respective outcomes of the AC_2050 are slightly increased, presenting

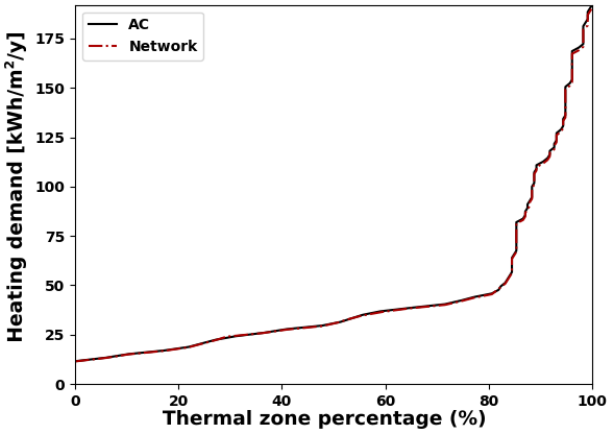

Figure 5.22: Cumulative frequency of energy demand at zone level during the heating period for the extreme scenario.

a minimum of 11.6 kWh/m^2 and a maximum of 66.1 kWh/m^2. Again, as in the base scenario, this local maximum represents the turning point of the diagram. The heating needs after it present a severe increase. The corresponding values for the poorly insulated thermal zones range from 65.5 kWh/m^2 to 190.5 kWh/m^2 and from 66.1 kWh/m^2 to 192.0 kWh/m^2 for the DEN_2050 and AC_2050 scenarios respectively.

The comparison between the standard and the projected meteorological files, shows a maximum decrease in heating needs of 25.8 kWh/m^2 for the poor-insulated buildings under the AC scenario, while for the network case the difference is slightly lower at 25.6 kWh/m^2. The maximum absolute difference for the well-insulated buildings is stable at 10 kWh/m^2 for both scenarios showing that the impact of the AC units is limited in that case.

On the contrary, the cooling needs present significant deviations between the tested scenarios. For the network case, the cooling demand of the well-insulated buildings, varies from 4.9 to 11.3 kWh/m^2 when at the same time the variation for the AC case ranges from 5.3 kWh/m^2 to 12.2 kWh/m^2, as shown in Figure: 5.23. The general increase of the cooling needs shifts the

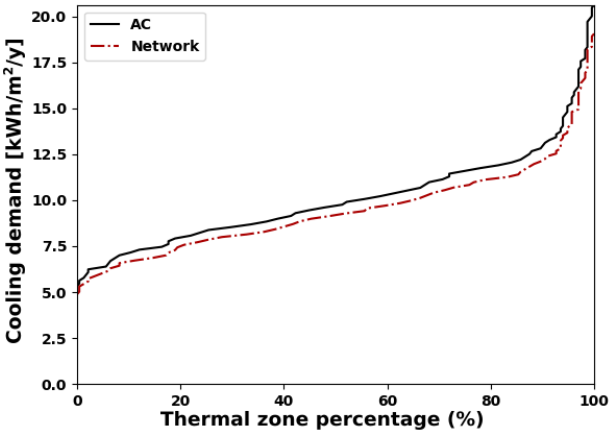

Figure 5.23: Cumulative frequency of energy demand at zone level during the cooling period for the extreme scenario.

turning point of the curve by almost 5 kWh/m^2 compared to the base case, leading to higher cooling demand the poorly insulated buildings. The respective maximum corresponds to 19.0 kWh/m^2 and 20.6 kWh/m^2 for the DEN_2050 and the AC_2050 scenarios respectively. The maximum relative difference between the AC_2050 and the DCN_2050 scenarios corresponds to 7.8%, showing the impact of the rejected heat flux to cooling energy demand. The sensitivity of poorly insulated buildings to outdoor conditions is confirmed both from relative and absolute difference analysis. The increased cooling needs are causing additional rejected heat in the local environment and its feedback affects the energy demand.

Notably, we can observe that the cooling needs are almost doubled in the extreme weather conditions compared to the standard. More in detail, the poorly insulated buildings present a relative increase of 53.8% and 51.5% for the AC_2050 and DEN_2050 scenarios respectively, while for the well-insulated ones the respective values are 45.1% and 41.5%. We can conclude that the usage of the local individual system will increase the environmental footprint and the cooling demand against the district energy solution regardless of the building type.

Building level: the building level analysis is held for the cooling period since the outcomes of the zone level analysis confirm once more that the impact of the energy system solution to building energy demand is more intense during this period. More in detail, for the AC_2050 scenario the minimum value corresponds to 10.1 kWh/m^2 and the maximum to 53.4 kWh/m^2 (Figure: 5.24), presenting a similar behavior per building as the previous simulated scenario. The DEN_2050 scenario presents extreme values of 9.1 kWh/m^2 and 51.0 kWh/m^2 for the minimum and the maximum respectively, as shown in Figure:5.25. This is also in accordance with the thermal outputs per building presented in the standard simulation scenario and can be explained from the fact that the implemented model is strongly dependent on the boundary wind speed and direction parameters. The projected meteorological file remains almost similar for these parameters, nevertheless, the dry bulb temperature presents strong deviations.

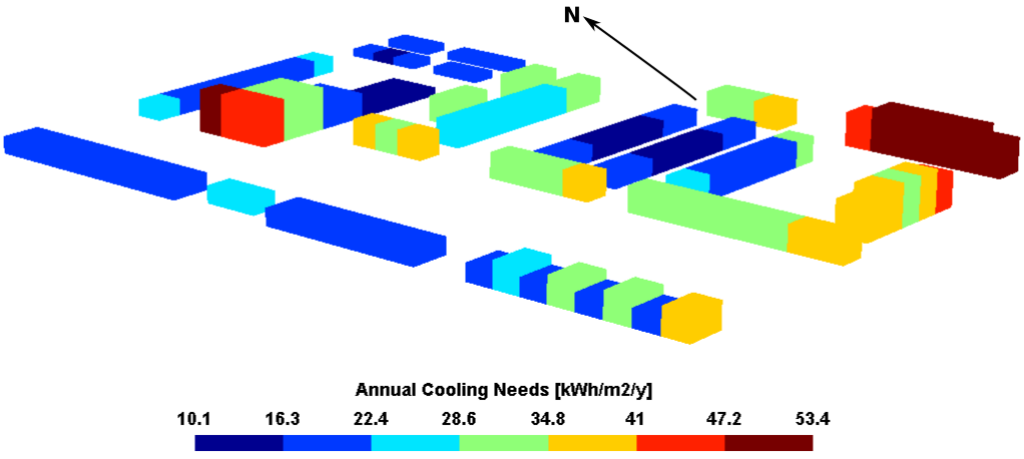

Figure 5.24: 3-D visualization of cooling needs per building for the AC_2050 scenario.

At first glance, we can observe that the cooling needs range is reduced by 1.4 kWh/m^2 in the DEN_2050 scenario, showing a more compact behavior of the neighborhood thermal response. Furthermore, although the minimum cooling needs diverge by 1.0 kWh/m^2, the maximum difference reaches the value of 2.4 kWh/m^2. In parallel, the minimum absolute difference between

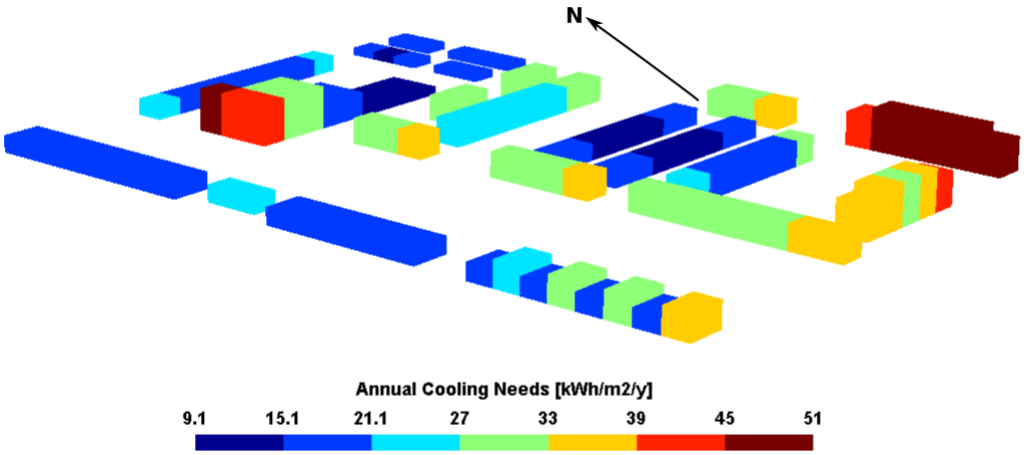

Figure 5.25: 3-D visualization of cooling needs per building for the DEN_2050 scenario.

the different climate scenarios is approximately 0.8 kWh/m^2, while the maximum one is almost 2.9 kWh/m^2, presenting deviations between the extreme meteorological file and the standard one of almost 86% and 75% respectively.

The relative difference between the implemented scenarios (AC_2050 and DEN_2050) is shown in Figure: 5.26. The poorly insulated buildings, present the highest relative difference on cooling loads, while for the well-insulated ones, the difference is higher in the lower albedo building blocks which are forming a canyon geometry. In parallel, the 15 m building block on the north part of the district is presenting also a significant absolute difference. According to Figure: 5.20 the southern part of this block has been evaluated as a hot spot during the cooling period, as the airflow at this point is very limited.

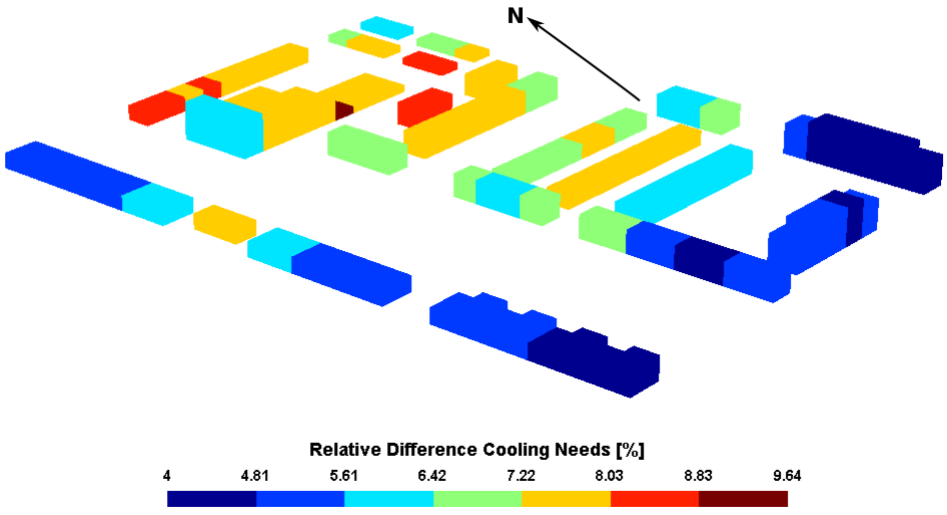

Figure 5.26: 3-D visualization of the relative difference on cooling needs per building for the implemented extreme scenarios.

Finally, comparing the outcomes of this extreme scenario (Figure: 5.26) with the respective ones of the standard meteorological file (Figure: 5.17), we can observe that both the minimum and maximum relative difference indexes are doubled showing once more the increased impact

of the local energy system under warmer conditions.

5.4.2.2 Microclimate Analysis

In this section, we present the microclimate analysis based on the outcomes of the simulation scenarios. The accumulated incident solar flux for the extreme scenario during the cooling period presents identical distribution with the standard scenario (Figure:5.18) but the range is changed. The minimum value correspond to 47.8 kWh/m^2 (increased by 1.6 kWh/m^2 compared to the standard meteorological scenario), while the maximum one ranges up to 732 kWh/m^2 (increased by 23 kWh/m^2).

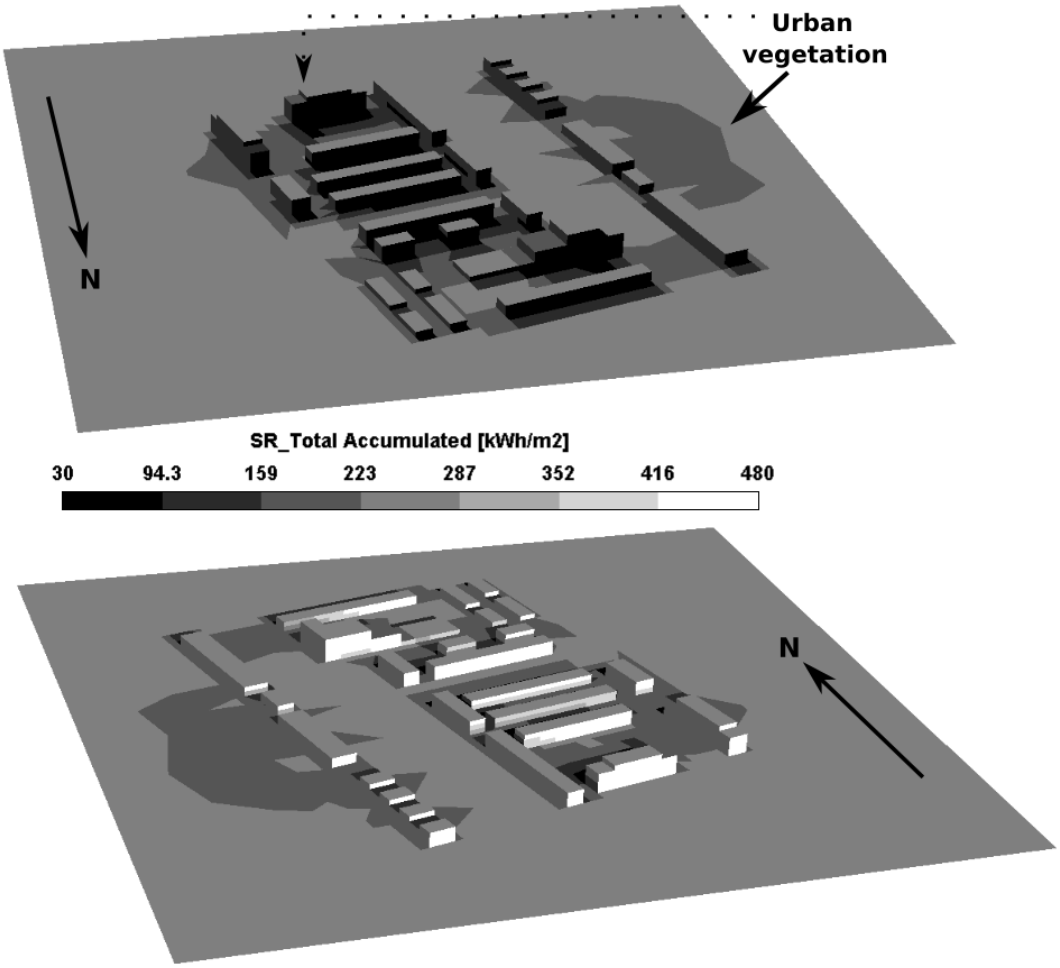

Figure 5.27: 3-D visualization of the accumulated incident solar flux for the extreme scenario during the cooling period.

On the contrary, in Figure: 5.27 we present the respective outcomes for the heating period, as we will need them in the following discussion. The accumulated incident solar flux for the extreme scenario during the heating period presents values ranging from 30 kWh/m^2 to 480 kWh/m^2. The northern façades receive the lowest amount of solar irradiance, ranging from 30 kWh/m^2 to 94.3 kWh/m^2 while the eastern ones receive an amount between 94.3 kWh/m^2 and 159.0 kWh/m^2. The western façades receive a higher amount found one step forward on the

value scales of Figure: 5.27. The roofs and the unshaded open space surfaces receive approximately an amount ranging from 223 kWh/m^2 to 287 kWh/m^2. The southern façades present a greater amount of received solar energy but also a lot of discrepancies due to shading effects of neighboring buildings. The maximum range varies between 416 kWh/m^2 and 480 kWh/m^2. The impact of the urban greenery is limited during the heating period as the selected trees are losing their leaves and thus the transmission factor used as input in the model is increased. Shaded surfaces from urban vegetation differ only by a scale range in Figure: 5.27, while for

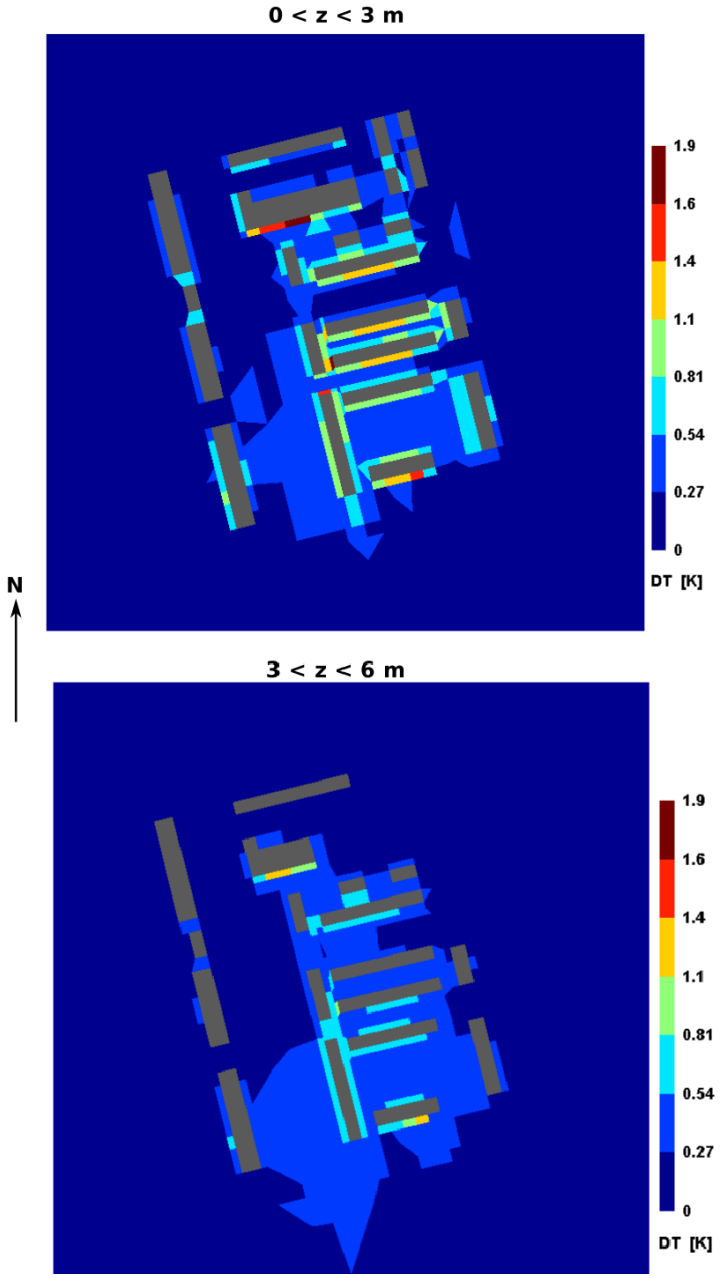

Figure 5.28: 3-D visualization of the air temperature difference [K] distribution between the AC_2050 and the DEN_2050 simulation scenarios for two horizontal canopy layers during the hottest time step of the meteorological file.

the cooling period this difference corresponds to a maximum of 5.

Additionally, Figure: 5.28 shows the impact of the rejected flux to the ambient environment when the AC units are considered as the cooling system, compared to the network implementation. Under extreme weather conditions the maximum air temperature difference during the highest recorded meteorological temperature reaches locally the 1.9 ^{o}C at pedestrian level. Most of the air cells around the district present a slight increase of around 0.27^{o}C, while those in the core of it present air temperature deviations ranging from 0.27^{o}C to 0.54^{o}C. Notably, the impact is more intense in the lee side of the buildings, considering that the wind direction is towards the south (Figure: 5.20). The maximum air temperature difference, occurs again four time steps later, presenting a local increase of 3.2^{o}C found in the air cells around the poor-insulated apartments.

The cooling degree hours difference for the implemented scenarios is depicted in Figure: 5.29. Evidently, the difference under the extreme weather conditions is more intense during the examined period presenting a maximum of 968 CDH. In the core of the district, the deviation presents values ranging between 276 and 543 CDH, while the majority of the air cells around it exhibits differences up to 276 CDH. Additionally, the air cells adjacent to roads, seem to be charged with a supplementary heat flux and thus they show higher variations.

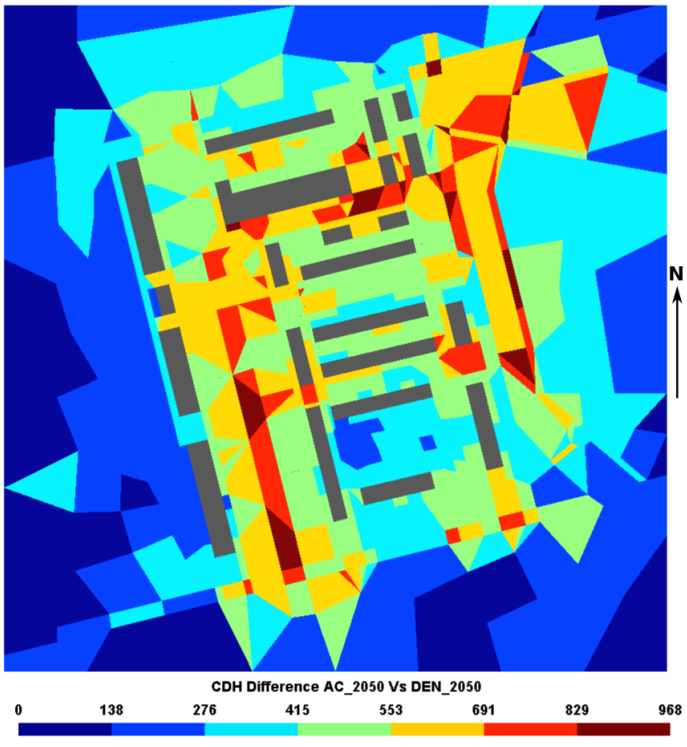

Figure 5.29: Visualization of the CDH difference between the AC_2050 and DEN_2050 simulation scenarios.

In general, the distribution of the differences is significantly extended around the core of the district compared to the basic meteorological conditions case (Figure: 5.21), where the deviations where sparsely distributed out of the neighborhood's core. Concerning the average canopy difference of the CDH and HDH indexes between the implemented scenarios, we can observe in Table: 5.10 a mean absolute difference of approximately 250 CDH and 63 HDH during the

cooling and heating periods respectively. In terms of relative difference, the cooling degree hours present a reduction of 13.2% in the DEN_2050 scenario compared to the AC_2050, while the heating degree hours present a tiny difference of 0.2%. At this time, the neighborhood total environmental footprint during the cooling period is more intense compared to the meteorological file outcomes (red signed), presenting an increased ratio of 50.6% in CDH. The respective increase ratio for the base scenario was 32.9%.

Table 5.10: Cooling and heating degree hours for the given base temperatures of the AC_2050 and DEN_2050 simulation scenarios. Coloured red: the reference meteorological ones.

Simulation scenario	**CDH (T_B=26°C)**		**HDH (T_B=19°C)**	
AC_2050	1879	952	36924	39661
DEN_2050	1631		36861	
Relative Difference [%]	**13.2**		**0.2**	

5.4.3 Extreme - Cool Scenario

5.4.3.1 Energy Analysis

Zone level: in this last scenario, the conventional surfaces are assumed to be replaced with highly reflective ones[4] both in building elements and outdoor space. To this end, the simulation results at the zone level are given in Figures: 5.30 and 5.31. The heating needs, are

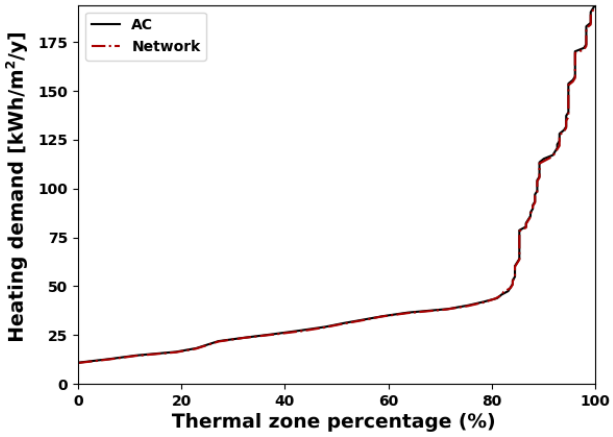

Figure 5.30: Cumulative frequency per zone during the heating period for the extreme cool scenario.

following a similar trend as the previously implemented scenarios, presenting small differences between the AC_2050_cool and DEN_2050_cool scenarios. The well-insulated buildings exhibiting a minimum value of 10.9 kWh/m^2 for the AC_2050_cool scenario, while the corresponding one for the DEN_2050_cool scenario is 10.7 kWh/m^2. The turning point of the curve is found at 54.8 kWh/m^2 and 54.4 kWh/m^2 for each scenario respectively. Eventually, the poor-insulated buildings present once more higher heating needs, approximating 194.0 kWh/m^2 for

[4]see Table: 5.5

the AC_2050_cool and 193 kWh/m^2 for the DEN_2050_cool scenarios. Surprisingly, the heating needs are lower than the ones presented in section: 5.4.2.1 representing the base scenario without the cool materials. This is an outcome that needs further investigation, as we expected the application of cool materials to increase the heating loads and decrease the cooling ones. To do so, the microclimate analysis will provide the necessary data to proceed with it.

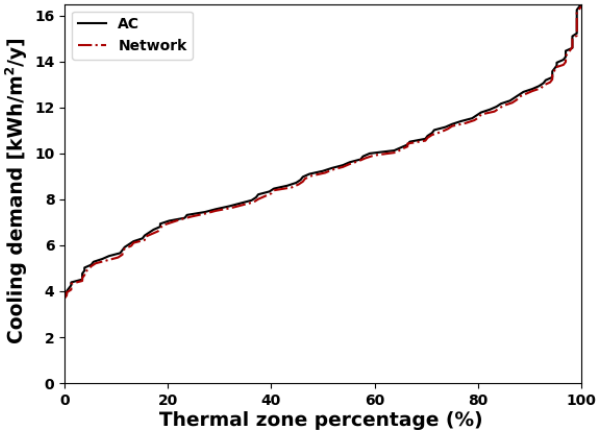

Figure 5.31: Cumulative frequency per zone during the cooling period for the extreme cool scenario.

On the contrary, the cooling needs are reduced compared to the base extreme scenario in most of the thermal zones, as expected. More in detail, the minimum cooling needs are presenting values of 3.8 kWh/m^2 and 3.7 kWh/m^2 corresponding to a reduction of 28.3% approximately 24.5% compared to the basic extreme case. The maximum values are found at 12.2 kWh/m^2 and 12.0 kWh/m^2.

Evidently, the reduction is more significant in the AC scenarios, as the rejected flux from the AC units is limited, and thus the outdoor environment is not overcharged. Moreover, the implementation of cool materials, leads the poor-insulated buildings to a much better thermal performance during the cooling period compared to the basic extreme case, while for the well-insulated buildings the thermal needs are lower but the reduction is much smaller. Nevertheless, a more precise inspection of Figure: 5.31, reveals a key observation. There is a small amount of zones that present a tiny increase in cooling loads. The accumulated data at the building level will point emphasis on this, given in the next section.

Building level: the building level analysis shows once more the differences in cooling needs at building level between the implemented scenarios. When the individual energy system is considered (Figure: 5.32), the minimum energy consumption corresponds to single-floor old apartments with values ranging from 4.8 kWh/m^2 to 11.9 kWh/m^2. In parallel, the maximum cooling needs are found in high rise buildings, ranging from 47.7 kWh/m^2 to 54.8 kWh/m^2. Similarly, the DEN_2050_cool scenario presents a minimum on cooling needs of 4.7 kWh/m^2 while the maximum corresponds to 54.4 kWh/m^2, as shown in Figure: 5.33. Evidently, the deviations between the two scenarios are limited, as the implementation of cool materials on building surfaces is minimizing the cooling needs for both scenarios, especially in the poor-insulated buildings. Thus, the rejected flux is not extensively distributed to the outdoor space and the effect of the increased air temperature is also limited.

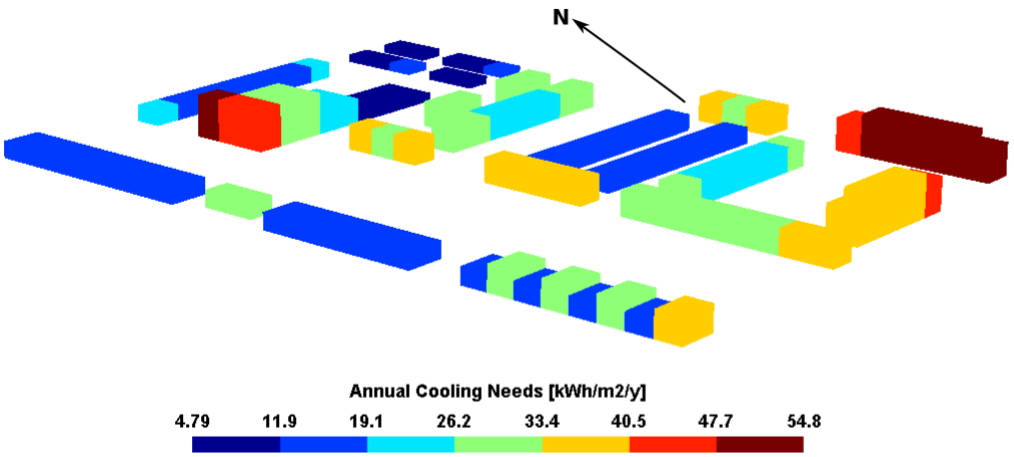

Figure 5.32: 3-D visualization of cooling needs per building for the AC_2050_cool scenario.

In terms of absolute values, the minimum difference (which approximates zero) is found on well-insulated two-floor buildings located on the west side of the district. The maximum absolute difference, corresponds to the poor-insulated buildings on the core of the district, ranging from 0.8 kWh/m^2 to 0.9 kWh/m^2. Obviously, the extreme absolute differences (max-min) do not correspond to the respective difference of the extreme values, but they are located inside the extreme value scales of Figures: 5.32 and 5.33. Figure: 5.34, presents the relative difference

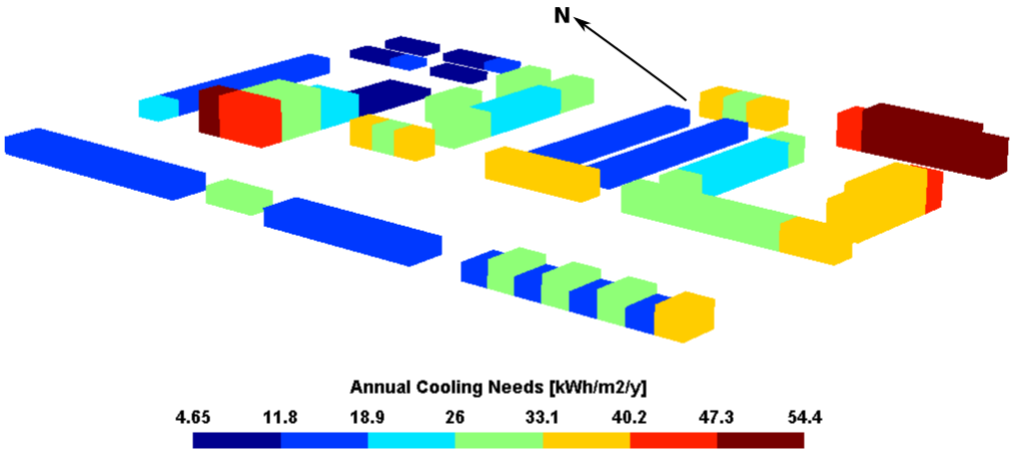

Figure 5.33: 3-D visualization of cooling needs per building for the DEN_2050_cool scenario.

between the implemented scenarios during the cooling period. As stated already, the poorly insulated buildings exhibit the highest relative difference with values ranging from 2.5% to 2.9%, while the minimum ones vary from 0% to 0.4%. Once more it is proven that the feedback of the rejected heat affects the poor-insulated buildings, as they are more sensitive to the outdoor conditions.

The thermal behavior of the buildings under the extensive cool scenario presents some inconsistencies that need to be further investigated. As a matter of fact, we can observe that the minimum building cooling demand is halved compared to the extreme basic scenario, but the maximum one has slightly increased. The poor-insulated buildings seem to benefit from the

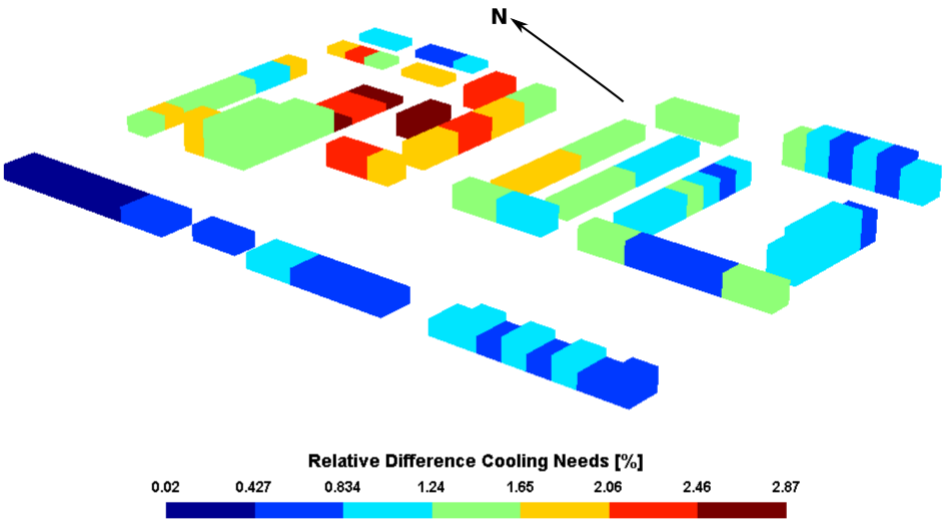

Figure 5.34: 3-D visualization of the relative difference on cooling needs per building for the implemented extreme cool scenarios.

implementation of cool materials, while at the same time the well-insulated ones are presenting slightly decreased thermal behavior, as depicted in Figure: 5.35. In the latter, the absolute and relative differences between the basic and the cool extreme scenarios under the utilisation of AC units are presented. As we can observe, the poorly insulated buildings with the installation of cool materials are saving almost 57% on cooling loads. This load reduction is a combination of:

- reduced surface temperature on building elements and thus reduced conductive heat flux through the skin of the building (Figure: 5.39),
- reduced ambient temperature and thus minimization of the bulk convective heat flux through the ventilation system, (Figure: 5.38)
- single-floors or maximum two-floor building footprints which are partly shaded from neighboring buildings,
- specific orientation combined with window position

On the other hand, the impact of cool materials application on well-insulated buildings is limited, ranging from 0.7% to 7% for the majority of them, whereas some of them present deviations up to 26%. The specific location inside the district and the amount of the incident solar irradiance are affecting their thermal behavior and leading to cooling demand alterations. As an example, the well-insulated building at the center of the southern part of the district consists of windows exposed to the south. In well insulated buildings, the impact of the ambient environment is reduced and thus, the respective impact of the cool materials application is balanced due to the increased solar gains and the increased transmitted heat flux through windows. This negative effect is partly balanced from the implemented temperature-based blind control during the cooling period.

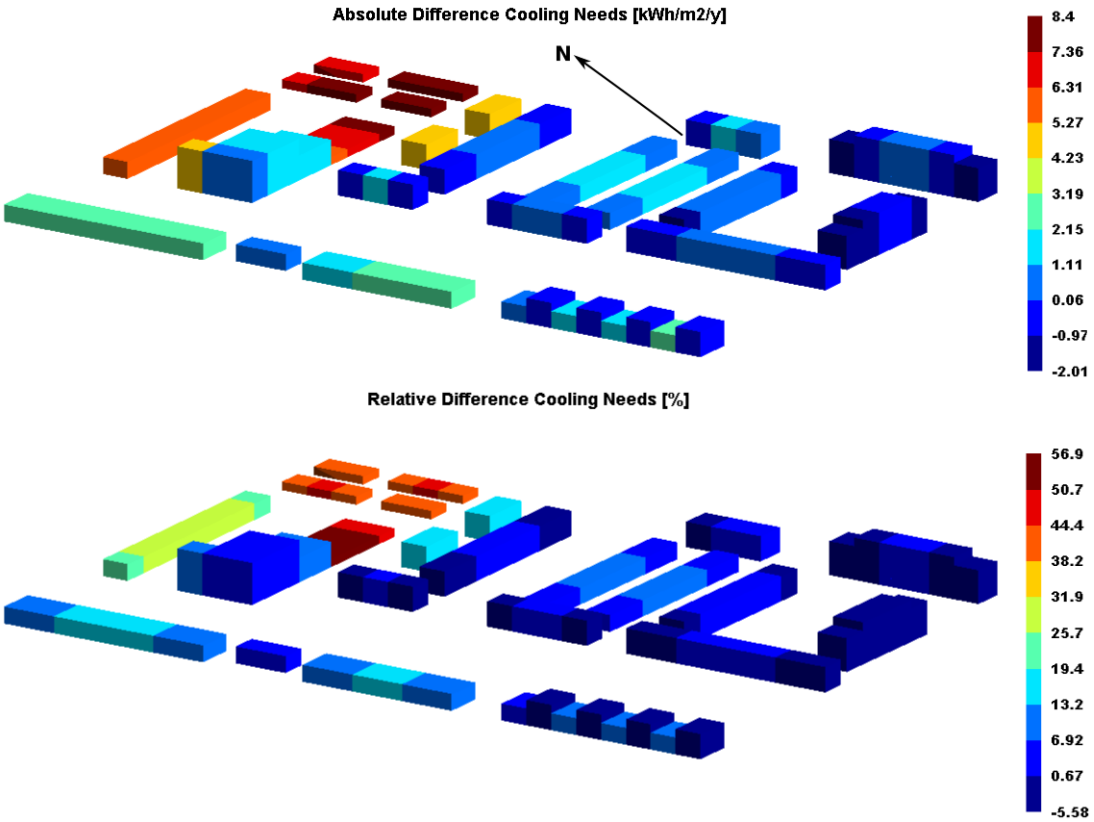

Figure 5.35: 3-D visualization of absolute and relative differences on cooling needs per building between the basic and the cool extreme scenarios.

5.4.3.2 Microclimate Analysis

In this section, the outcomes of the extreme cool simulation scenario are presented in terms of microclimate parameters. To this end, the accumulated incident solar flux for the extreme cool scenario during the cooling period presents a maximum value of 763 kWh/m^2, increased by 31 kWh/m^2 compared to the extreme basic scenario, found on roofs and horizontal surfaces of the outdoor space. The minimum value corresponds to 55.6 kWh/m^2 (increased by 7.8 kWh/m^2). The impact of urban vegetation can reduce the amount of incident solar flux by approximately 52%. In addition, wall elements shaded by neighboring buildings present a decrease of solar gains ranging from 22% to 36%. At the same time, the average reflected component is increased by almost 45%. As shown in Figure: 5.36 the reflected component is almost doubled in most of the building surfaces, especially for the first two floors of the well-insulated building in the center of the southern part of the district, explaining the small increase of cooling loads in the specific building.

In the same manner, the accumulated incident solar flux for the extreme cool scenario during the heating period exhibits a steady augmentation. The maximum value is 528 kWh/m^2, increased by 48 kWh/m^2 compared to the basic extreme scenario, while the minimum presents a value of 41.5 kWh/m^2 increased by 11.5 kWh/m^2. During the heating period, the southern walls receive the maximum solar gains. In parallel, the reflected radiation is steadily increased also during the heating period, as shown in Figure: 5.37. The inconsistencies found on the

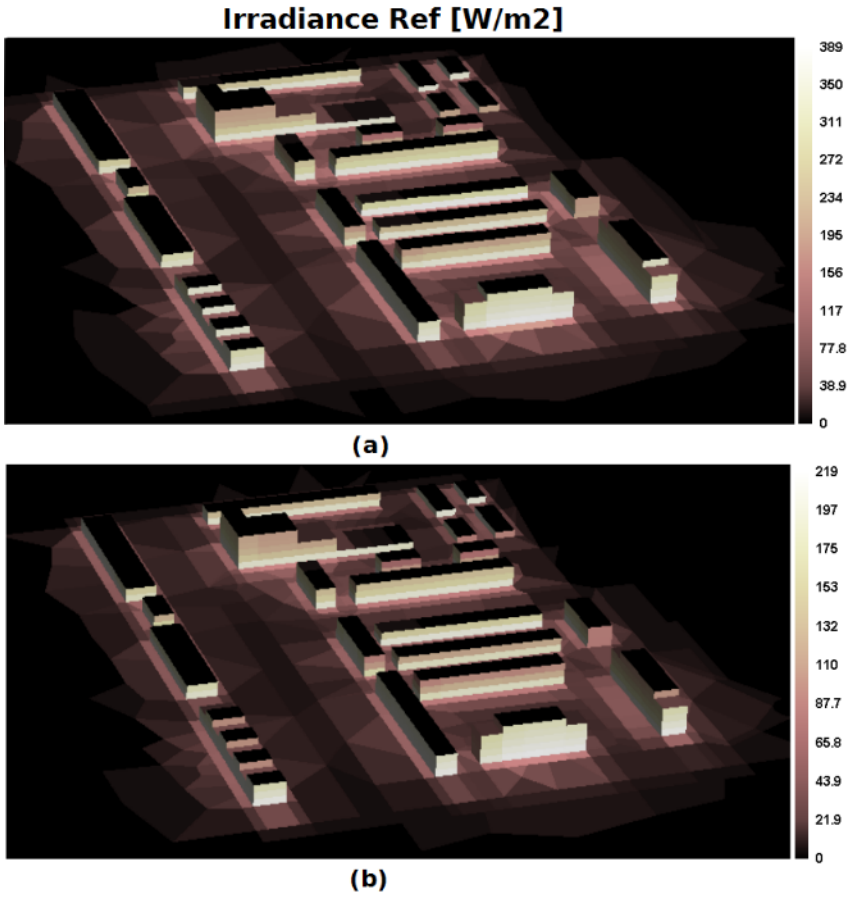

Figure 5.36: 3-D visualization of the maximum incident reflected radiation (a) cool and (b) basic extreme scenarios during the summer period of the south-western surfaces.

energy results of the previous section, can now be explained by the aforementioned analysis.

Moreover, the CDH and HDH indices do not present significant differences between the AC_2050_cool and DEN_2050_cool simulation scenarios. Table: 5.11 summarizes the results for the cooling and heating periods. As we can observe, the CDH index presents a small increase of approximately 1.6% when the AC units are considered against the district cooling network. In the same manner, the impact during the heating period is limited with a relative increase of 0.2% for the tested scenarios.

Apparently, the respective comparison between the basic extreme scenario and the cool extreme exhibits a significant difference on CDH, reaching an average on the entirety of the canopy cells of 560 degree hours (Table: 5.11). The latter is mainly observed in the first canopy layer ($0<z<3$) for the air cells adjacent to urban surfaces, as depicted in Figure: 5.38. At this level, the rejected flux of the systems combined with the thermal fluxes of low albedo roads and concrete side-walks, transfer added heat flux to the adjacent air cells and contribute to the observed intensity. In parallel, the air cells adjacent to roofs are also charged with added thermal. The modification of the albedo values under the cool scenario causes a significant reduction of CDH at these two canopy levels. The respective amount in terms of relative difference reaches 27.1%. On the contrary, during the heating period, an increase of 0.7% is observed on heating degree hours for the cool scenario, corresponding to an absolute deviation of 256 HDH.

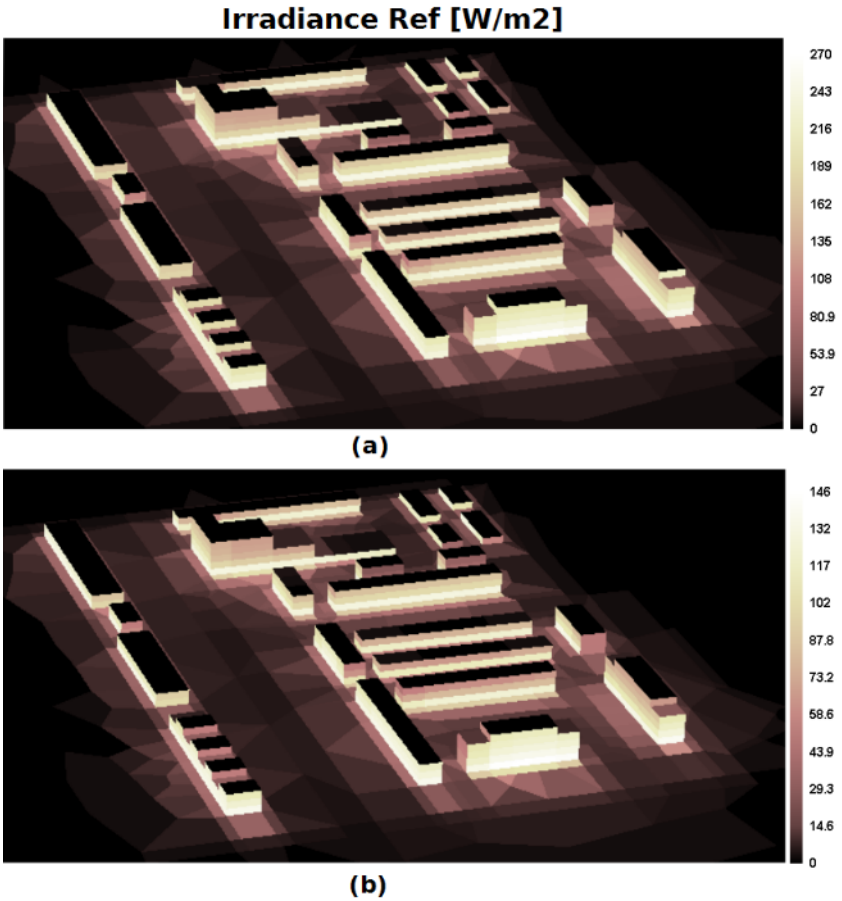

Figure 5.37: 3-D visualization of the maximum incident reflected radiation (a) cool and (b) basic extreme scenarios during the winter period of the south-western surfaces.

Table 5.11: Cooling and heating degree hours for the given base temperatures of the AC_2050_cool and DEN_2050_cool simulation scenarios. Coloured red: the reference meteorological ones.

Simulation scenario	**CDH (T_B=26°C)**		**HDH (T_B=19°C)**	
AC_2050_cool	1369	952	37168	39661
DEN_2050_cool	1347		37096	
Relative Difference [%]	**1.6**		**0.2**	
AC_2050	1879	-	36924	-
Relative Difference [%]	**27.1**		**-0.7**	

Finally, in Figure: 5.39, the surface temperature difference between the conventional and the highly reflected urban surfaces is shown. The plot corresponds to the hour of the maximum air temperature for the extreme scenario. The roofs of the well-insulated buildings present the maximum decrease reaching 18.9 K, as expected due to the higher albedo increase. The poor-insulated roofs present a respective decrease of the surface temperature of around 12.3 K while the urban surfaces present a variable decrease, ranging from 6.6 to 8.1 K in most of the cases. Regarding the temperature reduction on building walls, obviously, the south-western oriented

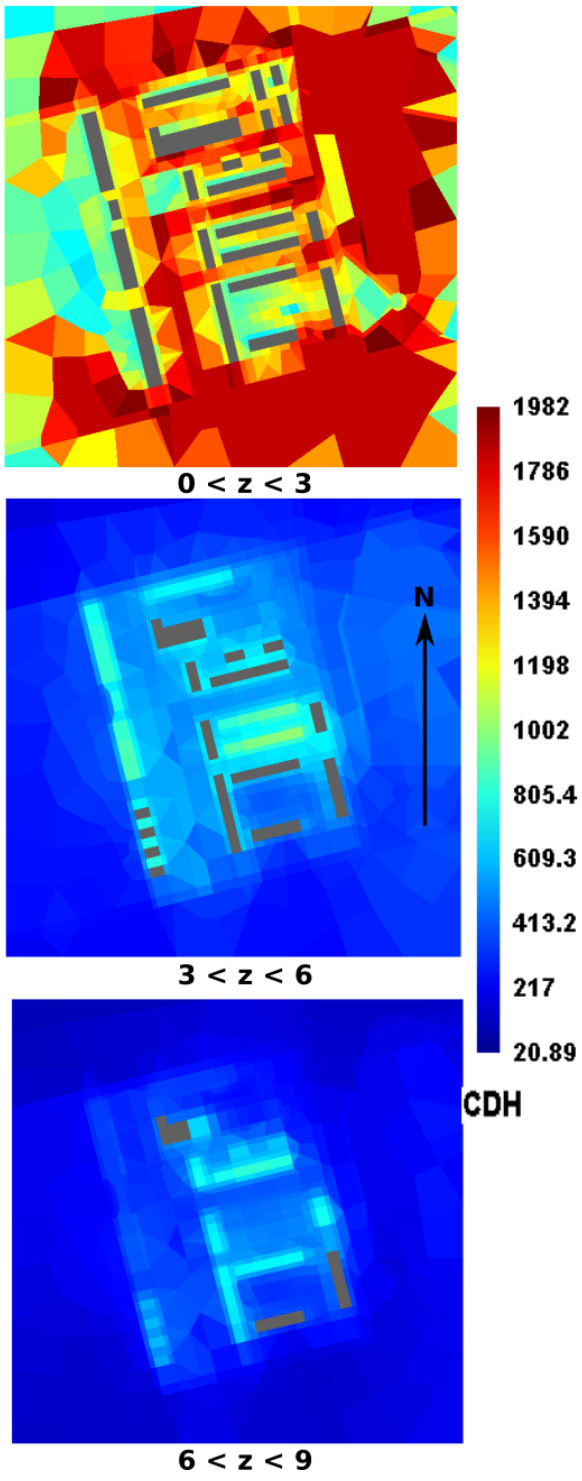

Figure 5.38: Visualization of the CDH difference between the AC_2050 and the AC_2050_cool simulation scenarios for various heights.

façades present the maximum surface temperature decrease, as during the referenced time-step the solar azimuth corresponds to 227.3^o. The respective surface temperature difference varies from 7.3 K to 8.2 K. For the rest of the walls, the impact of cool materials is slightly decreased

but still significant, ranging from 1.3 K to 4.7 K. The dark blue coloured areas of Figure: 5.39, correspond to soil surfaces, where the albedo was kept identical in all of the simulated scenarios and thus the difference is limited at around 0.3 K mainly due to the reduction of the air temperature in the area.

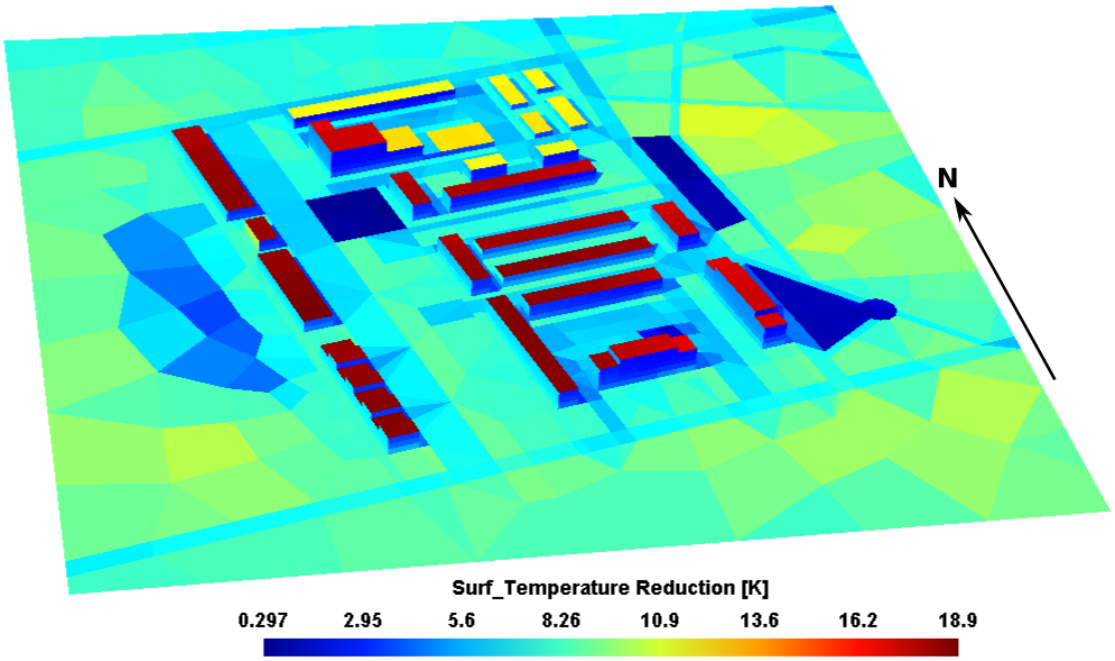

Figure 5.39: Visualization of the surface temperature difference between the conventional and the highly reflected urban surfaces during the maximum air temperature of the extreme scenario.

5.4.4 Comparative Results

5.4.4.1 District level

This section provides a comparative analysis of the simulated results at district level. Considering, a district energy network, the energy hub (district generator) provides usually chilled or hot water, through an insulated underground piping circuit. Nevertheless, inside the network configuration, an amount of energy is lost due to the thermal exchanges with the ground. This amount is strongly dependent on tube diameters, thermal insulation level of the tubes as well as fluid and ground temperature.

In this context, the final thermal outcomes of the district generator are compared against the respective accumulated outcomes of the local energy system installation. The total, heating, and cooling thermal demand of the district are plotted for the simulated scenarios in Figures: 5.40, 5.41, 5.42. The grey-coloured bars represent the standard meteorological file, while the red-coloured and blue-coloured represent the extreme and the extreme cool scenarios respectively. Moreover, the hatched bars represent the district energy network (DEN) outcomes, while the rest of them the AC units.

More in detail, the total district needs are higher under the standard simulation scenario, as shown in Figure: 5.40. This is due to the increased heating needs of the district, under the spe-

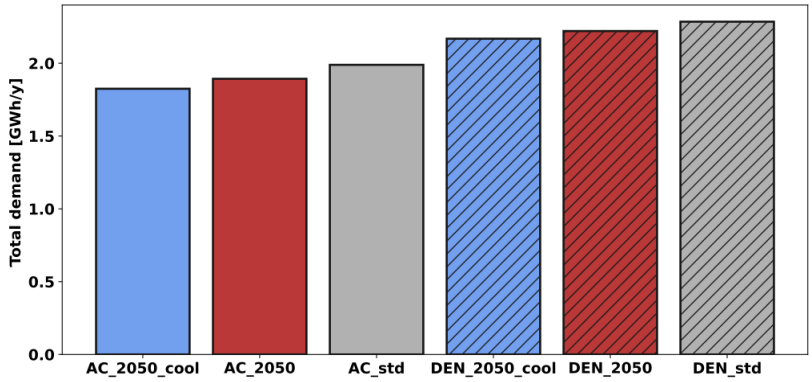

Figure 5.40: Bar plots of the total needs of the district for the implemented scenarios.

cific meteorological conditions. The DEN_std scenario presents the highest value, approximating the 2.3 GWh/y, increased by almost 13% compared to the AC_std scenario which exhibits total needs of almost 2.0 GWh/y. The DEN_2050 follows with a value of almost 2.2 GWh/y deviating by almost 14.8% from the AC_2050 scenario. The corresponding outcome of the last is 1.9 GWh/y. The minimum energy consumption is found at the AC_2050_cool scenario with a value of 1.82 GWh/y when at the same time the respective outcome of the DEN_2050_cool is 2.17 GWh/y increased by 15.85%. All of the cases are in agreement concerning the most energy-consuming scenario.

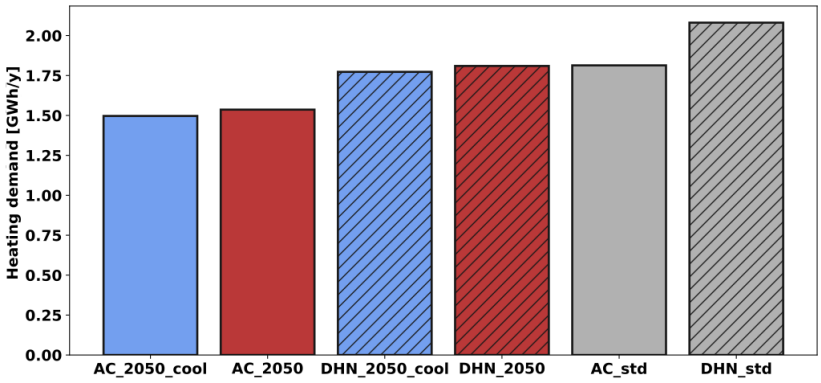

Figure 5.41: Bar plots of the heating needs of the district for the implemented scenarios.

In Figure: 5.41 the respective outcomes for the heating season are plotted. The general trend remains similar, as the network scenarios present always increased values compared to the AC ones. Obviously, the standard meteorological conditions present the maximum heating needs and thus the minimum relative difference between the two cases. More in detail, the district heating network, DHN_std scenario, presents the highest energy consumption with a value at around 2.1 GWh/y while the respective outcome for the AC_std is decreased by 14.1% reaching the 1.8 GWh/y. The heating needs are reduced for the standard extreme meteorological file, by 0.28 GWh/y and 0.27 GWh/y for the AC_2050 and DEN_2050 scenarios respectively. Notably, the energy penalty that we expected to see in the AC_2050_cool scenario during the heating period, is not observed, mainly due to the slightly reduced thermal needs of the well-insulated buildings caused by the highly increased transmitted heat flux through the windows. Other

factors that contributed to this were analysed in the previous sections.

Finally, during the cooling period, we can observe that the extreme meteorological conditions have almost doubled the cooling needs of the district compared to the normal meteorological file, as shown in Figure: 5.42. The DCN_2050 scenario presents the highest energy

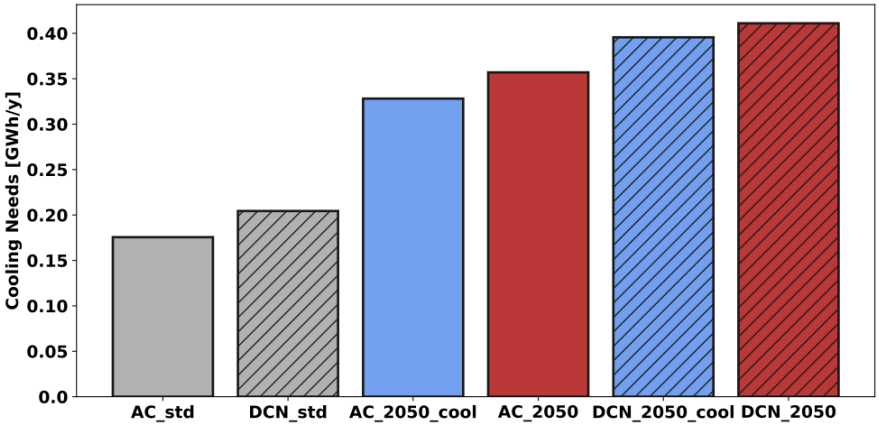

Figure 5.42: Bar plots of the cooling needs of the district for the implemented scenarios.

consumption with a value of 0.41 GWh/y when the AC_2050 scenario records 0.36 GWh/y, presenting a relative decrease of around 13.2%. At the same time, the DCN_2050_cool scenario exhibits cooling needs of approximately 0.4 GWh/y, when the AC_2050_cool is differentiated by 17.1% with a value of 0.33 GWh/y. Obviously, the implementation of cool materials reduces the energy consumption for cooling when the ACs are considered as the cooling providing system. On the contrary, the district network seems to be beneficial during the extreme scenario. The higher the cooling needs, the feedback of system's rejected heat is more intense and consequently the local energy demand is higher. In this case the cooling network prevents the generation of this added flux and contributes to mitigate the increased energy demand. However, the cooling network records higher cooling demand due to the energy penalty (losses) of the piping circuit.

Nevertheless, we demonstrated in Table: 5.10 the impact of the district network to outdoor thermal comfort conditions. In the presence of the cooling network, the index of cooling degree hours is reduced by almost 256 CDH. In order to employ another tangible proof that assures the aforementioned outcome, we calculate the average canopy temperature difference during the cooling period between the two scenarios and we correlate it with the respective energy penalty, defined as the difference of the accumulated cooling demand of the zones, including the ground losses for the network scenario, with the accumulated one including the rejected heat for the air conditioner scenario, as shown in Figure: 5.43. Under the extreme scenario, the energy network can effectively reduce the average canopy temperature during the cooling season by 0.2 K for an energy penalty of approximately 54 MWh/y. The concurrent implementation of cool materials and district cooling network tends to eliminate the potential benefit of it. In this case, the energy demand difference is increased due to the reduced energy needs in the AC scenario. Hence, the air temperature difference is limited at around 0.06 K. As a closing remark, we mention that the potential air temperature reduction from the installation of cool materials is almost doubled approximating the 0.4 K under the AC scenario.

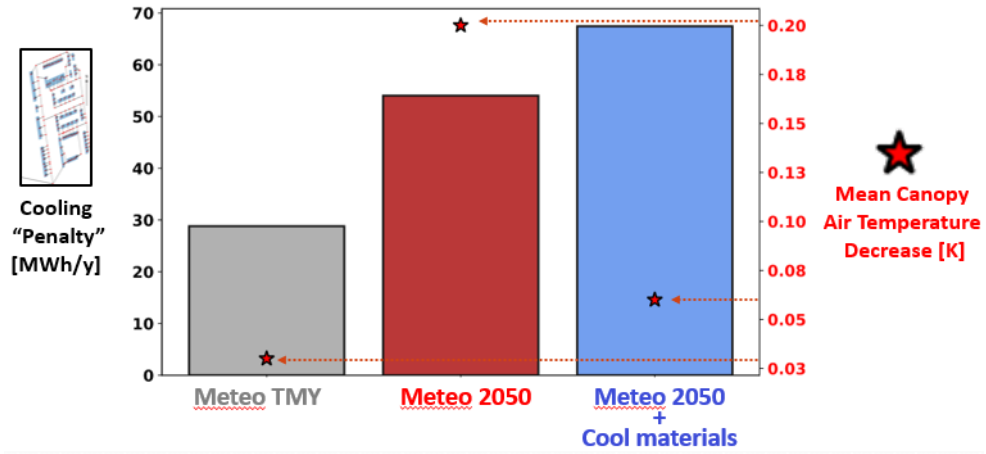

Figure 5.43: Bar plots of the cooling penalty of the district for the implemented scenarios. Red stars depict the canopy average air temperature difference.

5.5 Chapter Conclusions

In this last chapter, the developed simulation model has been used to study the thermal conditions of a district representing an area of 63800 m^2 in the city of La Rochelle. The neighborhood building stock corresponds to 87 mixed old and newly built apartments, divided into 232 thermal zones. Two main scenarios were examined in terms of building energy demand and outdoor thermal comfort. The first one considers an individual energy system at zone level and the second one a centralized energy network. Both scenarios were tested under different meteorological conditions.

Under standard meteorological conditions, the zone level analysis revealed that the peak energy demand during the heating period is reduced by 0.6 kW/m^2 for well-insulated buildings and 1.7 kW/m^2 for poorly insulated, while the respective decrease during the cooling period is 0.1 kW/m^2 and 0.2 kW/m^2 between the individual (AC) and the centralized (network) energy solutions. The microclimate analysis assessed slightly better thermal comfort conditions by 2.8% during the cooling period. At the pedestrian level, the maximum difference in thermal comfort conditions was 58 CDH, while the maximum air temperature difference recorded a value of 1.8 ^oC in the air cells next to old apartments. The respective outcomes for the heating period do not present significant deviations.

Under future meteorological conditions, the zone level analysis showed that the peak energy demand during the heating period is reduced by 0.6 kW/m^2 for well-insulated buildings and 1.5 kW/m^2 for poorly insulated, while the respective decrease during the cooling period is 0.9 kW/m^2 and 1.6 kW/m^2 between the individual (AC) and the centralized (network) energy solutions. The microclimate analysis assessed better thermal comfort conditions by 13.2% during the cooling period. At the pedestrian level, the maximum difference in thermal comfort conditions was 968 CDH, while the maximum air temperature difference recorded a value of 3.2 ^oC in the air cells next to old apartments. During the heating period, the thermal comfort conditions remained stable. Both scenarios showed that the poorly insulated buildings are more sensitive to outdoor conditions and they are mostly affected by the waste heat of the AC units.

Despite the reduced energy consumption at zone or building level when the centralized

energy system is considered, the district level analysis revealed that the annual energy penalty due to the network ground losses is almost 14%. Under extreme weather conditions, during the cooling period, an energy penalty of around 13% is correlated with a mean air temperature difference of approximately 0.2 K.

The extensive application of cool materials both on building and outdoor surfaces reduces the energy differences between the systems scenario, as the waste heat is minimized. Moreover, the implementation of cool materials is beneficial for single-floor poorly insulated buildings, as it can reduce the cooling needs up to 50% when at the same time south-oriented well-insulated buildings presented a slight increase of 5.6% due to the solar gains rise. The outdoor thermal comfort (in terms of canopy air temperature) during the cooling period is ameliorated by almost 27.1%.

As a conclusion, we clarify that both the district energy network scenario and the cool one are ideal. Our purpose is to demonstrate the capabilities of the developed model and not to derive general results regarding the potential thermal behavior of either an energy network installation or cool materials applications.

Chapter 6

Conclusions and Perspectives

Contents

6.1 Conclusions

The global and the local climate change constitute unequivocally major issues of nowadays with manifold environmental and social impacts. At the local scale, climate change is described in terms of the so-called Urban Heat Island (UHI) effect, which so far, has been documented for hundreds of cities around the world. Evidently, the built environment comprises the key artificial contributor, leading to the modification of thermal balance, while it also constitutes the dominant energy consumer in urban systems. In this context, buildings critically affect the local climate, while the latter, has emerged the quest for novel standards in the building construction and integrated systems. The existing challenges arising due to the bidirectional dependency between buildings and local climate change, put in the foreground the pursuit of alternative solutions for the controllability of their interactions.

The present computational work seeks to bind several physical models leading to a prototype to account for urban energy demand, individual and district energy systems, and urban microclimate; serving the neighborhood scale under explicit urban geometries and annual temporal conditions. The selected tools to perform the binding process correspond to the urban building energy model (UBEM) Dimosim and the zonal microclimate tool EnviBatE. The first, provides a detailed description of the energy systems and the indoor environment, while the second one accounts for the site-specific microclimate effects based on heat and mass transfer modelling, leading to conclude that the one can compensate for the limitations of the other. The building model is the common object in both tools, comprising the starting point of the coupling strategies.

To this end, different coupling strategies between the selected models have been developed and presented in Chapter 4 for a representative case study of an urban neighborhood in La Rochelle, France. We clustered the coupling methods to synchronous and asynchronous, depending on the examined variable. The synchronous coupling schemes are established with the employment of the ping-pong approach through the development of a co-simulation platform, while the asynchronous ones are based on the chaining method. The research objective is focused on the assessment of the energy demand and specifically on the implications of the site-specific effects on it. Moreover, the feedback of the rejected heat to the outdoor environment has been studied. For comparison purposes, we selected a coupling variable (outdoor air temperature) to quantify the variability between different methods of coupling implementation.

More in detail, the synchronous coupling methodology was distinguished to building-based (CS1) and microclimate-based (CS2-CS3) coupling variables. For each coupling strategy, the rejected heat of the operating energy system (ACU) is considered. The coupling strategy CS1a employs the exterior surface temperature of wall elements as the coupling parameter, assuming that it tracks the microclimate footprint. We showed that the average cooling demand rise is 5.1% during the entire cooling period, while the average peak reaches 10.4% at the building level. The peak relative difference on cooling loads between the coupled model and the referenced standalone in the entire neighborhood is 27%, observed late at night. Similar outcomes were found in coupling strategy CS1b in which the additional coupling variable of the indoor air temperature slightly affects the energy demand. Nevertheless, this coupling strategy allows EnviBatE to consider a more realistic representation of the indoor environment. In coupling strategy CS2 the calculated building sensible fluxes of Dimosim's RC zone model were injected into the zonal cells of the urban canopy in EnviBatE. At the same time, the incident solar irra-

diance along with the radiative exchanges of the urban surfaces and the average air temperature of the air cells adjacent to every thermal zone feed the RC model with enhanced boundary conditions. This scheme assessed significant variations on cooling demand presenting an average increase of approximately 19% compared to the referenced standalone simulation during the cooling period, while the overall peak relative difference of the cooling demand fluctuated up to 75%, showing the capacity of the outdoor air temperature as a coupling variable. The investigation of the variation between identical coupling variables and different coupling methodology is conducted through the development of CS3. The coupling strategy CS3a-CS3b, described by an asynchronous mono-nodal representation of the outdoor environment, concluded to an average difference between coupled and standalone models of approximately 13% and 9% respectively, in terms of cooling demand.

The evaluation of ACs waste heat feedback to energy demand has been assessed in the synchronous coupling schemes, CS1 and CS2, in which a set of fully coupled simulations is compared to a similar one where the rejected heat of the operating system was not considered. The maximum percentage difference in cooling demand for the entire neighborhood fluctuates from 0.4% to 2% for the referenced coupling strategies respectively. At the same time, the aforementioned methodology enabled us to evaluate the local air temperature rise due to ACs. The CS1 scheme assessed a maximum absolute difference of the outdoor air temperature close to 1.4^{o}C while the respective variation of CS2 is almost 2.0^{o}C. Both were found late in the afternoon for limited wind speed conditions and peak ambient boundary temperatures.

In order to study the sensitivity of the developed coupled models and their response under different boundary conditions and distinct envelope thermal characteristics, a parametric study was conducted. In the case of a Mediterranean climate with dry and hot summers, where the amount of energy demand is almost halved between cooling and heating loads, the average relative difference in cooling needs is significantly increased compared to the heating one when the microclimate is considered. For well insulated buildings reaches 10.3% against almost 3%, while for poorly insulated is 13.4% against 4.8% for the cooling and heating periods respectively. The latter shows the necessity of microclimate integration to building energy simulation, especially for cooling energy assessments, as the cooling demand is adversely affected compared to the heating. Additionally, the insulation increase reduces the site-specific implications to energy demand, however increases the variations between different coupling approaches. Lastly, the canopy temperature overheating is decisively affected by the insulation performance when the system rejected heat is studied. By correlating the waste heat with the local air temperature difference, we showed that even for a lower boundary air temperature (-0.4^{o}C) the poorly insulated buildings were responsible for higher canopy temperature differences compared to well-insulated ones, up to 2 ^{o}C.

In the last part of this manuscript, the developed integrated model has been used to evaluate the thermal performance of a residential neighborhood in the city of La Rochelle, covering a total floor area of 63800 m^2. The micro-urban energy study aimed to assess the energy demand of the neighborhood at different scales, from zone to neighborhood level, by comparing the application of individual (AC) and centralized energy systems, such as a district energy network (DEN), with respect to the local environment. This active mitigation solution aims to tackle the anthropogenic heat released at the zone level, therefore it was also tested for projected climate conditions and compared with a passive one, such as the extensive implementation of cool materials.

Under typical meteorological conditions the overall cooling savings of the neighborhood reached 5 MWh in the DEN scenario attributed to the elimination of the heat emissions at the zone level. The microclimate analysis assessed slightly better outdoor thermal comfort conditions during the cooling period, reaching the value of 2.8% in terms of the outdoor CDH indicator. However, the latter is associated with a cooling penalty of approximately 30 MWh when the ground losses of the piping circuit are considered.

In the case of future meteorological conditions, the overall energy savings at the zone level during the cooling period were up to 22 MWh under the DEN scenario, presenting a respective reduction of the outdoor CDH indicator of around 13%. The latter is attributed to a mean canopy air temperature reduction of 0.2 K for the entire cooling period. Nevertheless, the cooling penalty of the thermal network reached 54 MWh due to the overall increased energy demand compared to the typical meteorological conditions.

The implementation of a passive mitigation solution, such as the extensive application of cool materials, limits the overall cooling savings between the different system configurations to almost 4 MWh. This is attributed to the severe decrease of the cooling loads under the AC scenario, especially for single-floor poorly insulated buildings which presented energy savings up to 50%. The latter is also associated with a peak cooling penalty as the ground losses remained constant but the energy demand deviation between the system scenarios is limited. Moreover, the model assessed a peak surface temperature reduction of 18.9^{o}C and 8.3^{o}C in building roofs and outdoor surfaces, attributed to an albedo increase of approximately 50% and 24% respectively. The reduced surface temperatures and thus the reduced air temperature of the adjacent canopy cells revealed a maximum mitigation potential of approximately 27.1% in terms of the outdoor CDH indicator under the AC scenario. Consequently, the modeling study confirmed the efficiency of the passive solution to counterbalance the local overheating but also established the capability of the coupled model to perform comparative studies of complex physical interactions.

To conclude, this work presented the development of a coupled model that can effectively support urban mitigation strategies by evaluating the comparative performance of energy conservation measures in terms of both energy savings and heat emissions for distinct building and system configurations as well as locally variable environmental conditions of the urban neighborhoods.

6.2 Perspectives

The development of numerical platforms requires maintenance, testing, automated deployment and all of the aspects that the notion of continuous integration includes. For this purpose, the required tasks to account for both scientific and technical issues are mentioned in the next paragraphs.

The major obstacle of the coupled model arises from the consideration of the forced convection component of air circulation. This drawback can be tackled with the development of a buoyancy model. The study of Dallman, et. al. [230] can provide a tangible framework towards its integration. However, the existing airflow object of the microclimate model has to be reformed, otherwise, the tool will miss its characteristic attribute which lies in fast calculations.

Moreover, various implementations of additional urban greenery both on outdoor spaces and building facades have arisen the last years. In parallel, the latent phenomena can play an impor-

tant role in the energy balance of the urban environment. The developed model considers only the sensible heat fluxes of the urban environment. The potential development of a latent module will allow us to consider the latent energy transfers and to extend the model's capabilities in terms of urban mitigation assessments.

The developed methodology in this study has been designed in a flexible way, allowing the integration of a further coupling scheme. It is strongly advised in the future, an extended version of the model, which will include a mesoscale model. This possible extension will allow a holistic assessment of the UHI effect, by considering all of the overground types of the phenomenon. However, a crucial point in this effort deals with the boundary matching and the temporal discretisation of each submodel.

Although all of the individual models are validated against real experimental data, for the developed coupled model a validation test has not been yet performed. Given the participation of the author in the SINERGIE (SINgaporean network on renewable enERGIEs) project as well as the selection of the UBEM (Dimosim) to act as the key modeling environment on the development of a DESTEST (District Energy Simulation Test) [231], a potential validation space emerges. The SINERGIE project can provide extensive monitoring data of microclimate parameters, as well as recorded data regarding the building energy demand in a tropical climate. On the other hand, the DESTEST development can provide a framework that can be used as a reference environment for testing new technologies and innovative solutions in the context of district energy systems.

The generation of the various urban meshes has been established with GMSH [190] software. The actual allowable simulation domain is limited to a spatial scale of approximately 1000 $\times$ 1000m (depending on building heights), due to the software's restrictions. The published python library "pygmsh" can tackle this limitation, but requires the concurrent development of new objects that will treat the indexations between the various meshes.

From a technical point of view, the microclimate modules need to be updated in order to be coherent with the actual releases of Python versions. Although a big effort was made during this thesis to clean, document, and reform as possible the developed code, there are still lots to do for the development of a user friendly and stable version of the simulation package.

Bibliography

[1] U. Nations, "World urbanization prospects," tech. rep., Department of Economic and Social Affairs, Population Division, 2019.

[2] Eurostat, "Energy balance sheets 2016 data." https://ec.europa.eu/eurostat/documents/3217494/9172750/KS-EN-18-001-EN-N.pdf/474c2308-002a-40cd-87b6-9364209bf936, 2018.

[3] C. général au développement durable, "Bilan énergétique de la france pour 2018," 2020.

[4] Eurostat. https://appsso.eurostat.ec.europa.eu/nui/submitViewTableAction.do.

[5] IEA, "Tracking buildings." https://www.iea.org/reports/tracking-buildings, 2020.

[6] M. Santamouris, "Cooling the buildings - past, present and future.," *Energy and Buildings*, vol. 128, no. 3, pp. 617–638, 2016.

[7] E. Commission, "Energy efficiency, buildings [online] available at: https://ec.europa.eu/energy/en/topics/energy-efficiency/buildings.," 2015.

[8] "Directive 2010/31/eu of the european parliament and of the council of 19 may 2010 on the energy performance of buildings.," 2010.

[9] M. Economidou, B. Atanasiu, C. Despret, J. Maio, I. Nolte, and O. Rapf, "Europe's buildings under the microscope. a country-by-country review of the energy performance of buildings," *Buildings Performance Institute Europe (BPIE)*, pp. 35–36, 2011.

[10] A. Synnefa, K. Vasilakopoulou, G.-E. Kyriakodis, V. Lontorfos, R. De Masi, E. Mastrapostoli, T. Karlessi, and M. Santamouris, "Minimizing the energy consumption of low income multiple housing using a holistic approach," *Energy and Buildings*, vol. 154, pp. 55–71, 2017.

[11] 100RC, "100 resilient cities." http://www.100resilientcities.org/how-to-develop-a-resilience-strategy/, 2016.

[12] G. Kyriakodis and M. Santamouris, "Using reflective pavements to mitigate urban heat island in warm climates-results from a large scale urban mitigation project," *Urban Climate*, vol. 24, pp. 326–339, 2018.

[13] M. Santamouris, L. Ding, F. Fiorito, P. Oldfield, P. Osmond, R. Paolini, D. Prasad, and A. Synnefa, "Passive and active cooling for the outdoor built environment–analysis and assessment of the cooling potential of mitigation technologies using performance data from 220 large scale projects," *Solar Energy*, vol. 154, pp. 14–33, 2017.

[14] Y. Saheb, S. Shnapp, and C. Johnson, "The zero energy concept: making the whole greater than the sum of the parts to meet the paris climate agreement's objectives," *Current opinion in environmental sustainability*, vol. 30, pp. 138–150, 2018.

[15] A. Caramizaru and A. Uihlein, "Energy communities: An overview of energy and social innovation," *JRC Science for Policy Report JRC119433*, 2020.

[16] B. Kampman, J. Blommerde, and M. Afman, *The potential of energy citizens in the European Union*. CE Delft, 2016.

[17] I. Dincer and M. A. Rosen, *Exergy: energy, environment and sustainable development*. Newnes, 2012.

[18] H. Shu, L. Duanmu, C. Zhang, and Y. Zhu, "Study on the decision-making of district cooling and heating systems by means of value engineering," *Renewable Energy*, vol. 35, no. 9, pp. 1929–1939, 2010.

[19] L. Zhen, D. Lin, H. Shu, S. Jiang, and Y. Zhu, "District cooling and heating with seawater as heat source and sink in dalian, china," *Renewable energy*, vol. 32, no. 15, pp. 2603–2616, 2007.

[20] B. Rismanchi, "District energy network (den), current global status and future development," *Renewable and Sustainable Energy Reviews*, vol. 75, pp. 571–579, 2017.

[21] W. Gang, S. Wang, D. Gao, and F. Xiao, "Performance assessment of district cooling systems for a new development district at planning stage," *Applied energy*, vol. 140, pp. 33–43, 2015.

[22] M. Santamouris, *Energy and climate in the urban built environment*. Routledge, 2013.

[23] M. Santamouris, "Analyzing the heat island magnitude and characteristics in one hundred asian and australian cities and regions.," *The Science of the total environment*, vol. 512-513, pp. 582–598, 2015.

[24] M. Santamouris and D. Kolokotsa, *Urban climate mitigation techniques*. Routledge, 2016.

[25] B. Ferguson, K. Fisher, J. Golden, L. Hair, L. Haselbach, D. Hitchcock, K. Kaloush, M. Pomerantz, N. Tran, and D. Waye, "Reducing urban heat islands: compendium of strategies-cool pavements," 2008.

[26] T. Oke, "The heat island of the urban boundary layer: characteristics, causes and effects," in *Wind climate in cities*, pp. 81–107, Springer, 1995.

[27] J. A. Voogt and T. Oke, "Effects of urban surface geometry on remotely-sensed surface temperature," *International Journal of Remote Sensing*, vol. 19, no. 5, pp. 895–920, 1998.

[28] J. A. Voogt and T. R. Oke, "Thermal remote sensing of urban climates," *Remote sensing of environment*, vol. 86, no. 3, pp. 370–384, 2003.

[29] K. Zhu, P. Blum, G. Ferguson, K.-D. Balke, and P. Bayer, "The geothermal potential of urban heat islands," *Environmental Research Letters*, vol. 5, p. 044002, oct 2010.

[30] "Arrêté du 28 décembre 2012 relatif aux caractéristiques thermiques et aux exigences de performance énergétique des bâtiments nouveaux et des parties nouvelles de bâtiments autres que ceux concernés par l'article 2 du décret du 26 octobre 2010 relatif aux caractéristiques thermiques et á la performance énergétique des constructions(2012)," 2012.

[31] H. Akbari, "Cooling our communities. a guidebook on tree planting and light-colored surfacing," 2009.

[32] D. Sailor, "Urban heat islands, opportunities and challenges for mitigation and adaptation," *Sample Electric Load Data for New Orleans, LA (NOPSI, 1995). North American Urban Heat Island Summit. Toronto, Canada*, pp. 1–4, 2002.

[33] M. Santamouris, C. Cartalis, A. Synnefa, and D. Kolokotsa, "On the impact of urban heat island and global warming on the power demand and electricity consumption of buildings-a review," *Energy and Buildings*, vol. 98, pp. 119–124, 2015.

[34] M. Kolokotroni, I. Giannitsaris, and R. Watkins, "The effect of the london urban heat island on building summer cooling demand and night ventilation strategies," *Solar Energy*, vol. 80, no. 4, pp. 383–392, 2006.

[35] S. Hassid, M. Santamouris, N. Papanikolaou, A. Linardi, N. Klitsikas, C. Georgakis, and D. Assimakopoulos, "The effect of the athens heat island on air conditioning load," *Energy and Buildings*, vol. 32, no. 2, pp. 131–141, 2000.

[36] L. Papada and D. Kaliampakos, "Measuring energy poverty in greece," *Energy Policy*, vol. 94, pp. 157–165, 2016.

[37] B. Atanasiu, E. Kontonasiou, and F. Mariottini, "Alleviating fuel poverty in the eu: investing in home renovation, a sustainable and inclusive solution," *Buildings Performance Institute Europe (BPIE), Brussels*, 2014.

[38] M. Baccini, A. Biggeri, G. Accetta, T. Kosatsky, K. Katsouyanni, A. Analitis, H. R. Anderson, L. Bisanti, D. D'Ippoliti, J. Danova, *et al.*, "Heat effects on mortality in 15 european cities," *Epidemiology*, pp. 711–719, 2008.

[39] D. D'Ippoliti, P. Michelozzi, C. Marino, F. De'Donato, B. Menne, K. Katsouyanni, U. Kirchmayer, A. Analitis, M. Medina-Ramón, A. Paldy, *et al.*, "The impact of heat waves on mortality in 9 european cities: results from the euroheat project," *Environmental Health*, vol. 9, no. 1, p. 37, 2010.

[40] D. Hemon and E. Jougla, "La canicule du mois d'août 2003 en france," 2004.

[41] J.-M. Robine, S. L. K. Cheung, S. Le Roy, H. Van Oyen, C. Griffiths, J.-P. Michel, and F. R. Herrmann, "Death toll exceeded 70,000 in europe during the summer of 2003," *Comptes rendus biologies*, vol. 331, no. 2, pp. 171–178, 2008.

[42] F. Rossi, E. Bonamente, A. Nicolini, E. Anderini, and F. Cotana, "A carbon footprint and energy consumption assessment methodology for uhi-affected lighting systems in built areas," *Energy and Buildings*, vol. 114, pp. 96–103, 2016.

[43] M. Santamouris, K. Paraponiaris, and G. Mihalakakou, "Estimating the ecological footprint of the heat island effect over athens, greece," *Climatic Change*, vol. 80, no. 3-4, pp. 265–276, 2007.

[44] E. Stathopoulou, G. Mihalakakou, M. Santamouris, and H. Bagiorgas, "On the impact of temperature on tropospheric ozone concentration levels in urban environments," *Journal of Earth System Science*, vol. 117, no. 3, pp. 227–236, 2008.

[45] C. Sarrat, A. Lemonsu, V. Masson, and D. Guedalia, "Impact of urban heat island on regional atmospheric pollution," *Atmospheric Environment*, vol. 40, no. 10, pp. 1743–1758, 2006.

[46] K. Y. Kondratyev and C. A. Varotsos, "Global total ozone dynamics," *Environmental Science and Pollution Research*, vol. 3, pp. 153–157, Sep 1996.

[47] H. Taha, "Modeling the impacts of large-scale albedo changes on ozone air quality in the south coast air basin," *Atmospheric Environment*, vol. 31, no. 11, pp. 1667–1676, 1997.

[48] Y. Zhang, Z. O'Neill, B. Dong, and G. Augenbroe, "Comparisons of inverse modeling approaches for predicting building energy performance," *Building and Environment*, vol. 86, pp. 177–190, 2015.

[49] S. A. Kalogirou, "Applications of artificial neural-networks for energy systems," *Applied energy*, vol. 67, no. 1-2, pp. 17–35, 2000.

[50] S. Karatasou, M. Santamouris, and V. Geros, "Modeling and predicting building's energy use with artificial neural networks: Methods and results," *Energy and buildings*, vol. 38, no. 8, pp. 949–958, 2006.

[51] University of Wisconsin–Madison. Solar Energy Laboratory, *TRNSYS, a transient simulation program*. Madison, Wis. : The Laboratory, 1975., 1975.

[52] J. Clarke and D. McLean, "Esp-a building and plant energy simulation system," *Strathclyde: Energy Simulation Research Unit, University of Strathclyde*, 1988.

[53] D. B. Crawley, L. K. Lawrie, F. C. Winkelmann, W. F. Buhl, Y. J. Huang, C. O. Pedersen, R. K. Strand, R. J. Liesen, D. E. Fisher, M. J. Witte, *et al.*, "Energyplus: creating a new-generation building energy simulation program," *Energy and buildings*, vol. 33, no. 4, pp. 319–331, 2001.

[54] C. Inard, H. Bouia, and P. Dalicieux, "Prediction of air temperature distribution in buildings with a zonal model," *Energy and buildings*, vol. 24, no. 2, pp. 125–132, 1996.

[55] L. Mora, A. Gadgil, E. Wurtz, and C. Inard, "Comparing zonal and cfd model predictions of indoor airflows under mixed convection conditions to experimental data," in *Proceedings of 3rd European conference on energy performance and indoor climate in buildings, Lyon, France*, pp. 23–26, 2002.

[56] F. Haghighat, Y. Li, and A. C. Megri, "Development and validation of a zonal model-poma," *Building and environment*, vol. 36, no. 9, pp. 1039–1047, 2001.

[57] M. Abadie, M. De Camargo, K. Mendonça, and P. Blondeau, "Improving the prediction of zonal modeling for forced convection airflows in rooms," *Building and Environment*, vol. 48, pp. 173–182, 2012.

[58] P. Riederer, D. Marchio, and J.-C. Visier, "Modèle de zone adapté aux essais de régulateurs de systèmes de chauffage et de climatisation," *Cahiers du CSTB*, vol. Cahier 3446, Livraison 437, p. 16 p., Mar. 2003.

[59] J. Clarke, *Energy simulation in building design*. Routledge, 2007.

[60] R. Lamberts and J. L. Hensen, *Building performance simulation for design and operation*. Spoon Press, 2011.

[61] *Cooling load calculations by thermal response factor method*.

[62] S. Rousseau, *Simulation numérique du comportement thermique des locaux d'habitation: évaluation de l'influence de la radiation solaire, des conditions climatiques et des paramètres caractéristiques du bâtiment*. Phd thesis, University Claude Bernard, 1978.

[63] J. Palyvos, "A survey of wind convection coefficient correlations for building envelope energy systems modeling," *Applied thermal engineering*, vol. 28, no. 8-9, pp. 801–808, 2008.

[64] J. Caroll, "An 'mrt method' of computing radiant energy exchange in rooms," in *Proceedings of the second Systems Simulation and Economic Analysis Conference*, (San Diego), pp. 343–348, 1980.

[65] T. R. Oke, G. Mills, A. Christen, and J. A. Voogt, *Urban climates*. Cambridge University Press, 2017.

[66] J. Strømann-Andersen and P. Sattrup, "The urban canyon and building energy use: Urban density versus daylight and passive solar gains," *Energy and Buildings*, vol. 43, no. 8, pp. 2011 – 2020, 2011.

[67] A. Marsh, "The application of shading masks in building simulation," in *Ninth International IBPSA Conference*, pp. 725–732, 08 2005.

[68] S. Freitas, C. Catita, P. Redweik, and M. Brito, "Modelling solar potential in the urban environment: State-of-the-art review," *Renewable and Sustainable Energy Reviews*, vol. 41, pp. 915 – 931, 2015.

[69] B. F. and B. JE., "A time analysis of sunshine," *Transaction of the Illumination Engineering Society*, vol. 34, pp. 200–203, 1939.

[70] J. A. Duffie and W. A. Beckman, *Solar engineering of thermal processes*. John Wiley & Sons, 2013.

[71] D. Robinson, *Computer Modelling for Sustainable Urban Design: Physical Principles, Methods and Applications*. Earthscan Publications, Limited, 2011.

[72] H. H. C. and W. B. B., "The performance of flat plate solar-heat collectors," *Transactions of the ASME*, vol. 64, pp. 64–91, 1942.

[73] B. Y. Liu and R. C. Jordan, "The long-term average performance of flat-plate solar-energy collectors: With design data for the u.s., its outlying possessions and canada," *Solar Energy*, vol. 7, no. 2, pp. 53 – 74, 1963.

[74] R. Perez, P. Ineichen, R. Seals, J. Michalsky, and R. Stewart, "Modeling daylight availability and irradiance components from direct and global irradiance," *Solar Energy*, vol. 44, no. 5, pp. 271 – 289, 1990.

[75] F. Kasten and A. T. Young, "Revised optical air mass tables and approximation formula," *Applied optics*, vol. 28, no. 22, pp. 4735–4738, 1989.

[76] S. Jensen, "Validation of building energy simulation programs. final report," *PASSYS Model Validation Sub-group*, 1994.

[77] *Thermal Analysis Research Program- Reference Manual*.

[78] G. Clark and C. Allen, "The estimation of atmospheric radiation for clear and cloudy skies," in *Proc. 2nd National Passive Solar Conference (AS/ISES)*, pp. 675–678, 1978.

[79] T. Kusuda and P. Archenbach, "Earth temperature and thermal diffusivity at selected stations in the united states," tech. rep., ASHRAE Transactions, 1965.

[80] G. William and L. Gold, "Les temperatures du sol," *NRC Publications Archive*, 1977.

[81] C. Colucci, L. Mauri, and V. Andrea, "About the shortwave multiple reflections in an urban street canyon building related to three different european climates," in *XI International Conference on Computational Heat, Mass and Momentum Transfer (ICCHMT 2018)*, vol. 240, 2018.

[82] S. Tsoka, K. Tsikaloudaki, and T. Theodosiou, "Coupling a building energy simulation tool with a microclimate model to assess the impact of cool pavements on the building's energy performance application in a dense residential area," *Sustainability*, vol. 11, no. 9, p. 2519, 2019.

[83] A. Vallati, L. Mauri, and C. Colucci, "Impact of shortwave multiple reflections in an urban street canyon on building thermal energy demands," *Energy and Buildings*, vol. 174, pp. 77–84, 2018.

[84] E. Bozonnet, R. Belarbi, and F. Allard, "Modelling solar effects on the heat and mass transfer in a street canyon, a simplified approach," *Solar Energy*, vol. 79, no. 1, pp. 10–24, 2005.

[85] F. P. Incropera, A. S. Lavine, T. L. Bergman, and D. P. DeWitt, *Fundamentals of heat and mass transfer*. Wiley, 2007.

[86] D. Robinson and A. Stone, "A simplified radiosity algorithm for general urban radiation exchange," *Building services engineering research and technology*, vol. 26, no. 4, pp. 271–284, 2005.

[87] D. Robinson and A. Stone, "Solar radiation modelling in the urban context," *Solar energy*, vol. 77, no. 3, pp. 295–309, 2004.

[88] D. Robinson and A. Stone, "Holistic radiation modelling with a fast simplified radiosity algorithm," in *Proc. Ninth Int. IBPSA Conf., Building Simulation*, Citeseer, 2005.

[89] R. Meroney, "Turbulent diffusion near buildings," *Engineering Meteorology*, 1982.

[90] T. R. Oke, *Boundary layer climates*. Routledge, 2002.

[91] T. R. Oke, "Street design and urban canopy layer climate," *Energy and buildings*, vol. 11, no. 1-3, pp. 103–113, 1988.

[92] T. R. Oke, "Urban environments," *The surface climates of Canada*, pp. 303–327, 1997.

[93] E. J. Plate and H. Kiefer, "Wind loads in urban areas," *Journal of Wind Engineering and Industrial Aerodynamics*, vol. 89, no. 14-15, pp. 1233–1256, 2001.

[94] R. B. Stull, "An introduction to boundary layer meteorology," *Atmospheric Sciences Library, Dordrecht: Kluwer, 1988*, 1988.

[95] J. A. Businger, J. C. Wyngaard, Y. Izumi, and E. F. Bradley, "Flux-profile relationships in the atmospheric surface layer," *Journal of the atmospheric Sciences*, vol. 28, no. 2, pp. 181–189, 1971.

[96] S. E. Nicholson, "A pollution model for street-level air," *Atmospheric Environment (1967)*, vol. 9, no. 1, pp. 19–31, 1975.

[97] C. Grimmond and T. R. Oke, "Aerodynamic properties of urban areas derived from analysis of surface form," *Journal of applied meteorology*, vol. 38, no. 9, pp. 1262–1292, 1999.

[98] A. G. Davenport, C. S. B. Grimmond, T. R. Oke, and J. Wieringa, "Estimating the roughness of cities and sheltered country," in *15th conference on probability and statistics in the atmospheric sciences/12th conference on applied climatology, Ashville, NC, American Meteorological Society*, pp. 96–99, 2000.

[99] J. Counihan, "Adiabatic atmospheric boundary layers: a review and analysis of data from the period 1880–1972," *Atmospheric Environment (1967)*, vol. 9, no. 10, pp. 871–905, 1975.

[100] R. M. Cionco, "A mathematical model for air flow in a vegetative canopy," *Journal of Applied Meteorology*, vol. 4, no. 4, pp. 517–522, 1965.

[101] E. Inoue, "On the turbulent structure of airflow within," *Journal of the Meteorological Society of Japan. Ser. II*, vol. 41, no. 6, pp. 317–326, 1963.

[102] R. Macdonald, "Modelling the mean velocity profile in the urban canopy layer," *Boundary-Layer Meteorology*, vol. 97, no. 1, pp. 25–45, 2000.

[103] C. F. Reinhart and C. C. Davila, "Urban building energy modeling–a review of a nascent field," *Building and Environment*, vol. 97, pp. 196–202, 2016.

[104] M. Santamouris, "Energy and climate in the urban built environment," 2001.

[105] J. Allegrini, K. Orehounig, G. Mavromatidis, F. Ruesch, V. Dorer, and R. Evins, "A review of modelling approaches and tools for the simulation of district-scale energy systems," *Renewable and Sustainable Energy Reviews*, vol. 52, pp. 1391–1404, 2015.

[106] M. Kavgic, A. Mavrogianni, D. Mumovic, A. Summerfield, Z. Stevanovic, and M. Djurovic-Petrovic, "A review of bottom-up building stock models for energy consumption in the residential sector," *Building and environment*, vol. 45, no. 7, pp. 1683–1697, 2010.

[107] L. G. Swan and V. I. Ugursal, "Modeling of end-use energy consumption in the residential sector: A review of modeling techniques," *Renewable and sustainable energy reviews*, vol. 13, no. 8, pp. 1819–1835, 2009.

[108] N. Fumo, "A review on the basics of building energy estimation," *Renewable and Sustainable Energy Reviews*, vol. 31, pp. 53–60, 2014.

[109] L. Pedersen, "Use of different methodologies for thermal load and energy estimations in buildings including meteorological and sociological input parameters," *Renewable and Sustainable Energy Reviews*, vol. 11, no. 5, pp. 998–1007, 2007.

[110] H.-x. Zhao and F. Magoulès, "A review on the prediction of building energy consumption," *Renewable and Sustainable Energy Reviews*, vol. 16, no. 6, pp. 3586–3592, 2012.

[111] A. Sola, C. Corchero, J. Salom, and M. Sanmarti, "Simulation tools to build urban-scale energy models: A review," *Energies*, vol. 11, no. 12, p. 3269, 2018.

[112] L. Frayssinet, L. Merlier, F. Kuznik, J.-L. Hubert, M. Milliez, and J.-J. Roux, "Modeling the heating and cooling energy demand of urban buildings at city scale," *Renewable and Sustainable Energy Reviews*, vol. 81, pp. 2318–2327, 2018.

[113] J. Keirstead, M. Jennings, and A. Sivakumar, "A review of urban energy system models: Approaches, challenges and opportunities," *Renewable and Sustainable Energy Reviews*, vol. 16, no. 6, pp. 3847–3866, 2012.

[114] F. Chen, H. Kusaka, R. Bornstein, J. Ching, C. Grimmond, S. Grossman-Clarke, T. Loridan, K. W. Manning, A. Martilli, S. Miao, *et al.*, "The integrated wrf/urban modelling system: development, evaluation, and applications to urban environmental problems," *International Journal of Climatology*, vol. 31, no. 2, pp. 273–288, 2011.

[115] T. K. Lim, M. Ignatius, M. Miguel, N. H. Wong, and H.-M. H. Juang, "Multi-scale urban system modeling for sustainable planning and design," *Energy and Buildings*, vol. 157, pp. 78–91, 2017.

[116] W. T. Chow, F. Salamanca, M. Georgescu, A. Mahalov, J. M. Milne, and B. L. Ruddell, "A multi-method and multi-scale approach for estimating city-wide anthropogenic heat fluxes," *Atmospheric environment*, vol. 99, pp. 64–76, 2014.

[117] A. A. Baklanov and R. Nuterman, "Multi-scale atmospheric environment modelling for urban areas," *Advances in Science and Research*, vol. 3, p. 53, 2009.

[118] P. A. Mirzaei and F. Haghighat, "Approaches to study urban heat island–abilities and limitations," *Building and environment*, vol. 45, no. 10, pp. 2192–2201, 2010.

[119] P. Remmen, M. Lauster, M. Mans, M. Fuchs, T. Osterhage, and D. Müller, "Teaser: an open tool for urban energy modelling of building stocks," *Journal of Building Performance Simulation*, vol. 11, no. 1, pp. 84–98, 2018.

[120] M. Lauster, M. Fuchs, M. Huber, P. Remmen, R. Streblow, and D. Müller, "Adaptive thermal building models and methods for scalable simulations of multiple buildings using modelica," in *the 14th International IBPSA Conference*, 2015.

[121] R. De Coninck, F. Magnusson, J. Åkesson, and L. Helsen, "Grey-box building models for model order reduction and control," in *Proceedings of the 10 th International Modelica Conference; March 10-12; 2014; Lund; Sweden*, no. 096, pp. 657–666, Linköping University Electronic Press, 2014.

[122] "Ideas: Integrated district energy assessment by simulation." `https://www.energyville.be/en/research/integrated-district-energy-assessment-simulation-ideas`.

[123] R. Baetens, R. De Coninck, J. Van Roy, B. Verbruggen, J. Driesen, L. Helsen, and D. Saelens, "Assessing electrical bottlenecks at feeder level for residential net zero-energy buildings by integrated system simulation," *Applied Energy*, vol. 96, pp. 74–83, 2012.

[124] F. Jorissen, G. Reynders, R. Baetens, D. Picard, D. Saelens, and L. Helsen, "Implementation and verification of the ideas building energy simulation library," *Journal of Building Performance Simulation*, vol. 11, no. 6, pp. 669–688, 2018.

[125] D. Robinson, F. Haldi, P. Leroux, D. Perez, A. Rasheed, and U. Wilke, "Citysim: Comprehensive micro-simulation of resource flows for sustainable urban planning," in *Proceedings of the Eleventh International IBPSA Conference*, no. CONF, pp. 1083–1090, 2009.

[126] T. Hong, Y. Chen, S. H. Lee, and M. A. Piette, "Citybes: A web-based platform to support city-scale building energy efficiency," *Urban Computing*, vol. 14, 2016.

[127] Y. Chen, T. Hong, and M. A. Piette, "Automatic generation and simulation of urban building energy models based on city datasets for city-scale building retrofit analysis," *Applied Energy*, vol. 205, pp. 323–335, 2017.

[128] Y. Chen, T. Hong, and M. A. Piette, "City-scale building retrofit analysis: a case study using citybes," *Build. Simul*, 2017.

[129] J. A. Fonseca, T.-A. Nguyen, A. Schlueter, and F. Marechal, "City energy analyst (cea): Integrated framework for analysis and optimization of building energy systems in neighborhoods and city districts," *Energy and Buildings*, vol. 113, pp. 202–226, 2016.

[130] J. A. Fonseca and A. Schlueter, "Integrated model for characterization of spatiotemporal building energy consumption patterns in neighborhoods and city districts," *Applied Energy*, vol. 142, pp. 247–265, 2015.

[131] R. Nouvel, K.-H. BRASSEL, M. BRUSE, E. DUMINIL, V. COORS, U. EICKER, and D. ROBINSON, "Simstadt, a new workflow-driven urban energy simulation platform for citygml city models," in *Proceedings of International Conference CISBAT 2015 Future Buildings and Districts Sustainability from Nano to Urban Scale*, no. CONF, pp. 889–894, LESO-PB, EPFL, 2015.

[132] P. Wate and V. Coors, "3d data models for urban energy simulation," *Energy Procedia*, vol. 78, pp. 3372–3377, 2015.

[133] P. Riederer, V. Partenay, N. Perez, C. Nocito, R. Trigance, and T. Guiot, "Development of a simulation platform for the evaluation of district energy system performances," in *Fourteenth International IBPSA Conference*, pp. 2499–2506, 2015.

[134] Y. Toparlar, B. Blocken, B. Maiheu, and G. Van Heijst, "A review on the cfd analysis of urban microclimate," *Renewable and Sustainable Energy Reviews*, vol. 80, pp. 1613–1640, 2017.

[135] M. Bruse and H. Fleer, "Simulating surface–plant–air interactions inside urban environments with a three dimensional numerical model," *Environmental modelling & software*, vol. 13, no. 3-4, pp. 373–384, 1998.

[136] P. A. Mirzaei, "Recent challenges in modeling of urban heat island," *Sustainable Cities and Society*, vol. 19, pp. 200–206, 2015.

[137] W. Liang, J. Huang, P. Jones, Q. Wang, and J. Hang, "A zonal model for assessing street canyon air temperature of high-density cities," *Building and Environment*, vol. 132, pp. 160–169, 2018.

[138] F. S. de La Flor and S. A. Domınguez, "Modelling microclimate in urban environments and assessing its influence on the performance of surrounding buildings," *Energy and buildings*, vol. 36, no. 5, pp. 403–413, 2004.

[139] E. Bozonnet, R. Belarbi, and F. Allard, "Modelling air flows around buildings in urban environment," in *International workshop on energy performance and environmental quality of buildings, Milos island, Greece*, 2006.

[140] D. Mauree, N. Blond, M. Kohler, and A. Clappier, "On the coherence in the boundary layer: Development of a canopy interface model," *Frontiers in Earth Science*, vol. 4, p. 109, 2017.

[141] H. Kusaka, H. Kondo, Y. Kikegawa, and F. Kimura, "A simple single-layer urban canopy model for atmospheric models: Comparison with multi-layer and slab models," *Boundary-layer meteorology*, vol. 101, no. 3, pp. 329–358, 2001.

[142] B. Bueno, L. Norford, J. Hidalgo, and G. Pigeon, "The urban weather generator," *Journal of Building Performance Simulation*, vol. 6, no. 4, pp. 269–281, 2013.

[143] V. Masson, "A physically-based scheme for the urban energy budget in atmospheric models," *Boundary-layer meteorology*, vol. 94, no. 3, pp. 357–397, 2000.

[144] A. Afshari, "A new model of urban cooling demand and heat island-application to vertical greenery systems (vgs)," *Energy and Buildings*, vol. 157, pp. 204–217, 2017.

[145] G. A. Grell, J. Dudhia, D. R. Stauffer, *et al.*, "A description of the fifth-generation penn state/ncar mesoscale model (mm5)," 1994.

[146] W. C. Skamarock, J. B. Klemp, J. Dudhia, D. O. Gill, D. M. Barker, W. Wang, and J. G. Powers, "A description of the advanced research wrf version 2," tech. rep., National Center For Atmospheric Research Boulder Co Mesoscale and Microscale., 2005.

[147] A. Martilli, "Numerical study of urban impact on boundary layer structure: Sensitivity to wind speed, urban morphology, and rural soil moisture," *Journal of Applied Meteorology*, vol. 41, no. 12, pp. 1247–1266, 2002.

[148] A. Martilli, "Current research and future challenges in urban mesoscale modelling," *International Journal of Climatology: A Journal of the Royal Meteorological Society*, vol. 27, no. 14, pp. 1909–1918, 2007.

[149] R. D. Bornstein, "The two-dimensional urbmet urban boundary layer model," *Journal of Applied Meteorology*, vol. 14, no. 8, pp. 1459–1477, 1975.

[150] J. P. Lafore, J. Stein, N. Asencio, P. Bougeault, V. Ducrocq, J. Duron, C. Fischer, P. Héreil, P. Mascart, V. Masson, *et al.*, "The meso-nh atmospheric simulation system. part i: Adiabatic formulation and control simulations," vol. 16, no. 1, pp. 90–109, 1997.

[151] P. Le Moigne, A. Boone, J. Calvet, B. Decharme, S. Faroux, A. Gibelin, C. Lebeaupin, J. Mahfouf, E. Martin, V. Masson, *et al.*, "Surfex scientific documentation," *Note de centre (CNRM/GMME), Météo-France, Toulouse, France*, 2009.

[152] S. Dupont and P. G. Mestayer, "Parameterization of the urban energy budget with the submesoscale soil model," *Journal of Applied Meteorology and Climatology*, vol. 45, no. 12, pp. 1744–1765, 2006.

[153] J. Noilhan and J.-F. Mahfouf, "The isba land surface parameterisation scheme," *Global and planetary Change*, vol. 13, no. 1-4, pp. 145–159, 1996.

[154] C. S. B. Grimmond, M. Blackett, M. Best, J. Barlow, J. Baik, S. Belcher, S. Bohnenstengel, I. Calmet, F. Chen, A. Dandou, *et al.*, "The international urban energy balance models comparison project: first results from phase 1," *Journal of applied meteorology and climatology*, vol. 49, no. 6, pp. 1268–1292, 2010.

[155] Y. Sun and G. Augenbroe, "Urban heat island effect on energy application studies of office buildings," *Energy and Buildings*, vol. 77, pp. 171–179, 2014.

[156] K. Gobakis and D. Kolokotsa, "Coupling building energy simulation software with microclimatic simulation for the evaluation of the impact of urban outdoor conditions on the energy consumption and indoor environmental quality," *Energy and Buildings*, vol. 157, pp. 101–115, 2017.

[157] V. L. Castaldo, A. L. Pisello, C. Piselli, C. Fabiani, F. Cotana, and M. Santamouris, "How outdoor microclimate mitigation affects building thermal-energy performance: A new design-stage method for energy saving in residential near-zero energy settlements in italy," *Renewable Energy*, vol. 127, pp. 920–935, 2018.

[158] C. Y. Yi and C. Peng, "Microclimate change outdoor and indoor coupled simulation for passive building adaptation design," *Procedia Computer Science*, vol. 32, pp. 691–698, 2014.

[159] A. Urano, K. Syoji, T. Sato, H. Koyanagi, M. Oguro, and Y. Morikawa, "Coupling simulation system of annual building energy and microclimate," in *Building Simulation*, vol. 7, pp. 123–129, Springer, 2014.

[160] S. Ramesh and K. P. Lam, "Urban energy information modeling–a framework for coupling macro-micro factors affecting building energy consumption," in *14th International IBPSA Conference, edited by J. Mathur and V Garg*, pp. 601–608, 2015.

[161] M. Palme and A. Salvati, "Uwg-trnsys simulation coupling for urban building energy modeling," 2018.

[162] G. Evola, L. Marletta, and D. Cimino, "Weather data morphing to improve building energy modeling in an urban context," *Mathematical Modelling of Engineering Problems*, vol. 5, no. 3, pp. 211–216, 2018.

[163] J. Bouyer, C. Inard, and M. Musy, "Microclimatic coupling as a solution to improve building energy simulation in an urban context," *Energy and Buildings*, vol. 43, no. 7, pp. 1549–1559, 2011.

[164] L. Malys, M. Musy, and C. Inard, "Microclimate and building energy consumption: Study of different coupling methods," *Advances in Building Energy Research*, vol. 9, no. 2, pp. 151–174, 2015.

[165] E. R&D, "Code saturne 1.3.2 theory and programmer's guide." http://www. code-saturne. org, 2008.

[166] K. Athamena, J.-F. Sini, J.-M. Rosant, and J. Guilhot, "Numerical coupling model to compute the microclimate parameters inside a street canyon: Part i: Methodology and experimental validation of surface temperature," *Solar Energy*, vol. 174, pp. 1237–1251, 2018.

[167] J. Allegrini, V. Dorer, and J. Carmeliet, "Influence of the urban microclimate in street canyons on the energy demand for space cooling and heating of buildings," *Energy and Buildings*, vol. 55, pp. 823–832, 2012.

[168] D. Mauree, S. Coccolo, J. Kaempf, and J.-L. Scartezzini, "Multi-scale modelling to evaluate building energy consumption at the neighbourhood scale," *PloS one*, vol. 12, no. 9, 2017.

[169] J. Allegrini and J. Carmeliet, "Simulations of local heat islands in zürich with coupled cfd and building energy models," *Urban climate*, vol. 24, pp. 340–359, 2018.

[170] D. Maiullari, M. Martin, and M. Pijpers-Van Esch, "Urban microclimate and energy performance,"

[171] A. Gros, *Modelisation de la demande energetique des batiments a l' echelle d' un quartier*. Phd thesis, University of La Rochelle, 2013.

[172] Y. Kikegawa, Y. Genchi, H. Yoshikado, and H. Kondo, "Development of a numerical simulation system toward comprehensive assessments of urban warming countermeasures including their impacts upon the urban buildings' energy-demands," *Applied Energy*, vol. 76, no. 4, pp. 449–466, 2003.

[173] C. de Munck, G. Pigeon, V. Masson, F. Meunier, P. Bousquet, B. Tréméac, M. Merchat, P. Poeuf, and C. Marchadier, "How much can air conditioning increase air temperatures for a city like paris, france?," *International Journal of Climatology*, vol. 33, no. 1, pp. 210–227, 2013.

[174] F. Salamanca, A. Martilli, M. Tewari, and F. Chen, "A study of the urban boundary layer using different urban parameterizations and high-resolution urban canopy parameters with wrf," *Journal of Applied Meteorology and Climatology*, vol. 50, no. 5, pp. 1107–1128, 2011.

[175] Y. Wen and Z. Lian, "Influence of air conditioners utilization on urban thermal environment," *Applied Thermal Engineering*, vol. 29, no. 4, pp. 670–675, 2009.

[176] C.-M. Hsieh, T. Aramaki, and K. Hanaki, "The feedback of heat rejection to air conditioning load during the nighttime in subtropical climate," *Energy and Buildings*, vol. 39, no. 11, pp. 1175–1182, 2007.

[177] D. J. Sailor, "A review of methods for estimating anthropogenic heat and moisture emissions in the urban environment," *International journal of climatology*, vol. 31, no. 2, pp. 189–199, 2011.

[178] J. Blanke, C. Beder, E. Twomey, S. A. Ozdemir, and M. Klepal, "E2district: Behaviour demand response," in *Multidisciplinary Digital Publishing Institute Proceedings*, vol. 1, p. 691, 2017.

[179] S. Y. Abdelouadoud, R. Girard, and T. Guiot, "Planning-oriented yearly simulation of energy storage operation in distribution system for profit maximization, voltage regulation and reserve provisioning," 2013.

[180] M. Bourdeau, P. Riederer, Y. Rezgui, and J. Desmedt, "An ict framework for coupling renewables and energy storage in low carbon districts and cities," in *2013 1st International Conference & Exhibition on the Applications of Information Technology to Renewable Energy Processes and Systems*, pp. 133–138, IEEE, 2013.

[181] "Resilient project-coupling renewable, storage and icts, for low carbon intelligent energy management at district level." `https://cordis.europa.eu/project/id/314671`. Accessed: 2012-09-01.

[182] "Thermoss project-building and district thermal retrofit and management solutions." `https://thermoss.eu/dimosim/`. Accessed: 2016-09-01.

[183] J. Brau, J.-J. ROUX, P. Depecker, J. Croizier, and A. Gaignou, "Micro-informatique et comportement thermique des bâtiments en régime dynamique: Codyba," *Génie climatique*, no. 11, pp. 15–23, 1987.

[184] "Pyephem astronomy library." `https://pypi.org/project/pyephem/`. Accessed: 2012-09-01.

[185] J. Bernard, E. Bocher, G. Petit, and S. Palominos, "Sky view factor calculation in urban context: Computational performance and accuracy analysis of two open and free gis tools," *Climate*, vol. 6, no. 3, 2018.

[186] W. Holmgren, C. Hansen, and M. Mikofski, "pvlib python: A python package for modeling solar energy systems," *Journal of Open Source Software*, vol. 3, no. 29, p. 884, 2018.

[187] C. Doswell, "Thermodynamic analysis procedures at the national severe storms forecast center," in *Conference on Weather Forecasting and Analysis, 9 th, Seattle, WA*, pp. 304–309, 1982.

[188] F. W. Dittus, "Heat transfer in automobile radiators of the tubler type," *Univ. Calif. Pubs. Eng.*, vol. 2, p. 443, 1930.

[189] A. P. Colburn, "A method of correlating forced convection heat transfer data and a comparison with fluid friction," *Trans Am Inst Chem Engrs*, vol. 29, pp. 174–210, 1993.

[190] C. Geuzaine and J.-F. Remacle, "Gmsh: A 3-d finite element mesh generator with built-in pre- and post-processing facilities," *International Journal for Numerical Methods in Engineering*, vol. 79, no. 11, pp. 1309–1331, 2009.

[191] F. Miguet, *Paramètres physiques des ambiances architecturales: Un modèle numérique pour la simulation de la lumière naturelle dans le projet urbain.* PhD thesis, University of Nantes, France, 2000.

[192] F. Miguet and D. Groleau, "A daylight simulation tool for urban and architectural spaces-application to transmitted direct and diffuse light through glazing," *Building and Environment*, vol. 37, no. 8, pp. 833 – 843, 2002.

[193] J. Spencer, "Fourier series reprensentation of the position of the sun," *Search*, vol. 2, no. 5, p. 172, 1971.

[194] R. Kittler and P. Valko, "Radiance distribution on densely overcast skies: comparison with cie luminance standard," *Solar Energy*, vol. 51, no. 5, pp. 349–355, 1993.

[195] R. Perez, R. Seals, and J. Michalsky, "All-weather model for sky luminance distribution-preliminary configuration and validation," *Solar energy*, vol. 50, no. 3, pp. 235–245, 1993.

[196] *Thermal Analysis Research Program Reference Manual, National Bureau of Standards*.

[197] R. Röckle, *Bestimmung der Strömungsverhältnisse im Bereich komplexer Bebauungsstrukturen*. PhD thesis, 1990.

[198] M. J. Brown, "Urban dispersion: challenges for fast response modeling," tech. rep., Los Alamos National Laboratory, 2004.

[199] A. Gowardhan, M. Brown, D. Decroix, E. Pardyjak, and M. Nelson, "Evaluation of the quic pressure solver using wind-tunnel data from single and multi-building experiments," in *6th AMS Urban Environmental Symposium, Atlanta, GA*, 2006.

[200] M. D. Williams, M. J. Brown, and E. M. Pardyjak, "Development of a dispersion model for flow around buildings," in *Fourth Symposium on the Urban Environment*, 2002.

[201] H. Kaplan and N. Dinar, "A lagrangian dispersion model for calculating concentration distribution within a built-up domain," *Atmospheric Environment*, vol. 30, no. 24, pp. 4197–4207, 1996.

[202] D. Boswell and M. Brown, "Quic start guide quick urban & industrial complex (quic) dispersion modeling system," *Los Alamos National Laboratory*, 2004.

[203] N. Bagal, E. Pardyjak, and M. Brown, "Improved upwind cavity parameterization for a fast response urban wind model," in *84th Annual AMS Meeting. Seattle, WA*, 2004.

[204] R. Hosker, "Flow and diffusion near obstacles," *Atmospheric science and power production*, 1984.

[205] J. Fackrell, "Parameters characterising dispersion in the near wake of buildings," *Journal of Wind Engineering and Industrial Aerodynamics*, vol. 16, no. 1, pp. 97–118, 1984.

[206] W. Snyder and R. Lawson Jr, "Wind-tunnel measurements of flow fields in the vicinity of buildings," tech. rep., American Meteorological Society, Boston, MA (United States), 1994.

[207] N. Dinar, "Mass consistent models for wind distribution in complex terrain-fast algorithms for three dimensional problems," *Boundary-layer meteorology*, vol. 30, no. 1-4, pp. 177–199, 1984.

[208] M. Neophytou, A. Gowardhan, and M. Brown, "An inter-comparison of three urban wind models using oklahoma city joint urban 2003 wind field measurements," *Journal of Wind Engineering and Industrial Aerodynamics*, vol. 99, no. 4, pp. 357–368, 2011.

[209] P. Depecker, C. Menezo, J. Virgone, and S. Lepers, "Design of buildings shape and energetic consumption," *Building and Environment*, vol. 36, no. 5, pp. 627–635, 2001.

[210] *Room thermal response factors*.

[211] A. Gros, E. Bozonnet, and C. Inard, "Cool materials impact at district scale-coupling building energy and microclimate models," *Sustainable Cities and Society*, vol. 13, pp. 254–266, 2014.

[212] B. Delaunay *et al.*, "Sur la sphere vide," *Izv. Akad. Nauk SSSR, Otdelenie Matematicheskii i Estestvennyka Nauk*, vol. 7, no. 793-800, pp. 1–2, 1934.

[213] E. Bozonnet, *Impact des microclimats urbains sur la demande énergétique des bâtiments : Cas de la rue canyon*. PhD thesis, University of La Rochelle, La Rochelle, 2005.

[214] "Google sketchup." https://www.sketchup.com.

[215] QGIS Development Team, *QGIS Geographic Information System*. Open Source Geospatial Foundation, 2009.

[216] I. D. Stewart and T. R. Oke, "Local climate zones for urban temperature studies," *Bulletin of the American Meteorological Society*, vol. 93, no. 12, pp. 1879–1900, 2012.

[217] N. Tornay, R. Schoetter, M. Bonhomme, S. Faraut, and V. Masson, "Genius: A methodology to define a detailed description of buildings for urban climate and building energy consumption simulations," *Urban Climate*, vol. 20, pp. 75–93, 2017.

[218] M. F. Jentsch, P. A. James, L. Bourikas, and A. S. Bahaj, "Transforming existing weather data for worldwide locations to enable energy and building performance simulation under future climates," *Renewable Energy*, vol. 55, pp. 514 – 524, 2013.

[219] N. Nakicenovic, R. Swart, *et al.*, "Emissions scenarios. special report of the intergovernmental panel on climate change," 2000.

[220] L. Mora, *Prédiction des performances thermo-aérauliques des bâtiments par association de modèles de différents niveaux de finesse au sein d'un environnement orienté objet*. PhD thesis, Université de la Rochelle, 2003.

[221] M. Santamouris and P. Wouters, *Building ventilation: the state of the art*. Routledge, 2006.

[222] J. Hensen, "Modelling coupled heat and airflow: ping pong vs. onions," in *DOCUMENT-AIR INFILTRATION CENTRE AIC PROC*, pp. 253–253, OSCAR FABER PLC, 1995.

[223] W. Keilholz, P. Riederer, and V. Ducreux, "Solving differential equations in trnsys without programming," in *Proc. Eleventh International IBPSA Conference (IBPSA)*, 2009.

[224] J. R. C. of the European Commission and J. Bloem, *System Identification Applied to Building Performance Data*. European Commission, 1994.

[225] N. Lauzet, A. Rodler, M. Musy, M.-H. Azam, S. Guernouti, D. Mauree, and T. Colinart, "How building energy models take the local climate into account in an urban context–a review," *Renewable and Sustainable Energy Reviews*, vol. 116, p. 109390, 2019.

[226] A. Perera, S. Coccolo, J.-L. Scartezzini, and D. Mauree, "Quantifying the impact of urban climate by extending the boundaries of urban energy system modeling," *Applied Energy*, vol. 222, pp. 847–860, 2018.

[227] R. Geiger, "Überarbeitete neuausgabe," *Köppen-Geiger/Klima der Erde.(Wandkarte 1: 16 Mill.)–Klett-Perthes, Gotha*, 1961.

[228] W. Köppen, "Versuch einer klassifikation der klimate, vorzugsweise nach ihren beziehungen zur pflanzenwelt," *Geographische Zeitschrift*, vol. 6, no. 11. H, pp. 593–611, 1900.

[229] P. Consultants, "Analyse détaillée du parc résidentiel existant," tech. rep., Agence Qualite Construction, 2017.

[230] A. Dallman, S. Magnusson, R. Britter, L. Norford, D. Entekhabi, and H. J. Fernando, "Conditions for thermal circulation in urban street canyons," *Building and environment*, vol. 80, pp. 184–191, 2014.

[231] D. Saelens, I. De Jaeger, F. Bünning, M. Mans, A. Vandermeulen, B. Van der Heijde, E. Garreau, A. Maccarini, Ø. Rønneseth, I. Sartori, *et al.*, "Towards a destest: a district energy simulation test developed in ibpsa project 1," in *Building SimulationConference of International Building Performance Simulation Association*, pp. 3569–3577, IBPSA, 2019.